Interfacial Rheometry: from Lipid Monolayers Towards Bilayers

Damian Renggli

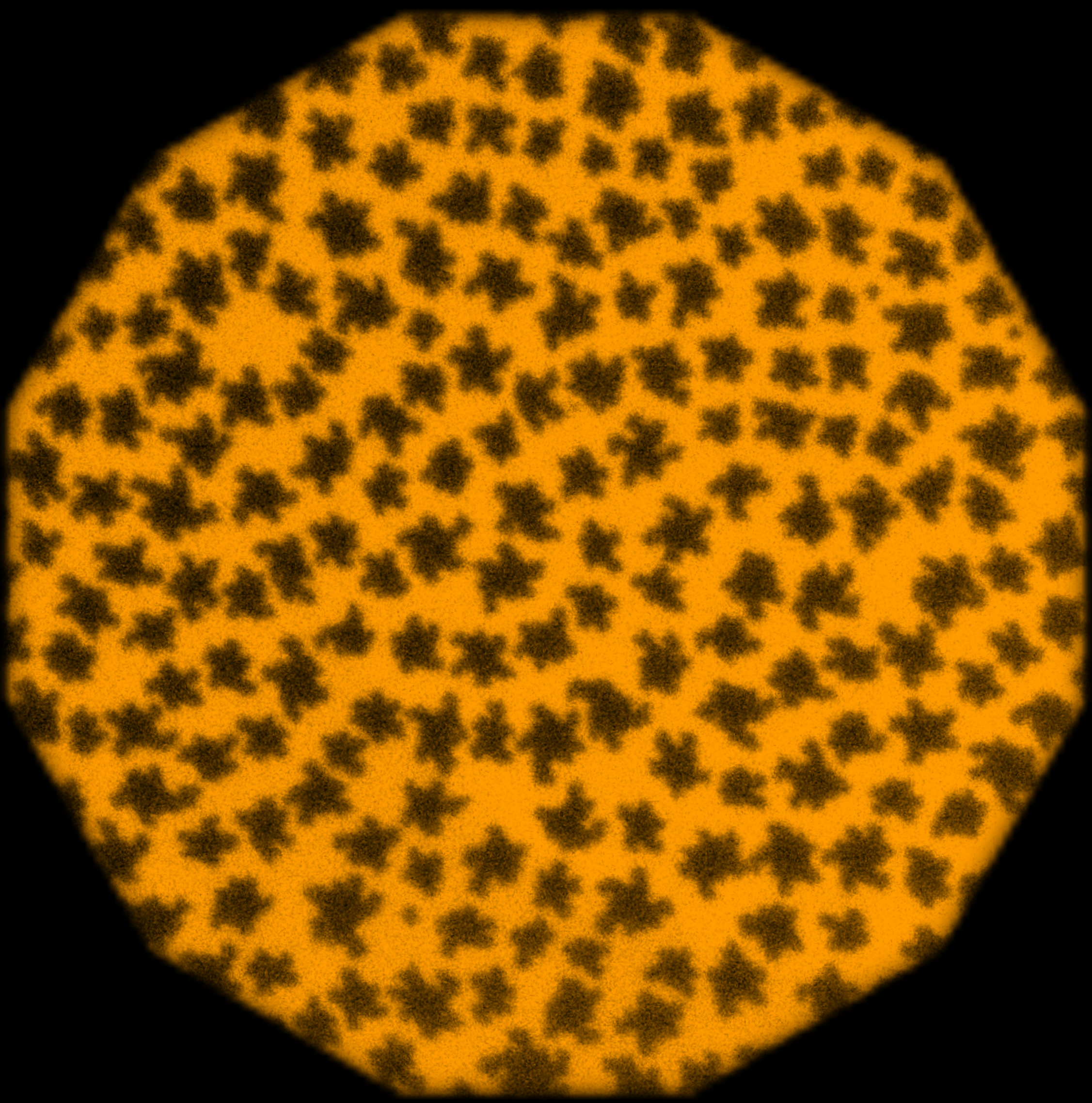

Supervisor:
Prof. Dr. Jan Vermant

Diss. No. ETH 28296
Zürich 2022

DISS. ETH NO. 28296

Interfacial Rheometry: from Lipid Monolayers Towards Bilayers

A thesis submitted to attain the degree of

DOCTOR OF SCIENCES of ETH ZURICH

(Dr. Sc. ETH ZURICH)

presented by

DAMIAN RENGGLI

MSc ETH in Materials, ETH Zürich

born on 22.08.1991

citizen of Luzern LU, Switzerland
and Entlebuch LU, Switzerland

accepted on the recommendation of

Prof. Dr. Jan Vermant, (examiner, doctoral thesis supervisor)
Prof. Dr. Lucio Isa, (co-examiner)
Prof. Dr. Hans-Christian Öttinger, (co-examiner)
Prof. Dr. Todd Squires, (co-examiner)

2022

Acknowledgments

I would like to thank Jan Vermant for giving me the opportunity to work on this project and introducing me to the rheology community. I appreciated the freedom for independent and individualistic work strategies. I greatly enjoyed the possibility to visit many international conferences and getting exposed to research groups at world renowned institutes. One example is the acquaintance with Randy Ewoldt, who was spending his sabbatical in our group. Many hours of discussion in the Soft Living room led to the development of operating windows and my first paper as first author.

My greatest thanks go to each current and previous member of the Soft Materials group. Each softie contributed to an extremely nice and productive environment, where friendships beyond regular work colleagues are made. Kirill has to be mentioned in particular. He contributes a lot to a very welcoming atmosphere and can be thought of the spirit of the group, in addition to all his kind and always immediate help in the lab. I am also very grateful on how he handled us and brought us through the difficult times of the pandemic.

The limoncello-team led by Stephan and joined by Florence and Geppetto was recently contributing countless hours of joy in Geordies and on the terrace. The curiosity to find new flavors led to an amazing variety of different cellos of which there was always a suitable choice for each moment. Stephan was not only there for spirits, but also helping with creative solutions to many technical challenges. Christian Furrer was always very helpful to turn these creative solutions into feasible projects and designed and constructed many parts for me.

I am very glad that I ended up in the Softiez group and enjoyed every moment. Therefore, I would also like to thank Lucio Isa who recommended me to Jan after I finished my master's thesis in his lab.

I had always amazing office peeps throughout my time in H504: Martina, Victoria, Laura, Alexandra, Pierre, and Maria Clara thank you for contributing to a very nice office environments. We might have neglected some plants in the office, but we always had a lookout for each other regarding difficult experiments, deciphering hand writings, etc. Special thanks go also to Raphi Schaller for integrating me in the group when I arrived and his cozy invitations with delicious food.

During the beginning of my PhD, I had a lot of valuable experiences with people from music platform. It was amazing to witness the growth and dynamics of the music network, the participation of concerts, parties (ESF), courses, open mics, and connections to other associations like the academic orchestra. Thank you all for providing this very nice community.

Last but not least, I would like to thank my family and friends for supporting me in all situations.

Abstract

This thesis investigates what is known as fluidity – or more precisely the interfacial rheology – of phospholipid bilayers and monolayers. Bilayers are of interest because they constitute the cell membrane and their fluidity is important in many biological processes for the physiology of the cell, e.g. cell homeostasis, cell signaling, and the formation of the metastatic cancer cells. Phospholipid monolayers have a relevance in itself, e.g. in lung surfactant functioning, and are used in this thesis as model material fora bilayer's leaflet. First, operating windows for interfacial rheometry are developed. They enable the measurement of these materials with clean kinematics. In a second step, the interfacial rheology of these monolayers is evaluated at conditions to be relevant in biological applications and to be comparable to phospholipid bilayers.

Interfacial rheology becomes important when surface active species such as surfactants, particles or proteins are present in sufficient quantities at liquid-liquid interfaces and interact (laterally) between themselves. Interfacial rheometry is however challenging for various reasons. The mechanical response of the thin interface is often weaker compared to that of bulk materials, simply due to the smaller material volume probed, and so one is often measuring close to the lower force and torque limits of rheometers, hence signal to noise ratios merit close attention. Also the role of both instrument and sample inertia is more important for interfacial, compared to bulk rheometrical methods. Effects of misalignment and imperfections of the measurement geometries lead to effects of surface and line tension. Finally, peculiar for interfacial rheometry is the need to de-convolute the contributions of flow and deformation in the surrounding phases from that at the interface. Whereas some of these aspects have received attention in previous work, a clear and unambiguous view on the operating limits of interfacial rheometers has been missing. In the present work, we investigate the different experimental challenges and develop a generic methodology which provides a clear definition of the operating limits of various interfacial rheometers including the interfacial needle shear rheometer, the double wall ring and the bi-cone geometries. We validate this methodology by investigating the limitations defined intrinsically by the instrument as well as the ones emerging from the properties of the interface of interest for an interface composed of fatty alcohols which represents a challenging test-case. The results provide cautionary examples and clear guidelines for anyone measuring interfacial rheology with these direct rheological

techniques.

Langmuir monolayers of 1,2-dipalmitoyl-*sn*-glycero-3-phosphocholine (DPPC) phospholipids at the liquid–liquid interface are investigated for their mechanical properties and phase behavior. DPPC monolayers undergo a phase separation between liquid expanded (LE) and liquid compressed (LC) phases because of the efficient packing of the fully saturated palmitic acid tails. The interface was thermally annealed before being compressed to relevant interfacial pressures to arrive at *thermally structured* interfaces due to the high melting temperature of the hydrophobic tails ($T_m = 42\,^{\circ}\mathrm{C}$). The interfacial needle stress rheometer (ISR) was upgraded with a custom built epi-fluorescent microscope to measure the small amplitude shear rheology and phase morphology of the phase separated monolayer *in situ*.

Interfacial rheology can be carefully measured within the operating windows and the influence of different bulk phases on the interactions between the lipid molecules is investigated. On the one hand, introducing a salt buffer as aqueous bulk phase to the liquid–air system reduces the repulsive dipolar interactions between the headgroups of the phospholipid moieties. As a consequence, compression isotherms show a negative hysteresis during compression and expansion isotherms, and the domains formed by the LC phases are less dendritic which is agreement with the theory by McConnell and coworkers [1]. On the other hand, adding an oil phase as upper bulk phase modifies the van der Waals interactions with oil molecules which most likely leads to a swelling of the interface. The interfacial viscosity increases by orders of magnitude because the lipids spread much better into the liquid expanded phase. Furthermore, relative elastic contributions to the complex interfacial viscosity are large and the interface is strongly viscoelastic with a limited linear regime.

The interfacial rheology of DPPC at water–air and temperatures of 20 °C and below shows an increasing norm of the complex interfacial viscosity and an increasing elastic contribution with increasing interfacial pressure, hence the data agrees with Hermans et al. [2]. At higher temperatures, the ratio between viscous and elastic contributions does not depend on surface pressures in a systematic way any more. The same was observed for DPPC at interfaces with an upper oil bulk phase.

The fluorescent images revealed a strong deformation of the LC phases during the compression prior to the rheological measurements. This leads to a mixing of the LE and LC phases which affects both the elastic contribution as well as the norm of the complex viscosity. In the case of water–air interfaces, the presence of "slip lines" or shear localized banding within the interface was observed. This demonstrates the necessity of preventing pre-shear of the interface during the compression of the interface to relevant surface pressures.

To simulate crowding of the interface, as e.g. by high concentration of embedded proteins in a lipid membrane, the complex interfacial shear viscosity is measured as a function of the area fraction of the solid-like LC phase. For this, suspended monolayers of phospholipid mixtures at a salt buffer–oil interface are investigated as a model material for one leaflet of a phospholipid bilayer. The interfacial pressure is comparable to those normally encountered in a phospholipid bilayer ($30\,\mathrm{mN\,m^{-1}}$ to $40\,\mathrm{mN\,m^{-1}}$ [3]). The interface is carefully prepared to avoid pre-shear, by compression at high temperatures, where the LC phase is fully molten. The completely homogeneous monolayer is then cooled at constant interfacial area and undergoes a *temperature induced phase separation*.

The area fraction of the LC phase is varied by changing the temperature and adding the phospholipid and 1,2-dioleoyl-*sn*-glycero-3-phosphocholine (DOPC), which is not able to form the LC phase, to DPPC. With this approach, the large deformation of LC phases and the emergence of shear banding reported previously can be prevented and the norm of the complex interfacial viscosity, as well as its elastic contribution, has a more intuitive dependence on interfacial pressure.

Furthermore, it is shown that the complex interfacial viscosity does not diverge at the highest area fractions of the LC phase (*i.e.* crowding of the interface) in contrast to what would be expected for a hard disk system. The presence of a finite interfacial compressibility of the LE phase could prevent the lubrication pressure from diverging. In bulk systems, the medium is always assumed to be incompressible, which makes it difficult to find a compressible analogue for interfacial systems. Furthermore, the mismatch in compressibility of the interface and the incompressible bulk phases does require complicated recirculating currents, orthogonal to the interface, or the presence of an as yet not measurable slip between the interface and bulk phases.

Preliminary data from microrheological experiments on free-standing and planar bilayers using the LAMBs setup, which was developed in our group [4], are acquired to compare the magnitude of the complex interfacial shear viscosity in phospholipid monolayers and bilayers. The measured diffusion coefficients were found to be larger than predicted by the Saffman-Delbrück model, which describes the lateral diffusive motion of a cylinder embedded in an incompressible membrane. Further investigation is necessary to identify appropriate hydrodynamic models and to translate the insights on crowded phospholipid monolayer systems acquired in the presented work to bilayer systems.

Zusammenfassung

In dieser Arbeit wird die Fluidität – oder Grenzflächenrheologie – von Phospholipid-Doppelschichten untersucht. Dieses Material ist von Interesse, weil es die Zellmembran bildet und seine Fluidität für viele biologische Prozesse wichtig ist, z.B. Zellhomöostase, Zellsignalisierung und die Bildung von metastatischen Krebszellen. Phospholipid-Monoschichten werden als Modellmaterial für eine Seite der Doppelschicht verwendet. Zunächst werden Betriebsfenster entwickelt, die es ermöglichen, diese Materialien mit sauberer Kinematik zu messen. In einem zweiten Schritt wird die Grenzflächenrheologie dieser Monoschichten unter relevanten Bedingungen gemessen, um mit Phospholipid-Doppelschichten zu vergleichen.

Die Grenzflächenrheologie wird wichtig, wenn oberflächenaktive Stoffe wie Tenside, Partikel oder Proteine in ausreichender Menge an Flüssig-Flüssig-Grenzflächen vorhanden sind und wechselwirken. Messungen der Grenzflächenrheometrie sind aus verschiedenen Gründen eine Herausforderung. Die mechanische Reaktion der dünnen Grenzfläche ist oft schwächer als die von Bulk-Materialien, so dass man oft in der Nähe der unteren Kraft- und Drehmomentgrenzen von Rheometern misst und das Signal-Rausch-Verhältnis grössere Aufmerksamkeit verdient. Auch die Rolle der Trägheit von Instrument und Probe ist bei der Grenzflächenrheometrie wichtiger als bei der Volumenrheometrie. Auswirkungen von Ausrichtungsfehlern und Unzulänglichkeiten der Messgeometrien führen zu Auswirkungen der Oberflächen- und Linienspannung. Eine Besonderheit der Grenzflächenrheometrie ist schliesslich die Notwendigkeit, die Beiträge des Fliessens und der Verformung in den umgebenden Phasen von denjenigen an der Grenzfläche zu trennen. Während einige dieser Aspekte in früheren Arbeiten bereits berücksichtigt wurden, fehlte bisher eine klare und eindeutige Aussage über die Einsatzgrenzen von Grenzflächenrheometern. In der vorliegenden Arbeit untersuchen wir die verschiedenen experimentellen Herausforderungen und entwickeln eine generische Methodik, die eine klare Definition der Betriebsgrenzen verschiedener Grenzflächenrheometer, einschliesslich des Grenzflächen-Nadelscherrheometers, des Doppelwandrings und der Bi-Konus-Geometrie, ermöglicht. Wir validieren diese Methodik, indem wir die durch das Instrument selbst definierten Grenzen sowie die Grenzen, die sich aus den Eigenschaften der interessierenden Grenzfläche ergeben, für eine aus Fettalkoholen bestehende Grenzfläche untersuchen, die einen schwierigen Testfall darstellt. Die Ergebnisse liefern warnende Beispiele und klare Richtlinien für alle, die die

Grenzflächenrheologie mit diesen direkten rheologischen Techniken messen.

Langmuir-Monoschichten aus 1,2-Dipalmitoyl-*sn*-glycero-3-phosphocholin (DPPC) Phospholipiden an der Flüssig-Flüssig-Grenzfläche werden auf ihre mechanischen Eigenschaften und ihr Phasenverhalten untersucht. DPPC-Monoschichten durchlaufen eine Phasentrennung zwischen flüssigen expandierten (LE) und flüssigen komprimierten (LC) Phasen aufgrund der effizienten Packung der vollständig gesättigten Palmitinsäureschwänze. Die Grenzfläche wurde vor dem Komprimieren auf relevante Grenzflächendrücke temperiert, um aufgrund der hohen Schmelztemperatur der hydrophoben Schwänze ($T_m =$ 42 °C) zu *thermisch strukturierten* Grenzflächen zu gelangen. Das Grenzflächen-Nadelscherrheometers (ISR) wird mit einem speziell angefertigten Epifluoreszenzmikroskop aufgerüstet, um die Scherrheologie mit kleiner Amplitude und die Phasenmorphologie der phasenseparierten Monoschicht *in situ* zu messen.

Die Grenzflächenrheologie wird innerhalb des Betriebsfensters sorgfältig gemessen und der Einfluss der verschiedenen volumetrischen Phasen auf die Wechselwirkungen zwischen den Lipidmolekülen untersucht. Einerseits reduziert die Einführung eines Salzpuffers als wässrige Bulkphase in das Flüssig-Luft-System die abstossenden dipolaren Wechselwirkungen. Infolgedessen zeigen die Kompressionsisothermen eine negative Hysterese bei Kompression, die LC-Phasen sind weniger dendritisch, was mit der Theorie von McConnell übereinstimmt, und die Phasen aggregieren. Andererseits können die Lipidmoleküle durch das Hinzufügen einer Ölphase als obere Massephase van der Waals-Wechselwirkungen mit Ölmolekülen eingehen, was zu einer Quellung der Grenzfläche führt. Die Grenzflächenviskosität nimmt um Grössenordnungen zu, da sich die Lipide viel besser in der flüssigen expandierten Phase ausbreiten. Darüber hinaus ist der relative elastische Beitrag zur komplexen Grenzflächenviskosität gross und die Grenzfläche ist stark viskoelastisch mit einem begrenzten linearen Bereich.

Die Grenzflächenrheologie von DPPC bei Wasser-Luft und Temperaturen von 20 °C und darunter zeigt eine zunehmende Norm der komplexen Grenzflächenviskosität und einen zunehmenden elastischen Beitrag mit zunehmendem Grenzflächendruck, so dass die Daten mit Hermans et al. [2] übereinstimmen. Bei höheren Temperaturen hängt das Verhältnis zwischen viskosen und elastischen Beiträgen nicht mehr systematisch von den Oberflächendrücken ab. Das Gleiche wurde für DPPC an Grenzflächen mit einer oberen Öl-Phase beobachtet.

Die Fluoreszenzbilder zeigten eine starke Verformung der LC-Phasen während der Kompression vor den rheologischen Messungen. Dies führt zu einer Vermischung der LE- und LC-Phasen, was sich sowohl auf den elastischen Beitrag als auch auf die Norm der komplexen Viskosität auswirkt. Im Fall von Wasser-Luft wurde das Vorhandensein von “Gleitlinien” oder Scherbändern an der Grenzfläche beobachtet. Dies zeigt, dass eine Vorscherung der Grenzfläche während der Kompression der Grenzfläche auf relevante Oberflächendrücke verhindert werden muss.

Um dichte Grenzfläche zu simulieren, wie sie z.B. durch eine hohe Konzentration von eingebetteten Proteinen in einer Lipidmembran entsteht, wird die komplexe Grenzflächen-Scherviskosität als Funktion des Flächenanteils der feststoffartigen LC-Phase gemessen. Dazu wurden Phospholipid-Monoschichten aus 1,2-Dipalmitoyl-*sn*-glycero-3-phosphocholin (DPPC) und 1, 2-Dioleoyl-*sn*-glycero-3-phosphocholin (DOPC), die an einer Salzpuffer-Öl-Grenzfläche suspendiert sind, bei Grenzflächendrücken untersucht, die mit dem Zustand in einer Phospholipid-Doppelschicht ($30\,\mathrm{mN\,m^{-1}}$ bis $40\,\mathrm{mN\,m^{-1}}$) als Modellmaterial für eine Seite einer Phospholipid-Doppelschicht vergleichbar sind. Die Grenzfläche wird sorgfältig präpariert, um eine Vorscherung zu vermeiden, indem sie bei hohen Temperaturen komprimiert wird, bei denen die flüssige kondensierte Phase vollständig geschmolzen ist. Die vollständig homogene Monoschicht wird dann bei konstanter Grenzfläche abgekühlt und erfährt eine *temperaturinduzierte* Phasentrennung.

Der Flächenanteil der LC-Phase wird durch Änderung der Temperatur und Zugabe des Phospholipids DOPC variiert, das nicht in der Lage ist, die LC-Phase zu bilden. Mit diesem Ansatz kann die starke Verformung der LC-Phasen und das Auftreten von Scherbändern, über die zuvor berichtet wurde, verhindert werden, und die Norm der komplexen Grenzflächenviskosität sowie ihr elastischer Beitrag haben eine intuitivere Abhängigkeit vom Grenzflächendruck.

Darüber hinaus wird gezeigt, dass die komplexe Grenzflächenviskosität im Gegensatz zu einem Festplattensystem nicht als Funktion des Flächenanteils der LC-Phase (d.h. der Belegung der Grenzfläche) divergiert. Das Vorhandensein einer endlichen Kompressibilität der LE-Phase könnte verhindern, dass der Schmierungsdruck divergiert. In volumetrischen Systemen wird das Medium immer als inkompressibel angenommen, was es schwierig macht, ein kompressibles Analogon für Grenzflächensysteme zu finden. Ausserdem erfordert die unterschiedliche Kompressibilität der Grenzfläche und der inkompressiblen volumetrischen Phasen komplizierte Zirkulationsströme orthogonal zur Grenzfläche oder Schlupf zwischen der Grenzfläche und den Bulk-Phasen.

Vorläufige Daten aus mikrorheologischen Experimenten an freistehenden und planaren Doppelschichten unter Verwendung des LAMBs-Aufbaus, der in unserer Gruppe entwickelt wurde [4], werden zum Vergleich der komplexen Grenzflächen-Scherviskosität in Phospholipid-Monoschichten und Doppelschichten herangezogen. Die gemessenen Diffusionskoeffizienten sind grösser als vom Saffman-Delbrück-Modell vorhergesagt, das die laterale Diffusionsbewegung eines in eine inkompressible Membran eingebetteten Zylinders beschreibt. Weitere Untersuchungen sind erforderlich, um geeignete hydrodynamische Modelle zu finden und die Erkenntnisse über überfüllte Phospholipid-Monoschichten auf Doppelschichten zu übertragen.

Contents

1 Introduction 1

1.1 Lipidomics . . . 3

1.2 Membrane fluidity . . . 7

1.3 Experimental challenges . . . 9

2 Operating Windows for Interfacial Shear Rheology 13

2.1 Introduction . . . 14

  2.1.1 General interfacial momentum balance equation . . . 16

  2.1.2 Interfacial rheometers . . . 18

  2.1.3 Oscillatory measurements of viscoelastic properties . . . 19

2.2 Materials and methods . . . 21

  2.2.1 Monolayer preparation . . . 21

  2.2.2 Interfacial needle shear rheometer . . . 22

  2.2.3 Double wall ring . . . 24

  2.2.4 Bi-cone . . . 25

  2.2.5 Quantifying noise floor and resolution: Fourier analysis . . . 26

2.3 Results . . . 27

  2.3.1 Primary observables . . . 28

  2.3.2 Amplitude ratio and phase angle . . . 31

  2.3.3 Limit lines and operating windows . . . 34

  2.3.4 Instrument limitations . . . 38

  2.3.5 Coupling with the bulk phase . . . 42

  2.3.6 Further experimental difficulties . . . 46

2.4 Conclusion . . . 49

2.5 Supplementary material . . . 51

2.6 Acknowledgments . . . 51

2.7 Appendix: Operation windows . . . 52
    2.7.1 Hexadecanol . . . 52
    2.7.2 DWR noise amplification example . . . 52
    2.7.3 Operating windows for different DWR sizes . . . 53

3 Interfacial Shear Rheology of Phospholipid Monolayers 55
3.1 Introduction . . . 56
3.2 Materials and methods . . . 58
    3.2.1 Chemicals . . . 58
    3.2.2 Bulk phases and lipid handling . . . 59
    3.2.3 Langmuir trough . . . 60
    3.2.4 Interfacial needle shear rheometer (ISR) . . . 60
    3.2.5 Fluorescent setup . . . 61
    3.2.6 Lipid monolayer preparation . . . 62
3.3 Results . . . 64
    3.3.1 Compression isotherms and phase morphology of DPPC at 25 °C . 64
    3.3.2 Interfacial rheology at 25 °C and 30 $\mathrm{mN\,m^{-1}}$ . . . 74
    3.3.3 Effect of temperature and interfacial pressure . . . 79
3.4 Conclusion . . . 85
3.5 Acknowledgments . . . 86

4 Crowded Phospholipid Monolayers Are Fluid 87
4.1 Introduction . . . 88
4.2 Results . . . 92
    4.2.1 Prevention of mechanical history effects . . . 92
    4.2.2 Rheology of mixed lipid monolayers . . . 94
    4.2.3 Crowding the interface . . . 98
    4.2.4 Comparison of a lipid monolayer with a bilayer . . . 101
4.3 Conclusion . . . 103
4.4 Acknowledgments . . . 105
4.5 Materials and methods . . . 105
    4.5.1 Monolayer sample preparation . . . 105
    4.5.2 Bilayer sample preparation . . . 106
    4.5.3 Image analysis . . . 106

5 Conclusion and Outlook **109**

Bibliography **113**

A Supplemental Information: Operating Windows **127**

A.1 Subphase correction algorithm . . . 127
A.2 ISR calibration example . . . 129
A.3 ISR bad data Fourier spectrum example . . . 132
A.4 Noise for DWR ring sizes and driving frequency . . . 133
A.5 Bi-cone Fourier spectrum example and noise . . . 135
A.6 Conversion factors . . . 138
A.7 Torque controlled frequency sweep . . . 140
A.8 DWR compliance . . . 141
A.9 Subphase correction . . . 142
A.10 Probe positioning . . . 143

B Supplemental Information: DPPC Monolayers **147**

B.1 Phase shift induced by inductance of magnetic coils . . . 147
B.2 Brewster angle microscope of DPPC at water–air . . . 149
B.3 Second compression of DPPC at water–air . . . 150
B.4 Second compression of DPPC at buffer–air . . . 151
B.5 Second compression of DPPC at water–oil . . . 152
B.6 Compression without annealing . . . 153

C Supplemental Information: Crowded Interfaces **155**

C.1 Magnetic probes . . . 155
C.2 Stress amplitude sweeps as a function of resulting strain . . . 157
C.3 Deformation of the liquid condensed phase . . . 158
C.4 Two-point tracking results . . . 159

D Scientific Achievements **161**

D.1 Publications in peer-reviewed scientific journals . . . 161
D.2 Contributions to conferences . . . 162
D.3 General contributions to science . . . 163

E Curriculum Vitae **165**

F List of Symbols **167**

G List of Tables **173**

H List of Figures **175**

1 Introduction

A biological cell membrane separates the interior of a cell from the surrounding environment [5]. The membrane consists of small amphiphilic molecules assembled in a double layer, as sketched in Fig. 1.1 in an artist's rendering. The amphiphiles are known as phospholipids and have two hydrophobic tails attached via a glycerol backbone to a polar head group. The hydrophobic interactions, presumably van der Waals interactions, stabilize the formation of the sheet-like structure of the double layer in an aqueous environment [3].

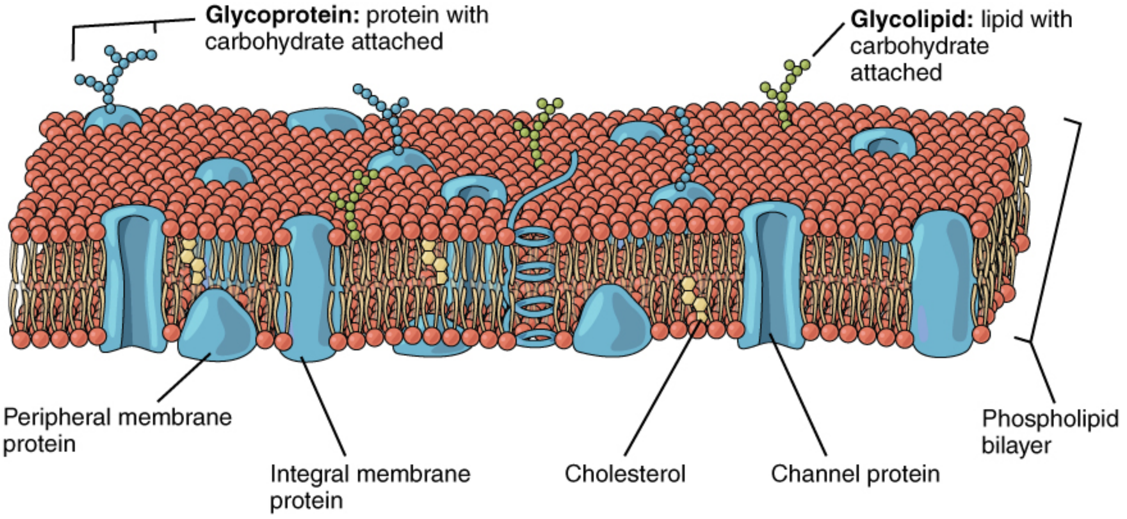
Glycoprotein: protein with carbohydrate attached
Glycolipid: lipid with carbohydrate attached
Peripheral membrane protein
Integral membrane protein
Cholesterol
Channel protein
Phospholipid bilayer

Figure 1.1: **An artist's interpretation of a cell membrane:** Proteins and other molecules are embedded in the phospholipid bilayer. Reproduced from Version 8.25 of the textbook *Anatomy and Physiology*, OpenStax, published April 25, 2013 (`https://openstax.org/books/anatomy-and-physiology/pages/3-1-the-cell-membrane`).

The hydrophobic core of the membrane creates a barrier for water soluble species. However, the relatively large permeability for water and ions suggests that channels have to be present in the membrane [6]. Integral proteins are indeed embedded and span across the membrane to facilitate controlled transport and signaling across the membrane. These transmembrane proteins can act, for example, as ion pumps to maintain a concentration difference of certain ions against their chemical potential gradient. Other proteins are embedded as well and are necessary for numerous tasks like sensing and anchoring, signaling, transport of small molecules, etc. [5]

The first suggestion of an oily layer around a cell for separating the extracellular fluid from the cytoplasm was made in 1904 [7]. Meyer and Overton suggested in their "lipoid theory of narcosis" that the membrane consists of lecithin, another nomenclature of phospholipids, and cholesterol [8]. Capacitance measurements by Fricke in 1925 gave a first estimation of the thickness of a biological membrane, being in the order of several nanometers [9]. There have been efforts to spread lipids, extracted from erythrocyte cells, as monolayer onto a Langmuir trough and compare the monolayer area with the surface area of the cells [10]. Despite flaws in the experiments and mistakes in the analysis, the correct ratio of 2/1 was identified and the structure of a bilayer was proposed. The invention of transmission electron microscopy (TEM) made it possible to confirm the double layer structure by Sjöstrand et al. in 1958 [11]. One of the first TEM images of a synaptic complex showing two membranes is presented in Fig. 1.2A together with a microdensiometer plot which suggests a thickness of a few nanometers, by the two maxima on each peak [12]. Another example of a single membrane is shown in Fig. 1.2B, where the two dark bands represent the polar headgroup region [13]. The absorbance profile in Fig. 1.2C confirms the membrane thickness of a few nanometers.

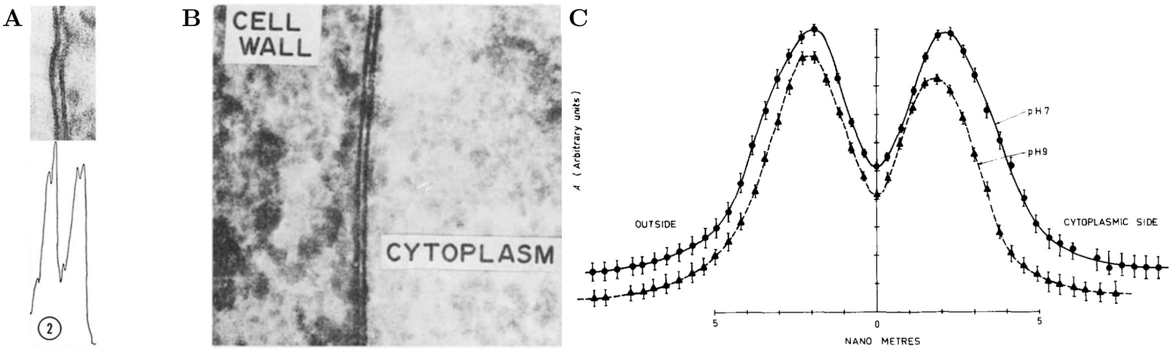

Figure 1.2: **Proof of the bilayer structure:** Transmission electron micrographs of **(A)** a synaptic complex and microdensiometer (reproduced from Robertson [12]) and **(B)** a single plasma membrane at pH 7 with the numerically averaged absorbance profile **(C)** (reproduced from Coster et al. [13]).

Lipid bilayers not only form the cell membrane in mammalian cells but in all eukaryotic and prokaryotic cells. In plants, the cell membrane is anchored to the cell wall by proteins embedded in the membrane. Even viruses can have a phospholipid bilayer as an envelope around the capsid.

The interpretation of phospholipids as a simple solvent for the other constituents in the fluid-mosaic model has been proven too simplified, mostly because of the vast variety of different lipids (lipidomics) and the importance of a tuned membrane fluidity, which are both discussed in the following paragraphs.

1.1 Lipidomics

Lipids is the name used to describe a large variety of biomolecules which are soluble in non-polar solvents. They are classified in eight categories: fatty acids, glycerolipids, glycerophospholipids, sphingolipids, sterols, prenols, saccharolipids, and polyketides [14]. Glycerophospholipids are often referred to as phospholipids. Sphingomyelin are also classified as such but belong to sphingolipids, though. The focus in this work lies on phospholipids because they are the key component in lipid bilayers.

An overview of the chemical structures of some phospholipids is shown in Fig. 1.3. Phospholipids are amphiphilic molecules composed of a hydrophilic *head* containing a phosphate group (shown in red) and two hydrophobic *tails* derived from fatty acids, which are linked either by a glycerol molecule (shown in green) or another alcohol derivative in the case of sphingomyelin (shown in blue).

The hydrophobic tails differ mostly in the length of the carbon chains and the saturation of the hydrogen atoms *i.e.* the presence of double or triple bonds between the carbon atoms. Longer hydrocarbon chains can undergo van der Waals interactions which leads to an increasing melting temperature of the hydrophobic tails with increasing chain length. The presence of unsaturated tails increases their stiffness as rotations are prevented therefore limiting the amount of gauche conformations. However, they disturb an efficient packing of the hydrophobic tails and thus reduces the hydrophobic interactions. [15]

The chemistry of the head group is also important in the geometric structure of the phospholipid. A phosphatidylcholine (PC) head group results in a more cylindrical shape compared to phosphatidylethanolamine (PE) [16], hence the inner leaflet of highly curved regions of the membrane will be enriched with the latter. The head group plays a crucial role in sensing and signaling, for example the presence of phosphatidylserine (PS) head groups on the outer leaflet of the plasma membrane is responsible for initiating cell apoptosis [17]. Other mechanisms, such as degradation of phospholipids in the membrane,

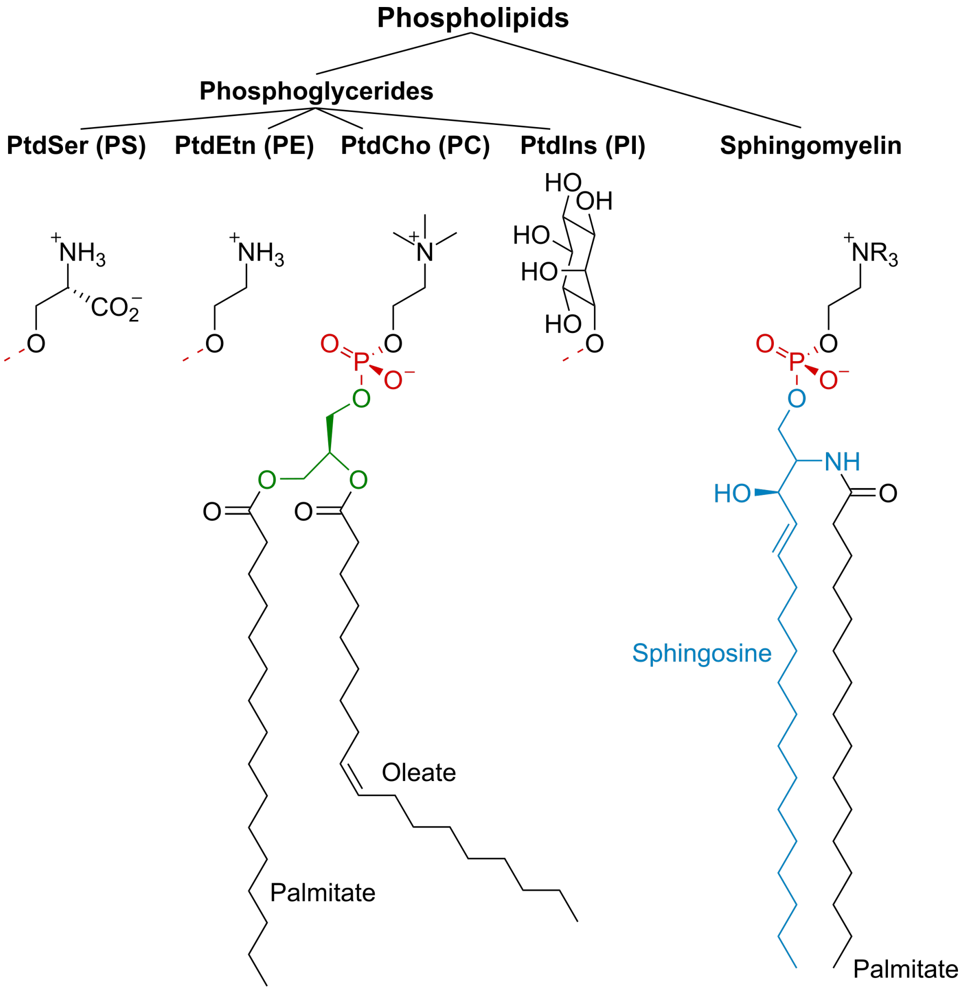
Phospholipids
Phosphoglycerides
PtdSer (PS)
PtdEtn (PE)
PtdCho (PC)
PtdIns (PI)
Sphingomyelin
Sphingosine
Oleate
Palmitate
Palmitate

Figure 1.3: **Chemical structures of membrane phospholipids:** Variations in the phosphoglycerides are shown in the hydrophilic head groups phosphatidylserine (PS), -ethanolamine (PE), -choline (PC), -inositole (PI), and the hydrophobic tail. Image adapted from Wikipedia (`https://commons.wikimedia.org/w/index.php?curid=63827468`, 2022).

allow for signaling phenomena, therefore they can act as first and second messengers in signal transduction and molecular recognition processes [18].

In eukaryotic cells, the cell membrane accounts only for around 50 % of the amount of phospholipid bilayer present [18]. Organelles such as the endoplasmatic reticulum (ER) or mitochondria are also contained by a phospholipid bilayer. The ER is responsible for most of the phospholipids synthesis, however sphingomyelin is synthesized only at the Golgi apparatus. Other organelles are involved as well, as summarized in Fig. 1.4. The phospholipid composition varies strongly throughout the cell. Furthermore, the plasma membrane can be highly asymmetric with respect to the outer and inner leaflets of the membrane, whereas the membrane of the ER is completely symmetric. The phospholipids involved in signaling are mostly synthesized in the the plasma membrane itself. [18]

This subsection demonstrates the complexity both in variety and distribution of lipid molecules as well as their interactions. This is not accounted for in the fluid mosaic model.

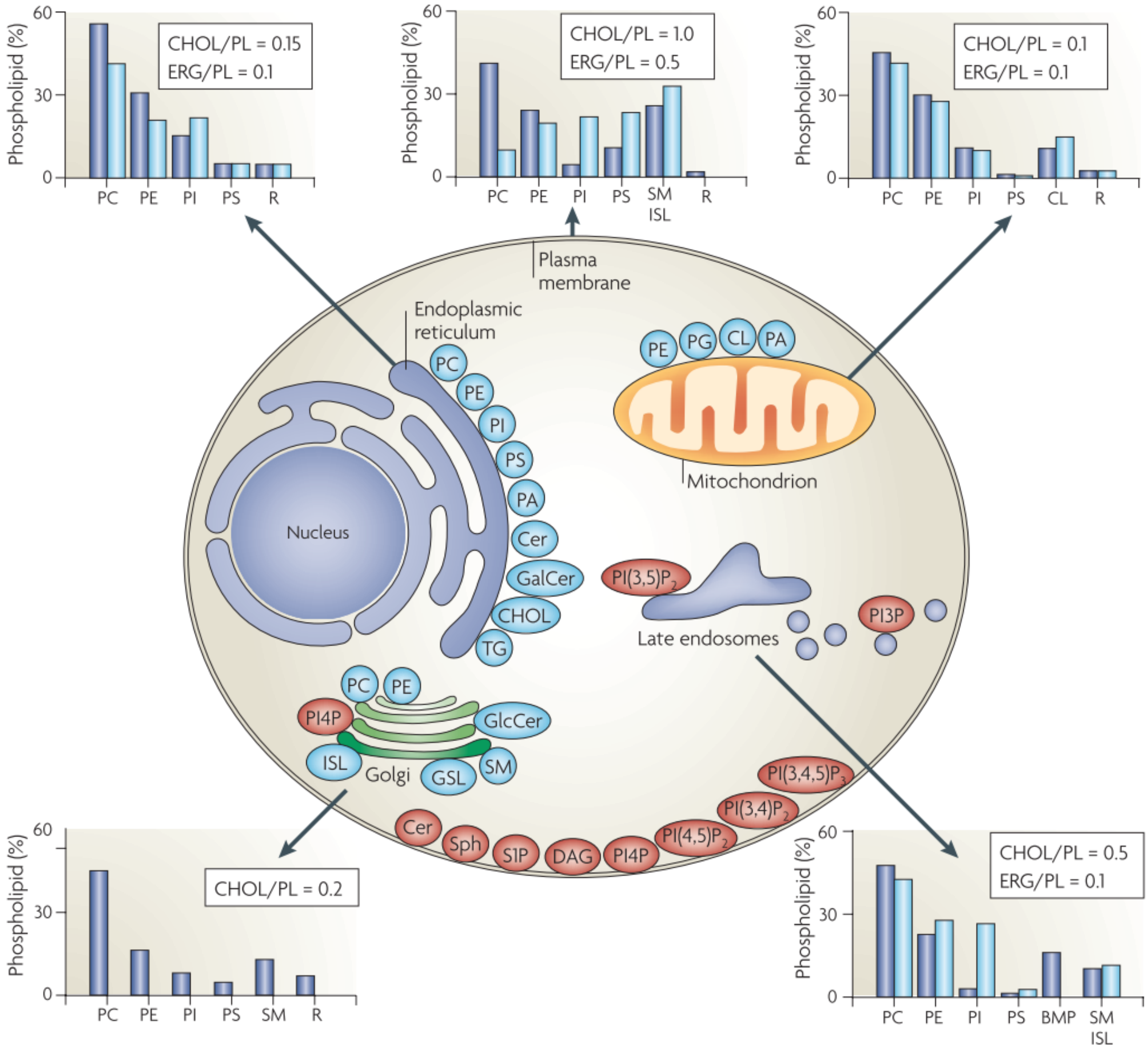
Phospholipid (%)
60
30
0
PC PE PI PS R
CHOL/PL = 0.15
ERG/PL = 0.1
CHOL/PL = 1.0
ERG/PL = 0.5
PC PE PI PS SM ISL R
CHOL/PL = 0.1
ERG/PL = 0.1
PC PE PI PS CL R
Plasma membrane
Endoplasmic reticulum
PC PE PI PS PA Cer GalCer CHOL TG
Nucleus
PE PG CL PA
Mitochondrion
PI(3,5)P2
Late endosomes
PI3P
PC PE PI4P GlcCer ISL Golgi GSL SM
Cer Sph S1P DAG PI4P PI(4,5)P2 PI(3,4)P2 PI(3,4,5)P3
CHOL/PL = 0.2
PC PE PI PS SM R
CHOL/PL = 0.5
ERG/PL = 0.1
PC PE PI PS BMP SM ISL

Figure 1.4: **Lipid synthesis and steady-state composition of cell membranes:** The lipid composition is shown as percentage of the total phospholipid (PL) as molar ratio of cholesterol (in mammals, blue) and ergosterol (in yeast, light blue). The site of synthesis is shown for major phospholipids (blue) and lipids that are involved in signaling (red). Abbreviations are explained in Table 1.1 and the given reference. *R* are remaining lipids. Image reproduced from Meer et al. [18].

Table 1.1: **Lipid terminology:** Abbreviations for the chemical compounds presented in the presented work.

PS	PtdSer	Phosphatidylserine
PE	PtdEtn	Phosphatidylethanolamine
PC	PtdCho	Phosphatidylcholine
PI	PtdIns	Phosphatidylinositole
PG		phosphatidylglycerol
SM		Sphingomyelin
Cer		Ceramide
PA		Phosphatic acid
TG		Triacylglycerol
GalCer		Galactosylceramide
GSLs		Glycosphingolipids
ISL		yeast inositol sphingolipid
DAG		Diacylglycerol
CL		Cardiolipin

Industrial applications

Drug delivery is one of the largest areas for commercial applications of phospholipid systems. The self-assembly of the sheet-like structure into a vesicle, also known as liposomes, makes them ideal for encapsulating hydrophilic drugs. Furthermore, the toxicity is very low since the constituting phospholipids are biomolecules and can be reused for another cell membrane.

Vesicles can even be engineered and utilized in *targeted* drug delivery [19]. Proteins incorporated in the vesicle's membrane can bind to receptors on the target cell and release their drug in very close proximity to them. This type of therapy drastically reduces the secondary effects of drugs as it is only applied at specific sites instead of the whole body. Targeted drug delivery is widely used in cancer treatment [20].

Modification of the composition in order to adjust fluidity, among other parameters, leads to a drastic decrease in adsorption of proteins from the serum. Hence identification by the immune system and degradation by phagocytosis can be greatly prevented [21]. This increases the lifetime of the vesicle. Therefore the circulating time in the blood stream. So-called “stealth” vesicles can be engineered by grafting polyethylene glycol onto the vesicle's surface [22].

Further technical applications are biosensors [23] and permeability studies of drugs through membranes [24].

1.2 Membrane fluidity

In addition to the complexity of cellular lipidomics and the variety of lipids present in the membrane, the mechanical properties have to be tunable depending on the requirements and stimuli of the physiological environment.

Relatively low bending moduli and compressional elasticity, as reported in the work of Boal et al. [25], have been shown to be important for containing and taking up stresses acting on the cell. It has been shown that the membrane is fluid and allows for lateral diffusion of lipids and proteins [18]. The lateral diffusion of membrane components is essential for cell homeostasis. As a consequence, cell signaling and other functions can be regulated by adapting the fluidity of phospholipid bilayers [26].

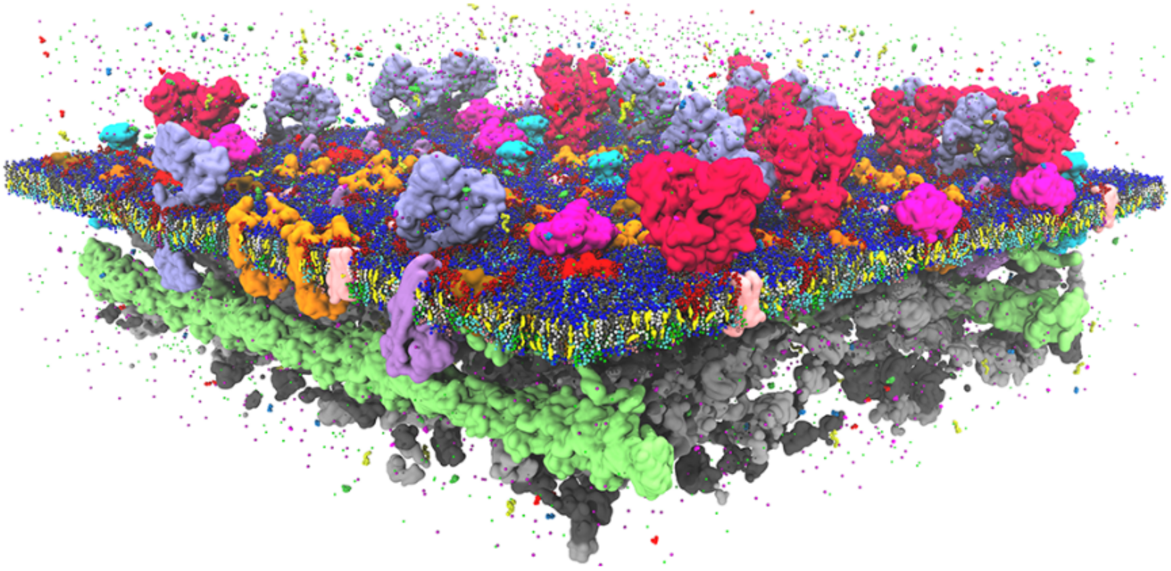

Figure 1.5: **Model of the plasma membrane in full complexity:** A large variety of embedded proteins, actin, cytoskeleton, ions, and solutes are shown. Image reproduced from Marrink et al. [27].

The signal transduction from a heterotrimetric G-protein-couplet hormone receptor relies strongly on membrane fluidity [26]. The binding of the first messenger occurs at the outer surface of the membrane, but transmission to the second messenger passes through the cytosolic phase of the membrane. On the one hand, an increased membrane fluidity is accompanied by an increase in collision frequency. Contrary to expectations, this leads to a decrease in receptor efficiency, because the coupled receptor components can leave the receptor site. On the other hand, a reduction in membrane fluidity results in an insufficient recycling rate of the receptor components. Other types of receptors express an opposite behavior of their mobility upon activation [28]. This demonstrates that the membranes fluidity has to be carefully tuned for structuring the receptor components.

Some membranes can be crowded with proteins and membrane components. A study of the red blood cell membrane revealed highly concentrated regions with only 100 lipids per protein [29]. Recent developments in computational simulation techniques enabled the investigation of realistic and dense membranes, showing anomalous lateral diffusion depending on packing and protein crowding [27, 30, 31]. A more realistic representation of a crowded membrane is shown in Fig. 1.5 compared to the artist's render.

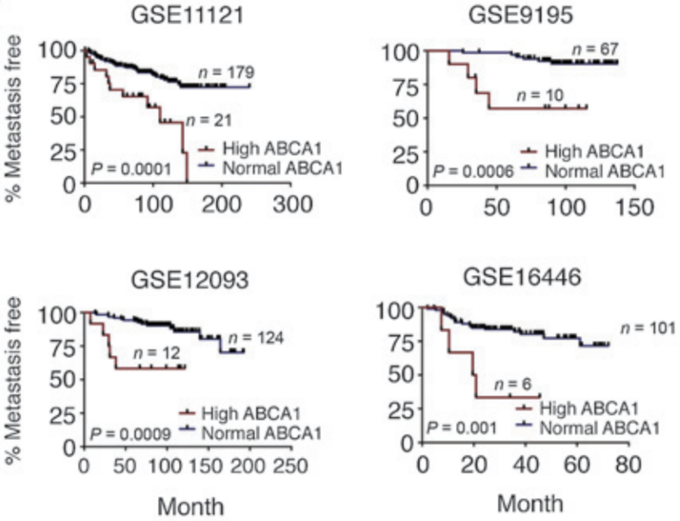

Figure 1.6: **Effect on membrane fluidity on cancer metastasis:** Four independent datasets showing the percentage of human breast cancer patients free of distant metastasis over time. ABCA1 is a membrane cassette transport protein which serves as a cholesterol efflux channel and therefore reduces the membrane fluidity. Image reproduced from Zhao et al. [32].

Membrane fluidity plays also a crucial role in the formation of cancer metastasis. Cancer cells exhibit an increased membrane fluidity, which improves the cells motility and deformability potential necessary for metastatic activities [33, 34]. It has been observed, that successful antimetastasis drugs significantly reduce the membrane fluidity of metastatic cancer cells [32]. The regulation of the cassette transporter ABCA1 protein, which serves as a cholesterol efflux channel, stiffens the membrane and can lead to a significant reduction of metastatic activity *in vitro* and *in vivo* as shown in the publicly available datasets of breast cancer patients which were monitored for distant metastases (see Fig. 1.6).

The investigation of the transport phenomena of phospholipid bilayers is crucial in order to study these systems. The lateral diffusion in crowded interface seems to be of the highest interest.

1.3 Experimental challenges

The membrane fluidity is often investigated in terms of lateral diffusion of a probe embedded in the membrane. An example of a measuring technique is fluorescence recovery after photobleaching (FRAP), where a fluorescently labeled phospholipid membrane is locally bleached and the time until the bleached molecules diffuse and the membrane homogenizes is measured. It has been shown that results can be erroneous and depend on the fluorescent dye [35]. Instead of using fluorescent labeled lipid molecules, larger probes such as micrometer sized particles can be tracked as well. This technique is termed *microrheology* and is widely applied in measuring the rheological behavior of bulk fluids, because it requires very small sample volumes. Methods to calculate a variety of structural material properties from these experiments are available [36]. The mobility of the tracer particles often originates from the thermal energy, displaying a Brownian behavior, or alternatively the force can be applied externally using active microrheological methods.

Tracer particles can be attached to, or embedded in, giant unilamellar vesicles (GUVs) and the particle's mobility can provide insights into the fluidity and thus the shear rheology of the bilayer [37]. However, the generalized Stokes-Einstein relation cannot be used to calculate the interfacial viscosity from the diffusion constant of these tracking experiments. The presence of the interface renders the particle's environment non-homogeneous and exposes each particle to a different drag from the interfacial viscosity in addition to the drag from the surrounding bulk fluid. The interface could even introduce a finite compressibility in lateral direction. Therefore, adequate hydrodynamic models are needed to interpret these particle tracking results. The difficulty of a microrheology experiment is demonstrated by the retraction of Harland et al., who claimed that bilayers of single phospholipids are viscoelastic but unfortunately mistakes in the data analysis had occurred [38]. Furthermore, discrepancies by many orders of magnitude between micro- and macrorheological measurements for monolayer interfaces have been reported for monolayer interfaces [39, 40]. Despite these difficulties, microrheological experiments of tracer particles tethered to lipid membranes have been performed. It is experimentally challenging to have a well-defined local environment of the tracer particles. The tethering bond can distort the membrane, thus affecting the effective size of the tracer particles [41]. Another approach is to track the mobility of domains within a lipid membrane composed of two lipids DOPC/POPC where the difference in the hydrophobic tail results in a phase separation within the interface [42].

A macroscopic approach to investigate the mechanical properties of lipid bilayers is the micropipette aspiration, which measures the bending rigidity. However, the applied deformations are complicated and the sample has to be prepared very carefully [43]. Macrorheological measurements have also shown discrepancies in literature. Espinosa et al. measured the rheology of various lipid monolayers and showed strongly varying responses subtly depending on composition and claimed to observe yielding [44]. A clear viscoelastic response of phospholipid monolayers could be shown in [2, 45] but the response has a complex dependence on the concentration of the lipids in the interface, deformation amplitudes and shear history. Furthermore, other effects such as interleaflet friction could be present in bilayers and the extrapolation from monolayers to bilayers is not straightforward. It is evident, from this brief review, that appropriate experimental techniques have to be developed to investigate phospholipid mono- and bilayer rheology.

Outline of the thesis

The strategy in this thesis is to start from phospholipid monolayers, suspended at a water–oil interface, as a model material of one leaflet of the bilayer and apply macrorheological tools to measure the interfacial rheology with clean kinematics and at an equivalence interfacial pressure so as to be at comparable states as in a lipid membrane [3].

The challenge is addressed in three chapters, which are briefly outlined here. First, operating windows for macroscopic interfacial rheometers are developed, taking into account the primary time-dependent observables and other experimental difficulties such as instrument inertia, capillarity induced by wetting imperfections, and coupling of the interfacial flow field with the bulk subphase. These limitations are tested with hexadecanol, a fatty alcohol with a purely viscous response. The rigorous definition of the operation limits ensures clean kinematics of the interfacial experiments and improves the confidence of the acquired data. Second, the interfacial rheology of phospholipid monolayers is measured carefully within these operating windows. The influence of a different bulk phase on the interactions between the lipid molecules is investigated. Starting with a clean water–air interface, a salt buffer is introduced to the lower aqueous bulk phase to mimic physiological conditions and an upper oil phase is added to simulate the interactions with an infinitely thick second leaflet. In the third chapter, crowded phospholipid monolayers are carefully prepared to avoid any shear history. The interfacial rheology measurements suggest no divergence of the viscosity occurs, even when the layer becomes crowded and approaches maximum packing. Furthermore, the result is compared with preliminary microrheological experiments on free-standing and planar bilayers using the LAMBs setup, which was developed in our group [4]. However further investigation with appropriate hydrodynamic models is required to translate the insights obtained on crowded monolayers to structured bilayers.

2 Operating Windows for Interfacial Shear Rheology

This chapter is published as:
D. Renggli, A. Alicke, R. H. Ewoldt, and J. Vermant. *Journal of Rheology* 64(1), **2020**, DOI: 10.1122/1.5130620.

Interfacial rheology becomes important when surface active species such as surfactants, particles or proteins are present in sufficient quantities at liquid-liquid interfaces and interact between them. Interfacial rheometry measurements are challenging for various reasons. The mechanical response of the thin interface is often weaker compared to that of bulk materials and so one is often measuring close to the lower force and torque limits of rheometers, hence signal to noise ratios merit closer attention. Also the role of both instrument and sample inertia are more important for interfacial, compared to bulk rheometry. Effects of misalignment and imperfections of the measurement geometries lead to effects of surface and line tension. Finally, peculiar for interfacial rheometry is the need to de-convolute the contributions of flow and deformation in the surrounding phases from that at the interface. Whereas some of these aspects have received attention in previous work, a clear and unambiguous view on the operating limits of interfacial rheometers has been missing. In the present work, we investigate the different experimental challenges and develop a generic methodology which provides a clear definition of the operating limits of various interfacial rheometers including the interfacial needle shear rheometer, the double wall ring and the bi-cone geometries. We validate this methodology by investigating the limitations defined intrinsically by the instrument as well as the ones emerging from the properties of the interface of interest for an interface composed of fatty alcohols which represents a challenging test-case. The results provide cautionary examples and clear guidelines for anyone measuring interfacial rheology with these direct rheological techniques.

2.1 Introduction

Interfacial rheology can be used to characterize the mechanical behavior of interfaces present in large interface area systems such as foams, emulsions and thin films. Further applications are manifold and range from bacterial biofilms over antibubbles and can be found in recent reviews [46, 47]. Some specific recent examples are the investigation of interfacial rheological properties for understanding the stability of emulsions stabilized by either particles [48, 49], nanocrystalline cellulose [50] and proteins [51, 52], the consequences of surfactants in crude oil recovery [53] and the development of pharmaceuticals related to lung surfactant replacements to prevent lung collapse during expiration [54, 55].

The thermodynamic state variable surface tension σ is usually sufficient to describe the properties of so-called simple interfaces. However, interfaces can be modified by surface active species such as amphiphiles, proteins, particles, and combinations thereof. This leads to highly structured and complex fluid-fluid systems, also known as soft matter interfaces [47] in congruence with bulk soft matter [56], and such complex interfaces can have a significant interfacial viscoelastic response. As a result, the surface tension is no longer sufficient to describe the interfacial properties in dynamic conditions and investigating the interfacial rheology is necessary. In the present work we focus on providing a framework to identify the operating limits for shear rheometry, for which different measurement techniques have been proposed, which mimic their bulk counterparts. These include the equivalent of the sliding plate rheometer, i.e. the magnetic rod rheometer [57, 58], where a rodlike magnetic probe translates in a channel, the interfacial disk- or bi-cone rheometer [59] mimics the Couette device and the double wall ring is the 2D equivalent of a double wall Couette device [60]. The dilatational properties of interfaces that emerge due to their large compressibility are not discussed here, although much of the methodology presented here carries over.

Accurate measurements of interfacial rheological material functions remain difficult. First there is the inherent sensitivity of the different devices as the ratio of the perimeter in contact with the interface to the overall surface area in contact with the bulk fluids differs for a rod, a disk and a ring [60]. Second, as the interfaces are thin (obviously), the force on the rod or the torque on the disks or rings is typically weak compared to the case of bulk materials, so often one is operating close to the limits of the rheometers.

As a consequence of the relatively weak contributions of the interface and low viscous bulk phases, the inertia of the tool and instruments will influence measurements sooner compared to bulk rheometry [58]. Moreover, as most geometries are centimeters deep, fluid inertia of the bulk phases can be an issue as well which is too often ignored. Effects of misalignment and imperfections of the measurement geometries lead to effects of surface and line tension. Finally, peculiar for interfacial rheometry is the need to use iterative procedures and algorithms to find the correct interfacial deformation profile to deconvolute the contributions of flow and deformation in the surrounding phases from that at the interface. Whereas some of these aspects have received attention in previous work, a clear and unambiguous view on the operating limits of interfacial rheometers has been missing.

Most likely, the lack of procedure to identify clear operating windows has led to contradicting results when using different rheometers. For example the behavior of the phospholipid DPPC at the water-air interface measured with the double wall ring [2] showed a predominant viscoelastic fluid behavior with the low frequency limit being determined by the free surface area per molecule, whereas earlier investigations with the bi-cone had suggested that such phospholipids would behave as gels at similar surface pressures and temperature [44]. Furthermore, studies with the magnetic micro-button rheometer underlined the importance of shear history on the interfacial rheology and the dependence on the free surface area per molecule as well as the influence of incorporation of molecules like cholesterol, fibrinogen or palmitic acid [45, 61–64]. Data on an even simpler molecule, hexadecanol, differ significantly between different instruments [40, 65]. Also a significant discrepancy between moduli measured by microrheology and macrorheology by many orders of magnitudes has been reported [39, 40, 66]. One of the concerns which needs to be addressed is that some of this reported data is outside of the window of operation of the devices and not all reported data may be reliable, and a clear and generic method to asses the operating window needs to be agreed upon.

Some of the problems are also observed in bulk rheometry and a rigorous approach has been developed by Ewoldt et al. [67]. In the present work we will derive a similar approach for interfacial rheometry. We will start by identifying the error in the primary variables and the subsequent error propagation and uncertainty. However, a fundamental difference between interfacial and bulk rheology is the coupling of the flow field at the interface with the surrounding bulk fluid. Therefore, it is necessary to correct the data to separate the interfacial contribution from the subphase and instrument contributions to the rheological signal and the question arises as down to which level this can be achieved reliably. This introduces further difficulties which are discussed in this work. So far this has only been done for numerically generated signals [66, 68, 69].

Experimental issues such as positioning and contact line variations will also be touched upon. Overall the goal of this work is to provide a methodology on how to define diagrams with the desired variables (e.g. linear viscoelastic interfacial moduli) and provide appropriate limit lines and operating windows for the specific rheometry in use. This approach is similar in spirit to the operating windows for microrheology [36].

This paper will begin with the relevant momentum balances and introduce the different interfacial shear rheometers. The materials and methods will be discussed with some attention to all the experimental details between the different rheometers before going into the construction of the operating diagrams. Then the different limits are discussed based on data of hexadecanol at an air-water interface as well as measurements of clean air-water interfaces, which present the most difficult case. A key element is using a Fourier analysis method to identify the noise on the primary experimental observables.

2.1.1 General interfacial momentum balance equation

For insoluble layers or systems where the mass transport between the interface and the adjacent bulk phases is slow compared to momentum exchange, the interfacial momentum balance equation for sharp interfaces of constant composition can be written as [46, 70]

$$\rho_s \frac{D}{Dt} \boldsymbol{v}_s - \boldsymbol{\nabla}_s \cdot \boldsymbol{\sigma}_s = ||\boldsymbol{\sigma} \cdot \boldsymbol{n}|| \quad , \tag{2.1}$$

where ρ_s is an interfacial density $[\mathrm{kg\,m^{-2}}]$, $\frac{D}{Dt}$ is the surface material derivative, $\boldsymbol{v}_s$ is the interfacial velocity, $\boldsymbol{\nabla}_s = \boldsymbol{I}_s \cdot \nabla$ is the surface gradient operator, $\boldsymbol{I}_s$ is the surface unit tensor, $\boldsymbol{\sigma}_s$ is the interfacial stress tensor, $\boldsymbol{\sigma}$ is the bulk stress tensor, $\boldsymbol{n}$ is the unit vector normal to the surface and $||\ldots||$ denote jump terms as defined in [46], their Eq. 7. The left hand side in Eq. (2.1) denotes interfacial inertia and stress while the right hand side corresponds to the jump of momentum of the two adjacent bulk phases across the interface. As a consequence, the interfacial stress tensor $\boldsymbol{\sigma}_s$ is always coupled with the bulk stress tensor $\boldsymbol{\sigma}$.

The interfacial stress tensor can be decomposed into the interfacial tension $\sigma(\Gamma, T)$, which is a thermodynamic state variable dependent on the surface excess concentration Γ and temperature T, and the extra stress tensor $\boldsymbol{\tau}$, which is related to the mechanical stress, as [54, 70, 71]

$$\boldsymbol{\sigma}_s = \sigma(\Gamma, T)\boldsymbol{I}_s + \boldsymbol{\tau} \quad . \tag{2.2}$$

This equation shows that the mechanical response of structured interfaces cannot be fully described by the sole knowledge of interfacial tension σ. Constitutive models relating $\boldsymbol{\tau}$ with strain for elastic or strain-rate for viscous interfaces are discussed in [70]. An objective quasi linear neo-Hookean model has recently been derived rigorously from the strain energy function [71].

Using a viscous interfacial constitutive equation with the momentum balance equation (2.1) results in the interfacial Navier-Stokes equation [72]

$$\begin{aligned}\rho_s \frac{D}{Dt}\boldsymbol{v}_s - \boldsymbol{\nabla}_s \cdot \left(\sigma(\Gamma, T)\boldsymbol{I}_s + \left[(\kappa_s - \eta_s)\boldsymbol{\nabla}_s \cdot \boldsymbol{v_s}\right]\boldsymbol{I}_s + 2\eta_s \boldsymbol{D}_s\right) \\ = ||\boldsymbol{\sigma} \cdot \boldsymbol{n}||\end{aligned} \tag{2.3}$$

where $\boldsymbol{D}_s = \left(\boldsymbol{\nabla}_s \boldsymbol{v}_s \cdot \boldsymbol{I}_s + \boldsymbol{I}_s \cdot (\boldsymbol{\nabla}_s \boldsymbol{v}_s)^T\right)/2$ is the interfacial rate-of-deformation tensor and κ_s and η_s are the interfacial dilatational and shear viscosities, respectively. Assuming a perfectly flat water-air interface ($\eta_{b,\text{upper phase}} = 0\,\text{Pa s}$) with a constant surface pressure, a purely viscous bulk fluid behavior with bulk viscosity η_b and rescaling to non-dimensional form simplifies Eq. (2.3) to

$$Re_s \frac{D}{Dt^\dagger}\boldsymbol{v}_s^\dagger + \boldsymbol{\nabla}_s^\dagger \cdot 2\boldsymbol{D}_s^\dagger = \frac{1}{Bq} 2\boldsymbol{D}_1^\dagger \cdot \boldsymbol{n} \quad , \tag{2.4}$$

where † denotes non-dimensional variables. The interfacial Reynolds number Re_s and the Boussinesq number Bq arise naturally as the two relevant non-dimensional groups

$$Re_s = \frac{\omega \rho_s l^2}{\eta_s} \qquad\qquad Bq = \frac{\eta_s}{\eta_b l} \quad , \tag{2.5}$$

where η_s and η_b are the interfacial and bulk viscosity, ω and l are characteristic frequency and length scales, respectively.

The importance of interfacial effects compared to those of bulk viscosity is given by Bq but the choice of the characteristic length scale l is not straightforward. For example, for a driven oscillatory flow Fitzgibbon et al. [73] used the 'natural' Stokes boundary layer length scale

$$l_\omega = \sqrt{\frac{\nu}{\omega}} \quad , \tag{2.6}$$

where ν is the kinematic viscosity. With increasing η_s, the diffusion of momentum at the interface increases and can dominate the one to the bulk. By balancing the interfacial stress with the viscous stress in the bulk, an interfacial length scale can be defined over which the interfacial momentum is attenuated as:

$$l_\omega^s = \sqrt{\frac{\eta_s l_\omega}{\eta_b}} \quad . \tag{2.7}$$

However, many other publications use a macroscopic Boussinesq number which has proven useful in analyzing the inherent sensitivity of rheometers, defined as [74]

$$Bq = \frac{\text{interface}}{\text{bulk phase}} = \frac{\eta_s \frac{V}{L_s} P_s}{\eta_b \frac{V}{L_b} A_b} = \frac{\eta_s}{\eta_b a} \quad , \tag{2.8}$$

where η_s and η_b are the interfacial and bulk viscosity, L_s and L_b are the lengths over which the velocity V decays in the interface and bulk phase, P_s is the perimeter between probe and interface and A_b is the contact area between probe and bulk phase. In this macroscopic definition of Bq the ratio of A_b to P_s results in a length scale a which is characteristic of the geometry and should obviously be as small as possible. It is typically assumed that $\frac{V}{L_s} = \frac{V}{L_b}$ [60]. The macroscopic choice of a for the characteristic length scale is usually done to define it in conjunction with an instrument. During the analysis, the correct length scale (see Eq. (2.6) or (2.7)) can be retrieved.

2.1.2 Interfacial rheometers

Plateau was the first to suggest the concept of interfacial viscosity and used a magnetic compass needle on an interface to generate a shear flow [75]. However, the rotation of the needle caused concentration gradients of the surfactants which resulted in large Marangoni forces interfering with his measurements [76]. An adaptation of the needle device is the interfacial stress rheometer (ISR) by Shahin in 1989 [57] which has been improved by Brooks et al. [77] and analyzed in [58, 60, 68, 73]. Alternative geometries for direct rheometry are the magnetic micro disc [45], bi-cone [59, 66] and double wall ring (DWR) [60].

Measuring the surface pressure $\pi = \sigma_{\text{clean}} - \sigma(\Gamma)$ as a function of interfacial area where the shape is maintained can give insights in the dilatational interfacial rheology. A trough with radial geometry was developed to eliminate the shear components present during area changes in a rectangular trough [71]. An alternative to measuring the surface pressure with a Wilhelmy plate is the use of micro tensiometers [78]. An overview of modern interfacial rheometers can be found in [70].

The interfacial shear rheometry setups studied in this work are those which are commercially available, i.e. the ISR, DWR and bi-cone (Fig. 2.1). The ISR uses a magnetic probe in the shape of a needle suspended at the interface which is confined in a glass channel. By applying a different current through the two Helmholtz coils a gradient in magnetic field is generated which drives the magnetic needle along the glass channel and the resulting needle position is captured by a camera. The DWR and bi-cone are fixtures for rotational rheometers hence they can be used with the functionality of commercial rheometers. Because of the definition of the macroscopic Bq number, and the use of the characteristic geometry probe a, the sensitivity of the ISR is expected to be higher than the DWR. The radius of the magnetic probe can be reduced by using magnetic micro wires [79]. Because of the large contact area with the subphase, the bi-cone is expected to be the least inherently sensitive of the three instruments.

2.1.3 Oscillatory measurements of viscoelastic properties

Conventional bulk rheometry can be extended to interfaces in the linear viscoelastic regime using surface excess quantities [47], at least when the interface is ‘sharp’ [70] and for a specific top and bottom phase. In oscillatory shear deformation, an interface can therefore be described by a frequency dependent interfacial elastic modulus $G'_s(\omega)$ and viscous modulus $G''_s(\omega)$. This means a purely elastic interface has $G''_s(\omega) = 0\,\mathrm{Pa\,m}$

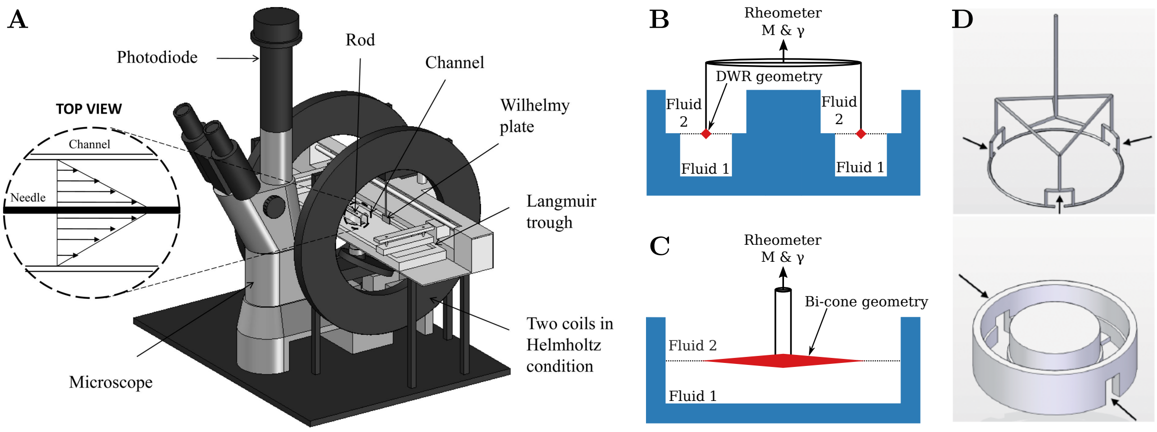
A
Photodiode
Rod
Channel
Wilhelmy plate
TOP VIEW
Channel
Needle
Langmuir trough
Two coils in Helmholtz condition
Microscope
B
Rheometer
M & γ
DWR geometry
Fluid 2
Fluid 2
Fluid 1
Fluid 1
C
Rheometer
M & γ
Bi-cone geometry
Fluid 2
Fluid 1
D

Figure 2.1: **Commonly used interfacial rheometry setups: A)** ISR with inset showing magnetic needle and glass channel (reprinted with permission from [80] © 2011 American Chemical Society), **B)** DWR and **C)** bi-cone. **D)** Modification of small DWR and cup (reproduced from [2] with permission from The Royal Society of Chemistry).

whereas a purely viscous interface is described with $G_s'(\omega) = 0\,\mathrm{Pa\,m}$. Interfaces which have an intermediate behavior of elastic and viscous are called viscoelastic and can be described using a complex linear viscoelastic modulus

$$G_s^*(\omega) = |G_s^*(\omega)|e^{i\delta_s(\omega)} = G_s'(\omega) + iG_s''(\omega) \quad , \tag{2.9}$$

where $|G_s^*(\omega)|$ is the norm and $\delta_s(\omega)$ is the phase angle of the complex interfacial shear modulus:

$$|G_s^*(\omega)| = \sqrt{G_s'(\omega)^2 + G_s''(\omega)^2} \quad , \tag{2.10}$$

$$\delta_s(\omega) = \arctan\left(\frac{G_s''(\omega)}{G_s'(\omega)}\right) = \arctan\left(\frac{\Im\left(|G_s^*(\omega)|e^{i\delta(\omega)}\right)}{\Re\left(|G_s^*(\omega)|e^{i\delta(\omega)}\right)}\right) \tag{2.11}$$

or

$$\Re(G_s^*) = G_s' = |G_s^*|\cos\delta_s \tag{2.12}$$

$$\Im(G_s^*) = G_s'' = |G_s^*|\sin\delta_s \quad . \tag{2.13}$$

With the two relations

$$G_s^*(\omega) = -i\omega\eta_s^*(\omega) \quad \& \tag{2.14}$$

$$\eta_s^*(\omega) = \eta_s'(\omega) - i\eta_s''(\omega) \quad , \tag{2.15}$$

where $\eta_s'(\omega)$ is the dynamic interfacial shear viscosity and $\eta_s''(\omega)$ is the out-of-phase shear viscosity. Eq (2.8) can be generalized for viscoelastic interfaces as the complex Boussinesq number [80]

$$Bq^*(\omega) = \frac{G_s''(\omega) - iG_s'(\omega)}{\omega a \eta_b} = \frac{\eta_s'(\omega) - i\eta_s''(\omega)}{a\eta_b} \quad . \tag{2.16}$$

The preferred representation of viscoelastic properties in this work is chosen to be the norm and phase angle of the complex interfacial shear modulus (Eq. (2.10) and (2.11)). For the widely used representation of G_s' and G_s'', the uncertainties of amplitudes and phase angle are combined because of Eq. (2.11) and the discussion is less straightforward. Other linear viscoelastic material functions are the time dependent modulus $G_s(t)$ and the compliance $J_s(t)$.

2.2 Materials and methods

2.2.1 Monolayer preparation

The Langmuir trough and barriers (Delrin©, KSV NIMA, Biolin Scientific, Finland) were thoroughly cleaned with detergent, ethanol and repeated rinsing with milli-Q water (18.2 MΩ cm at 25 °C, Merck Millipore, USA) and filled with milli-Q water. A Wilhelmy plate (KSV NIMA, Finland) was flame treated and placed at the interface by a microbalance (KSV NIMA, Finland). The cleanliness of the interface was verified by a measurement of the surface tension of 71.9 $\mathrm{mN\,m^{-1}}$ at 25 °C and a maximum increase of surface pressure π below 0.2 $\mathrm{mN\,m^{-1}}$ upon compression of the pristine interface was found to be acceptable.

1-Hexadecanol was purchased from Sigma Aldrich (ReagentPlus©, 99 %, USA) and dissolved in 2-propanol (VWR chemicals, $\geq$ 99.7 %, AnalaR NORMAPUR© ACS, USA) at a concentration of 1 $\mathrm{g\,L^{-1}}$ and stored below 5 °C for not longer than one week. After ultrasonication for 5 min to homogenize the sample, the hexadecanol solution was then added dropwise to the water-air interface with a micro liter syringe. After spreading, the interface was left for 30 min to allow the 2-propanol to evaporate and the interface to reach equilibrium. A compression speed of 5 $\mathrm{mm\,min^{-1}}$ and initial coverage of 1.33 $\mathrm{mg\,m^{-2}}$ were used. All experiments were conducted at 24 °C and relative humidity of 50 %. A surface pressure area compression isotherm is shown in Fig. 2.12 in Appendix 2.7.1.

2.2.2 Interfacial needle shear rheometer

Setup: A custom built ISR based on the design of Brooks et al. [77] and Reynaert et al. [58] was used (see Fig. 2.1A), and is similar to commercially available instruments of this type. Two magnetic coils were positioned in Helmholtz configuration and powered by two power supplies (Agilent 6644A, Keysight technology, USA). A constant base current of 0.75 A was applied trough each coil to position the probe and modulated by a function generator (Agilent 33120A, Keysight technology, USA) in an anti-Helmholtz fashion. The function generator was controlled through LabVIEW (National Instruments, USA). The two current signals were acquired by measuring the voltage parallel to the two coils with an acquisition board (NI PXIe-6356, National Instruments) and an acquisition rate of 50 Hz. Two voltage dividers were used to transform the voltage signals to the acquisition range of the NI board. The two voltage signals were divided by the resistance of the coils and subtracted from each other resulting in the driving current $I(t) = (V_1 - V_2)/R = I_0 \sin(\omega t - \delta_I)$.

The position of the probe was acquired by a 1400 × 1080 pixel CMOS camera (VCXG-15M, Baumer, Switzerland) which was connected via GigE vision to a Frame Grabber (PXIe-8234, National Instruments) and processed by LabVIEW at a rate of 25 Hz. The images were processed in real time with NI vision and the edge of the needle is tracked resulting in the position signal $z(t) = z_0 \sin(\omega t - \delta_z)$. The camera was mounted on an inverted microscope (Eclipse TS 100, Nikon, Japan) equipped with a 4× and a 10× Plan objective. The microscope is mounted on a two-axis linear stage (M-401, Newport Corporation, USA) and the focus could be adjusted with an electric motor controlled by an Arduino Uno. The illumination was done by a DC-950 (Dolan Jenner, USA). The temperature of the Langmuir trough was controlled by a fluids bath (FP35-MC, Julabo, Germany) and the temperature of the subphase was measured by a thermocouple (USB-TC01, National Instruments). To reduce noise from vibrations and air flows, the ISR is enclosed by a Plexiglas box and placed on an active vibration isolation table (Vario Series, Accurion, Germany).

Experiment: The properties of the two magnetic probes are shown in Table 2.1. A needle was purchased from KSV and a microwire was kindly provided by Tajuelo (as in ref. [79]). A glass channel with a width of 12 mm was rinsed thoroughly with acetone, ethanol and milli-Q water and plasma cleaned. The hexadecanol solution was spread at the interface as described above. The needle remained on the interface during spreading while the microwire was removed because the strong Marangoni flows during the spreading would push it out of the channel. The acquisition time was chosen to be 10 oscillation periods after the sample has been conditioned for 5 oscillation periods for all experiments. Between measurements of different surface pressures, the interface was allowed to relax for 5 min.

Table 2.1: **Properties of the magnetic probes for the ISR:** l, r and m are the length, radius and mass of the probe, respectively and λ is the ratio of channel radius to probe radius. k^{-1} is the instrument compliance and C_{I-F} the force constant described in Eq. (A.3). k and C_{I-F} result from the calibration.

	l [mm]	r [µm]	m [mg]	λ [-]	k [N m^{-1}]	C_{I-F} [N A^{-1}]
Needle	23.5	200	5.8	30	2.9×10^{-5}	4.6×10^{-6}
Microwire	6.3	17.5	2.3×10^{-3}	343	8.8×10^{-7}	2.2×10^{-8}

Data processing: The discrete Fourier transforms of the current $I(t)$ and position $z(t)$ signals were performed with LabVIEW and the resulting amplitude ratio I_0/z_0 (units [A/pixel]) and phase angle difference were calculated. The subphase correction described by Verwijlen et al. [80] is performed using a finite difference method. The algorithm is described in SI A.1 and the implemented codes are available for download (`https://softmat.mat.ethz.ch/opensource.html`). The performance of the algorithm was verified by using a test solution where all properties and velocity profiles were known a priori, by comparing with the predictions of an analytical model and by particle tracking experiments to measure the velocity profile at the interface.

Calibration: To find the instrument compliance k^{-1}, which can be interpreted as a system stiffness k with respect to an 'equilibrium' position of the magnetic probe depending on the inhomogeneity of the magnetic field and the interface (e.g. meniscus imperfections or wall interactions), and the force constant C_{I-F} relating the applied current I with the force F acting on the magnetic probe as

$$F = C_{I-F} I \quad , \tag{2.17}$$

a calibration procedure as proposed in [79] has been performed on a clean interface prior to spreading of hexadecanol. There, $Bq^* = 0$ is assumed and the interfacial and subphase drag forces are calculated with the same algorithm as for data analysis. The calculated amplitude ratio is then fit to the measured amplitude ratio with the instrument compliance k^{-1} and C_{I-F} as two fitting parameters. A calibration example is shown in SI A.2.

2.2.3 Double wall ring

Setup: The double wall ring (DWR) is described by Vandebril et al. [60] and is commercially available. The ring was attached to a stress controlled rheometer (DHR-3, TA Instruments, USA) which was placed on an active vibration isolation table (Vario Series, Accurion, Germany) and enclosed by a Plexiglas box to reduce air flow. Three different rings were used of which two have the same dimensions (see Table 2.2) but different materials. The large diameter ring with the larger geometry inertia I_g is commercially available (Pt/Ir alloy, TA instruments), while the other two rings were 3d-printed with a surface roughness of 4 to 7 µRa (Ti6Al4V alloy, 3d Systems (formerly Layerwise), Belgium).

A schematic of a ring is shown in Fig. 2.1B which was used with a Delrin$^{\copyright}$ cup that was placed directly on the Peltier heated bottom plate of the rheometer. Two large rings were used only to investigate clean water-air interfaces without any material present at the interface. The modifications of the small diameter ring and Teflon cup have been discussed in [2]. Small openings in ring and cup, in combination with a Langmuir trough (Ribbon trough, Biolin Scientific, Finland) enable control over the surface pressure during a rheological experiment (see Fig. 2.1D).

Table 2.2: **Properties of the rings for the DWR:** $R_{\circ}^{\square}$ denotes the outer and inner ($\square$) radius of the cup and the ring ($\circ$). I_g is the geometry inertia and the instrument inertia is $I_{\text{instr}} = 20.93\,\text{mg}\,\text{m}^2$.

	$R_{\text{cup}}^{\text{inner}}$ [mm]	$R_{\text{ring}}^{\text{inner}}$ [mm]	$R_{\text{ring}}^{\text{outer}}$ [mm]	$R_{\text{cup}}^{\text{outer}}$ [mm]	I_g [mg m^2]
Small ring	14.25	17	18	22	1.00

Experiment: After cleaning the trough with detergent, ethanol and milli-Q water and aligning the cup inside the trough, milli-Q water was added as *Fluid 1* (*Fluid 2* was air). The rings were cleaned by rinsing with ethanol and milli-Q water and dried before attaching to the rheometer. The instrument and geometry inertia were measured (see Table 2.2). The friction of the geometry was measured and a rotational (3 iterations in precision mode) and oscillatory mapping of the stress head were performed. After having spread the hexadecanol solution as described above, the ring was placed at the interface until the interface appeared flat. The rectangular cross section of the ring and the step in the cup ensures a good pinning of the interface. The sample was conditioned for one period and data was acquired for six periods.

Data processing: The data was corrected for instrument and geometry inertia by the software of the rheometer. The subphase correction for the DWR is explained by Vandebril et al. [60] and both the algorithm and implementation are similar to those for the subphase correction for the ISR. The velocity field in the bulk fluid and at the interface (v^*) is calculated in an iterative algorithm and the interfacial viscosity is adjusted according to the ratio of the measured torque to the calculated torque (see SI A.1).

2.2.4 Bi-cone

Setup: The bi-cone, as for example discussed in [59], is shown schematically in Fig. 2.1C. Bi-cones manufactured both from TA instruments as well as from Anton Paar were used, see Table 2.3. The first was attached to the DHR-3 (described in the DWR section) and the the second (Interfacial Rheology System of Anton Paar, Austria) was attached to a MCR series 302 (Anton Paar). On the MCR the experiments were performed with the direct strain oscillation (DSO) method [81]. All oscillatory measurements were conducted for six periods after conditioning for one period. The strain controlled measurements were performed with the TruStrain™ method enabled. The raw data could only be saved for one period.

Experiment: After having cleaned the cell and the bi-cone with acetone, ethanol and milli-Q water, the cell was mounted on the Peltier bottom plate of the rheometer. The instrument (I_{instr}) and geometry (I_g) inertia as well as variations of the air bearing

Table 2.3: **Properties of the bi-cone geometries:** R_{cup} and R_{ring} are the radii of the cup and the ring, respectively, h is the penetration depth, β is the cone angle and I_g is the geometry inertia. Instrument inertia of the MCR 302 is $I_{\text{instr}} = 92.04\,\text{mg}\,\text{m}^2$.

	R_{cup} [mm]	R_{cone} [mm]	h [mm]	β [°]	I_g [mg m^2]
TA Instruments	40	34	2.98	5	31.44
Anton Paar	40	34.065	2.99	5.017	20.23

properties at different positions of the rotor were calibrated. The cup was filled with milli-Q water (*Fluid 1*, *Fluid 2* was air) and the bi-cone was placed at the interface until the interface appeared flat. Then, the hexadecanol solution was spread as described above. No subphase correction was performed because no data above the noise level could be acquired. More information about the subphase correction for the bi-cone can be found in [69, 82].

2.2.5 Quantifying noise floor and resolution: Fourier analysis

The use of different geometries, approaches and instruments from different manufacturers makes it difficult to directly compare the operating limits based on measurement noise or resolution. Here we propose an independent method to evaluate the performance of the overall setups, using a method that can be applied by anyone choosing to do so. The proposed method starts by calculating the signal-to-noise ratio (S/N) by performing a Fourier analysis on the primary experimental observables, i.e. the raw data of displacement and either force or torque, both as a function of time, and then defining a noise floor. The initial point of the time window (t_1) can be chosen arbitrarily. The end of the time window (t_2) was chosen such that an integer number of periods is analyzed. Unless otherwise specified, five periods were found to be sufficient to obtain representative results. The discrete Fourier transform (dft) was then performed with the `fft` function in Matlab which corresponds to :

$$\begin{aligned} \hat{f}(\omega) &= \frac{1}{t_2 - t_1} \int_{t_1}^{t_2} f(t) e^{-i\omega t} dt \qquad (2.18) \\ \hat{f}(k) &= \sum_{j=1}^{n} f(j) W_n^{(j-1)(k-1)} \qquad \text{where} \quad W_n = e^{(-2\pi i)/n} \quad , \end{aligned}$$

where t_1 and t_2 identify the borders of the time window, $f(t)$ is the function in the time domain and $\hat{f}(\omega)$ denotes its Fourier transform. The magnitude of the single sided spectrum $|\hat{f}(\omega)|$ will be used to determine the signal to noise ratio, thus its units are the same as $f(t)$.

Displacement drift of the measurement probe can be an issue, especially for water-air interfaces due to convective air currents above the interface. Additionally the experiments are also subject to standard electronic flicker noise. To separate these effects, a power law curve was fit to the experimentally obtained spectrum $|\hat{f}(\omega)|$ (excluding the driving frequency) which characterizes the average *background* noise. A *noise floor* is then defined by adjusting the prefactor of this fit until it equals the highest point in the spectrum $|\hat{f}(\omega)|$, excluding the fundamental and the first 5 odd harmonics. In this manner, we obtain a noise level independent of manufacturer specifications which allows meaningful comparison with different devices. Clearly signal analysis can be improved in each and every instrument, for example by oversampling strategies, but this will result in relatively small variations. In practice we have found the proposed procedure to give a realistic lower limit for all the different devices.

2.3 Results

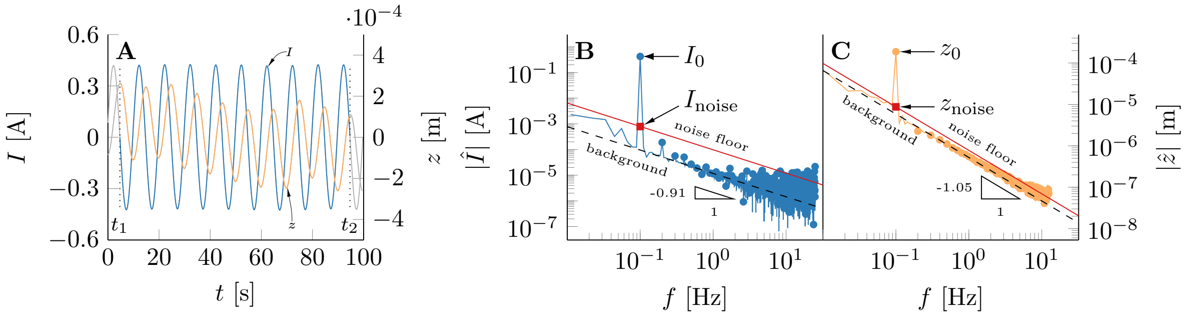

Figure 2.2: **Representative data set of an ISR experiment:** Primary observables **A)** Current $I(t)$ and displacement $z(t)$ in the time domain. **B)** Current signal in the frequency domain $|\hat{I}(f)|$ indicating I_0 and I_{noise}. **C)** Displacement signal in the frequency domain $|\hat{z}(f)|$ indicating z_0 and z_{noise}. Dots represent integer harmonics of the fundamental.

2.3.1 Primary observables

A representative data set of the primary observables as measured from the ISR for a water-air interface is shown in Fig. 2.2. The current $I(t)$ is applied while the rod position $z(t)$ is being measured. The signal for the driving current shows a very clean sinusoid, but the measured displacement $z(t)$ shows a superimposed drift which is mainly due to convection. A discrete Fourier transform of the displacement signal $\hat{z}(f)$ in Fig. 2.2.C shows a high frequency tail with a slope of -1 confirming that the noise is mostly dominated by drift. The Fourier transform of the current signal $\hat{I}(f)$ Fig. 2.2.B shows only a minute drift below 1 Hz where the slope is close to -1. At larger frequencies flicker or pink noise dominates. An example with strong visible drift in $I(t)$ is shown in SI A.3. In the data set in Fig. 2.2B & C, the fitting for the current and displacement background signals were performed from 0.01 Hz to 1 Hz and 10 Hz, respectively, since the nature of the noise changes at larger frequencies. The noise floors can be defined which make it possible to define signal to noise at the driving frequency 0.1 Hz for current and displacement (I_{noise}, z_{noise}). The choice of frequency range over which the fit is performed might in certain cases be refined, e.g. using the nearby non-integer harmonics as noise near the signal of interest. However, including the spectrum over a larger frequency range seemed to be most compatible with the fatty alcohol under investigation in this work.

The Fourier analysis is performed for multiple stress amplitude sweeps of the ISR for monolayers of hexadecanol at different surface pressures (1–35 $\mathrm{mN\,m^{-1}}$) at the water air interface. The resulting signal amplitudes and noise values on the primary variables are shown in Fig. 2.3. The noise on the current is always smaller than I_{min} and essentially constant over the complete range of the power supply. However, the noise on the measured displacement of the needle, z_{noise}, is not constant and can even become larger than the measured displacement signal amplitude at small amplitudes. This effectively imposes a lower displacement limit. The main limiting factor for the displacement is however the presence of drift. It should be noted that the ISR was contained in a box as to minimize convective currents, so this effect can be worse for instruments which are open to the air. With an increased interfacial viscosity, drift is typically suppressed which therefore results in a smaller z_{noise}. There is no dependence of z_{noise} on changes in the optical train such as magnification of the objective. Only the maximum displacement z_{max} is determined by the field of view.

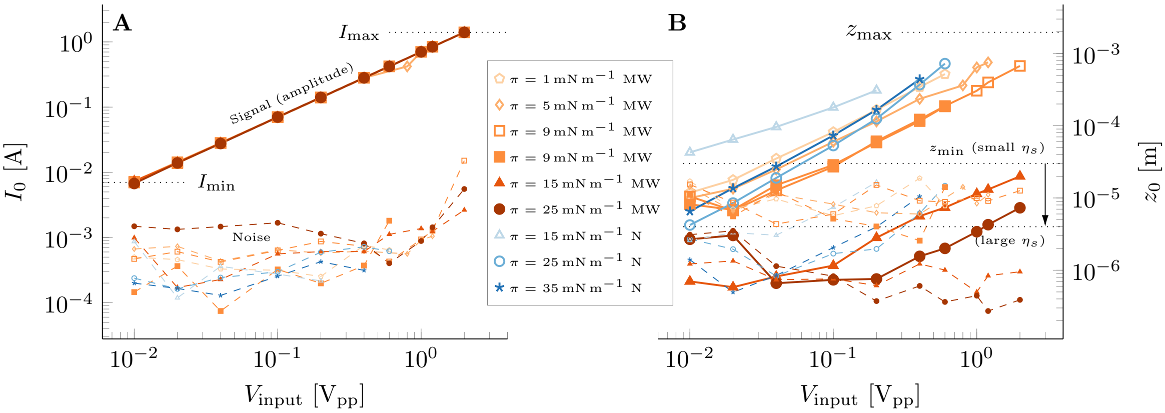

Figure 2.3: **Current and displacement signal amplitudes and the respective noise for the ISR:** data for hexadecanol at different surface pressure at the water-air interface measured with the ISR at $f = 0.1\,\text{Hz}$ as a function of input voltage of the function generator (V peak-to-peak). **A)** Current signal amplitude I_0 and noise I_{noise}. **B)** Position signal amplitude z_0 and noise z_{noise}. Big symbols and solid lines are signals, small symbols and dashed lines are noise while open and closed symbols denote the magnification of the objective (4× and 10×, respectively). The magnetic probe MW (microwire) and N (needle) is specified in the legend.

Analogous to the ISR, the Fourier analysis can be performed for the DWR using the primary variables torque $M(t)$ and displacement $\theta(t)$. The signal amplitude and noise values measured for hexadecanol at the water air interface are shown for a range of surface pressures from 15–45 mN m^{-1} for the small DWR in conjunction with a Langmuir trough in Fig. 2.4. A & B show signal amplitude and noise values as a function of input torque amplitude (stress amplitude controlled mode) and C & D of the input displacement amplitude (strain amplitude controlled mode). For the open loop stress controlled mode, the feedback is completely disabled and the lowest M_{noise} values are logically obtained but the noise on the measured displacement is quite substantial, again mainly due to a drift of the baseline as a consequence of residual torques in the air bearing of the instrument. The presence of an interfacial viscosity can reduce the drift to some extent as can be seen by the much larger $\theta_{\min}^{\text{water}}$ which shows the noise floor of a clean water-air interface measured with the DWR (data points not shown). The specific rheometer (Discovery HR-3) has a control loop (closed loop) which suppresses this drift in the displacement signal, thus the operation mode is not truly stress controlled any more. This improves the noise level on the displacement signal, but the feedback loop

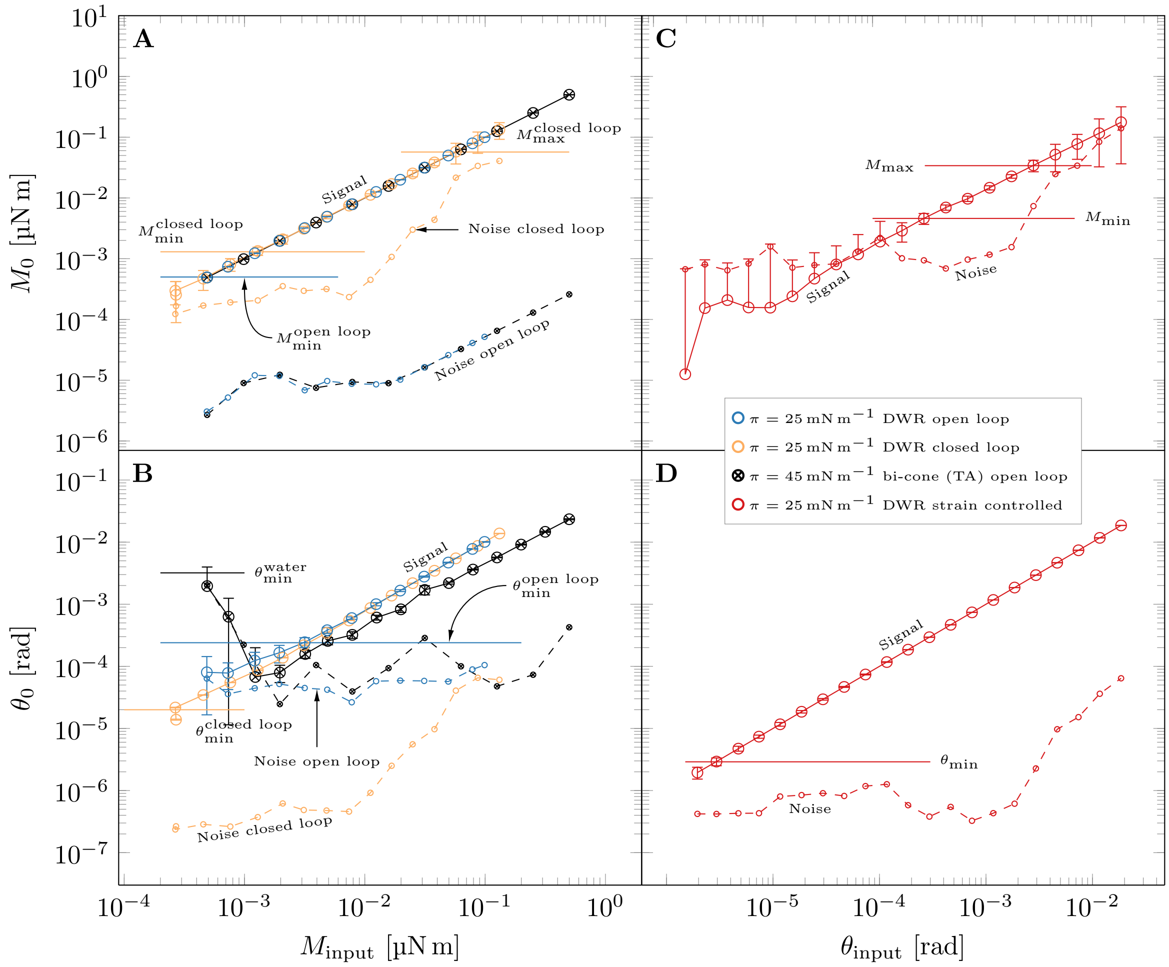

Figure 2.4: **Torque, strain and noise for the DWR (small diameter ring in conjunction with a Langmuir trough) and bi-cone: A)** Torque M_0 and **B)** displacement θ_0 signal amplitudes as a function of input torque for stress controlled experiments. *Closed loop* uses a feedback loop to avoid drift in $\theta(t)$. **C)** M_0 and **D)** θ_0 as a function of displacement for strain controlled experiments. Noise is shown as small symbols with dashed lines as well as error bars. Large symbols and solid lines are signal amplitudes. Min and max lines correspond to $S/N = 5$. Hexadecanol at different surface pressures at the water-air interface measured at $f = 0.1\,\text{Hz}$.

enhances the noise on the torque signal and the signal-to-noise ratio decreases to values even below 1 hence defining an upper torque limit much smaller than the instrument specification for this particular operating mode. When performing stress amplitude sweeps on interfaces, it is insightful to compare both operating modes. For the strain controlled mode, the noise amplification by the control loop is even more pronounced since the torque amplitude has to be adjusted during each cycle to arrive at the defined strain amplitude. A comparison of the noise amplifying effect of the different operating modes is shown in Appendix 2.7.2. Noise for the larger diameter DWR is shown in SI A.4.

The S/N of the bi-cone is expected to be smaller compared to the DWR due to the lower intrinsic sensitivity and the larger contribution of the bulk phases for a given value of η_s. The amplitude and noise values of the bi-cone of TA instruments is shown for an open loop stress controlled test in Fig. 2.4. Even though the noise values are comparable to the small DWR no successful measurement can be reported even for the hexadecanol interface at the highest surface pressure ($\pi = 45\,\mathrm{mN\,m^{-1}}$) because interfacial phase angles are always larger than 90° after correction for geometry inertia. For Anton Paar's bi-cone in the strain controlled mode, the S/N ratio for even the highest surface pressure hexadecanol interfaces is never bigger than one. For the stress-controlled mode only a very small operation window could be identified. However, the S/N is always smaller than 5 (see SI A.5). This demonstrates that both bi-cones are not suitable for measuring this system either because of large noise or large geometry inertia. This emphasizes the importance of evaluating the primary observable variables and not relying solely on the resulting rheological variables (e.g. shear modulus).

The limiting values of the primary variables for the ISR, DWR and bi-cone are summarized in Table. 2.4. To rigorously compare the noise of the two closed loop instruments, the analysis has to be performed in the Laplace space and the transfer functions of the motors, controllers and filter and feedback algorithms should be taken into account. This lies beyond the scope of the current work.

2.3.2 Amplitude ratio and phase angle

In the linear viscoelastic response regime, the rheological properties of the material can be calculated from the amplitude ratio AR and phase angle difference δ_s of the time dependent primary variables as:

$$\left|\frac{\tau_s}{\gamma_s}\right| = |G_s^*| = \frac{C_M}{C_\theta}\frac{M_0}{\theta_0} = \frac{C_I}{C_z}\frac{I_0}{z_0} \quad , \tag{2.19}$$

$$\delta_s = \delta_{M(t)} - \delta_{\theta(t)} = \delta_{I(t)} - \delta_{z(t)} \quad , \tag{2.20}$$

Table 2.4: **Primary measurable variables Limits:** Minimum and maximum for S/N ≥ 5 according to the Fourier analysis for the ISR and DWR. No limits could be found for the bi-cone which agree with S/N ≥ 5. Superscript * denotes values for large η_s.

	symbol	unit	min	max
ISR	$I(t)$	A	7.0×10^{-3}	1.4
	$z(t)$	m	3.0×10^{-5}	2.0×10^{-3}
			$4.0 \times 10^{-6*}$	
Small DWR + Langmuir trough	$M(t)$	N m	5.0×10^{-10} [a]	–
			1.3×10^{-9} [b]	5.7×10^{-8} [b]
			4.6×10^{-9} [c]	3.4×10^{-8} [c]
	$\theta(t)$	rad	3.2×10^{-3} [a]	–
			2.4×10^{-4} [a]*	–
			2.0×10^{-5} [b]	–
			2.9×10^{-6} [c]	–
Big DWR (3d-printed)	$M(t)$	N m	4.3×10^{-9} [b]	4.8×10^{-8} [b]
			1.0×10^{-8} [c]	3.9×10^{-8} [c]
	$\theta(t)$	rad	1.3×10^{-5} [b]	–
			1.1×10^{-5} [c]	–
Big DWR (TA)	$M(t)$	N m	2.1×10^{-9} [b]	5.1×10^{-8} [b]
			7.0×10^{-9} [c]	4.6×10^{-8} [c]
	$\theta(t)$	rad	1.1×10^{-5} [b]	–
			1.1×10^{-5} [c]	–

[a] Open loop stress controlled mode
[b] Closed loop stress controlled mode
[c] Strain controlled mode

where $C_\square$ denote geometrical conversion factors relating displacement with interfacial strain $\gamma_s = C_\theta \theta_0$ or $C_z z_0$ and torque or force with interfacial stress $\tau_s = C_M M_0$ or $C_I I_0$ (more details about $C_\square$ in SI A.6). The equality on the left hand side corresponds to the rotational geometries (DWR & bi-cone) while the right hand side corresponds to the ISR. $|G_s^*|$ and δ_s are the norm and phase angle of the complex interfacial shear modulus.

The uncertainty in $|G_s^*|$ and δ_s can be obtained from the propagation of the errors on the primary variables in Eq. (2.19) & (2.20) using the noise on the primary variables as the uncertainties. Assuming τ_s and γ_s to be uncorrelated, the uncertainties $u_{|G_s^*|}$ and u_{δ_s} are the standard deviations [83–85]

$$u_{|G_s^*|} = \sqrt{\left(\frac{\partial |G_s^*|}{\partial \tau_s} \Delta\tau_s\right)^2 + \left(\frac{\partial |G_s^*|}{\partial \gamma_s} \Delta\gamma_s\right)^2} \tag{2.21}$$

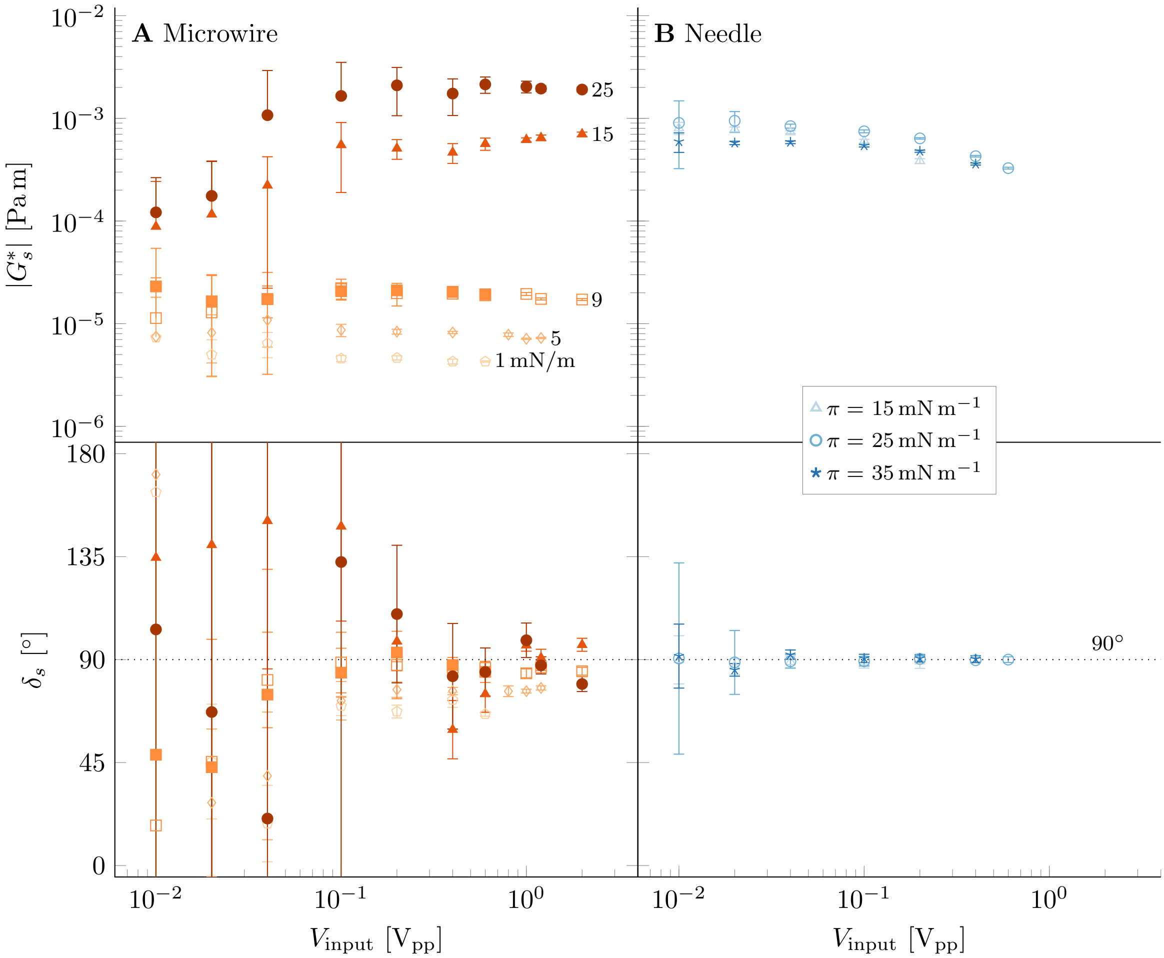

Figure 2.5: **Uncertainties of $|G_s^*|$ and δ_s measured with the ISR:** Data from Fig. 2.3 and corrected for bulk flow effects. **A)** $|G_s^*|$ and δ_s measured with the microwire. **B)** $|G_s^*|$ and δ_s measured with the needle, for different surface pressures and corresponding uncertainties calculated by Eq. (2.22) & (2.23). Open and closed symbols correspond to different magnifications of the objective (4× and 10×, respectively).

$$= \frac{C_M}{C_\theta}\sqrt{\frac{1}{\theta_0^2}M_{\mathrm{noise}}^2 + \left(\frac{M_0}{\theta_0^2}\right)^2\theta_{\mathrm{noise}}^2} \qquad = \frac{C_I}{C_z}\sqrt{\left(\frac{1}{z_0}\right)I_{\mathrm{noise}}^2 + \left(\frac{I_0}{z_0^2}\right)^2 z_{\mathrm{noise}}^2} \quad , \tag{2.22}$$

$$u_{\delta_s} = \sin^{-1}\left(\frac{M_{\mathrm{noise}}}{M_0}\right) + \sin^{-1}\left(\frac{\theta_{\mathrm{noise}}}{\theta_0}\right) \qquad = \sin^{-1}\left(\frac{I_{\mathrm{noise}}}{I_0}\right) + \sin^{-1}\left(\frac{z_{\mathrm{noise}}}{z_0}\right) \quad , \tag{2.23}$$

where again the equality on the left corresponds to the rotational geometries (DWR & bi-cone) while the one on the right equality is for the ISR, the subscripts *noise* and *0* are the noise and amplitude values defined in the previous section.

In deriving Eq. (2.23), the uncertainty on the phase angle is estimated by looking at the signal zero-crossing locations, and quantifying the uncertainty in these locations due to the finite strain and torque or force resolution of the rheometer following Singh et al. [85]. This consideration is more accurate for the ISR than for the rotational geometries, since in the latter, the phase angle is determined by cross-correlating the two signals and might result in a larger S/N ratio of G_s' and G_s'' and the phase angle is calculated as

$$\delta_s = \tan^{-1}\left(\frac{G_s''}{G_s'}\right) \quad , \tag{2.24}$$

where Eq. (2.12) and (2.13) are used. As a consequence of Eq. (2.24), measuring the phase angle of a purely viscous system ($\delta_s = 90°$) is very difficult because $\tan(\pi/2) \to \infty$. Since the details of the signal processing in the different rheometers are not known a priori and may evolve as signal processing algorithms continue to improve, Eq. (2.23) can be seen as an upper bound for the phase angle uncertainty.

An example for uncertainties $u_{|G_s^*|}$ and u_{δ_s} during a stress amplitude sweep on the ISR are shown in Fig. 2.5 for different surface pressures π at $f = 0.1\,\text{Hz}$. The uncertainties in terms of S/N are shown as error bars in these graphs using (2.22) and (2.23). The data is corrected for the effects of flows in the subphase. At small amplitudes, the uncertainty bars $u_{|G_s^*|}$ increase and become even larger than $|G_s^*|$ for the microwire. The same behavior is seen in u_{δ_s} where $\sin^{-1}(x) = \pi/2$ if $x \geq 1$. On the other hand, error bars become very small for large amplitudes. Similar to bulk rheological measurements, the noise is more important for the phase angle. A small decrease in $|G_s^*|$ with increasing stress amplitude is observed for the needle which denotes the limit of the linear response regime.

2.3.3 Limit lines and operating windows

Having identified the limiting values in displacement and force or torque as those where the noise becomes dominant, it is now possible to define operating windows. To measure the material response, it has to be larger than the minimum measurable value of displacement or torque

$$M_{\text{material}} > M_{\text{min}} \qquad\qquad z_{\text{material}} > z_{\text{min}} \quad . \tag{2.25}$$

Applying equation (2.19), M_{material} and z_{material} are expressed in terms of material functions and the displacement amplitude θ_0 and applied current amplitude I_0

$$\begin{aligned} \frac{C_\theta}{C_M}|G_s^*|\theta_0 &> M_{\text{min}} & \frac{C_I}{C_z}\frac{I_0}{|G_s^*|} &> z_{\text{min}} \\ |G_s^*| &> \frac{C_M}{C_\theta}\frac{M_{\text{min}}}{\theta_0} & |G_s^*| &> \frac{C_I}{C_z}\frac{I_0}{z_{\text{min}}} \quad , \end{aligned} \tag{2.26}$$

where $C_\square$ are conversion factors discussed in SI A.6.

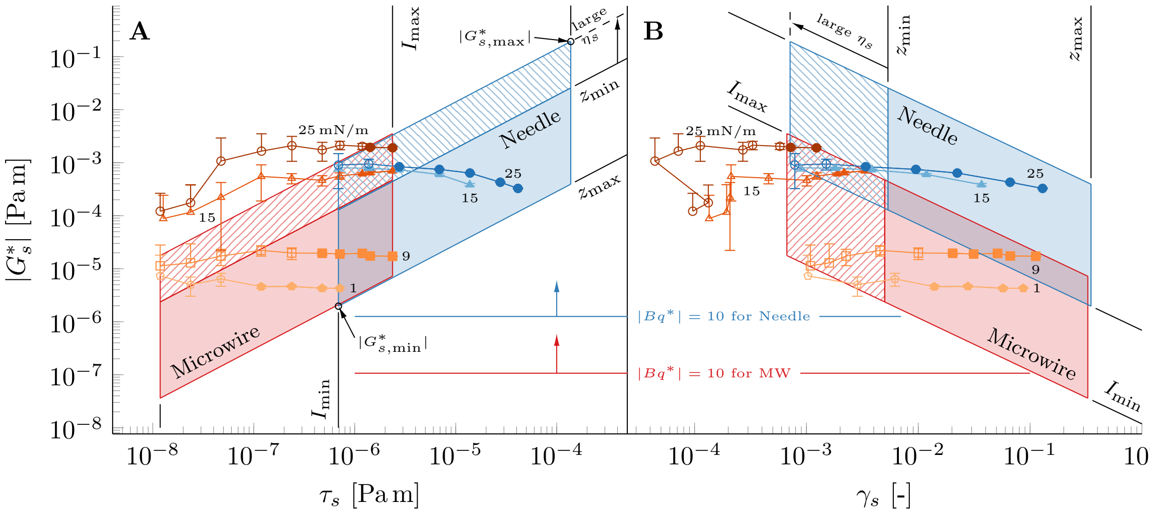

Figure 2.6: **Operating window for the ISR:** $|G_s^*|$ as function of interfacial stress amplitude **(A)** and interfacial strain amplitude **(B)**. Limits are defined in Table 2.4. The overlayed experimental data shows hexadecanol at the water-air interface measured at $f = 0.1\,\text{Hz}$ at different surface pressures indicated by small numbers. Error bars on the data are the calculated S/N ratios and symbols are filled for S/N ≥ 10. Lines for $|Bq^*| = 10$ for the microwire (MW) and needle (N) are drawn to guide the eye and the direction of increasing $|Bq^*|$ is indicated by arrows. Examples of maximal and minimal measurable $|G_s^*|$ are indicated for the needle as $|G^*_{s,\text{max}}|$ and $|G^*_{s,\text{min}}|$.

The same calculation as in Eq. (2.25) and (2.26) can be performed for the upper torque M_{max} and rod displacement z_{max} limits as well as the displacement for the rotational geometries and the input current for the ISR. The limit lines can then be drawn as functions of interfacial stress τ_s and interfacial strain γ_s which is shown for the ISR in Fig. 2.6. The area enclosed by the limit lines defines the operation window of the instrument.

By looking only at the experimental data in Fig. 2.6, the apparent interfacial modulus for hexadecanol at $\pi = 15\,\mathrm{mN\,m^{-1}}$ measured with the microwire is increasing before it reaches a plateau with increasing τ_s. Drawing the operation window reveals that the low amplitude data is outside the window and the error bars show that the signal-to-noise ratio is smaller than 1. As a consequence, the increase in $|G_s^*|$ is due to the z_{min} limitation and does not represent an intrinsic material property. The plateau value measured inside the window agrees well with the data measured with the needle at the same π. The agreement between the probes of different length at $\pi = 15\,\mathrm{mN\,m^{-1}}$ while having different aspect ratios $(l/2r)$ of 59 and 180 for the needle and microwire, respectively, suggests that end effects are negligible [40]. The data measured at $\pi = 25\,\mathrm{mN\,m^{-1}}$ with the microwire only enters the operating window at the very edge. As a consequence, the data measured with the needle at the same π might be more confident. To relate the subphase drag with the interfacial modulus, values of $|Bq^*| = 10$ are drawn for the microwire and needle in Fig. 2.6 as a guide to the eye, where higher $|Bq^*|$ correspond to more confidence in the data.

Representing the operating windows as function of primary variables might be helpful for defining the input parameters or selecting the right probe for a given expected $|G_s^*|$ or $|\eta_s^*|$.

The operating windows for the small DWR in conjunction with a Langmuir trough are shown in Fig. 2.7 as functions of τ_s and γ_s together with measured data for hexadecanol at $\pi = 25\,\mathrm{mN\,m^{-1}}$. The maximum displacement has been chosen at $\gamma_s = 2\,\%$ to remain in the linear viscoelastic regime for the fluid studied here and prevent the destruction of the materials microstructure. Three operating windows according to the three operation modes are drawn. As discussed previously, the open loop stress controlled mode results in the lowest torque limit but shows the largest displacement limit due to subphase drift. A line is drawn for a clean water-air interface where no interfacial viscosity is present to suppress this drift and as a result, the operating window is almost vanishing, i.e. η_s is undetectable with the DWR in this mode. The upper torque limit is $200\,\mathrm{mN\,m}$ according to the instrument specification, corresponding to stresses far beyond the range shown in Fig. 2.7, and thus the window is only drawn until an arbitrary maximum stress value.

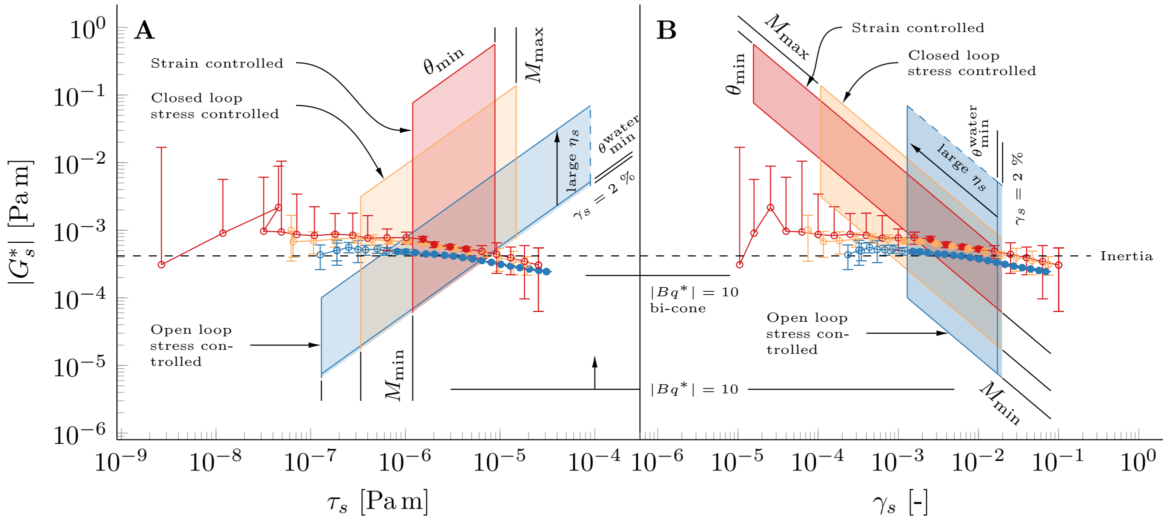

Figure 2.7: **Operating windows for the DWR (small diameter ring in conjunction with a Langmuir trough):** $|G_s^*|$ as function of **(A)** interfacial stress amplitude and **(B)** interfacial strain amplitude. The overlayed experimental data shows hexadecanol at the water-air interface measured at $f = 0.1\,\text{Hz}$ and $\pi = 25\,\text{mN}\,\text{m}^{-1}$ and are linked to the operation mode by the color code. Error bars denote S/N ratios of $|G_s^*|$ and filled symbols show S/N ≥ 10. Lines showing $|Bq^*| = 10$ are drawn for the DWR and bi-cone to guide the eye and the direction of increasing $|Bq^*|$ is indicated by the arrow. The magnitude of the contribution of the instrument and geometry inertia is indicated with the dashed line.

This large stress value will lead to a modulus of $10^3\,\text{Pa}\,\text{m}$ for $\gamma_s = 2\,\%$ and up to $10^6\,\text{Pa}\,\text{m}$ for smaller γ_s. This order of magnitude will of course never be observed in interfacial rheology and other effects like the violation of the no-slip boundary condition might come into play earlier. The window for the closed loop stress controlled mode shows a slightly larger $M_{\min}$ and lower $\theta_{\min}$. More striking is the appearance of a maximum torque limit much lower than the instrument specification. The feedback loop leads to an amplification of noise in the primary torque signal as shown in Fig. 2.4. This is valid for materials expressing very low rheological properties. Interfaces with stronger moduli might suppress the noise amplifying effect and shift $M_{\max}$ towards larger values. The strain controlled mode shows the lowest $\theta_{\min}$ but expresses the narrowest confinement in torque. The reason is the stronger feedback loop compared with the closed loop mode which results in an even stronger amplification of the noise.

The hexadecanol data again shows significant scatter outside the operation window and the signal-to-noise ratio can decrease to values smaller than 1. Within the operating windows, the S/N increases and error bars become smaller than the symbol size. Note that for the two operating modes with the feedback loop enabled, the uncertainty increases when the data hits the $M_{\max}$ limits. On the contrary, the closed loop stress control mode still has very small uncertainties even though $\gamma_s > 2\,\%$ because the $M_{\max}$ limitation is not present. The operating windows in terms of $|G_s^*|$ as a function of τ_s and γ_s for the larger diameter DWR can be found in Appendix 2.7.3.

2.3.4 Instrument limitations

The precision of measuring and accessible range of the primary variables is also affected by additional factors. Instrument and fluid inertia as well as instrument compliance are two other effects that can interfere with measurements, as in bulk (see e.g. [67] and references therein). The next section shows how the presence of instrumental effects can be identified.

Instrument inertia

The torque or force resulting from the material response has to be larger than the contribution from the instrument inertia, similar to the case of bulk rheology. The left hand equality corresponds to the rotational geometries (DWR & bi-cone) while the right hand side equality refers to the ISR.

$$M_{\text{material}} > M_{\text{inertia}} \qquad\qquad F_{\text{material}} > F_{\text{inertia}} \quad , \tag{2.27}$$

Rewriting the material and inertia contributions and applying the constitutive equation (2.19) leads to

$$\begin{aligned} \frac{C_\theta}{C_M}|G_s^*|\theta_0 &> I\theta_0\omega^2 & 2L\tau_s &> mz_0\omega^2 \\ |G_s^*| &> \frac{C_M}{C_\theta}I\omega^2 & |G_s^*| &> \frac{m}{2L}\frac{1}{C_z}\omega^2 \quad . \end{aligned} \tag{2.28}$$

where $I = I_{\text{instr}} + I_g$ is the sum of the instrument and geometry inertia, m and L are the mass and the length of the magnetic probe and ω is the driving frequency in $[\text{rad}\,\text{s}^{-1}]$. As a result of Eq. (2.28), the contribution of inertia to $|G_s^*|$ in a frequency sweep appears with a slope of +2 in a double logarithmic plot (or slope of +1 for the complex interfacial viscosity) and is constant in strain or stress amplitude sweeps.

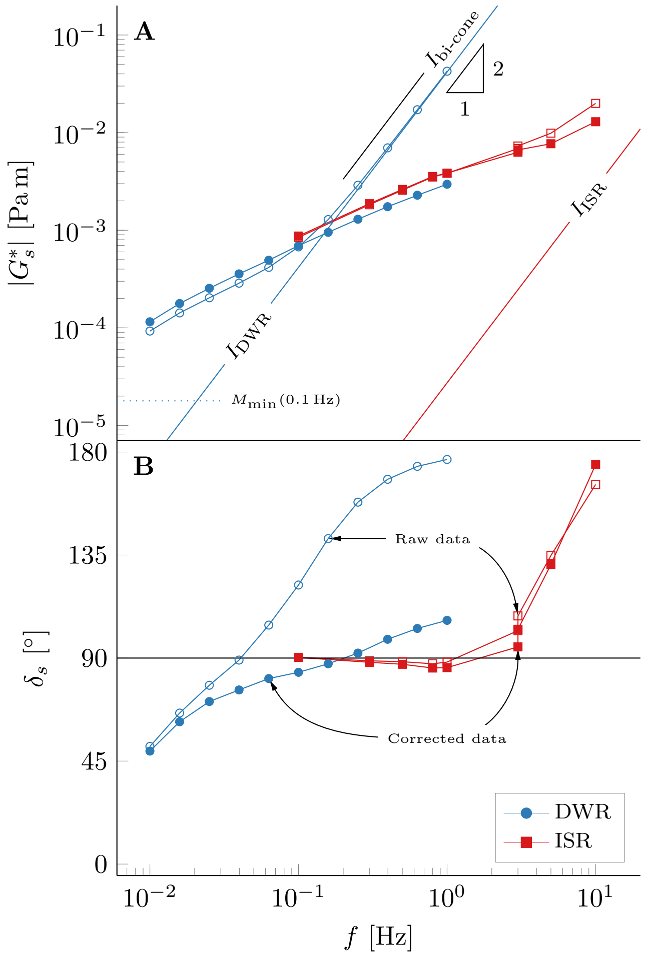

Figure 2.8: **Effects of Instrument inertia:** Frequency sweeps of hexadecanol at $\pi = 25\,\mathrm{mN\,m^{-1}}$ measured by the small diameter DWR in conjunction with a Langmuir trough (blue circles) and ISR (red squares). **A)** $|G_s^*|$ and **B)** δ_s. Open symbols are raw data and closed symbols are inertia and subphase flow corrected data. The solid lines $I_\square$ correspond to Eq. (2.28) for the ISR, small DWR and bi-cone.

An example of the effect of instrument inertia is shown in Fig. 2.8 where a frequency sweep of hexadecanol at $\pi = 25\,\mathrm{mN\,m^{-1}}$ is measured with the small DWR in conjunction with a Langmuir trough and ISR. The norm of the complex interfacial modulus $|G_s^*|$ reflects a viscous behavior with a slope versus frequency of +1 on a log-log scale. Once a certain frequency is reached for the DWR, the raw data increases its slope to +2 as predicted by Eq. (2.28). However, the raw data can be corrected for the instrument and geometry inertia by the instrument software which can also be seen by the very large decrease of phase angle δ_s for the DWR.

The raw and subphase corrected phase angle data of the ISR diverges towards 180° despite fulfilling Eq. (2.28) which due to the very low mass of the needle holds up to very large frequencies. It seems like the assumptions for the flow field are no longer valid for these large frequencies. This demonstrates that limitations can depend on specific instruments.

Compliance

There are two sources of instrument compliance. The first corresponds to a small restoring force with respect to an 'equilibrium' position of the probe due to inhomogeneities in the magnetic field or bearing in the rotational rheometer or meniscus imperfections of the interface. This effect acts 'in parallel' with the stiffness of the material and the same rationale used for the instrument inertia can be done to identify the limitation

$$M_{\text{material}} > M_{\text{compliance}} \qquad\qquad F_{\text{material}} > F_{\text{compliance}} \quad . \tag{2.29}$$

Using again Eq. (2.19), this equation can be rewritten as

$$\begin{aligned} \frac{C_\theta}{C_M}|G_s^*|\theta_0 &> k\theta_0 & \qquad 2L\tau_s &> kz_0 \\ |G_s^*| &> \frac{C_M}{C_\theta}k & \qquad |G_s^*| &> \frac{k}{2L}\frac{1}{C_z} \quad , \end{aligned} \tag{2.30}$$

where k^{-1} is the compliance of the instrument. The resulting limit line neither depends on amplitude nor on frequency thus it is imposing a general boundary to the instrument. As a result, it is most often encountered at very small driving frequencies in contrast to instrument inertia (see Eq. (2.28)). The nature of the instrument compliance as a restoring force will affect mainly the interfacial storage modulus G_s'. This might lead to misinterpretation of the material to be elastic instead of assigning the elevated elastic component to compliance. As a consequence, compliance could be the reason for the decrease of δ_s at low frequencies in Fig. 2.8. The observed stiffness corresponds to $\sim 5 \times 10^{-5}\,\text{Pa m}$ which would agree with [48]. The instrument compliance k^{-1} of the ISR is measured during the calibration process and is given for the used magnetic probes in Table 2.1.

Another source of compliance can be the limited rigidity of the geometry (stiffness of the shaft) and acts ‘in series’ with the stiffness of the material, therefore imposing an upper limitation in contrast to Eq. (2.30). The compliance of the small DWR has been measured by immobilizing the ring on the bottom plate of the rheometer and applying a creep test. The resulting compliance leads to an upper limitation of 38 Pa m for $|G_s^*|$ (see SI A.8 for more details). This limitation is smaller than the resulting $|G_s^*|$ of a maximum applicable torque amplitude of 200 mN m and therefore imposing the real upper limit for the open loop stress controlled mode. The bi-cone is expected to be even stiffer than the rings due to its solid structure thus the upper limit will be even larger.

Dynamic range

In addition to the limit lines, Figs. 2.6 & 2.7 show also the maximum (maximum force or torque at minimum displacement) and minimum (maximum displacement minimum force or torque) measurable $|G_s^*|$ for the selected geometries. The dynamic range describes the orders of magnitudes of measurable moduli and is calculated as

$$d = \log_{10}\left(\frac{|G^*_{s,\mathrm{max}}|}{|G^*_{s,\mathrm{min}}|}\right) \quad . \tag{2.31}$$

A list of dynamic ranges for each instrument can be found in Table 2.5.
In the case of the open loop stress controlled mode, the upper torque limit is mostly set by the compliance limitation. For the two closed loop operating modes, the limits reported in Table 2.4 have been used in order to calculate d. There M_{max} corresponds to a worst case scenario where noise is amplified by the feedback loop as discussed above. The maximum strain is arbitrarily chosen to to be $\gamma_s = 2\,\%$. Because of the different limiting values the DWR shows a range of d depending on the operation mode and used geometry.

The intrinsic dynamic range of the ISR does not depend on the choice of probe because the difference in $|G_s^*|$ lies only in the conversion factors. For very delicate samples, the dynamic range might be reduced since the maximum strain for the ISR is larger than 2 % and the microstructure of the interface might be destroyed. The bi-cones are not sensitive enough to measure hexadecanol, therefore no dynamic range can be given here.

Table 2.5: **Dynamic ranges Eq.** (2.31) **of ISR and DWR:** The ISR is an open loop stress controlled instrument. Only the open loop mode with the DWR is truly stress controlled. No operating window could be defined for both bi-cones.

	Stress controlled		Strain controlled
	Open loop	Closed loop	
ISR	5.0	[a]	[a]
Small DWR	6.8	3.9	4.0
Big DWR	[b]	3.3	2.9
Big DWR (TA)	[b]	3.7	3.1

[a] Operating mode not available.
[b] Operating mode not tested because of large subphase convection.

2.3.5 Coupling with the bulk phase

The flow at the interface is always coupled with the flow in the adjacent bulk phases. This coupling can lead to non-homogeneous velocity profiles which affect the local interfacial shear rate at the measurement probe. Moreover, the drag exerted by the bulk phases on the measurement probe needs to be accounted for. To be able to measure the interfacial properties accurately, the contribution of the interface drag has to be larger than the one from the subphase

$$F_{\text{Drag, interface}} > F_{\text{Drag, bulk}} \quad . \tag{2.32}$$

The inequality (2.32) can be rewritten as a ratio between the interfacial and bulk drag in terms of a macroscopic non-dimensional Boussinesq number Bq as shown in Eq. (2.8) in the introduction. Lines corresponding to $|Bq^*| = 10$ are drawn in Fig. 2.6 and 2.7 in order relate the Bq^* with the interfacial shear modulus and to guide the eye.

Effects of geometry

The characteristic length scale a in Eq. (2.16) is the ratio of the contact perimeter P_s between the probe and the interface to the contact area A_b between the probe and the bulk phase therefore it is set by the geometry of the measurement. To increase the sensitivity of a geometry, a has to be minimized. As a consequence, the bi-cone is expected to be the least sensitive. For the DWR, a depends on the thickness of the ring [60] which is difficult to reduce since it has to support mechanical stability to be connected to the rheometer. In the case of the ISR, a depends on the probe radius [58] which can be reduced by an order of magnitude by moving from glass capillaries to the used microwire [79]. The characteristic length scales for the different geometries used here are shown in Table 2.6.

Table 2.6: **Characteristic length scale a:** and resulting $|\eta_s^*|$ for $|Bq^*| = 1$ and $\eta_{\text{bulk}} = 1\,\text{mPa}\,\text{s}$ imposing a lower limitation.

Instrument	Geometry	a [mm]	$\lvert\eta_s^*(Bq = 1)\rvert$ [Pa m s]
ISR	Needle	$r = 0.200$	2.00×10^{-7}
	Microwire	$r = 0.0175$	1.75×10^{-8}
DWR	Small ring	$\frac{R_{\text{ring}}^{\text{outer}} - R_{\text{ring}}^{\text{inner}}}{2\sqrt{2}} \approx 0.707$	7.07×10^{-7}
	Big ring		
bi-cone	bi-cone	$R_{\text{cone}} = 34$	3.40×10^{-5}

Subphase correction

It has been shown by Reynaert et al. [58] that the coupling between the interface and the bulk phase leads to non-linear interfacial velocity profiles and apart from interfaces with very high Bq it is insufficient to linearly subtract the rheological response of a clean interface from the rheological response of a laden interface. Verwijlen et al. [80] suggested an iterative algorithm to decouple the interfacial drag from the bulk drag on the ISR probe and is sketched in SI A.1. The Navier-Stokes equations for the velocity field in the bulk and at the interface are calculated where the interface acts as a Boussinesq-Scriven type boundary condition for the bulk with a chosen initial Bq^*. From the calculated flow field, the interfacial and bulk drag on the probe are known and the resulting amplitude ratio is calculated. The chosen Bq^* is then refined according to the ratio between the measured to the calculated amplitude ratio. The refined Bq^* is used to redefine the boundary condition and the algorithm iterates until Bq^* converges. Note that the flows in the subphases are not necessarily low Re flows, and bulk fluid inertia can influence the interfacial velocity profiles [58]. Similar finite difference schemes have been reported for the DWR [60] (see also SI A.1) and for the bi-cone [59, 69]. A boundary integral method has been reported for the ISR which can result in better accuracy at low Bq^* [73], but it does not account for fluid inertial effects and hence is limited to low frequency data.

Precision

The precision of the subphase correction is evaluated by using amplitude ratios of defined complex Bq^*_{defined} as input to the subphase correction code and comparing the resulting $Bq^*_{\text{calculated}}$ with Bq^*_{defined}. The resulting differences for various magnitudes and phase angles are shown in Fig. 2.9. For $|Bq^*| \geq 1$ the error is smaller than 0.1 % and reaches 10^{-15} % at $|Bq^*| = 10$. The error of δ_s is given in absolute difference and not in percentage since also a defined angle of 0° is calculated and the relative error diverges towards infinity. At $|Bq^*| = 1$ the phase angle shows an error of $10^{-4\circ}$ and decreases with increasing Bq^*. The behavior of the error is mostly independent on defined phase angle. However, for very elastic interfaces ($\delta_s = 0°$) resonance behavior is observed in the subphase flow calculation and it behaves similar to a driven harmonic oscillator. It might be very difficult to experimentally observe resonance because other effects like plastic deformation or the presence of slip might be present.

The importance of the non-linear subphase correction is evident from Fig. 2.9 as the error for the linear correction is much larger in both magnitude and phase angle even at very large Bq^* (at $|Bq^*_{\text{defined}}| = 10^4$ the uncertainty is still ~ 5 %). The reason for the very large Bq^* lies within the definition as a macroscopic Boussinesq number in Eq. (2.8) instead of using a true intrinsic length scale as has been done by Fitzgibbon et al. [73]. The necessity highlights that the coupling of interfacial with bulk phase flows is strongly non-linear hence all the data presented in this work is non-linearly corrected for subphase flow.

The non-linear subphase correction also shows a large stability against noise in the amplitude ratio. At a signal-to-noise ratio of 100, the resulting error is smaller than 1 % for $|Bq^*| \geq 1$. However, noise in the phase angle of the amplitude ratio is also affecting the magnitude of the resulting Bq^* and vice versa (see SI A.9). Hence, it is very important to measure both magnitude and phase angle of the amplitude ratio precisely.

Lower limit

For interfaces with $|Bq^*| < 1$, there might still be a measurable decrease of amplitude ratio of the investigated interface compared to the clean interface. However, the algorithm mentioned above may no longer converge (see Fig. 2.9 and [80]) for any phase angle δ_s. This limit shows again the importance of using appropriate geometries to optimize for a large Bq^* i.e. minimizing a in Eq. (2.16). As a result, the lowest measurable complex

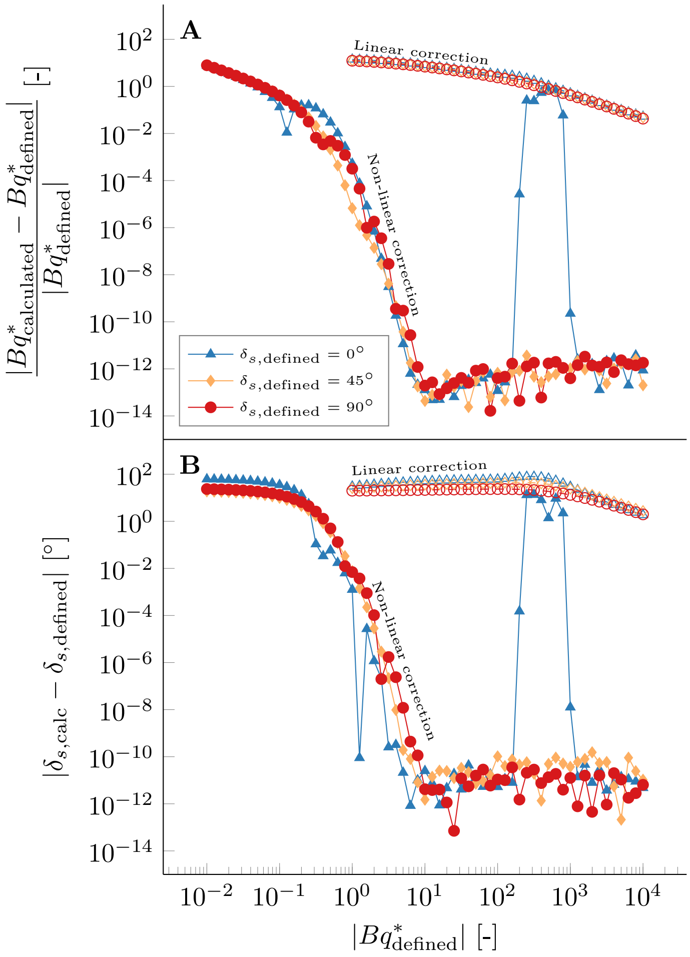

Figure 2.9: **Uncertainty of subphase correction:** Error of the magnitude $|Bq^*|$ (**A**) and phase angle δ_s (**B**) for defined Bq^*. Filled and empty symbols correspond to the non-linear and linear subphase correction of the ISR. Parameters of the microwire are used.

interfacial viscosity is given by using $|Bq^*| = 1$ in Eq. (2.16). The values of minimal $|\eta_s^*|$ for each geometry are given in Table 2.6. As can be seen in Fig. 2.6 and 2.7, this limit can be compromised by other effects, for example the noise amplification in the case of the DWR results in a larger $|\eta^*_{s,\text{ min}}|$.

Furthermore, the limitation of $|Bq^*| \geq 1$ for a converging analysis might not be relevant for technical applications. The response of the interface is smaller than the one of the bulk and might even become negligible. It might be sufficient to know the interfacial response is below a certain level in order to be irrelevant (for the ISR with the microwire probe $|\eta_s^*|_{Bq=1} \sim 10^{-8}\,\text{Pa m s}$) instead of knowing its exact value. In case this is not sufficient and the exact value of η_s^* has to be known, different analysis methods have to be used, e.g. the boundary integral method of [73] could extend the range, or the geometry has to be further optimized for an even smaller a.

2.3.6 Further experimental difficulties

Other experimental effects can lead to situations that violate the assumptions made in the introduction. Misplacing the geometry at the interface or a wetting behavior that is not ideal due to finite roughness or manufacturing imprecision can lead to curvature. These effects are discussed in the following paragraph.

Positioning at the interface

A vertical misplacement of the geometry with respect to the interface can lead to a curved or stretched interface. In the analysis discussed above, the interface is always assumed to be perfectly flat and the presence of curvature leads to an additional term $-\sigma \boldsymbol{\nabla}_s \cdot \boldsymbol{I}_s$ in the momentum balance (see Eq. (2.1)). Capillary waves could in principle also violate the assumption of a perfectly flat interfaces, but their characteristic time scale is several order of magnitudes faster compared to the measuring time scale. Since the geometries for the DWR and bi-cone are attached to a regular rheometer, the vertical placement of the geometry can be controlled in the software by the gap size. Effects like evaporation during long experiments can lower the level of the interface and introduce curvature. As a consequence, vertical position has to be adjusted regularly during the experiment. Experiments at different heights can be done to assess the influence of misplacement on the interfacial rheology. It was found that a height change up to ±350 µm is still within 20 % of the norm of the complex interfacial modulus (see SI A.10).

For the analysis of the ISR, a contact angle of 90° of the glass needles is assumed. To fulfill this assumption, the glass surface is usually rendered more hydrophobic using a silanization reaction. At contact angles smaller than 90° the needle has more contact with the water subphase. Due to the larger subphase drag, the analysis routine overestimates the complex interfacial modulus while underestimating the fluid inertia thus δ_s will be too large. The effect is opposite for contact angles bigger than 90°. The error resulting of a contact angle difference of ±15° can be up to 15 % for $Bq^* = 100$, i.e. low interfacial modulus, and decreases to below 0.5 % for $Bq^* = 10^5$ (see SI A.10). Fitzgibbon et al.

discusses the possibility of a different contact angle and the changes in the formalism that come alongside as long as there are combinations of contact angles and bulk densities that result in flat interfaces [73].

The density of the needle is also important since experiments can be carried out on surfaces with low surface tension and the ratio of buoyancy forces to interfacial forces can change, described by the Bond number

$$Bd = \frac{g(\rho_{\text{needle}} - \rho_{\text{bulk}})\pi a^2}{2\sigma} \quad , \tag{2.33}$$

where g is the gravitational force per unit mass, ρ_{needle} and ρ_{bulk} are the density of the needle and bulk phase, respectively, a is the characteristic length scale and σ is the surface tension. As a result, the vertical position of the needle with respect to the interface changes as a function of σ hence the focus has to be adjusted throughout an experiment involving measurements at various π. A heavy needle with large radius can even be submerged at low surface tensions [58].

Eccentricity

The bi-cone and large diameter DWR are well aligned by fixing the measuring cell and cup to the bottom plate of the rheometers. However, the modified cups for the DWR are placed in a Langmuir trough as shown in Fig. 2.1D and care has to be taken to align the cup properly. In the present work a custom built positioning tool is used which is attached to the rheometer and has a conical ring shape on the lower end. By lowering the positioning ring to the cup, the cup is centered below the rheometer and precisely aligned with respect to the rheometer shaft. For the fatty alcohol system under investigation, it was found that only significant displacements of the DWR cup up to 800 µm result in an increase in the elastic contributions (G'_s) and below 200 µm no significant change of the rheological properties can be observed (see SI A.10). The extent to which eccentricity plays a role depends on the compressibility of the interfaces, and the magnitude of the dilatational properties, see Verwijlen et al. for an analysis of geometrically perturbed DWR [86]. The positioning of the magnetic probe in the ISR is more difficult to control since the free floating probe can move during an experiment due to diffusion or subphase convection. Misplacing the probe results in different strain amplitudes on both sides of the needle. As a consequence, the probe might experience different responses on each side. Therefore, the motion of the probe will change from a perfectly linear towards a more elliptical motion. In case the ratio between channel and probe radius is large the two strain amplitudes are less different to each other and the effect is less pronounced.

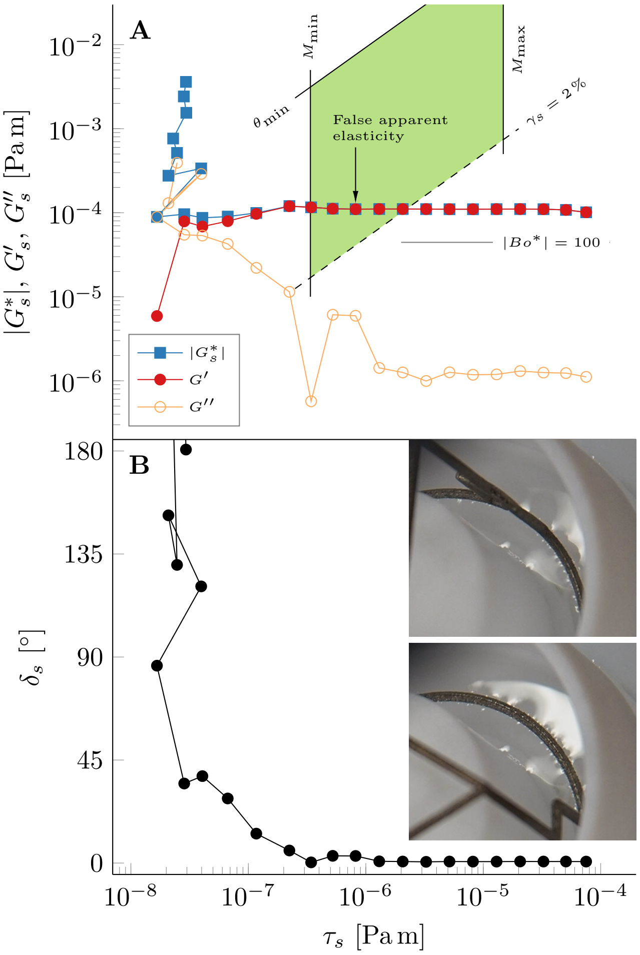

Figure 2.10: **Contact line variations leading to an apparent surface elasticity:** Data of a clean water-air interface measured with the small DWR in conjunction with a Langmuir trough and closed-loop stress controlled mode at $f = 0.1\,\mathrm{Hz}$. **A)** Norm and **B)** phase angle of complex interfacial modulus G_s^*. The operating window is shown in green and $|Bq^*| = 100$ is indicated to guide the eye. The pictures are taken at different times during an oscillation.

Contact line variations

A non-ideal contact line can not only result because of a bad positioning, but also because of non-perfect wetting of the geometry. The consequence is a contact line variation along the geometry as shown in Fig. 2.10. The mechanical data shows an apparent elastic response for a clean water-air interface ($\delta_s \rightarrow 0$) due to surface tension effects, akin to the effects in bulk rheology [87]. The images in Fig. 2.10B show the position of the geometry during different times of a measuring cycle of the data in Fig. 2.10A. The changes in reflections indicate a curvature of the interface that is dependent on the position θ which result in apparent elastic responses of the interface that are even stronger than a Bq of 100. Therefore, the elastic behavior is clearly an artifact and does not reflect an interfacial rheological property. The case of the clean water-air interface represents a worst case scenario, as surface active moieties will lower surface tension and increase the relative contributions of the interfacial moduli. It is good practice to quantify this effect for each geometry using a clean interface as a control, and to document the shape of the contact line with photos, as in Fig. 2.10B.

The capillary forces due to a non-ideal wetting of the magnetic probe or channel wall in the ISR will lead to a position of the probe within the channel to minimize the deformations of the meniscus. The increase in capillary force when the probe is displaced will lead to an apparent elastic response, observable as a decreased instrument compliance k^{-1}, similar to the case of the DWR discussed above. Careful cleaning of the channel wall can diminish this effect. A similar interaction can be observed when the end of the magnetic probe is close to the channel openings. Therefore, the channel should be much longer than the magnetic probe such that the probe can be placed in the center while interactions with the channel edge are suppressed.

2.4 Conclusion

There are several aspects, some intrinsic and some device related, which render interfacial rheometry challenging. In the present work we give an overview of the possible aspects which influence the accuracy of the obtained experimental data and derive operating windows where reliable data can be obtained. A first aspect which has been considered is the propagation of noise, which merits particular attention given that the torque or force

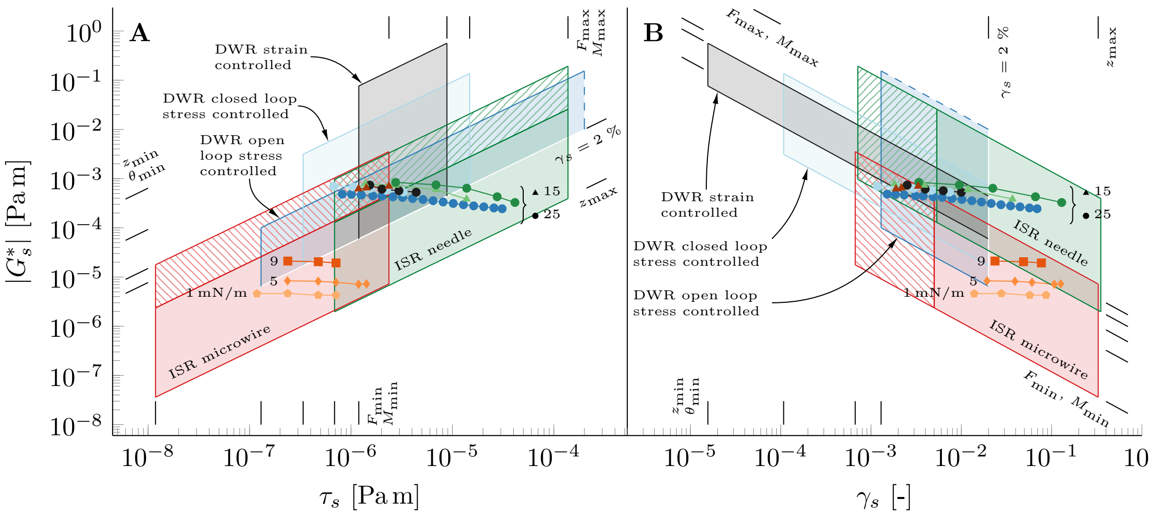

Figure 2.11: **Operating windows for ISR and the small diameter DWR:** as function of **(A)** interfacial stress and **(B)** interfacial strain. The overlaid experimental data show the response of hexadecanol at the water-air interface at different surface pressure and $f = 0.1\,\mathrm{Hz}$. The small diameter ring is used in conjunction with a Langmuir trough.

response of the interface is weak. Calculating the noise propagation makes it possible to quantify the uncertainties $u_{|G_s^*|}$ and u_{δ_s} (Eqs. (2.22) & (2.23)) to define uncertainty bars on the measured data which will give a direct indication of the quality of each individual measurement. A complicating matter is that this noise propagation depends on the properties of the interface. In the present work we used a fatty alcohol as a challenging material to characterize. Interfaces comprised of other materials such as polymers, proteins or colloidal particles can be non-linear viscoelastic (e.g. visco-plastic, shear thinning). Substituting Eq. (2.19) & (2.20) with the appropriate constitutive equation allows the presented analysis to be used for other types of interfaces as long as there are no artifacts such as slip or fast dissolution of soluble surfactants present. Aspects such as the role of drift, instrument and fluid inertia, compliance and the role of subphase corrections all contribute to possible measurement errors. To summarize all these effects, Fig. 2.11 gives the operating windows for the different devices. Fig. 2.11 summarizes the excellent sensitivity of the ISR and the impressive dynamic measuring range of the DWR. The bi-cone does not appear to be suitable for investigating fatty alcohols but will be appropriate for interfaces with higher moduli and viscosities. The procedure outlined to measure the noise propagation can be used for those cases. An overview of all the different aspects discussed with the governing equations or relevant figures is given in Table 2.7, which should serve as a useful guide for interfacial rheometry practitioners.

Table 2.7: Overview of contributing effects.

Investigated effect	Reference
Noise of primary variables	Fig. 2.3, 2.4, Table 2.4
Error propagation and uncertainty	Eq. (2.22), (2.23), Fig. 2.5
Limit lines and operating windows	Eq. (2.26), Fig. 2.6, 2.7
Instrument inertia and compliance	Eq. (2.28), (2.30), Fig. 2.8
Numerical error of subphase correction	Fig. 2.9
Low Boussinesq limit	Table 2.6
Positioning	Section 2.3.6
Contact line variation	Fig. 2.10

2.5 Supplementary material

See the supplementary material for (*i*) a description of the subphase correction algorithm for the ISR and DWR, (*ii*) a description of a calibration example of the ISR, (*iii*) a comparison of Fig. 2.2 with a “bad” data set of the ISR, (*iv*) noise for the large diameter DWR as well as the dependence on frequency for both DWR sizes, (*v*) Fourier spectrum examples for the bi-cone, (*vi*) conversion factors for ISR, DWR and bi-cone, (*vii*) an open loop torque controlled repeat experiment of Fig. 2.8, (*viii*) information about DWR compliance, (*ix*) a description of the error propagation of $Bq*$ in the subphase correction and (*x*) information about vertical and horizontal probe positioning.

2.6 Acknowledgments

Special thanks go to C. Furrer for construction improvements of the ISR and DWR. Furthermore, S. Busato is thanked for further technical assistance, T. Schweizer was very helpful with the bi-cone experiments and TA instruments is acknowledged for providing a bi-cone. The Swiss National Science Foundation Grant No. 200021_165974/1 and the Eidgenössische Technische Hochschule Research Grant ETH-0315-2 are acknowledged for financial support. AA and JV thank the Norwegian Research Council (Petromaks II program grant No. 255174) and the JIP Electrocoalesence Consortium.

2.7 Appendix: Operation windows

2.7.1 Hexadecanol

The surface pressure area compression isotherm of hexadecanol at $T = 23\,°\mathrm{C}$ and relative humidity of 50 % is shown in Fig. 2.12. The mean molecular area is calculated from the volume and concentration of the spread solution and the surface area of the trough and should be treated as an estimate of the actual MMA. All rheological experiments were conducted at a defined π hence the inaccuracy in MMA does not affect the measurements.

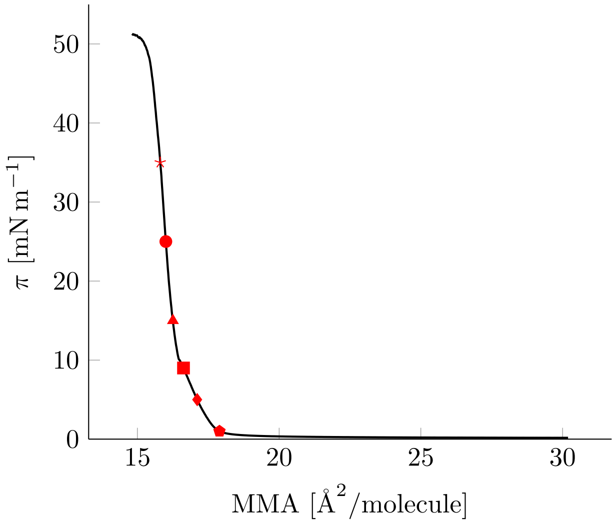

Figure 2.12: **Compression isotherm of hexadecanol:** Surface pressure π as function of mean molecular area MMA at $T = 23\,°\mathrm{C}$.

2.7.2 DWR noise amplification example

Typical data sets of primary variables measured with the small diameter DWR in conjunction with a Langmuir trough are shown in Fig 2.13. The open loop stress control has no feedback and therefore shows the a very low M_{noise} on one hand but a relatively large θ_{noise} due to subphase drift or air flow on the other hand. The closed loop stress control enables the feedback loop to suppress this drift in the position signal and decreases

θ_{noise} which is accompanied by an increase in M_{noise}. Therefore, this operation mode is not truly stress controlled. In the strain amplitude controlled mode, the feedback is adjusting the torque during each cycle to arrive at the defined strain amplitudes. The resulting θ_{noise} is very low but it also leads to very large M_{noise}.

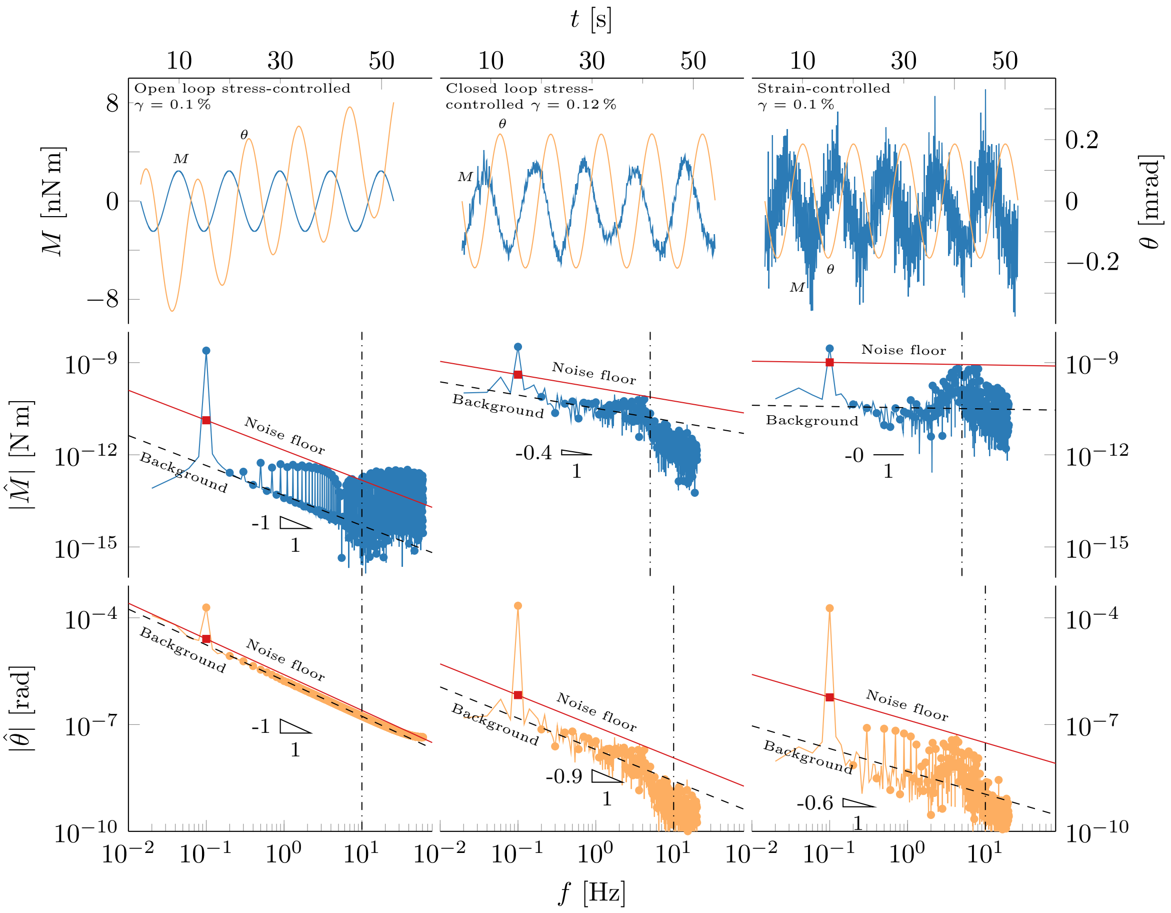

Figure 2.13: **Comparing operation modes of the DWR:** hexadecanol at $\pi = 25\,\text{mN}\,\text{m}^{-1}$ and 0.1 Hz measured with the small diameter ring in conjunction with a Langmuir trough. *Top:* $M(t)$ and $\theta(t)$ *Middle:* Fourier transform of $M(t)$. *Bottom:* Fourier transform of $\theta(t)$. Dots indicate integer harmonics of the signal.

2.7.3 Operating windows for different DWR sizes

The operating windows for the big and small DWR and operation modes are shown in Fig. 2.14 where the small diameter ring is used in conjunction with a Langmuir trough. The maximum displacement value is arbitrarily set to $\gamma_s = 2\,\%$ to remain in the linear viscoelastic regime. Since the surface pressure cannot be controlled with the cup of the big rings, the Fourier analysis is performed on data measured at a clean water-air interface to define limiting values that are comparable between different geometries. As a consequence, the operating loops for the open loop stress control mode are not reported since the noise in $\theta(t)$ is very large due to the drift in the subphase.

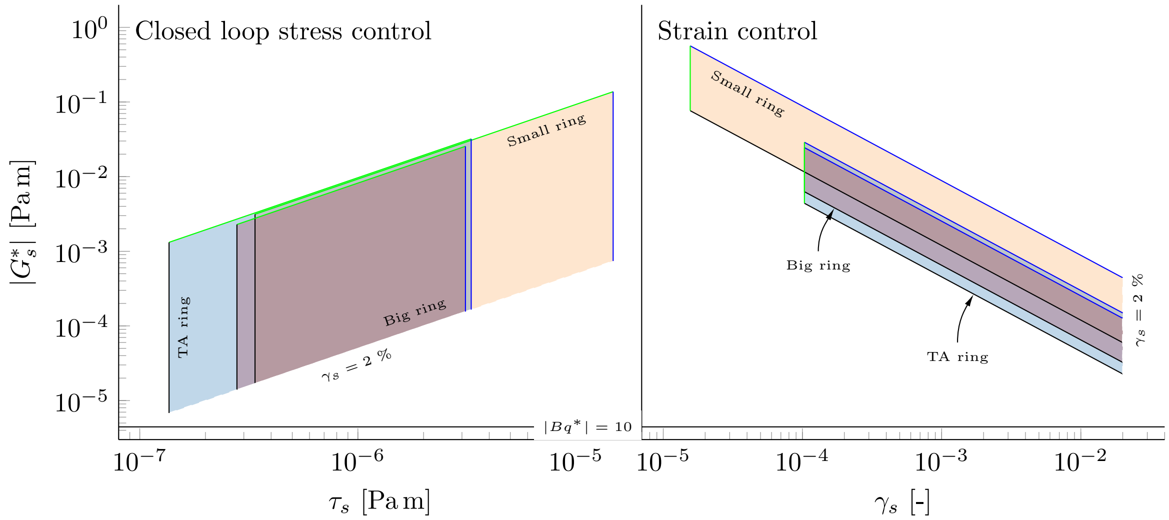

Figure 2.14: **Operating windows for the small and big DWR** as function of input interfacial stress amplitude τ_s and input interfacial strain amplitude γ_s. Limits determined for a clean water-air interface and at a driving frequency $f = 0.1$ Hz. The small diameter ring is used in conjunction with a Langmuir trough. $|Bq^*| = 10$ is indicated to guide the eye.

3 Interfacial Shear Rheology of Phospholipid Monolayers

Langmuir monolayers of 1,2-dipalmitoyl-*sn*-glycero-3-phosphocholine (DPPC) phospholipids at the liquid–liquid interface are investigated for their mechanical properties and phase behavior. DPPC monolayers undergo a phase separation between liquid expanded (LE) and liquid compressed (LC) phases because of the efficient packing of the fully saturated palmitic acid tails. An interfacial needle shear rheometer (ISR) was fitted with a home built epi-fluorescence microscope to measure the small amplitude shear rheology and phase morphology of the phase separated monolayer *in situ*.

The interfacial rheology is measured within the operating windows developed in Chapter 2 and the influence of different bulk phases on the interactions between the lipid molecules is investigated. On the one hand, introducing a salt buffer as aqueous bulk phase reduces the repulsive dipolar interactions relative to when pure water is used. As a consequence, compression isotherms show a negative hysteresis upon compression (indicative of attractive interactions), the LC phases are less dendritic which is in agreement with the theory by McConnell [1] and the phases aggregate. On the other hand, adding an oil phase as upper bulk phase allows the lipid molecules to undergo van der Waals interactions with oil molecules compared to liquid–air interfaces. The interfacial viscosity increases by orders of magnitude as the lipid tails extend much better into the liquid expanded phase. Furthermore, the relative elastic contributions to the complex interfacial viscosity is large and the interface is strongly viscoelastic with only a limited linear response regime.

The interfacial rheology of DPPC at the water–air interface at temperatures of 20 °C and below shows an increasing norm of the complex interfacial viscosity and increasing elastic contribution with increasing interfacial pressure and the data agrees with earlier measurements of Hermans et al. [2]. At higher temperatures, the ratio between viscous and elastic contributions does not depend on surface pressures in a systematic way any more. The same was observed for DPPC at interfaces with an upper oil bulk phase.

The fluorescent images revealed strong deformation of the LC phases during the compression prior to the rheological measurements. This leads to a mixing of the LE and LC phases which affects both the elastic contribution as well as the norm of the complex viscosity. In the case of water–air, the presence of “slip lines” or shear banding within the interface was observed. This demonstrates the necessity of preventing pre-shear of the interface during the compression of the interface to relevant surface pressures.

3.1 Introduction

Phospholipid monolayers are of interest because phospholipids take part in many biological processes. They play a crucial role in the neonatal respiratory distress syndrome (NRDS). Prematurely born infants usually lack pulmonary surfactants, whose main component are phospholipids and coats the lung as a monolayer. As a consequence of this deficiency, the lung collapses and can be fatal if left untreated [88]. Another example for a medical condition concerning lipid monolayers is the dry eye syndrome, where lipid films fail to stabilize the tear films of the eye [89].

Furthermore, phospholipid monolayers provide a model material to study the properties of one leaflet of lipid membranes. These monolayers can be investigated in a Langmuir trough, where the lipid molecules are spread on an aqueous subphase or at a water–oil interface. Compared to phospholipid bilayers, monolayers do not express a bending rigidity because they use the liquid–liquid interface as a template. Therefore, the resulting monolayers are very stable with very large interfacial areas (*i.e.* hundreds of centimeter squared), which makes investigation with macroscopic methods – such as the double wall ring (DWR) or interfacial needle shear rheometer (ISR) – feasible.

Phase behavior of phospholipid monolayers

The phospholipid dipalmitoylphosphatydilcholine (DPPC) consists of a phosphatidylcholine as hydrophilic head group and two fully saturated fatty acids (hexadecanoid or palmitic acid) as hydrophobic tails. DPPC is the main component in the outer leaflet of the plasma membrane as well as the pulmonary surfactant mentioned earlier. The structural formula of DPPC is shown in Fig. 3.1a. Monolayers of DPPC at the water–air interface compressed at a constant temperature in a Langmuir trough show a distinct phase behavior. Starting at very dilute concentrations, the lipids are in a liquid expanded (LE) phase which undergoes a phase transition into a liquid condensed (LC) phase at high surface pressures $\pi = \sigma_{\text{clean}} - \sigma(\Gamma)$. The surface pressure π is the change in surface tension $\sigma(\Gamma)$ compared to the clean interface without any lipid molecules present σ_{clean}. At intermediate surface pressures, there is a phase coexistence between the liquid expanded and liquid condensed phase [90]. The fully saturated nature of the hydrophobic tails allows them to pack very efficiently into an all-trans configuration and this leads to a solid-like hexatic phase with long range orientational order of the lipid molecules and a melting temperature of $T_{m,\text{DPPC}} = 42\,^{\circ}\text{C}$ [91–94]. The phase behavior can be investigated by fluorescence microscopy or Brewster angle measurements [95]. The former uses a small amount of a fluorescently labeled DPPC, where the label leads to steric hindrance in the fatty acid tails hence being excluded from the liquid condensed phase. The latter is a probe-free technique but often lacks lateral resolution.

The shape of the liquid condensed phase deviates from a simple circle. A shape instability occurs depending on the size and the line tension of the liquid condensed phase, as well as on a balance of the attractive van der Waals and repulsive dipolar interactions between the lipid molecules [1, 96–98]. Under certain circumstances, the liquid condensed phases exhibit a chiral shape, which is promoted by the chiral center at the central atom of the glycerol backbone of the lipid.

In contrast to DPPC, dioleoylphosphatidylcholine (DOPC) has one C-C double bond in each fatty acid of the hydrophobic tail (oleic acid, see Fig. 3.1b). This prevents efficient packing of the lipid tails and no liquid condensed phase is observed for these monolayers above $T_{m,\text{DOPC}} = -17\,^{\circ}\text{C}$.

Mechanical properties of phospholipid monolayers

The interfacial rheology of lipid monolayers has been investigated with various macroscopic interfacial rheometers. Squires and coworkers used a driven magnetic microbutton suspended at a water–air interface and found a free area model for the interfacial viscosity of the phase separated DPPC [61]. Zasadzinsky et al. investigated the effect of cholesterol, palmatic acid, hexadecanol, and curvature on the rheology and phase morphology of DPPC monolayers [55, 62, 64, 99] and compared the interfacial viscosity to a suspension of a two dimensional hard disk system [64]. Another study demonstrated that the sample preparation is of paramount importance and an annealing above $T_{m,\text{DPPC}}$ of the DPPC monolayer prior to compression was necessary to arrive at *thermally structured interfaces* with reproducible rheological results [2], and combined with a ribbon through this led to measurements at high surface pressures. Two macroscopic techniques have been used in this work: (i) the interfacial needle shear rheometer (ISR), where a magnetic needle is dragged along the interface analogue to the sliding plate rheometer; (ii) and the double wall ring (DWR) in conjunction with a commercial rheometer and analogue to the double wall couette.

Influence of the bulk liquid phase at relevant surface pressures

In this chapter, phospholipid monolayers consisting of DPPC will be studied as a model material for one leaflet of a bilayer. The phase morphology and interfacial rheology will be investigated at relevant temperatures and interfacial pressures compared the states of the phospholipid molecules in a bilayer (equivalence pressure [3]). Changing either one of the bulk phases influences the interactions between the lipids and affect both phase morphology and mechanical properties.

3.2 Materials and methods

3.2.1 Chemicals

The phospholipids 1,2-dipalmitoyl-*sn*-glycero-3-phosphocholine (DPPC) and 1,2-dioleoyl-*sn*-glycero-3-phosphocholine (DOPC) were obtained dissolved in chloroform from Avanti Polar Lipids. NaCl (99.99 %, metals basis) and $NaHCO_3$ were obtained from Alfa Aesar. $CaCl_2$ was purchased from Sigma-Aldrich, and n-hexadecane (99 %) from Acros Organics. Ultra-pure water was used (milli-Q, resistivity $> 18.2\,\mathrm{M\Omega\,cm}$ at 25 °C, Merck Millipore). The fluorescently labeled lipids 1-palmitoyl-2-6-[(7-nitro-2-1,3-benzoxadiazol-4-yl)amino]hexanoyl-*sn*-glycero-3-phosphocholine (NBD-PPC), 1,2-dipalmitoyl-*sn*-glycero-3-phosphoethanolamine-N-(lissamine rhodamine B sulfonyl) ammonium salt (DPPE-Rhod), and 1,2-dioleoyl-*sn*-glycero-3-phosphoethanolamine-N-(lissamine rhodamine B sulfonyl) ammonium salt (DOPE-Rhod) were also obtained dissolved in chloroform from Avanti Polar Lipids. The structural formulas of the phospholipids are shown in Fig. 3.1.

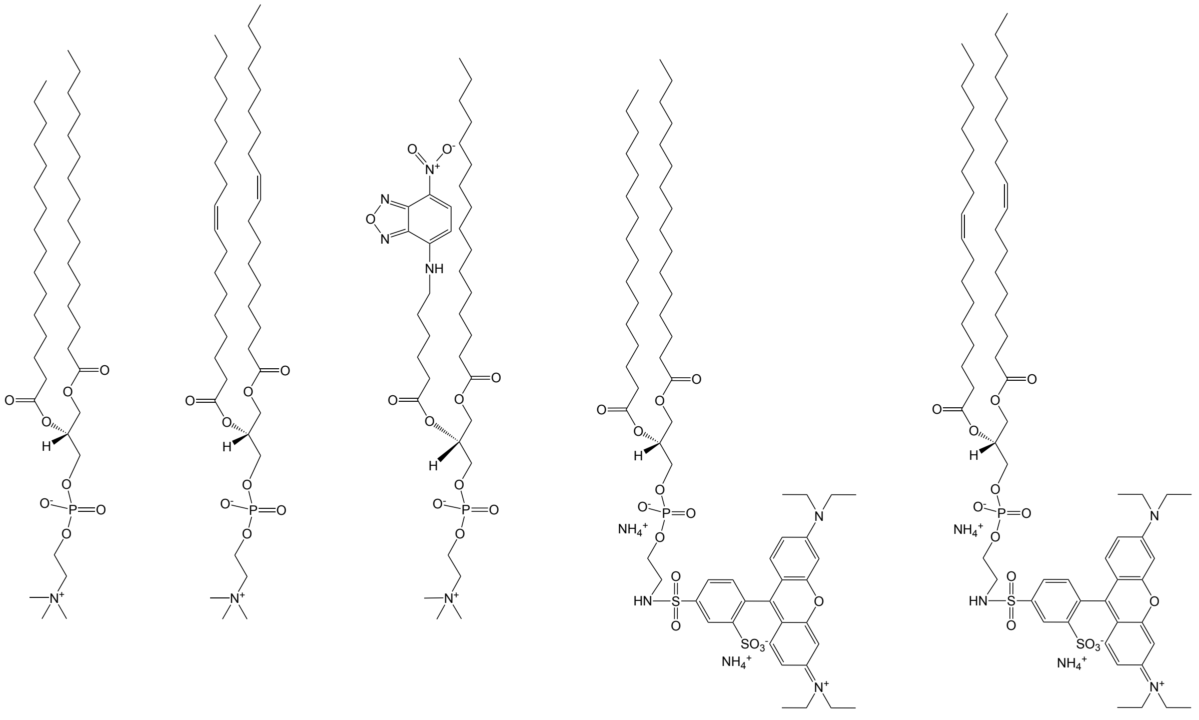

DPPC *(a)* **DOPC** *(b)* **NBD-PPC** *(c)* **DPPE-Rhod** *(d)* **DOPE-Rhod** *(e)*

Figure 3.1: **Structural formulas of phospholipids:** *(a)* DPPC, *(b)* DOPC, *(c)* NBD-PPC (tail labeled DPPC), *(d)* DPPE-Rhod (head labeled DPPC), and *(e)* DOPE-Rhod (head labeled DOPC).

3.2.2 Bulk phases and lipid handling

Two aqueous bulk phases were used as subphases; a pure milli-Q water subphase, and a salt buffer with 150 mM NaCl, 2 mM $CaCl_2$, and 0.2 mM $NaHCO_3$ prepared in milli-Q water and filtered with a 0.2 µm pore filter to remove any particulates. The buffer was used within two weeks. For the upper bulk phase, n-hexadecane was purified by filtering trough an alumina powder column following a standard technique [100] and subsequently saturated with milli-Q water.

All lipids were purchased as dissolved in chloroform and stored at −20 °C. Spreading solutions of concentration 1 mM were made by mixing the lipid stock solutions appropriately to arrive at the wanted composition and diluting with $CHCl_3$ ($> 99\,\%$, AnalaR NORMAPUR©, VWR Chemicals). The concentration of fluorescent lipids was kept from 0.5 mol % to 1 mol % in all samples. To reduce oxidation, the vials containing the lipid solutions were flushed with nitrogen and stored in vacuum sealed bags at −20 °C and used within two weeks. The stock solutions were used within six months.

3.2.3 Langmuir trough

The Langmuir trough and barriers were custom built. The trough was machined from an aluminum alloy where a step ensures pinning of the liquid–liquid interface. A channel was incorporated in the aluminium bottom part of the trough to allow efficient temperature control with circulating water from an external water bath (FP35-MC, Julabo). A plate closes the channels from below. To allow visual inspection of the liquid–liquid interface with an inverted microscope, a glass window with diameter of 50 mm was placed in the center of the trough. To ensure an appropriate wetting of the water–oil system, a polyurethane (PUR) coating, shown as green in Fig. 3.2, was applied by Ilag Industrielack AG (Switzerland).

The barriers were custom made from polyoxymethylene (POM) to fit the design of the trough and minimize leakage of the surfactants at the interface. Each barrier was composed of two POM pieces, where the lower piece extended to the water phase and had a spring geometry to tighten the barrier to the trough wall while the upper part was in contact with the oil phase. A non-magnetic steel part was added on top as third component to add some weight to the barriers.

The Langmuir trough and barriers were operated by a KSV NIMA (Biolin Scientific, Finland) system with integrated thermocouple, microbalance and platinum Wilhelmy plates.

3.2.4 Interfacial needle shear rheometer (ISR)

The interfacial needle shear rheometer (ISR) described in Section 2.2.2 was used for the rheological measurements of the phospholipid interfaces with the single modification of measuring the applied current in series to the magnetic coils (see SI B.1), and a COB-LED was used as light source. Glass channel widths of 12 mm and 20 mm and a magnetic probe from KSV NIMA, where a glass capillary with a diameter of 400 µm is filled with a magnetic powder, were used. The physical properties of the magnetic probe used in this chapter are shown in Table 4.2.

The small amplitude oscillatory shear rheology was measured where the first 3 periods were neglected to avoid any transience and the subsequent 10 periods were acquired to track the needle position after letting the interface relax for 15 min.

3.2.5 Fluorescent setup

The ISR setup was upgraded with a custom built upright microscope using Thorlabs components with epi-illumination fluorescence imaging mode to visualize the phase separation of the lipid monolayer and the interfacial rheology *in situ*. The Fluo-ISR is shown in Fig. 3.2.

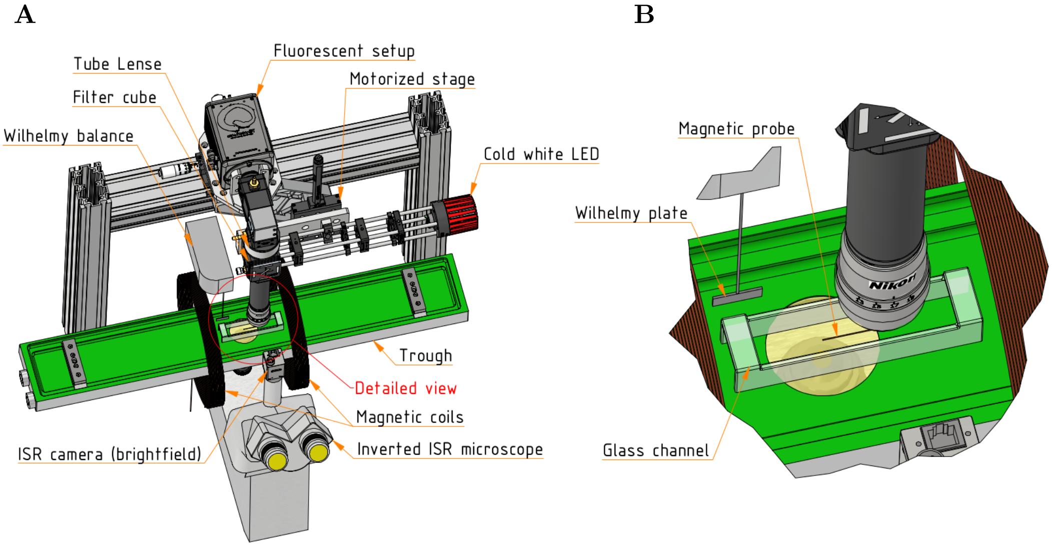
A
B
Tube Lense
Fluorescent setup
Motorized stage
Filter cube
Wilhelmy balance
Cold white LED
Trough
Detailed view
Magnetic coils
ISR camera (brightfield)
Inverted ISR microscope
Magnetic probe
Wilhelmy plate
Glass channel
Nikon

Figure 3.2: **Fluo-ISR:** A custom built device combines a Langmuir trough with a polyurethane coating indicated by the green color, interfacial needle shear rheometer, and upright epi-illumination fluorescence microscope. The detailed view in **(A)** is shown enlarged in **(B)**.

A Nikon 10× plan fluor lens was used in conjunction with a tube lense (TTL200) to make an infinity corrected optical system. Therefore, most optical components were placed outside the Helmholtz coils and magnetic interference with the ISR setup was minimized. The fluorescent light was detected by a CMOS camera (ORCA-Fusion C14440-20UP, Hamamatsu), which was connected to a PC with a CoaXPress interface card and images were acquired with micromanager. The camera is water cooled to reduce air flows originating from the cooling fans.

The light from a cold white LED (MCWHLP1, shown red in Fig. 3.2) is passed through a filter cube and focused on the back focal plane of the imaging lens, following the optical diagram provided by Thorlabs (WFA2001). The infinity corrected design allowed to move only the lower part of the microscope (lens, filter cube, and horizontal illumination arm) through a motorized DC servo actuator (Z852B, Thorlabs) in order to control the focus remotely and reduce any disturbance of the interface and rheological measurement.

Thorlabs filter sets TRITC (design fluorophore: tetramethylrhodamine isothiocyanate) and FITC (design fluorophore: fluorescein isothiocyanate) were used for Rhodamine B and NBD based fluorophores, respectively. An appropriate filter was used for the COB-LED light source for tracking the ISR needle. The entire setup is enclosed by a Plexiglas box and placed on an active vibration isolation table (Vario Series, Accurion, Germany) to reduce noise from vibrations and air flows.

3.2.6 Lipid monolayer preparation

The custom built Langmuir trough and barriers were thoroughly cleaned with detergent and repeatedly rinsed with technical grade propan-2-ol (IPA), ethanol, and milli-Q water before the aqueous phase was added. A platinum Wilhelmy plate (KSV NIMA) was flame treated and placed at the interface by a microbalance (KSV NIMA). The cleanliness of the interface was verified by a measurement of the surface tension of $71.9\,\mathrm{mN\,m^{-1}}$ at $25\,°\mathrm{C}$. A maximum increase of interfacial pressure π ($< 0.5\,\mathrm{mN\,m^{-1}}$ for milli-Q and $< 2\,\mathrm{mN\,m^{-1}}$ for the buffer) upon compression of the pristine interface was found to be acceptable. For the systems with an upper bulk phase, the filtered and saturated oil was then gently added and a second clean compression was performed to assess the quality of the clean two bulk phase interface ($< 6\,\mathrm{mN\,m^{-1}}$).

After the calibration of the ISR with the magnetic needle at the clean interface, the lipid solution was spread dropwise at the interface using a Hamilton syringe at room temperature. The high melting point of DPPC ($T_{m,\mathrm{DPPC}} = 42\,°\mathrm{C}$) requires the interface to undergo a temperature treatment to achieve a more homogeneous interface. The interface was heated to $T > T_{m,\mathrm{DPPC}}$ with subsequent cooling to $20\,°\mathrm{C}$ for at least 10 min each. Then, the temperature was equilibrated at the desired measuring temperature for at least 20 min. This procedure was proposed by Hermans et al. [2] and leads to *thermally structured* interfaces. An example of the spreading and annealing procedure is given for DPPC at water–air and buffer–oil in Fig. 3.3.

The compression of the interface was then performed at the constant measuring temperature which leads to an *interfacial pressure induced phase separation* of the LE and LC phases at sufficiently high interfacial pressures. The interfacial rheology was measured at desired interfacial pressures *i.e.* the barrier motion was halted and the interface was allowed to relax for 15 min before the rheological measurements commenced.

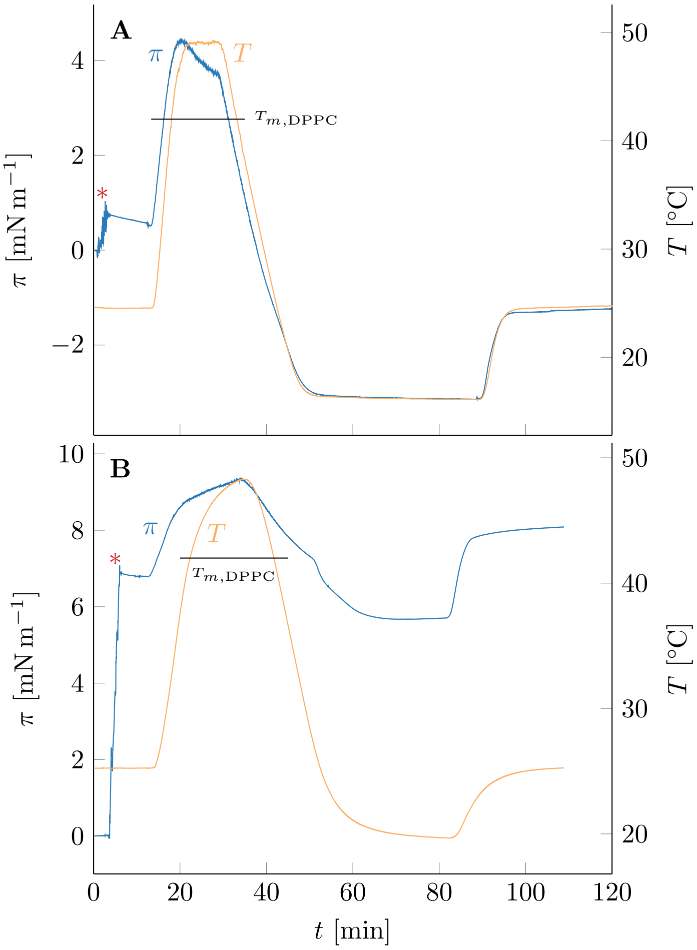

Figure 3.3: **Protocol for obtaining a thermally structured interface:** Interfacial pressure π and temperature T as a function of time t for DPPC at **(A)** water–air and **(B)** buffer–oil. The spreading of DPPC is marked with a red asterisk and the interface is annealed at $T > T_{m,\mathrm{DPPC}}$ for at least 10 min. The shown examples prepare for compressions at 25 °C.

Stress amplitude sweeps were conducted only as a final test to avoid the influence of a large strain amplitudes on the microstructure and future rheological tests.

3.3 Results

First, the compression isotherms and phase morphology of DPPC monolayers at all four interfaces are compared at 25 °C. Second, the interfacial rheology of these interfaces is presented. In a third section, the effect of temperature on the compression isotherm, phase morphology, and interfacial moduli of DPPC at the water–air and buffer–oil interfaces are investigated as a function of frequency and strain amplitude.

3.3.1 Compression isotherms and phase morphology of DPPC at 25 °C

Compression isotherms relating the interfacial pressure (π) with a calculated mean molecular area (MMA) are shown for DPPC at water–air in Fig. 3.4, buffer–air in Fig. 3.5, water–oil in Fig. 3.6, and buffer–oil in Fig. 3.7 at 25 °C. Each compression is measured on a fresh interface with the preceding annealing procedure described in Fig. 3.3.

Water–Air (W/A)

Fig. 3.4A shows three representative compression isotherms of DPPC at the pure water–air (W/A) interface. The data is reproducible, given that the three compressions are measured on separately prepared interfaces. Two mechanisms can be responsible for the small differences in the different datasets. The first is evaporation of the aqueous subphase during the annealing process prior to compression, which would lead to an offset in π. The second is the presence of very strong Marangoni forces during spreading. As a consequence, DPPC molecules could be pushed towards the trough or barrier walls and adsorb onto these walls. This gives rise to an offset in the calculated MMA.

The fluorescence microscopy images during a compression show the formation of the typical initial bean-shaped domains at moderate surface pressures (Fig. 3.4C & E). Upon further compression, the phases undergo a higher order shape instability to a more dendritic morphology at $\pi = 20\,\mathrm{mN\,m^{-1}}$ (Fig. 3.4D & F). The extent of the dendritic structure depends on the fluorophore. The tail-labeled NBD-PPC (used in Fig. 3.4C & D) is expected to provide a strong steric hindrance compared to the head labeled DPPE-Rhod (used in Fig. 3.4E & F) and therefore might be excluded more efficiently from the LC phase at very large π. The very strong shape instability away

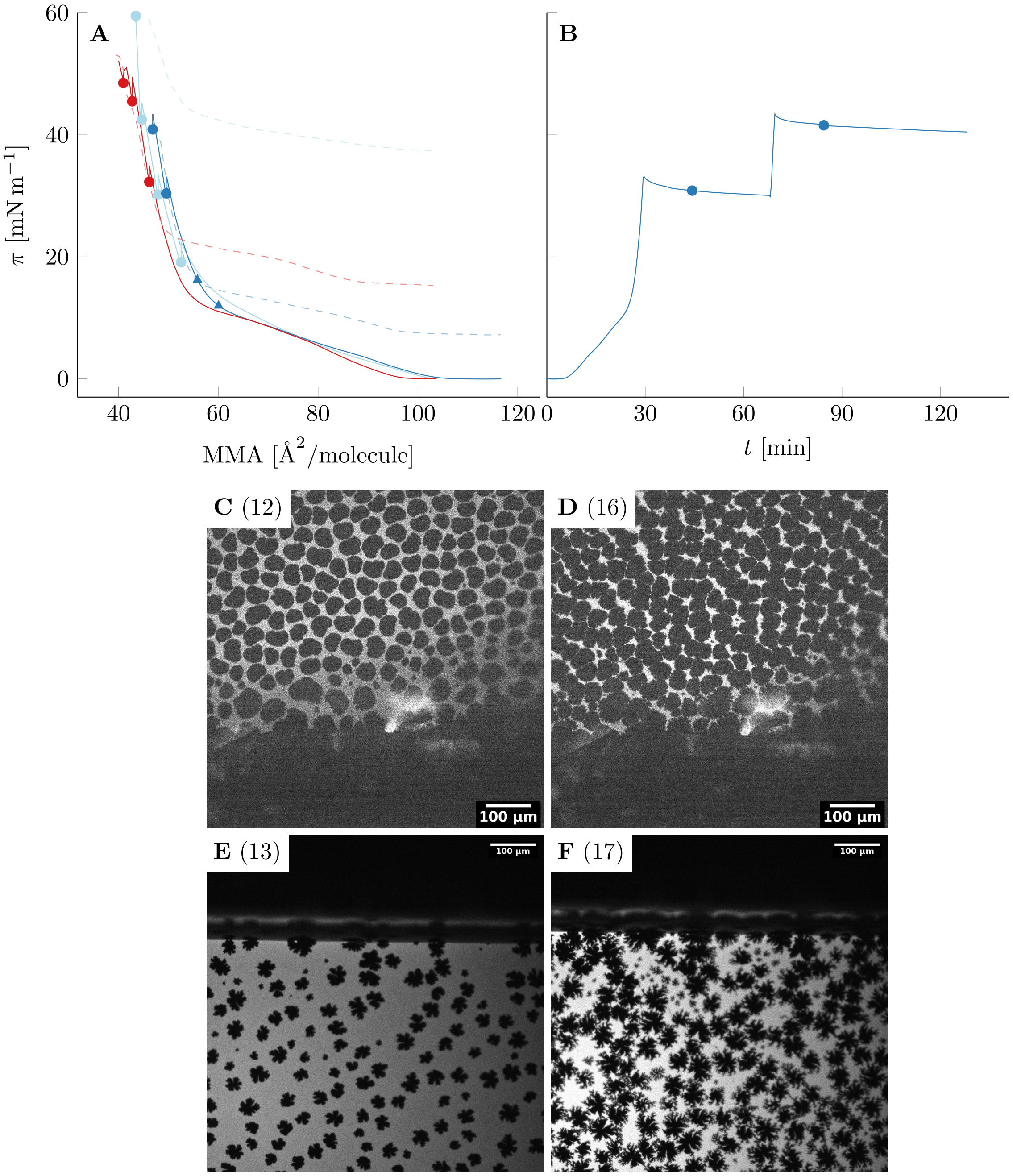

Figure 3.4: **DPPC at W/A and 25 °C: A)** Interfacial pressure (π) as a function of mean molecular area (MMA) with solid and dashed lines as compression and expansion, respectively. **B)** Compression of the same color as a function of time (t). Fluorescent images with the tail labeled NBD-PPC (**C** & **D**) at the position marked by the triangles in **(A)**, and head labeled DPPE-Rhod (**D** & **E**). The numbers denote the interfacial pressures in mN m^{-1}. Solid dots in **(A)** & **(B)** mark the locations of ISR experiments.

from a line tension dominated circular phase shape indicates a strong dominating dipolar repulsive force between the phospholipid molecules in the force balance. The strong effect of the fluorophore suggests that the line activity of these molecules plays an often underestimated role.

Contrary to expectations of a purely repulsive system, the expansion shows a large positive hysteresis with a dependence on the degree of compression with the dotted lines not relaxing to the initial values, for this specific decompression rate. This suggests a viscoelastic effect, for example due to the presence of a metastable state resulting from the high compression and a long equilibration time associated with redispersing of the individual lipid molecules into the LE phase.

Attractive van der Waals interactions between the hydrophobic tails of the lipids could stabilize a compressed metastable state, because the lipid molecules lower their free energy by the hydrophobic interactions between themselves compared to air. Furthermore, Brewster angle microscopy studies reveal large patches on the interface with less structure than the liquid-expanded (LE) phase (see SI B.2). Even a second annealing process was not sufficient to fully redisperse the lipids after the first compression cycle, as shown in SI B.3. This confirms the presence of a very long relaxation time.

The data of one compression is shown as a function of time in Fig. 3.4B. The velocity of the barriers is set to zero at a given time and after letting the interface relax, the ISR experiments are performed indicated by the filled dots on the data. It is evident that there is no significant leakage of lipids since π levels off to a constant value after a first relaxation.

Buffer–Air (B/A)

Compression isotherms of DPPC at the aqueous buffer–air (B/A) interface are shown in Fig. 3.5A. The presence of the ions in the aqueous salt buffer leads to a reduction of the repulsive forces between the lipids by screening the dipolar electrostatic interactions. As a consequence, the activation energy for homogeneous nucleation of the LC phase is reduced. This leads to more nuclei which in turn are distributed closer to each other, therefore resulting in a larger number of smaller LC phases compared to DPPC on pure W/A. This is confirmed by fluorescence microscopy showing the presence of LC phases even before compression is initiated, see Fig. 3.5C. Furthermore, the dendritic structure of the LC phases is less distinct (Fig. 3.5E) compared to the pure W/A case with the same fluorescently labeled lipid (DPPE-Rhod, Fig. 3.4F). This is consistent with a reduction of the repulsive dipolar interactions between the lipid molecules. The aggregation of the LC phases corroborates to argument of screened attractive dipolar interactions.

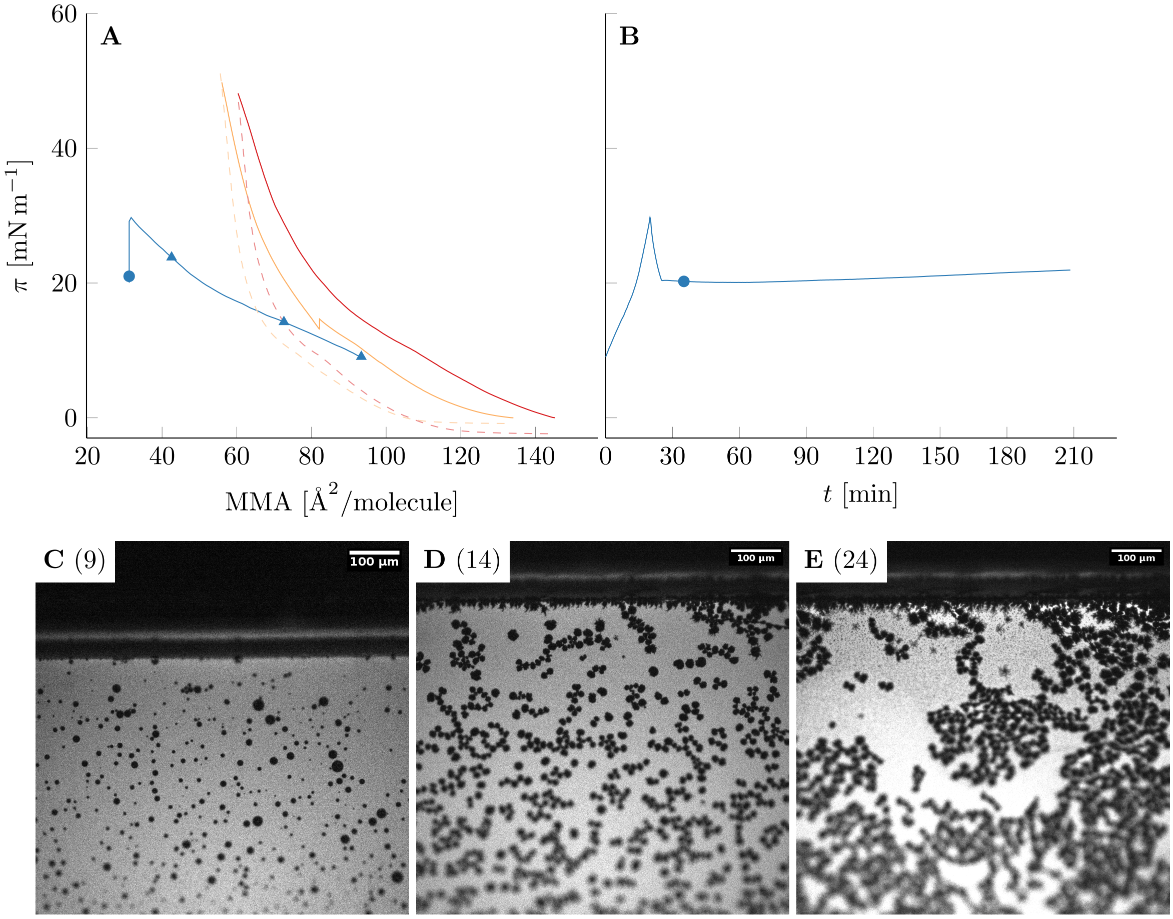

Figure 3.5: **DPPC at B/A and 25 °C: A)** Interfacial pressure (π) as a function of mean molecular area (MMA) with solid and dashed lines as compression and expansion, respectively. **B)** Compression of the same color as a function of time (t). Fluorescent images with the head labeled DPPE-Rhod (**C**, **D** & **E**) at the position marked by the triangles in **(A)**. The numbers denote the interfacial pressures in mN m^{-1}. Solid dots in **(A)** & **(B)** mark the locations of ISR experiments.

Both the reduced activation energy for nucleation and aggregation of the LC phases reduce the reproducibility of compression isotherms because small disturbances can change the microstructure of the interface. The interfacial pressure now shows small, and negative hysteresis upon expansion. This indicates the presence of attractive interactions. Microscopy images show how the material does not redisperse homogeneously into individual molecules but rather small aggregates. Brittle fracture as often observed with aggregated suspensions of latex microspheres at interfaces is the more extreme case of this phenomenon, leading to even more dramatic hysterersis, but this was not observed here. The data shown as a function of time in Fig. 3.5B reveals strong leakage. The fast and strong decrease in π right after stopping the motion of the barriers is an indication that the trough area is not well sealed and some lipid molecules are pushed towards the empty sides of the barriers. The sudden leveling is rather unexpected. A second compression on the same interface showed a very similar, but not identical response (see SI B.4). In the fully open position of the barrier position during the annealing step, the leakage is most likely against the previous flow direction of lipid molecules back towards the initial area of the interface.

Water–Oil (W/O)

Instead of changing the interactions between the hydrophilic head group, the presence of the oil can also be used to change the interactions between the hydrophobic tails of the lipids. The phases still show the presence of a shape instability away from a perfect line tension dominated circle but the higher order shape instabilities are not observed at $\pi = 20\,\mathrm{mN\,m^{-1}}$ (Fig. 3.6D). With the presence of the oil as upper bulk phase, the lipids can undergo van der Waals interactions in the diluted liquid expanded phase. The stronger increase in surface pressure when spreading the same moles of lipids indicates of an increased effective size and a more efficient spreading into the liquid expanded phase as shown in Fig. 3.3B.

The swelling of the monolayer by the oil phase leads to a very large positive hysteresis upon expansion interface in Fig. 3.6A. The cause for this may be that the interface becomes spatially very heterogeneous with a very dense center and less concentrated regions towards the regained interfacial area close to the barriers, as redispersion by diffusion is seemingly slow in this case. As a consequence, the Wilhelmy plate, which is placed in the center of the trough, still measures the dense region and is insensitive to the dilute regions close to the barriers. The time scale for this metastable state to survive is increased compared to the pure W/A interface and a second annealing could not bring the system back to the initial state even after very long annealing times (SI B.5). The presence of LC phases between second annealing and the second recompression was confirmed by fluorescence microscopy (see Fig. 3.6E), showing the presence of a compressed region towards the center of the trough.

Evaporation is not taking place because the aqueous subphase is covered by a hydrocarbon oil with a very low vapor pressure. As a consequence, the variation in the data would have to originate from another source. The compression data as a function of time in Fig. 3.6B shows almost no relaxation after compression is halted, hence confirming the absence of leakage.

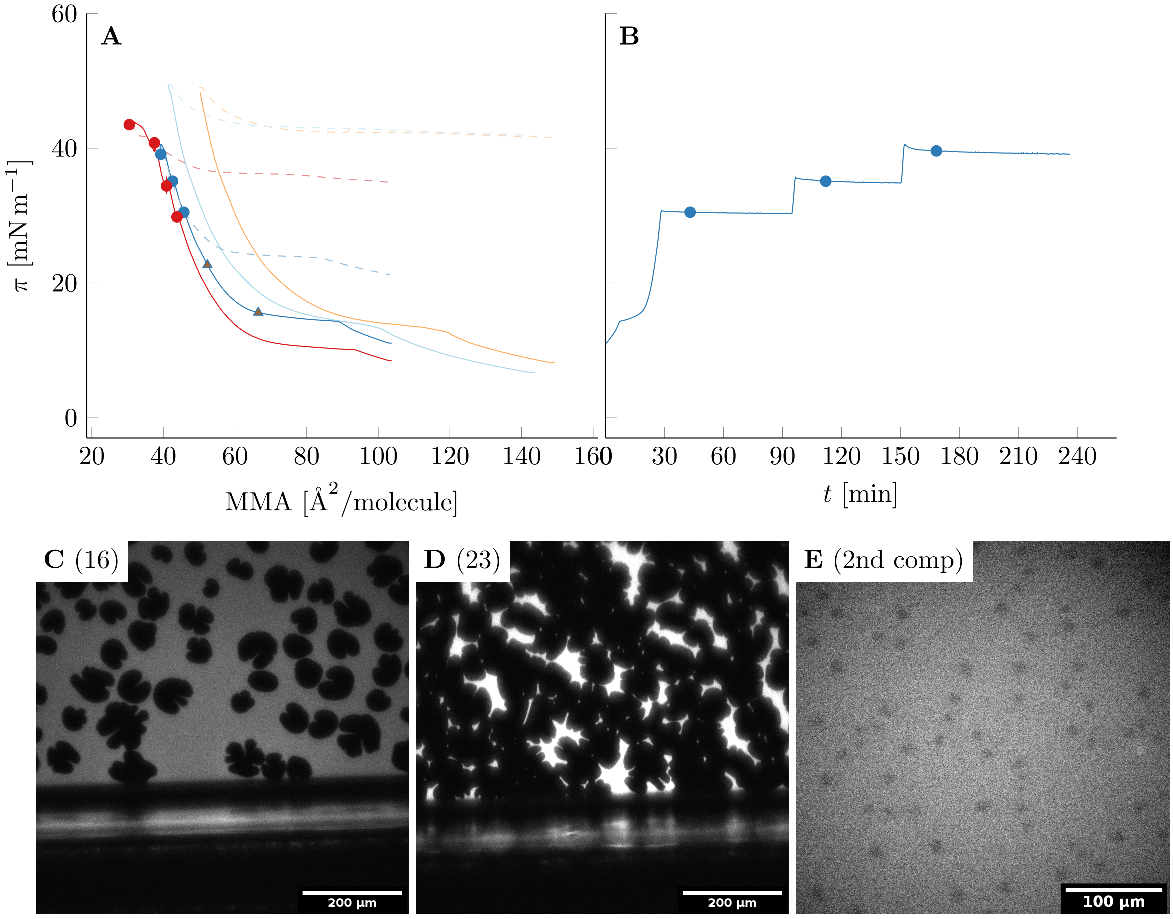

Figure 3.6: **DPPC at W/O and 25 °C: A)** Interfacial pressure (π) as a function of mean molecular area (MMA) with solid and dashed lines as compression and expansion, respectively. **B)** Compression of the same color as a function of time (t). Fluorescent images with the head labeled DOPC-Rhod (**C** & **D**) at the position marked by the triangles in **(A)**. The numbers denote the interfacial pressures in mN m^{-1}. **E)** Image taken after a second annealing at fully open barrier position. Solid dots in **(A)** & **(B)** mark the locations of ISR experiments.

Buffer–Oil (B/O)

Combining the two effects of the aqueous salt buffer (reducing repulsive dipolar interactions) as subphase and the oil (swelling of the interface) as upper bulk phase leads to the compression isotherms in Fig. 3.7A. The variation on the dilute (*i.e.* large MMA) regime originates from the initial lipid concentration similar to the case of DPPC at B/A. Nevertheless, the agreement at larger π is very good, which is the interfacial pressure region of interest in this work.

The phase morphology of the W/O and B/O systems differs mostly in the LC phase size, but not their shape (Fig. 3.7C-F). Screening of the electric dipolar interactions seem to facilitate nucleation of the LC phase, as already discussed for the B/A system. As a consequence, the activation energy of the liquid condensed phases is expected to be reduced and the nuclei can form at lower interfacial pressures.

Introducing the buffer into the liquid–liquid system results in the same trend of the hysteresis upon expansion compared to the liquid–air system. It is positive but can be very small. This demonstrates that the attractive and repulsive fores between the lipid molecules are more balanced compared to the other systems. The interfacial pressure as a function of time in Fig. 3.7B again shows a relaxation at lower interfacial pressures but confirms the absence of leakage.

Absence of the plateau in the compression isotherms

The plateau describing a phase coexistence between the LC and LE phase in the compression isotherms is mainly absent, even though slow compression speeds were used, and in strong contrast to many reports in literature. Many of these reports do not follow the procedure for thermally structuring the interface. The process is melting the LC domains ($T_{m,\mathrm{DPPC}} = 42\,^{\circ}\mathrm{C}$) and leads to a more homogeneous initial condition of the interface. Homogeneous nucleation requires a larger activation energy compared to heterogeneous nucleation. Because of the finite velocity of the trough barriers, nucleation and growth of the LC phases are temporally convoluted. In contrast in non thermally annealed systems, the interface is much more heterogeneous without performing the annealing step, hence offering much more nucleation sites for heterogeneous nucleation of the LC phase. Compression isotherms without the preliminary thermal annealing step results in the expected plateau in the compression isotherm assigned with a coexistence between LE and LC phases (see SI B.6).

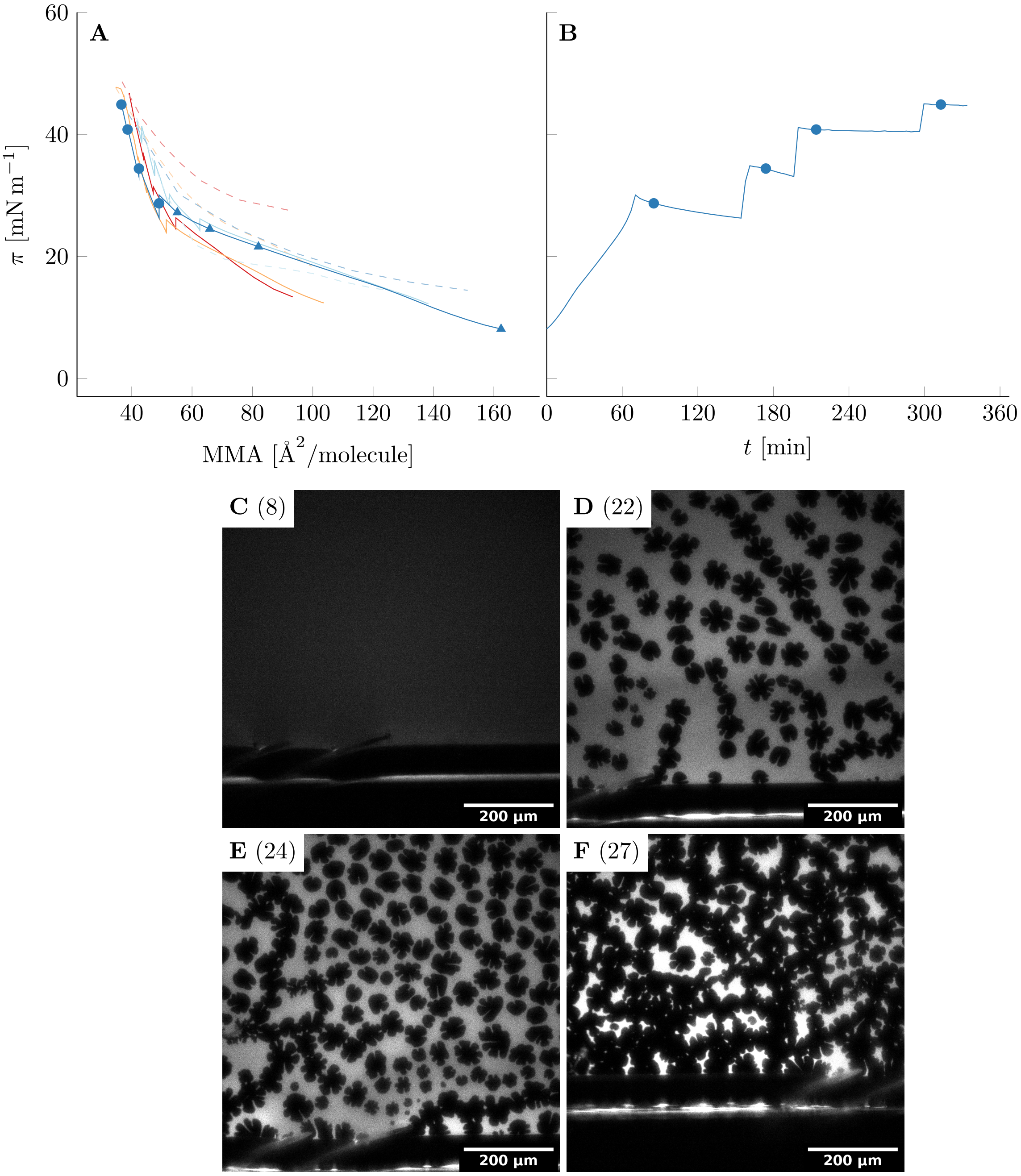

Figure 3.7: **DPPC at B/O and 25 °C: A)** Interfacial pressure (π) as a function of mean molecular area (MMA) with solid and dashed lines as compression and expansion, respectively. **B)** Compression of the same color as a function of time (t). Fluorescent images with the head labeled DOPC-Rhod (**C**, **D**, **E**, and **F**) at the position marked by the triangles in **(A)**. The numbers denote the interfacial pressures in mN m^{-1}. Solid dots in **(A)** & **(B)** mark the locations of ISR experiments.

The absence of the plateau in the thermally structured interfaces leads to the hypothesis of a *transport limited kinetic effect* and is tested in Fig. 3.8, where the compression rate is changed of DPPC at a buffer–oil interface. The interface was annealed in between each compression ($T > 42\,^{\circ}\mathrm{C}$ for at least 10 min) and evaporation is avoided by the presence of the oil phase as upper bulk phase. The MMA, where the compression isotherm is changing slope ($120\,\text{Å}^2$/molecule to $140\,\text{Å}^2$/molecule), is weakly dependent on compression speed in a systematic way. The first appearance of the LC phase is marked with filled circles in Fig. 3.8B and follows the same weak trend. This indicates that the mechanism in the presented work is of kinetic nature.

It is also observed that the degree of the shape instability depends on the compression speed where a larger speed results in ΔP as the excess pressure while very slow compressions lead to almost circular domains (McConnell et al. [1]). This observation poses the question if the compression isotherms should be seen as a thermodynamic phase diagram or whether an interpretation of a kinetically defined state diagram is more appropriate. This would rationalize the large dispersity in experimental results and also the relatively poor agreement observed with molecular simulations.

It is demonstrated that both the aqueous salt buffer and the oil phase have a strong effect on the compression isotherms and phase morphology of DPPC monolayers. The former reduces repulsive interactions by screening the electric dipoles and the latter reduces the attractive interactions by offering the opportunity of van der Waals interactions in the liquid expanded phase between the lipid and the oil molecules. Furthermore, the high reproducibility of DPPC at the W/A and B/O interfaces makes these systems suitable for detailed rheological investigation at interfacial pressures close to equivalence pressure in phospholipid membranes ($\pi = 30\,\mathrm{mN\,m^{-1}}$ to $40\,\mathrm{mN\,m^{-1}}$).

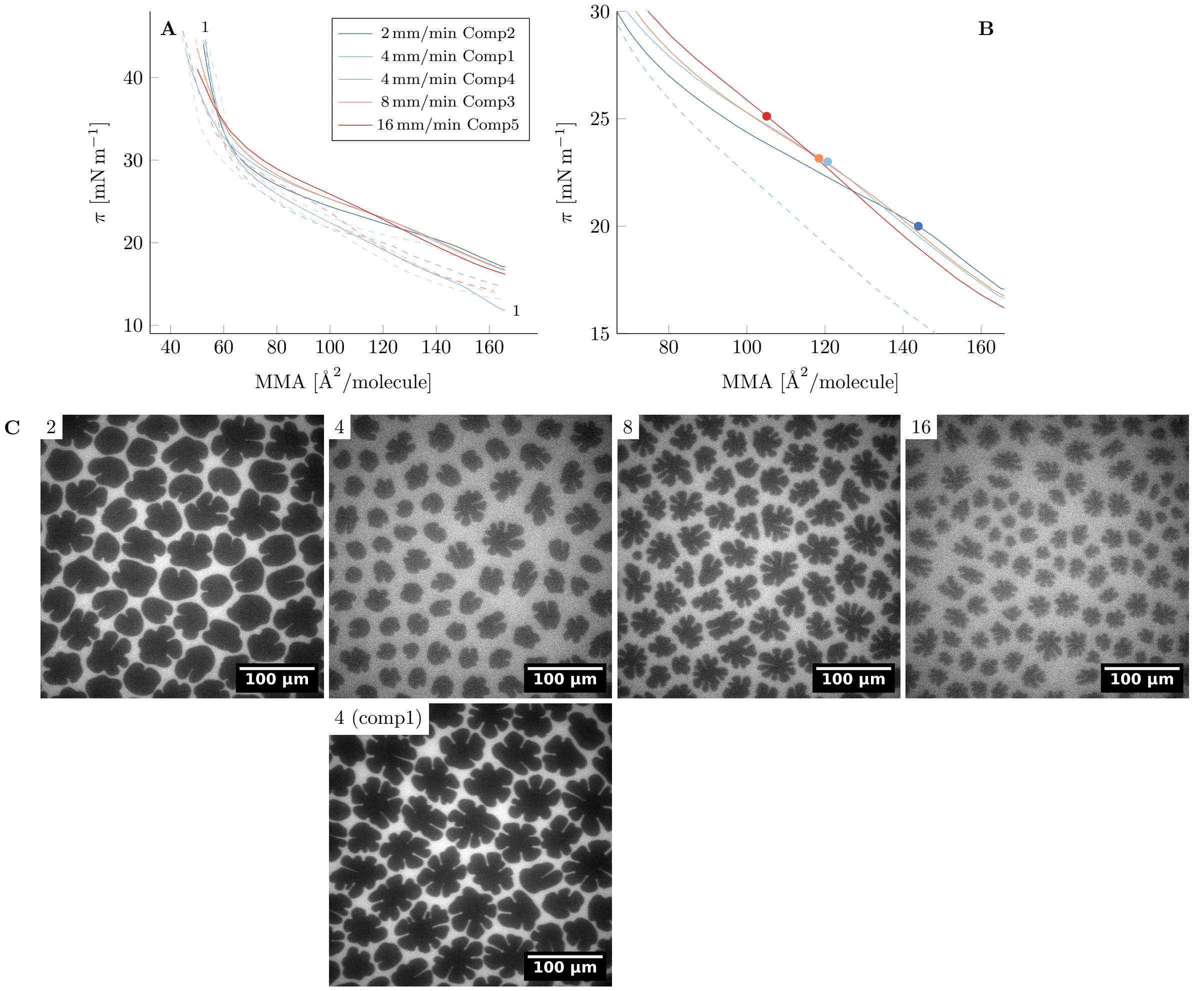

Figure 3.8: **Compression rate variation: A)** Compression isotherms of DPPC at B/O interface and 25 °C with different compression rates on the same interface. Solid and dashed lines represent compression and expansion, respectively. The annotation labels the first compression. **B)** enlarged version of **(A)** with the first compression shown as dashed line and the filled circles mark the first observation of LC phases. **C)** Fluorescence microscopy images at $\pi = 28\,\mathrm{mN\,m^{-1}}$ where the compression speed is given in each frame in $\mathrm{mm\,min^{-1}}$. The interface was annealed ($T > 42\,°\mathrm{C}$ for at least 10 min) in between each compression.

3.3.2 Interfacial rheology at 25 °C and 30 mN m^{-1}

ISR experiments at interfacial pressure and temperature of 30 mN m^{-1} and 25 °C are discussed to compare the effect of the different bulk phases on the interfacial rheology of DPPC monolayers. A compression of a representative example of each system is given in Fig. 3.9 as an overview.

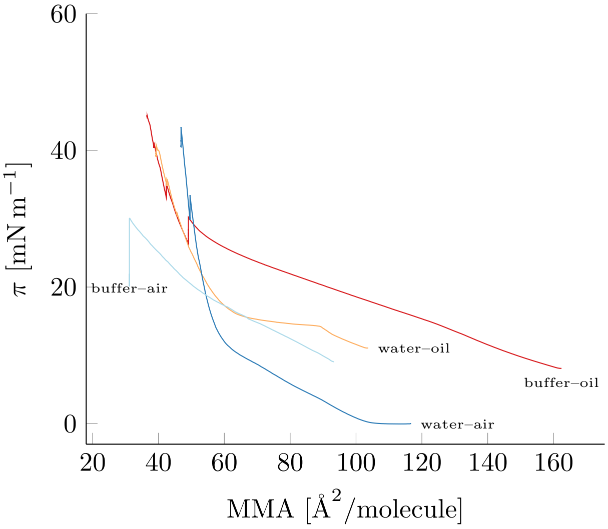

Figure 3.9: **Compression isotherms at 25 °C:** A representative example of each DPPC system showing interfacial pressure (π) as a function of mean molecular area (MMA).

The interfacial rheology of these systems is presented as a function of driving frequency f in Fig. 3.10. The data is shown in two representations: norm of the complex interfacial shear viscosity and phase angle ($|\eta_s^*|$, δ_s), as well as viscous and elastic contributions to the complex interfacial shear viscosity (η_s', η_s''). The systems are compared at surface pressures of 30 mN m^{-1} apart from DPPC at B/A where only 20 mN m^{-1} could be achieved because of the leakage problem described previously.

The norm of the complex viscosity of DPPC at buffer–air is approximately an order of magnitude lower compared to DPPC at clean W/A and comparable interfacial pressures. The reduced repulsive force allows the LC phases to aggregate as it can also be seen through fluorescent images (Fig. 3.11B). Because aggregation takes place below the percolation threshold, the norm of the complex viscosity is drastically reduced. This is accompanied by a reduction in phase angle *i.e.* an increase in the relative elastic contribution. The norm of the complex interfacial viscosity corresponds to $Bq = 10$, hence it is difficult to measure contributions much smaller than this. Nevertheless, errorbars calculated from the primary observables are smaller than the symbol size for the individual contributions and show up in the phase angle only at small frequencies. The low interfacial viscosity leads to large interfacial strain amplitudes even at the lowest applied stress amplitudes. Therefore, the measurement may have been performed beyond the linear viscoelastic regime.

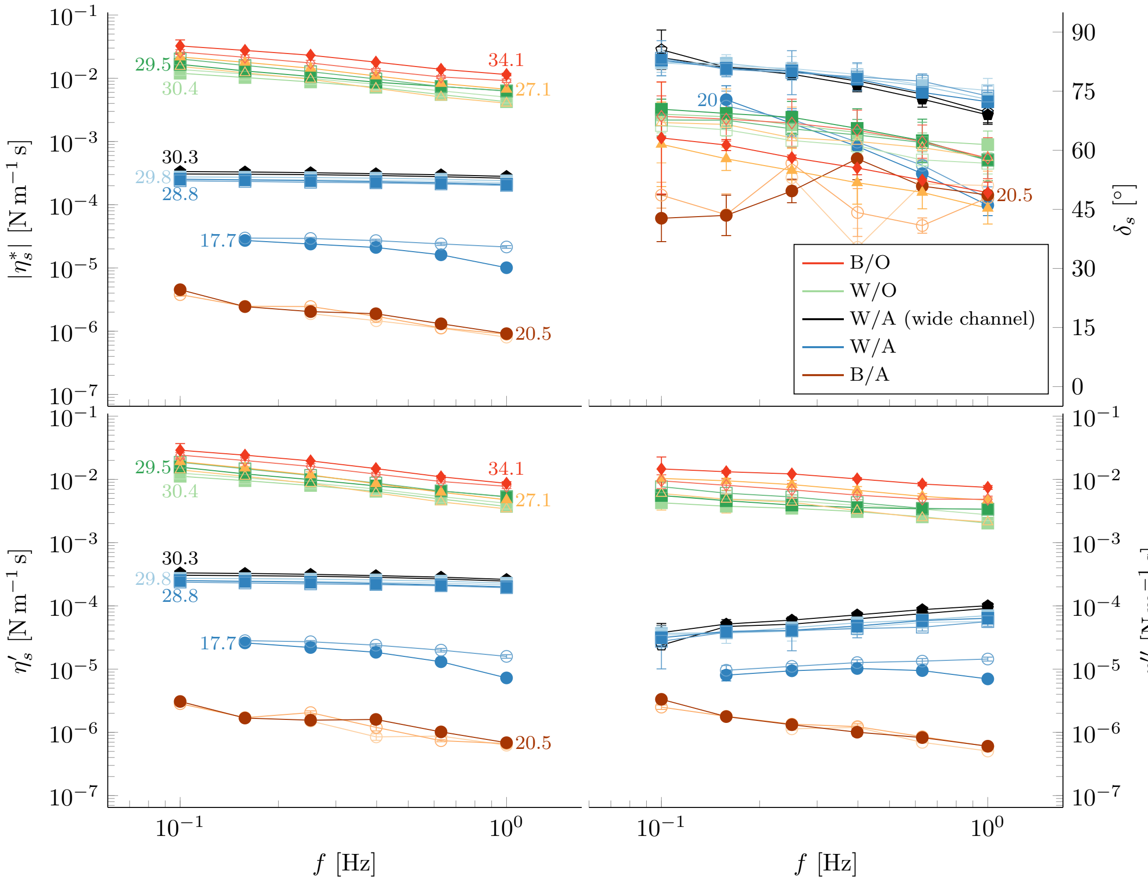

Figure 3.10: **Frequency sweep of DPPC monolayers at 25 °C:** Complex interfacial shear viscosity η_s^* as a function of frequency f in the linear viscoelastic regime. Data shown in two representations *top:* as norm and phase angle ($|\eta_s^*|$, δ_s) and *bottom:* as viscous and elastic contributions (η_s', η_s'') to η_s^*. The numbers show the interfacial pressure in mN m^{-1} of each measurement. Empty symbols show repetitions of the same test.

The W/A interface is almost completely viscous with weak elastic contributions growing with increasing f. This is in good agreement with Hermans et al [2]. Furthermore, data measured with different channel widths result in the same complex interfacial viscosities. A change in channel width corresponds to a varying gap and the insensitivity of the measurement to this variation demonstrates the absence of slip between the lipid monolayer and magnetic needle.

Adding oil as upper bulk phase increases the norm of the complex interfacial shear viscosity by more than an order of magnitude and renders the interface strongly viscoelastic. The presence of the aqueous salt buffer does not have as a strong effect compared to the interfaces without upper bulk phase which could be due to slight increase of the elastic contribution (decrease in phase angle). The compression isotherms and smaller LC phases at comparable interfacial pressures are more strongly affected than the mechanical properties. The data of DPPC at W/O consists of two measurements with different channel widths which again demonstrates the absence of slip as discussed above for the case of DPPC at W/A.

Stress amplitude sweeps of the same DPPC systems are shown in Fig. 3.12 at an interfacial pressure of $40\,\mathrm{mN\,m^{-1}}$. The stress amplitude sweeps were conducted exclusively as a final experiment, which leads to the comparison at a larger interfacial pressure than the frequency sweep presented in Fig. 3.10. Performing a stress amplitude sweep could lead to resulting strain amplitudes beyond the linear regime inducing a change in the microstructure affecting subsequent measurements. DPPC at W/A exhibits a very large linear viscoelastic regime. The magnetic probe in use was not able to reach its boundary and the entire stress amplitude sweep remained in the linear regime. On the contrary, DPPC at W/O and B/O have a limited linear regime and the phase angles show a strong viscoelastic behavior. The data presented in Fig. 3.10 are measured within the linear viscoelastic regime apart from the B/O interfaces. The comparison with DPPC at B/A is difficult because of the leakage problem mentioned before; only an interfacial pressure of $20\,\mathrm{mN\,m^{-1}}$ could be achieved.

In conclusion, the effect of the hydrophobic palmitoyl tail seems to have a much larger influence (oil vs. air) compared to the effect of the head group (buffer vs. air). This is consistent with the hysteretic effects observed in the compression/expansion effects where kinetic effects where most pronounced in the oil systems. Larson et al. discusses variations in published data of DPPC compression isotherms at W/A interfaces [101].

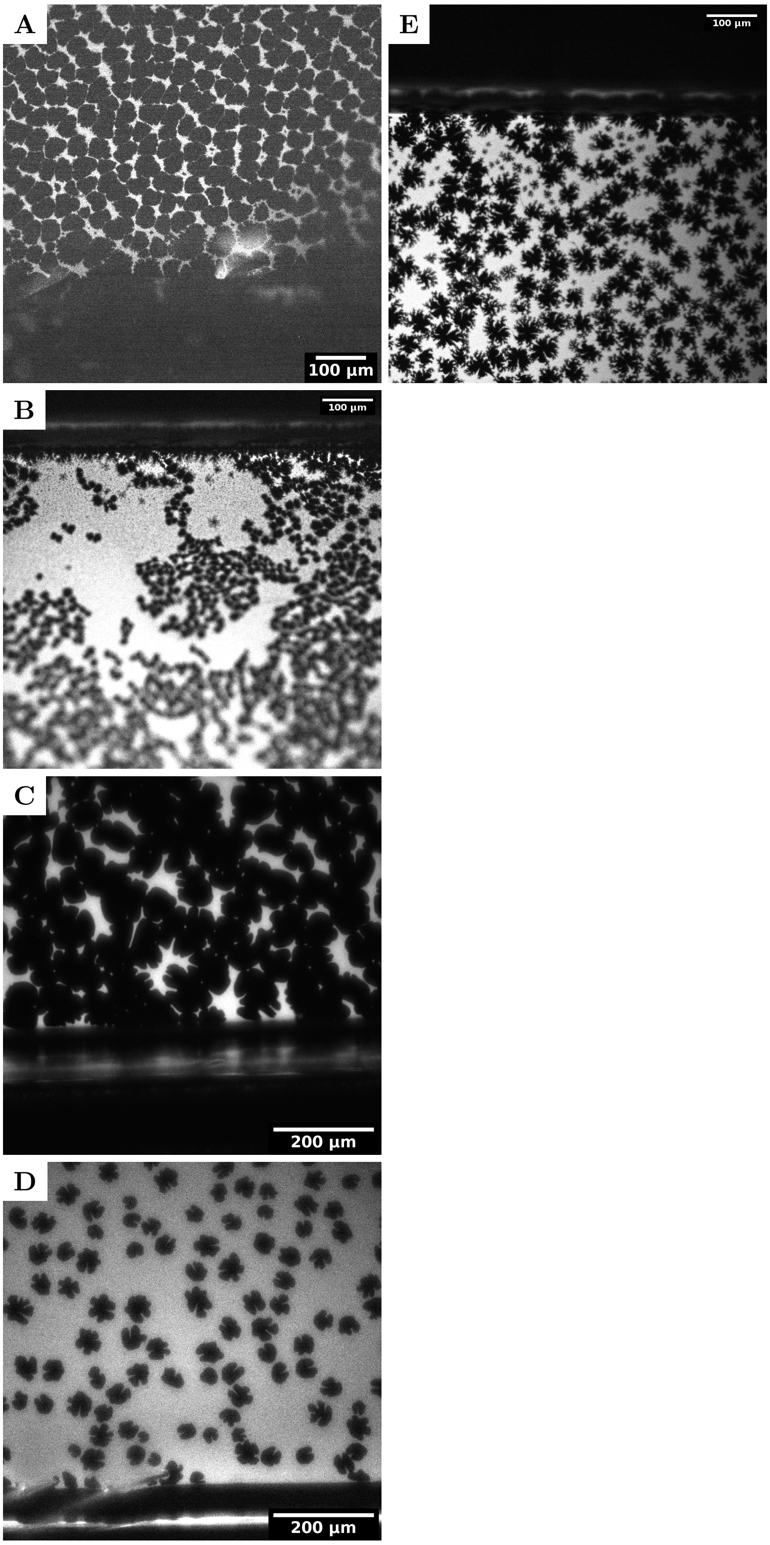
A
100 µm
E
100 µm
B
100 µm
C
200 µm
D
200 µm

Figure 3.11: **Fluorescent images of DPPC: (A)** W/A with NBD-PPC (& E with DPPE-Rhod), **(B)** B/A with DPPE-Rhod, **(C)** W/O with DOPE-Rhod, **(D)** B/O with DOPE-Rhod. Images taken at 25 °C and compressed to a surface pressure of $20\,\mathrm{mN\,m^{-1}}$.

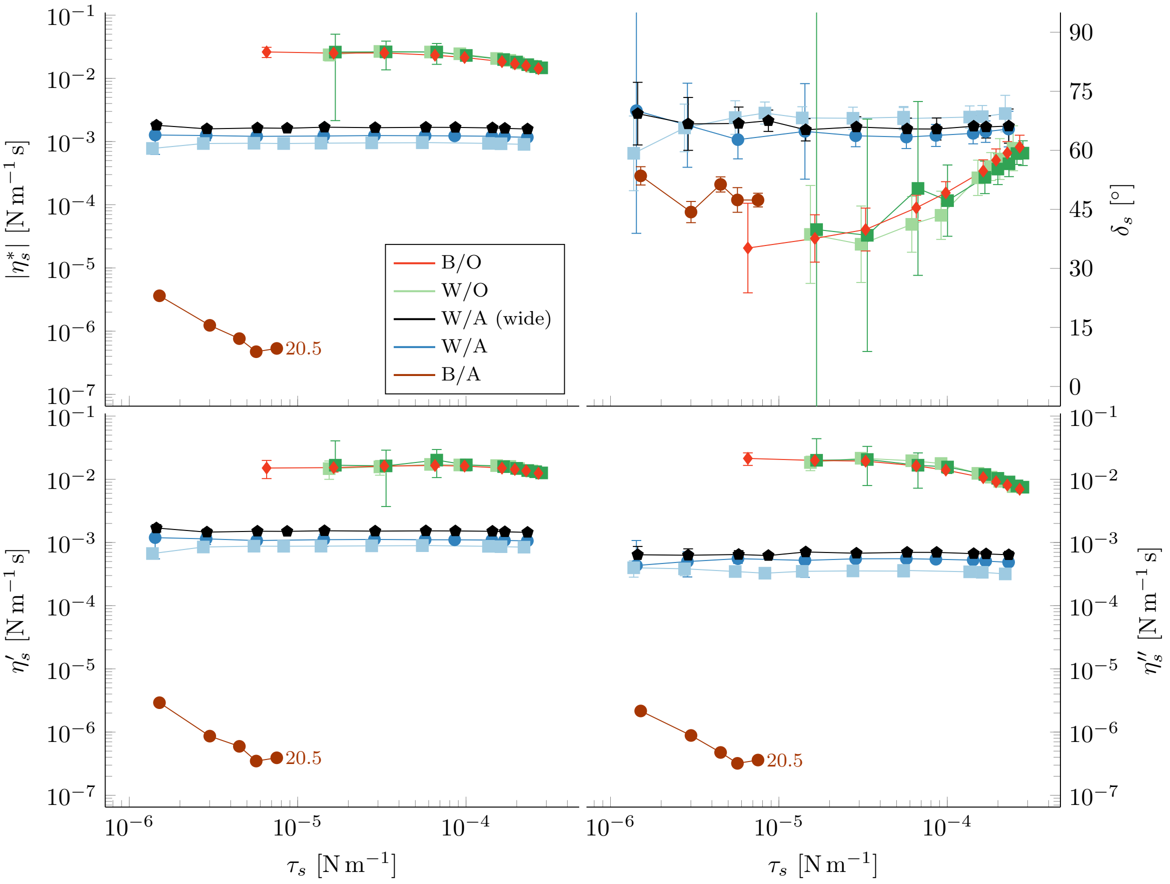

Figure 3.12: **Stress amplitude sweep of DPPC monolayers:** Complex interfacial shear viscosity η_s^* as a function of interfacial stress τ_s. Data shown in two representations *top:* as norm and phase angle ($|\eta_s^*|$, δ_s) and *bottom:* as viscous and elastic contributions (η_s', η_s'') to η_s^* at 25 °C and 40 mN m^{-1} apart for the B/A interface, which was measured at 20 mN m^{-1}. All measurements were conducted at $\omega = 3$ rad s^{-1}.

3.3.3 Effect of temperature and interfacial pressure

The influence of temperature and interfacial pressure was investigated for the two cases of DPPC at the W/A and B/O interfaces because these systems proved to be most reproducible as discussed in Section. 3.3.1. The effect of temperature on the compression isotherms is presented in Fig. 3.13. The final temperature of the compression was approached after completing the annealing process (Fig. 3.3). The interfacial pressure was then corrected by subtracting the temperature dependent change of interfacial tension of the clean interface before the compression is initiated.

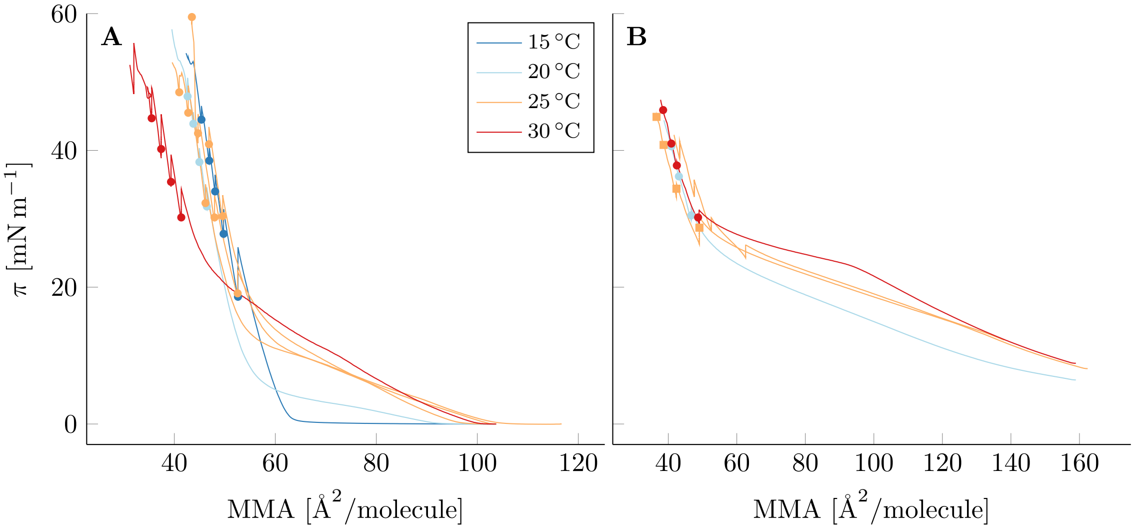

Figure 3.13: **Temperature dependence on compression isotherms:** DPPC at **(A)** W/A and **(B)** B/O at different temperatures. The filled symbols identify the ISR experiments shown in Fig. 3.14 and 3.17.

The compression isotherms show that the onset of the phase transition from LE and LC phase is shifted to smaller MMA and the coexistence region to larger interfacial pressure with increasing temperature. This trend is similar compared to reports from literature without a thermal annealing, yet less pronounced. The variability in the data of the W/A system is demonstrated by the three examples given at 25 °C and the agreement with other temperatures in the compressed state ($\pi > 20\,\mathrm{mN\,m^{-1}}$, see Fig. 3.13A). Possible reasons for the deviation of the compression at 30 °C might be leakage, strong evaporation because experiments were conducted above room temperature, or a too small initial MMA which leads to inaccurate concentration determination. The data of the B/O system are even more consistent (see Fig. 3.13B). The upper oil phase serves as a protective layer for the interface and at the same time prevents evaporation of the lower aqueous bulk phase. However, compressions at 15 °C are not measurable because the freezing temperature of hexadecane is 18 °C.

Fig. 3.14 shows the rheological properties of the W/A interfaces shown in Fig. 3.13A. The norm of the complex interfacial viscosity $|\eta_s^*|$ is increasing with increasing surface pressure and decreasing with increasing temperature which is in good agreement with Hermans et al. [2]. At the lower two temperatures, the phase angle δ_s decreases with increasing interfacial pressure. At low T, the interface is strongly viscoelastic and at the largest π the elastic contribution can even be dominant ($\delta_s < 45°$). At temperatures of 25 °C and above, the interfaces are predominantly viscous with a much smaller but measurable elastic contribution. Furthermore, the phase angle does not have a systematic dependence on π.

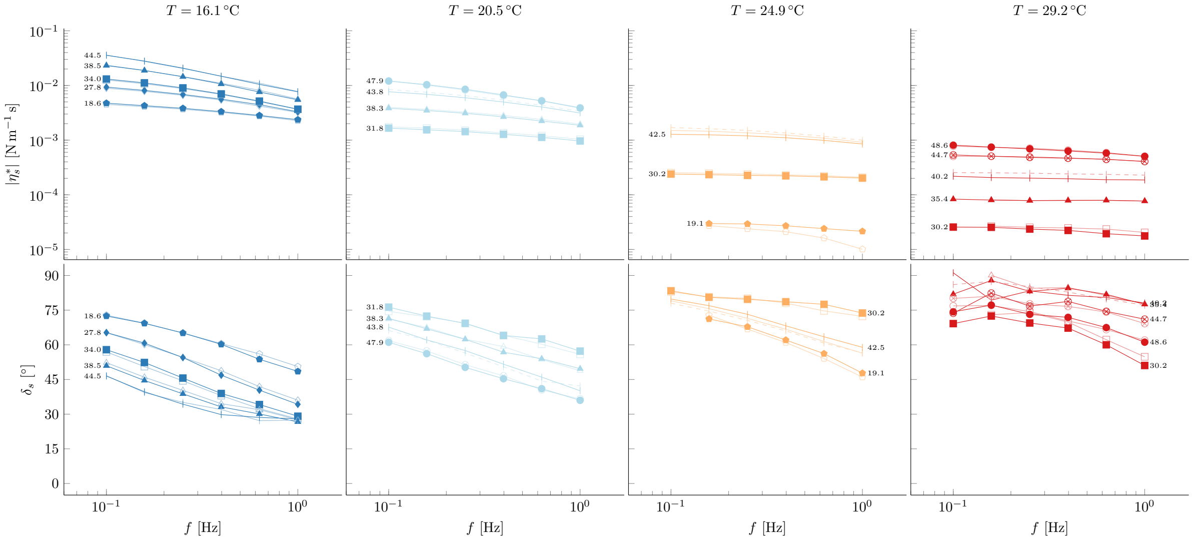

Figure 3.14: **Interfacial rheology of DPPC at W/A:** Norm and phase angle of the complex interfacial shear viscosity as a function of frequency. Empty symbols are repetitions with different stress amplitudes, dashed lines are test after an amplitude sweep. The numbers denote the interfacial pressure in mN m^{-1}.

Fluorescent images reveal that at 15 °C, the interface consists almost entirely of the LC phase, which is in agreement with the compression isotherm shown in Fig. 3.13A. At higher temperatures, an LC/LE phase coexistence is clearly visible in the fluorescent images. The LC phases are strongly sheared and individual domains can even deform towards the highest surface pressures. At 30 °C, shear banding or “slip-lines” are observed during the ISR experiments (see Fig. 3.16). This demonstrates on one hand, that the

LC phase has a solid character compared to the much more fluid LE phase at this temperature. On the other hand, η_s^* cannot be interpreted as material function any more, because highly localized plastic events are taking place. At low temperatures, the interface is almost exclusively black (LC) and the deformation of the phase does not have a big influence or they recover quickly. At higher temperatures, the interface has more content of LE phase and pre-shear leads to a mixing between the two phases, therefore weakening the interface and its elastic contribution.

The complex interfacial shear viscosities of DPPC at B/O are shown in Fig. 3.17. The presented data suggest that the norm of the complex shear viscosity and its elastic contribution increase with increasing temperature. Similar to the case for W/A, the phase angle does not show a systematic dependence on interfacial pressure. Furthermore, repetitions of the same frequency sweep at a smaller stress amplitude result in larger magnitudes of η_s^*. This demonstrates that the material is not as linear as the W/A interfaces. The fluorescence microscopy images reveal again a strong deformation of the LC phases upon compression in a Langmuir through. At higher temperatures, the liquid condensed phase only appears at larger surface pressures (no phases present at $20\,\mathrm{mN\,m^{-1}}$ and 30 °C according to Fig. 3.18C & D). Therefore, the shear deformation during the anisotropic compression in a Langmuir trough is only relevant towards the end of the compression and the LC domains have a smaller total strain. As a result, the interface appears to be more elastic with a stronger complex interfacial shear viscosity because it was not sheared as much as the interfaces at a lower temperature towards the end of the compression.

From the rheological data in Fig. 3.14 and 3.17, as well as the fluorescence microscopy images in Fig. 3.15 and 3.18, we can conclude, that the interfacial rheology of DPPC monolayers is strongly affected by pre-shear effects both in magnitude and elastic contribution of the complex interfacial shear viscosity. Data for the W/A system at low temperature seem to be less affected, which is however less relevant in the context of biological systems. This demonstrates that careful preparation of the interface and the observation of its microstructure is of paramount importance to identify the presence of localized plastic deformation which renders the interpretation of the measured η_s^* as a material function invalid.

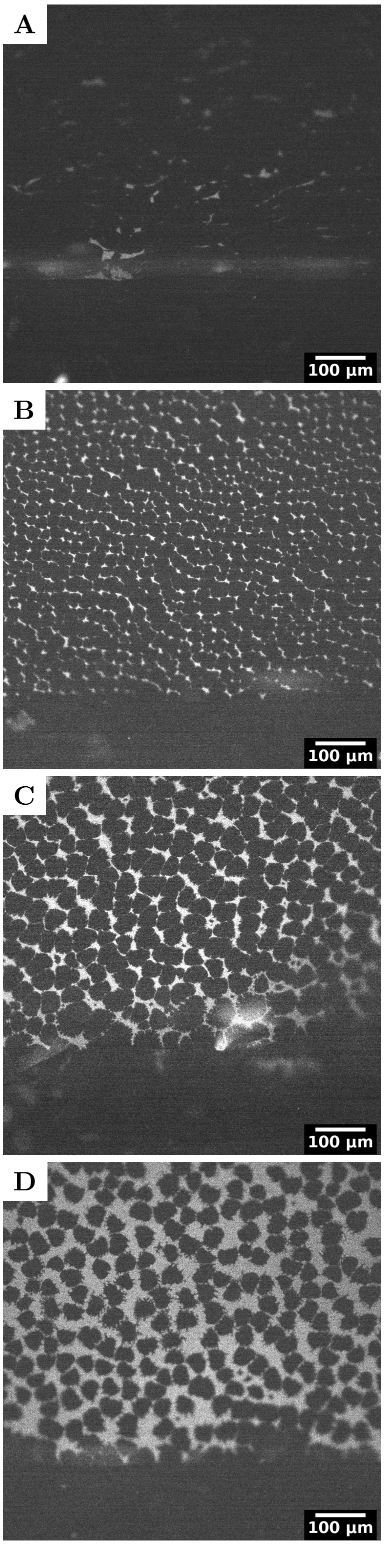
A
100 µm
B
100 µm
C
100 µm
D
100 µm

Figure 3.15: **Temperature effect on phase morphology at W/A:** DPPC at **(A)** 15 °C, **(B)** 20 °C, **(C)** 25 °C, and **(D)** 30 °C. All images were captured at $\pi = 20\,\mathrm{mN\,m^{-1}}$ and all samples used the tail labeled NBD-PPC lipid.

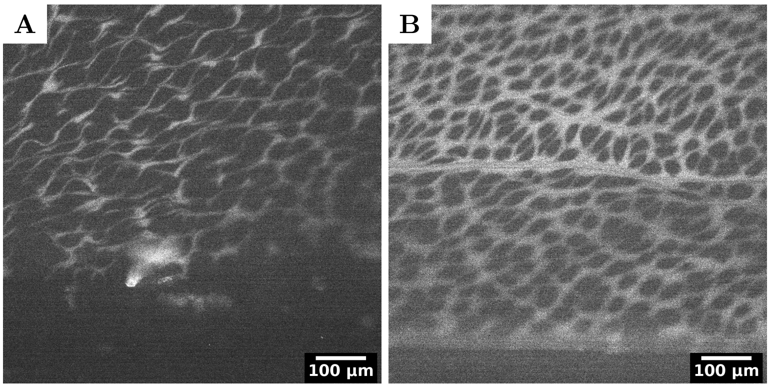

Figure 3.16: **Shear banding:** DPPC at W/A at **(A)** 25 °C and **(B)** 30 °C towards the end of the compression at 30 mN m^{-1}.

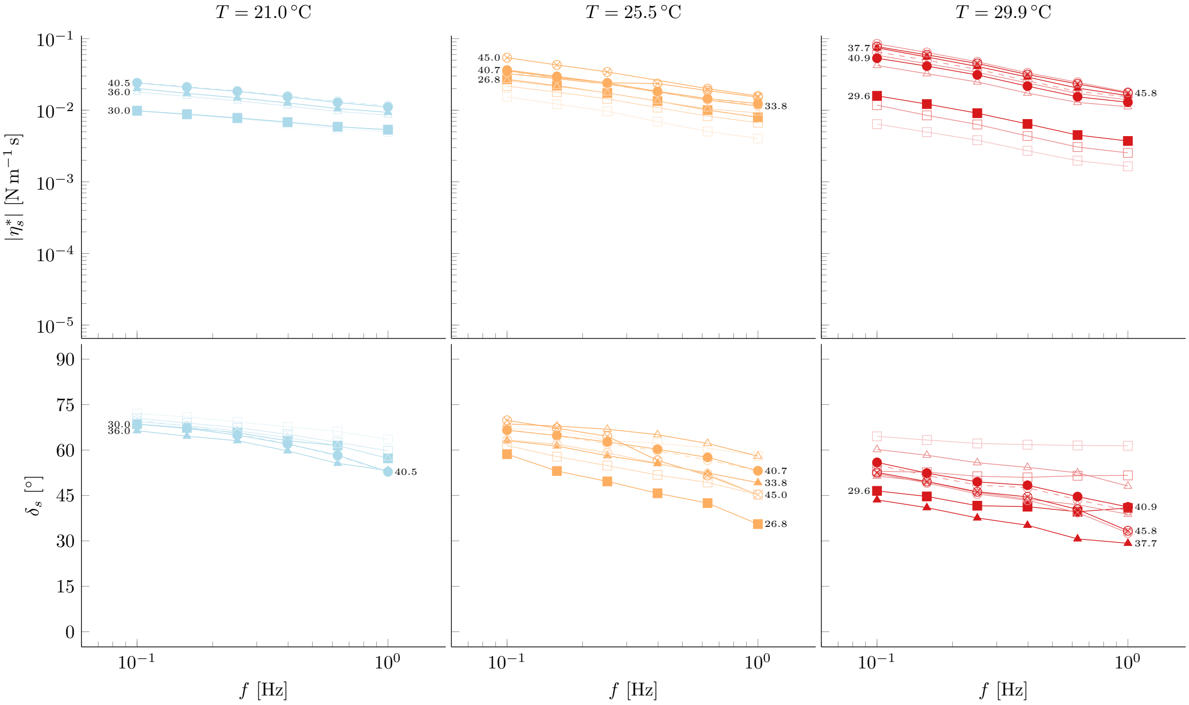

Figure 3.17: **Interfacial rheology of DPPC at B/O:** Norm and phase angle of the complex interfacial shear viscosity as a function of frequency. Empty symbols are repetitions with different stress amplitudes, dashed lines are test after an amplitude sweep. The numbers denote the interfacial pressure in mN m^{-1}.

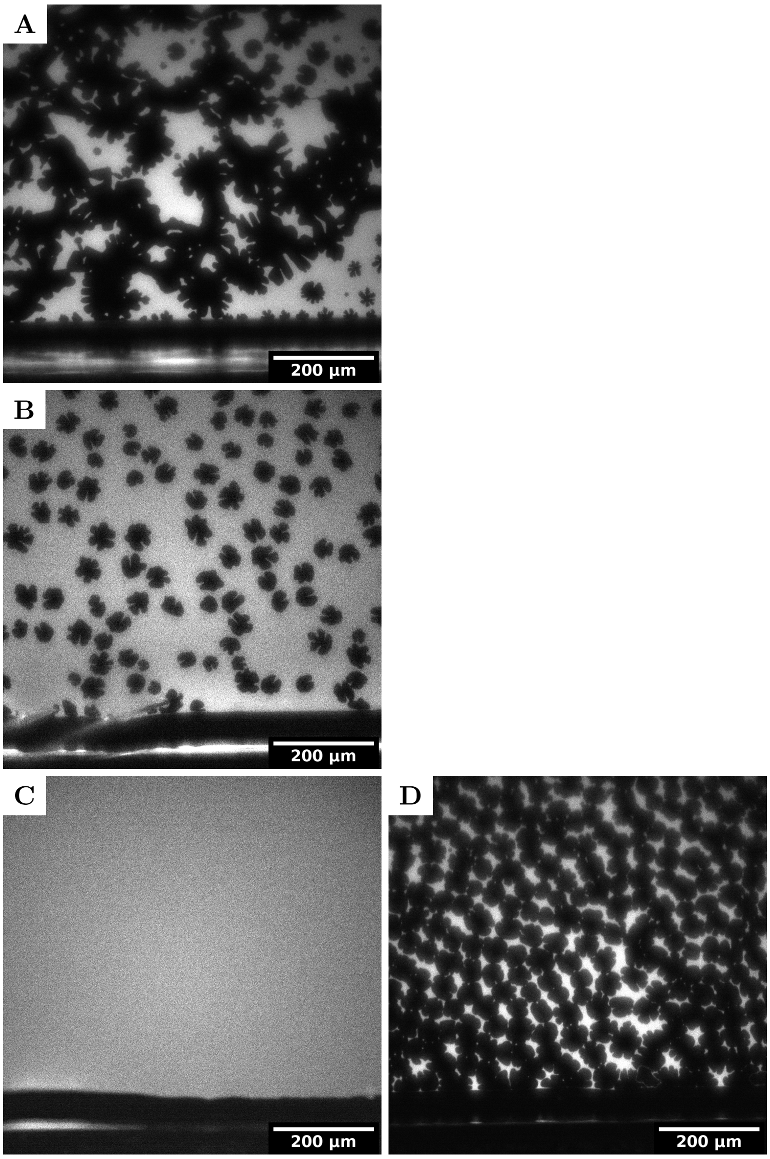

Figure 3.18: **Temperature effect on phase morphology at B/O:** DPPC at **(A)** 20 °C, **(B)** 25 °C, **(C)** and **(D)** 30 °C. All images were captured at $\pi = 20\,\mathrm{mN\,m^{-1}}$ apart from **(D)** at $30\,\mathrm{mN\,m^{-1}}$ and all samples used the head labeled DOPE-Rhod lipid.

3.4 Conclusion

DPPC monolayers at fluid–fluid interfaces of pure water–air (W/A), buffer–air (B/A), pure water–oil (W/O), and buffer–oil (B/O) are investigated in this chapter. Because of the high melting temperature of the lipid tails ($T_{m,\mathrm{DPPC}} = 42\,^{\circ}\mathrm{C}$), the interfaces are annealed at $T > T_{m,\mathrm{DPPC}}$ in between spreading and compressing. This procedure leads to *thermally structured* interfaces as introduced by Hermans et al. [2]. The DPPC interface phase separates into a liquid expanded (LE) and solid-like liquid condensed (LC) phase depending on temperature and interfacial pressure. The phase morphology of the liquid condensed phase at large interfacial pressure depends on a balance of attractive and repulsive forces between the lipid molecules. On the one hand, the repulsive forces can be reduced by changing the pure milli-Q subphase to an aqueous salt buffer because the ions screen the electric dipolar interactions. On the other hand, introducing oil as upper bulk phase allows the lipids to undergo van der Waals interactions with the oil molecules and swells the interface. This expected effect of the adjacent bulk phase on the interface is confirmed by three different measurements: Compression isotherms, fluorescence microscopy, and interfacial shear rheology. Introducing the salt buffer as subphase for DPPC at liquid–air interfaces shows a negative hysteresis in the compression-expansion isotherm, the dendritic shape instability of the LC phases is less distinct and phases aggregate below percolation threshold, and the complex interfacial shear viscosity has a much lower norm with a small increase in the relative elastic contribution. All these effects are in favor of a more attractive system compared to DPPC at the pure milli-Q W/A interface. Replacing air with oil as upper phase has a strong consequence on the hydrophobic interactions. The interfacial pressure shows a much stronger increase during spreading of the same concentration of lipid molecules at the liquid–liquid interface. The compression-expansion hysteresis is now strongly present and positive and very large for W/O as the interface becomes strongly viscoelastic with an increase over an order of magnitude of the complex interfacial shear viscosity. Introducing the salt buffer as subphase to the liquid–liquid system reduced the compression-expansion hysteresis dramatically which suggests a more subtle balance of attractive and repulsive interaction forces between the lipids. However, the effect on the complex interfacial shear viscosity is not significant. A comparison of the interfacial rheology and phase morphology at similar interfacial pressure and 25 °C is presented in Fig. 3.10 & 3.11. The effect of the hydrophobic chains by adding the oil phase have a stronger effect on the mechanical properties compared to the influence of the salt buffer on the hydrophilic head group.

Fig. 3.14 & 3.17 clearly show that the elastic contributions to the complex interfacial shear viscosity of DPPC at W/A does not depend on interfacial pressure in a systematic way at temperatures of 25 °C and larger. The same holds for the B/O system for the entire temperature range. Fluorescence microscopy images reveal the presence of strongly deformed LC phases when approaching high interfacial pressures and shear banding or "slip lines" appear at elevated temperatures (see Fig. 3.16). Shear deformation is present during a compression in a conventional Langmuir trough because of the shape change of the interface during a compression. As a consequence of these localized events, the measured complex interfacial shear viscosity cannot be interpreted as a material function. To overcome this problem, the interface has to be prepared in a way to limit pre-shear or delete shear history before measuring the rheological properties of the interface.

3.5 Acknowledgments

The help of Stephan Busato for the design of the optical upgrade and Christian Furrer for its construction is highly appreciated. Special thanks go to Maria Clara Novaes Silva for assisting with interfacial rheology experiments. Furthermore, Kirill Feldman is thanked for technical assistance.

4 Crowded Phospholipid Monolayers Are Fluid

Freely suspended phospholipid monolayers of 1,2-dipalmitoyl-*sn*-glycero-3-phosphocholine (DPPC) and 1,2-dioleoyl-*sn*-glycero-3-phosphocholine (DOPC) at a salt buffer–oil interface are investigated as a model material for one leaflet of a phospholipid bilayer. The interfacial pressure is chosen to be comparable to those normally encountered in a phospholipid bilayer ($30\,\mathrm{mN\,m^{-1}}$ to $40\,\mathrm{mN\,m^{-1}}$ [3]). The interfacial rheology in relation to the macroscopic two phase microstructure was investigated with the same Fluo-ISR device introduced in Chapter 3. Given the strong effects of preshear, the interface is carefully prepared using a thermo-mechanical protocol, compressing at sufficiently high temperatures, where the liquid condensed (LC) phase is fully molten. The completely homogeneous monolayer is then cooled at constant interfacial area and undergoes a *temperature induced phase separation.*

The area fraction of the structured LC phase is varied by changing temperature and adding the phospholipid DOPC, which is not able to crystallize at this temperature and effectively dilutes the phase separated structure. With this approach, the large deformation of LC phases during compression in a Langmuir through and emergence of inhomogeneous deformation (such as the shear banding reported in the previous chapter) can be prevented. The norm of the complex interfacial viscosity as well as its elastic contribution has a more intuitive dependence on interfacial pressure.

Furthermore, it is demonstrated that the complex interfacial viscosity does not diverge strongly as a function of area fraction of the LC phase (*i.e.* crowding of the interface) in contrast to a hard disk system. The presence of a finite compressibility of the liquid expanded (LE) phase could play a role as it could prevent the 2D interparticle lubrication pressure from diverging. In bulk systems, the medium is always assumed to be incompressible. This makes it difficult to find a compressible analogue for interfacial systems. Furthermore, the mismatch in compressibility between the interface and the incompressible bulk phases does require complicated recirculating flow orthogonal to the interface or slip between the interface and bulk phases.

Preliminary data from microrheological experiments on free-standing and planar bilayers using the LAMBs setup, which was developed in our group [4], are performed to compare the complex interfacial shear viscosity in phospholipid monolayers and bilayers. The measured diffusion coefficients of the LC domains were too large for both systems to be simply converted to interfacial viscosities by the Saffman-Delbrück model, most probably because of the presence of a finite compressibility, which is not accounted for by the model. Further investigation is necessary to find appropriate hydrodynamic models and to translate the insights on crowded phospholipid monolayers to bilayers.

4.1 Introduction

The cell membrane fluidity plays a central role in many biological processes such as cell homeostasis, cell signaling, and the formation of cancer metastasis, as mentioned in the introduction (Section 1.2).

In this chapter, we address the following question: does the lipid membrane maintain its fluidity in very crowded states? To investigate this, a crowded interface is mimicked by changing the extent of phase separation (amount of solid domains) between a fluid and a solid-like phase depending on lipid composition, temperature, and lateral surface pressure. We use a macroscopic interfacial rheometer, where a thin magnetic needle is dragged along the interface. The optical tracking of its tip allows to measure the interfacial viscosity accurately. A comparison between lipid monolayers to bilayers is done by tracking the diffusive motion of liquid condensed phases on the monolayer and aggregates on the bilayer at similar conditions.

Diffusion within an interface

A widely used technique to directly measure the mechanical properties of soft materials is microrheology, where the Brownian motion of a microsphere is tracked with a microscope, and the viscosity is calculated from the diffusivity by the generalized Stokes-Einstein relation (GSER). However, the presence of an interface with a finite compressibility introduces a non-homogeneous environment for the microsphere, which both leads to a breakdown of the GSER. This requires more complex hydrodynamic models with further approximations and assumptions [102, 103], and care has to be taken to capture the relevant physics of the material under investigation.

A seminal hydrodynamic model to describe lateral diffusion of a single protein with cylindrical shape and radius α embedded in a membrane with viscosity η_s (interfacial property with force per unit length multiplied by time $[\mathrm{N\,m^{-1}\,s}]$) surrounded by a bulk fluid with viscosity η_b (bulk property with force per unit area multiplied by time $[\mathrm{Pa\,s}]$) is the Saffman-Delbrück (SD) model [104, 105]

$$\langle r^2 \rangle = 4 D_T t \qquad\qquad \langle \theta^2 \rangle = 2 D_R t \tag{4.1}$$

$$D_T = k_B T b_T \qquad\qquad D_R = k_B T b_R \tag{4.2}$$

$$b_T = \frac{1}{4\pi\eta_s}\left(\log\frac{\eta_s}{\eta_b \alpha} - \gamma\right) \qquad\qquad b_R = \frac{1}{4\pi\eta_s\alpha^2} \quad , \tag{4.3}$$

where $\langle r^2 \rangle$ and $\langle \theta^2 \rangle$ are the mean squared displacement and angular rotation as a function of lag time t, respectively, and $\gamma \approx 0.5772$ is Euler's constant. The diffusion coefficient $D_\square$ is related to the mobility $b_\square$ by the Einstein relation with the Boltzmann's constant k_B and absolute temperature T. The subscripts T and R denote translational and rotational motion. For b_T in Eq. (4.3), the membrane viscosity was assumed to be much larger than the surrounding bulk viscosity ($\eta_b \ll \eta_s/h$ where h is the membrane thickness).

The slow decay of the flow field as $\log(\alpha^{-1})$ in Eq. (4.3) gives rise to very long range interactions along the membrane. However, computational studies have recently shown that stronger scalings of $b_T \sim \alpha^{-1}$ and $b_R \sim \alpha^{-3}$ are observed for crowded systems compared to the dilute behavior [106, 107].

Despite all the difficulties arising from studying diffusion in two dimensions, microrheological experiments at interfaces have been conducted. However, the particle's close environment can hardly be well defined, leading to large variations in the experimental data [41, 42, 108] which can even result in the retraction of published work [38]. This underlines the difficulty of microrheological experiments on membranes. There are other indirect methods to measure the mobility of phospholipid membranes, for example fluorescence recovery after photobleach (FRAP), the use of electric fields to strain membranes [109], and micropipette aspiration. However, there can still be large variations in published data [35], and a clean definition of the strain and deformation fields can be difficult.

Lipid monolayers as templates – one leaflet of the bilayer

Another approach is to investigate lipid monolayers by spreading the molecules on an aqueous subphase in a Langmuir trough, which has been discussed in the previous chapter. The bilayer is mimicked by spreading DPPC at the buffer–oil interface where the oil serves as an infinitely thick second leaflet, and measuring the interfacial rheology at a relevant interfacial pressure, which is comparable to membrane tension.

It was shown in the previous chapter that shear deformation during a compression in a Langmuir trough to arrive at the equivalence pressure and the ensuing complex mechanical deformation of the interface while pushing the material into the measurement geometry has a strong influence on the interfacial rheology and phase morphology. Therefore, another approach is followed in this chapter, where the interface is compressed at high temperatures which renders the interface completely fluid. The temperature is then lowered at fixed interfacial areas, which leads to the preparation of an interface without a large pre-shear.

Instrumentation and experimental procedure

In a first step, the interfacial rheology of DPPC monolayers at the buffer–oil interface at different temperature T, surface pressure π, and DOPC content was investigated. The diffusive motion of liquid condensed phases on the monolayer was then compared to lipid bilayers in a second step using Eq. (4.3).

The monolayers were investigated by a custom built device, shown in Fig. 3.2, and termed *Fluo-ISR*, where a Langmuir trough is used to control and monitor the temperature T and interfacial pressure π, an interfacial needle shear rheometer to measure the mechanical properties, and an epi-illumination fluorescence microscope to visualize the phase behavior of the phase separated phospholipid interface. The entire setup is placed on an antivibration table and enclosed by a Plexiglas box to reduce air flows.

The interface is prepared in a custom-built Langmuir trough with a polyurethane coating for optimal wetting of the water–oil system and a window to allow visual inspection by an inverted microscope. The trough can be connected to the thermal bath for temperature control and the surface pressure is measured by a Wilhelmy plate.

The interfacial needle shear rheometer, first introduced by Brooks et al. [77], uses a magnetic needle suspended at the interface and confined in a glass channel, which defines the boundary condition of the flow field at the interface. The needle can be driven by applying a difference in current ΔI trough the Helmholtz coils, therefore generating a homogeneous gradient in the magnetic field [77]. The needle's position is tracked by one of its edges with a bright field inverted microscope. Hence, it is a stress controlled rheometer. The interfacial contribution has to be deconvoluted from the bulk contribution by an iterative numerical method [80]. By applying an oscillatory $\Delta I(\omega)$ with frequency ω, it is possible to accurately measure the frequency dependent complex interfacial viscosity

$$\eta_s^* = \eta_s' - i\eta_s'' \quad , \tag{4.4}$$

where η_s' and η_s'' are the viscous (in-phase) and elastic (out-of-phase) contributions, respectively, and i is the imaginary number [110]. These are all interfacial viscosities with units force per unit length multiplied by time ($\mathrm{N\,m^{-1}\,s}$) in contrast to bulk viscosity ($\mathrm{Pa\,s}$).

The fluorescence microscopy setup was custom built from Thorlabs components. It uses a cold white LED, appropriate filter sets for the dye TRITC, and a lens tube for infinity correction. A digital CMOS camera from Hamamatsu captures the images. Fluorescent images were analysed with ImageJ.

An aqueous buffer at physiological conditions (150 mM NaCl, 2 mM $CaCl_2$, and 0.2 mM $NaHCO_3$) was used for the lower bulk phase. The upper bulk phase was chosen to be n-hexadecane to prevent evaporation and furthermore mimic the hydrophobic nature of the absent leaflet of the bilayer. After the preparation of the clean buffer–air interface in the Langmuir trough and placing the magnetic probe at the interface, the spreading solution was spread at the interface. The spreading solution contained the lipid mixture with the desired weight fraction of DOPC denoted with χ_{DOPC} dissolved in chloroform and 0.5 mol % of the fluorescently head-group labeled DOPC (DOPE-Rhod). The interface was heated to $T > T_{m,\mathrm{DPPC}}$ and compressed to surface pressures of $30\,\mathrm{mN\,m^{-1}}$ to $40\,\mathrm{mN\,m^{-1}}$ which is comparable to the state in lipid membranes in cells [3, 111, 112]. This sample preparation in a fully molten state ensures an isotropic and unstrained reference state at the end of the compression (see fluorescence microscopy images in Fig. 4.1).

The interface is then cooled to given temperatures at the fixed mean molecular area to measure the interfacial rheology. The phase coexistence allows to control the area fraction of the solid-like liquid condensed (LC) phase by changing temperature T, interfacial pressure π, or the DOPC content.

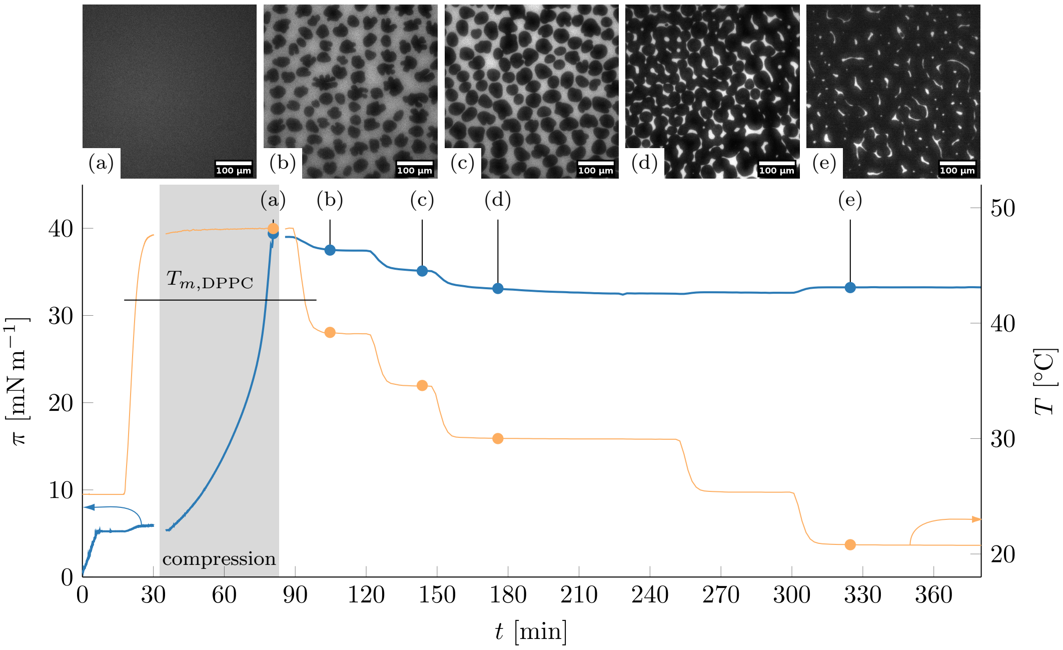

Figure 4.1: **Temperature induced phase separation:** Interfacial pressure π and temperature T as a function of time t. The procedure is composed of spreading, heating, compression, and stepwise cooling and measuring of the interfacial rheology. A pure DPPC monolayer at the buffer–oil interface is shown in this example. The microscopy images are taken at the times indicated by the filled circles and the scale bar corresponds to 100 µm.

In a second step, the Brownian motion of the liquid condensed phase is tracked on lipid monolayers and free standing lipid bilayers in order to relate the rheological properties of the bilayer with the macroscopically approved monolayer viscosity. Free standing phospholipid bilayers with composition DPPC/DOPC=3/2 were formed with the bikewheel chip described in [4] to compare the two techniques.

A more detailed description of the methods can be found in Section 4.5.

4.2 Results

4.2.1 Prevention of mechanical history effects

The sample preparation in this chapter leads to a phase separation induced by temperature instead of interfacial pressure. This minimizes the flow history with compression and shear deformations occurring during the loading of the sample into the gap of the rheometer, because in our experiments the compression is done on a fully molten interface. It allows to investigate undeformed, highly compressed interfaces. The complex interfacial shear viscosity of DPPC at buffer–oil interfaces following the temperature induced phase separation is shown in Fig. 4.2.

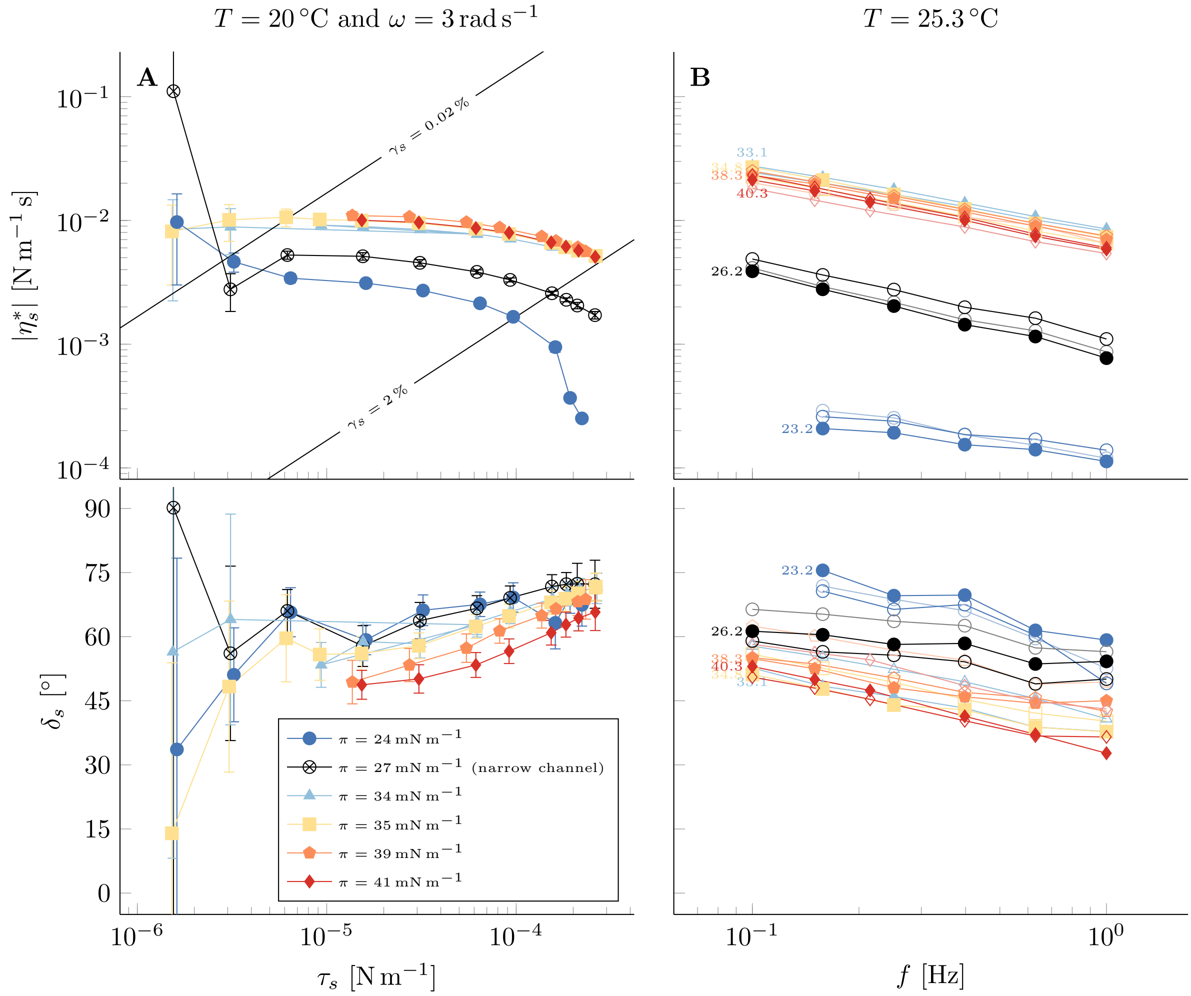

Figure 4.2: **Interfacial rheology of DPPC undergoing temperature induced phase separation:** Norm of the complex interfacial shear viscosity and phase angle. **(A)** Stress amplitude sweeps and **(B)** frequency sweep of DPPC at buffer–oil.

The interfacial stress amplitude shows a rather limited linear response regime regime and is in the same order of magnitude compared to the interfacial pressure induced phase separation shown in Fig. 3.17. However, the dependence of phase angle on interfacial pressure is more intuitive for both stress amplitude and frequency sweeps with an increase in elastic contribution with increasing π.

Scalings

The dependence of the magnitude of the complex interfacial shear viscosity $|\eta_s^*|$ and the phase angle δ_s on interfacial pressure and temperature is shown in Fig. 4.3. The data of DPPC at water–air (W/A) follows the trends explained in great detail by Hermans et al. [2], where a Barus, or pressure coefficient, was used to describe the dependence on interfacial pressure and a viscous activation energy for the exponential dependence on $1/T$, based on ideas on free area (akin to free volume in bulk). The fact that the interface is actually structured by the phase separation and not homogeneous seems not to be of importance for this behavior in case of the W/A system, which remains intriguing. The temperature and pressure effects seem to enter solely trough the LE suspending medium.

The buffer–oil (B/O) system seems to have a similar dependence on interfacial pressure than the W/A system. However as discussed earlier, the higher temperatures show a larger complex viscosity. Furthermore, the dependence on temperature is the opposite of what was observed to the W/A system and the phase angles are more scattered. The latter originates from the limited linear regime. Since the ISR is a stress controlled rheometer the resulting strain amplitude is difficult to control (we do not have a feedback loop on this instrument).

The B/O system with a *temperature induced phase separation* exhibits first of all a more intuitive dependence on interfacial pressure as well as temperature in the high-temperature regime. Surprisingly, the norm of the complex viscosity levels off and almost changes slope from positive to negative when low temperatures are approached. Responsible for this change in slope is not a change in area fraction (ϕ) of LC phase present in the interface since ϕ is increasing monotonically with inverse temperature. The problem of the unprecise control of the strain amplitude persists for the B/O data with thermally induced phase separation. Only data with resulting strain amplitudes between 0.04 % and 0.18 % are shown in Fig. 4.3. The stress amplitude sweep data is shown as a function of resulting strain amplitudes in SI C.2.

4.2.2 Rheology of mixed lipid monolayers

The interfacial shear rheology of phospholipid monolayers is shown in Fig. 4.4, where the weight fraction of DOPC is represented by χ_{DOPC}. All interfaces are compressed in a fully molten (hence homogeneous) state by heating the system to temperatures larger than the melting temperature of DPPC, as discussed in Fig. 4.1. The phase

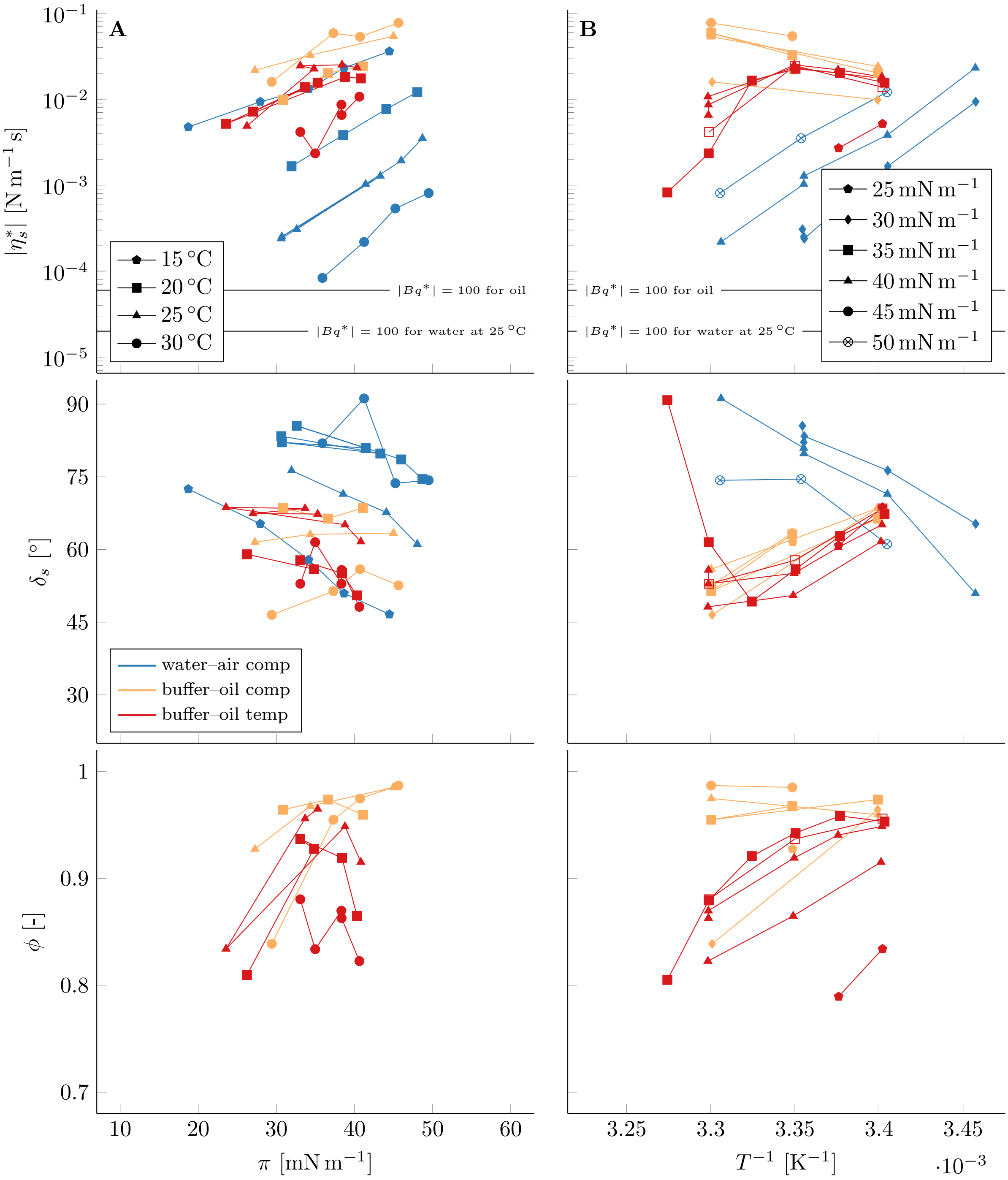

Figure 4.3: **Comparison between sample preparations:** Norm of the complex interfacial shear viscosity η_s^*, phase angle δ_s, and area fraction of the liquid condensed phase ϕ as a function of **(A)** surface pressure, **(B)** inverse temperature. *comp:* interfacial pressure and *temp* temperature induced phase separation, respectively.

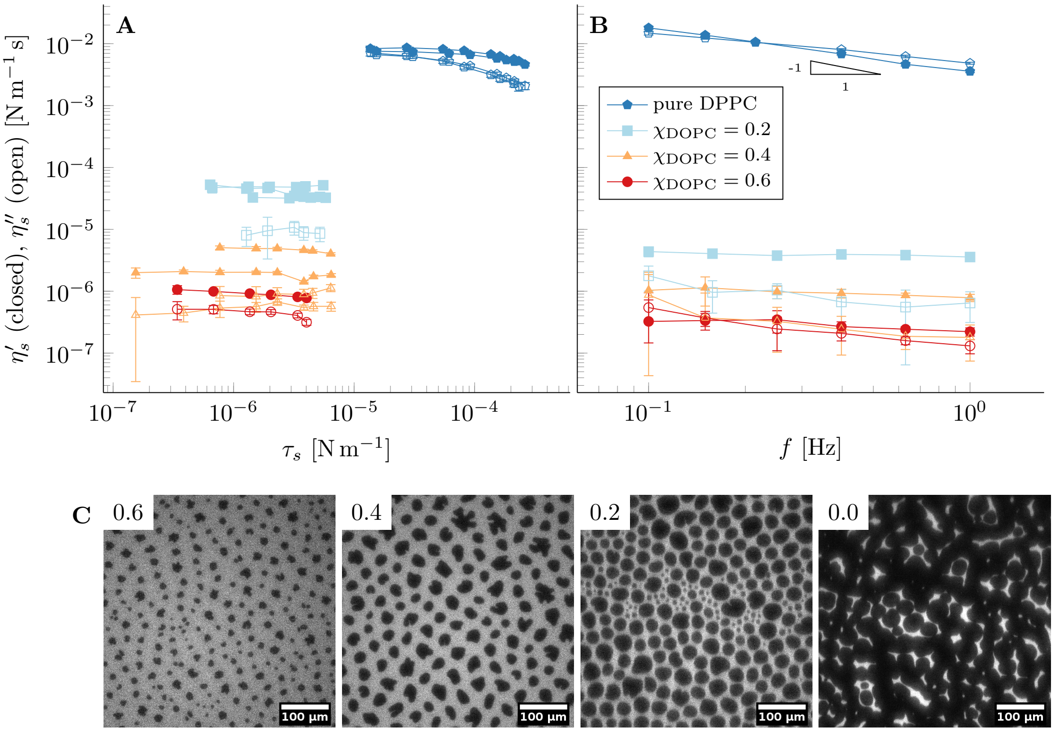

Figure 4.4: **Rheology of mixed lipid monolayers:** viscous (η'_s, closed symbols) and elastic (η''_s, open symbols) contribution to the complex interfacial shear viscosity of lipid mixtures at the buffer–oil interface as function of (**A**) interfacial stress amplitude τ_s at 20 °C and 3 rad s^{-1}, and (**B**) frequency at small strains ($\gamma_s < 2\,\%$) and 25 °C. All samples were measured at $\pi = 40$ mN m^{-1} apart from the largest DOPC concentration at $\pi = 45$ mN m^{-1}. The weight fraction of DOPC is indicated by χ_{DOPC}. **C**) Fluorescence microscopy images correspond to the data in B with χ_{DOPC} indicated in each upper left corner. The scale bar represents 100 µm and all samples contained 0.5 mol % of DOPE-Rhod.

separation is thermally induced by cooling the interface from this temperature to the desired measurement temperature so that a reproducible initial state is obtained.

The stress amplitude sweep performed at 20 °C and 3 rad s^{-1} in Fig. 4.4A shows a strong viscoelastic response for the pure DPPC monolayers, *i.e.* the magnitude of the elastic and viscous contributions are comparable. The addition of DOPC reduces the norm of the complex viscosity and renders the interface almost completely viscous. The small interfacial viscosity of the lipid mixtures requires a thinner probe diameter for increased sensitivity of the Fluo-ISR. Magnetic probes with different degrees of magnetization had to be used to cover the wide range of interfacial viscosities. Because the force acting on the magnetic probe depends on the gradient in magnetic field and the magnetisation of the probe, a different range of applied interfacial stress amplitudes (τ_s) is covered by each magnetic probe. The errorbars are calculated from the primary time depended observables stress $\tau_s(t)$ and strain $\gamma_s(t)$, and are defined for each individual datapoint as described in [110]. The errorbars are smaller than the symbol size apart from a few points at low stress amplitude and high DOPC content. On the contrary, the variability between freshly prepared interfaces increases with increasing DOPC content, while the data for different DPPC samples are almost identical (2, 3, 2, and 1 data sets are presented with increasing χ_{DOPC}).

The frequency sweep at 25 °C and small interfacial strain amplitudes ($\gamma_s < 2\,\%$) in Fig. 4.4B is in agreement with the stress amplitude sweep. Pure DPPC shows a strong viscoelastic response and a crossover from dominantly viscous to elastic behavior with increasing frequency is observed. The presence of DOPC in the mixed monolayers leads to a purely viscous interface with a strongly reduced viscosity. Furthermore, no significant dependence on frequency can be observed for the mixtures. The error-bars at low frequency and high χ_{DOPC} can be significantly larger than the symbol size. Convection in the bulk due to thermal gradients or air flows can lead to lateral drift of the magnetic probe at the interface. A high interfacial viscosity can dissipate the convection at the interface and reduce the drift, which has been shown to be the primary source of noise in this system. Furthermore, the applied stress at 0.1 Hz is very low to stay below a strain amplitude of 2 % rendering it even more susceptible to drift. As a consequence, the uncertainty in the rheological data increases with decreasing interfacial viscosity at low frequencies. As a consequence, the apparent dominant elastic behavior of the lipid mixtures with χ_{DOPC} 0.4 and 0.6 at low frequency is not confident. Only one dataset for each monolayer composition is presented in the frequency sweep since the variability between freshly prepared interfaces has already been discussed earlier for Fig. 4.4A.

The fluorescence microscopy images in Fig. 4.4C correspond to the data in Fig. 4.4B at 25 °C where χ_{DOPC} is indicated in the upper left corner of each image. The double bond in the fatty acid tails of DOPC as well as in the fluorescently labeled DOPE-Rhod prevents it from being incorporated into the liquid condensed phase due to steric hindrance, therefore appearing dark. As a consequence, increasing the DOPC content leads to a higher fraction of liquid expanded (LE) phase and the area fraction of liquid condensed phases decreases. The phase shape follows the instabilities discussed by McConnell et al. [1]. However, the phases do not appear very homogeneously, which might be a consequence of an absence of separation between nucleation and growth. Increasing the

DPPC content leads to very large phases, which eventually interconnect and form a network ($\chi_{\mathrm{DOPC}} = 0$). The presence of the phase coexistence still leads to some liquid expanded phase of DPPC despite the absence of any DOPC. The observed microstructure of the phospholipid monolayers agrees well with the reported rheological behavior. On the one hand, the interfaces with isolated liquid condensed phases ($\chi_{\mathrm{DOPC}} > 0$) have a low norm of the complex interfacial viscosity with a dominant viscous response and a very large linear regime. On the other hand, once the phases are interconnected, hence leading to a crowded interface, the norm of the complex interfacial viscosity increases by orders of magnitude and the elastic contribution becomes relevant, rendering the monolayer viscoelastic with a more limited linear regime.

4.2.3 Crowding the interface

The area fraction ϕ of the liquid condensed phase is calculated from the fluorescence microscopy images by image analysis with ImageJ where the images are first binarized. The norm of the complex interfacial viscosity (combined viscous and elastic contributions) is rescaled by a calculated medium interfacial viscosity $\eta_{s,M}$ of the bright phase. This medium viscosity is calculated with a linear mixing rule of pure DOPC and DPPC in the liquid expanded phase. The composition is calculated from the mixing ratio and the area fraction while the interfacial viscosity of the pure liquid expanded phase of DPPC is taken from literature ($\eta_{s,\mathrm{LE-DPPC}} = 1.6 \pm 0.3 \times 10^{-7}\,\mathrm{N\,m^{-1}\,s}$ [64]) and of the pure liquid expanded phase of DOPC is set to the minimum measurable viscosity of $5 \times 10^{-8}\,\mathrm{N\,m^{-1}\,s}$, which is larger than values reported for DOPC bilayers of $3 \times 10^{-9}\,\mathrm{N\,m^{-1}\,s}$ [41].

The rescaled complex interfacial viscosity, measured at a frequency of 0.1 Hz and within the linear response regime, for all measured lipid compositions, temperatures, and surface pressures collapses on an exponential dependence with area fraction of the liquid condensed phase, as shown in Fig. 4.5.

It is insightful to compare this curve to what would be expected for a two-dimensional system of hard disks, where only hydrodynamic interactions between the domains would be present. This is done by comparing the results with the two dimensional analogue of the Krieger-Dougherty (KD) equation. This is a phenomenological equation for large ϕ that generalizes the exact Einstein equation, which is only valid for very dilute

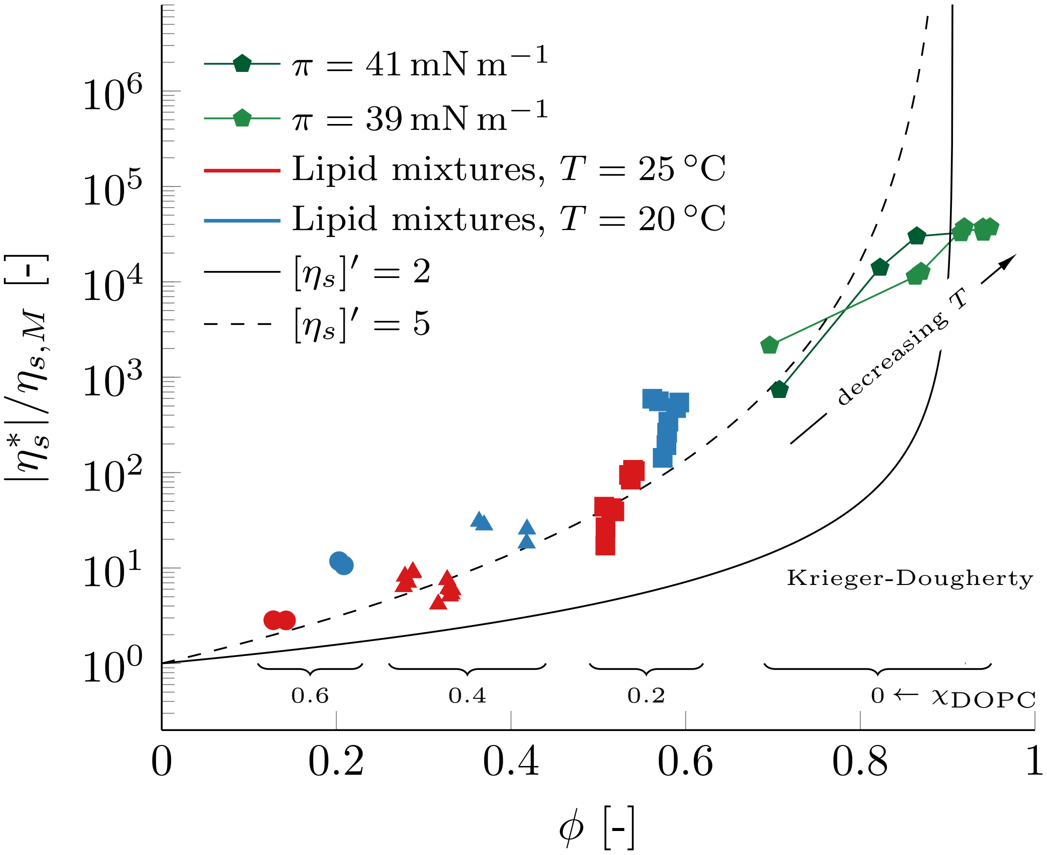

Figure 4.5: **Crowding of the lipid monolayers:** norm of the complex interfacial shear viscosity η_s^* of DPPC-DOPC mixtures at the buffer–oil interface, rescaled by a calculated medium viscosity $\eta_{s,M}$, as a function of area fraction of the liquid condensed phase ϕ. The weight fraction of DOPC is indicated by χ_{DOPC}. All data is at $\pi = 40\,\mathrm{mN\,m^{-1}}$ apart from the largest DOPC concentration at $\pi = 45\,\mathrm{mN\,m^{-1}}$. The solid and dashed lines represent a Krieger-Dougherty equation with intrinsic viscosities $[\eta_s]' = 2$ (hard disks) and $[\eta_s]' = 5$, respectively. Both use $\phi_{\max} = 0.906$ for maximum packing of disks in two dimensions.

suspensions, and relates the relative viscosity with a power law dependence on ϕ

$$\eta_r = \left(1 - \frac{\phi}{\phi_{\max}}\right)^{-[\eta_s]'\phi_{\max}} , \tag{4.5}$$

with a theoretical intrinsic viscosity of $[\eta_s]' = 2$ for hard disks [113] and maximum packing in two dimensional of $\phi_{\max} = 0.906$ [58].

It is obvious that the lipid monolayers in Fig. 4.5 deviate from the behavior of a hard disk system and rather follow an exponential dependence on ϕ such as a Mooney model [114]. At small area fractions ($\phi < 0.8$) the measured interfacial viscosity seems to follow rather the description of Eq. (4.5) with an intrinsic viscosity of $[\eta_s]' = 5$ instead of 2. One reason for this deviation can be the shape anisotropy of the dark phases due to the shape instability which increase the effective surface area, i.e. the hydrodynamic area could be larger compared to simple circles with identical area but it is questionable that this can explain the extent of the increase in the rescaled viscosity. Inaccuracy of the estimated medium viscosity could have a large effect. It should also be noted that there is a clear viscoelastic signal so other mechanisms will be contributing to the stress when the interface is deformed, and this is linked to the observation that mechanical history also has a strong effect. We have no direct explanation for this, possibly there is some equivalence to a distortional elasticity as observed in 3D liquid crystalline systems at the edge of solid domains.

The comparison with hard disk is however interesting and reveals an exiting result at high surface coverage. Upon approaching maximal packing of the domains the measured interfacial viscosity does not diverge and seems to plateau which is in contrast to any hard disk system [115]. This results suggests that hydrodynamic forces between the phases are not very strong and the interface maintains its fluidity even in a very crowded state. The accuracy of the area fraction in these very dense systems is smaller than the symbol size. Furthermore, the liquid condensed phases deform only at much larger interfacial stresses than generated by the Fluo-ISR in Fig. 4.4, as an isothermal compression of a pure DPPC monolayer demonstrates (see SI C.3).

A fundamental difference between a monolayer of surface active molecules at a liquid-liquid interface compared to bulk liquids is the presence of a compressibility at the interface, as a phase coexisting system has a very large compressibility. It is not trivial to find a two dimensional analogue of a compressible system because most liquids are assumed to be incompressible. Hence most hydrodynamic models (such as Eq. (4.5)) are developed for incompressible liquids. The presence of a phase coexistence leads to an almost fully compressible system since the lipids can locally change the phase and accommodate a change in surface pressure. (if there is a plateau in the isotherm it would be perfectly compressible) Furthermore, the liquid expanded phase is known to be compressible since it is not in a crystalline or ordered state. A compressible medium may remove the divergence in the lubrication pressure of two approaching hard disks and renders the hydrodynamic forces negligible. This could rationalize the non-diverging viscosity in Fig. 4.5 and points to the importance of the role of interface compressibility.

Another question arises regarding the interplay between the incompressible bulk phase and the compressible interface between two approaching liquid condensed phases. The liquid expanded phase between the condensed phase is thinner by 0.2 nm due to the randomization of the tail conformation [116] despite the slightly longer tails of DOPC by two carbon atoms. This most likely results in a capillary interaction between the liquid condensed phases. In contrast to the liquid expanded phase in between, the adjacent bulk phase is not compressible. To resolve this mismatch in compressibility, either complicated recirculation in the third dimension (orthogonal to the interface) or slip between the interface and bulk phase has to occur. The latter seems more reasonable but has not been quantified.

4.2.4 Comparison of a lipid monolayer with a bilayer

Particle tracking is used to compare the diffusive behavior in the lateral direction between lipid monolayers and bilayers of the same lipid composition ($\chi_{\mathrm{DOPC}} = 0.4$). The viscosity of the liquid expanded phase of the two systems can be compared with short-time single-particle microrheology whereas the long-time single-particle or the two-particle microrheology measures the entire interface. The latter is useful to compare the viscosity resulting from tracking with the viscosity measured by the ISR macroscopically. The domains are large in size, but remain Brownian due to their small thickness and hence mass.

An image series of a lipid monolayer with composition $\chi_{\mathrm{DOPC}} = 0.4$ was acquired at 25 °C with a full frame resolution and a time resolution of 0.1 s. The translational motion of the liquid condensed phases on the interface was tracked and corrected for uniform drift. The resulting mean squared displacement is presented in Fig. 4.6A.

The statistics for the two-points tracking is very low but the agreement with the single particle tracking at large lag times demonstrates the effective correction for drift. Only the single-point tracking is then used (see SI C.4). Both short-time and long-time diffusivities are surprisingly large and cannot be explained by the SD model described by Eq. (4.3) suggesting that the mobility is not determined by the in plane viscosity, most likely interleaflet friction is low. As shown in Fig. 4.6B, the largest possible value for the translational diffusion constant for monolayer is $D_{T,\mathrm{max}} = 1.3 \times 10^{-14}\,\mathrm{m}^2\,\mathrm{s}^{-1}$ which corresponds to an interfacial viscosity on the order of $1 \times 10^{-8}\,\mathrm{N\,m}^{-1}\,\mathrm{s}$ (see Table 4.1).

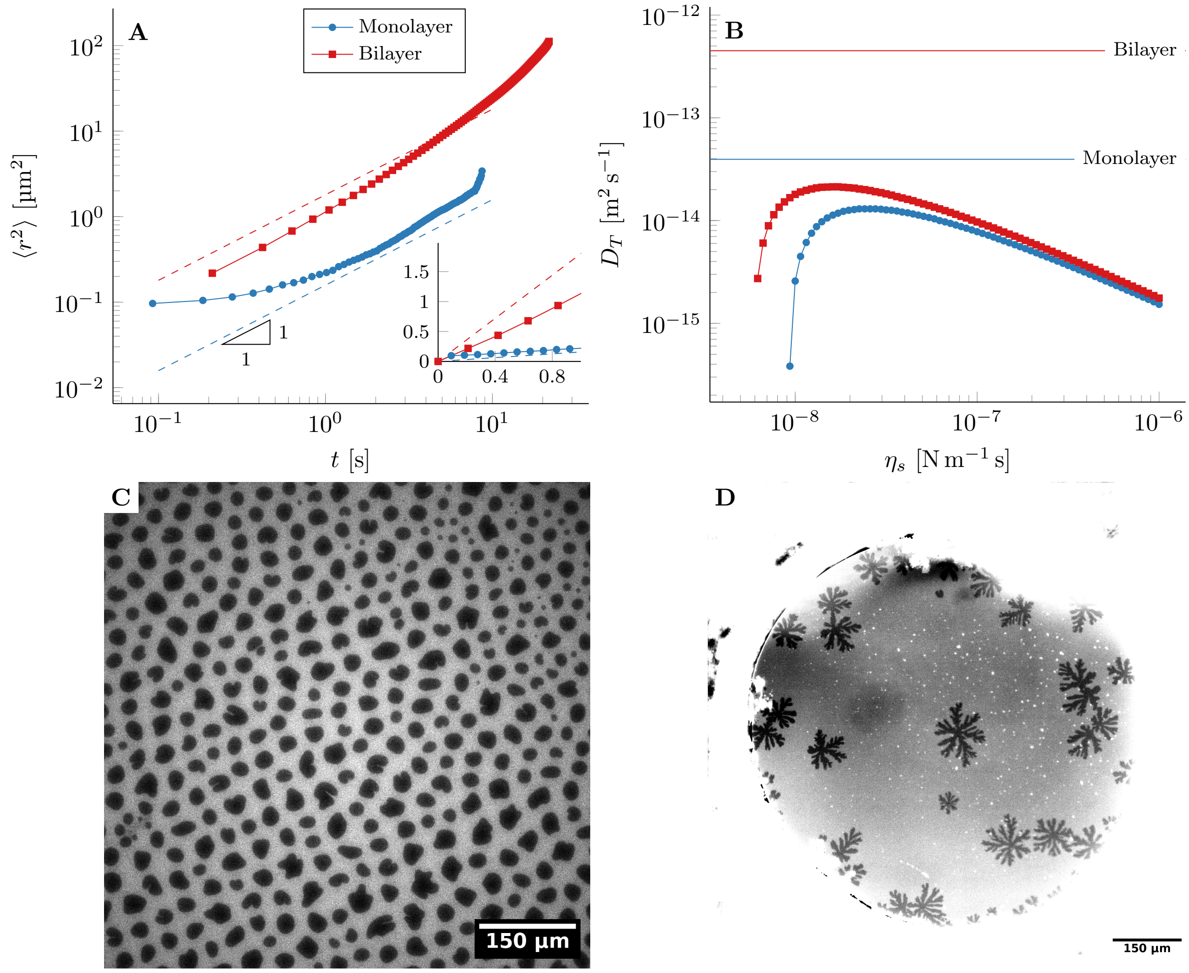

Figure 4.6: **Comparison to lipid bilayers: (A)** Mean squared displacement $\langle r^2 \rangle$ as a function of lag time t showing the translational diffusive motion of LC domains in monolayers **(C)** and bilayers **(D)**. The dashed line shows the fit and the inset is the same data with axes in linear scale. **(B)** predictions of the Saffman-Delbrück model Eq. (4.3) for the two systems. Horizontal lines show the measured diffusion coefficients.

This upper value of an interfacial viscosity could be used for an order of magnitude estimate of the liquid expanded phase and lies within the values found in literature for the liquid expanded phases consisting of pure DPPC and DOPC mentioned above. Unfortunately, the very large long-time diffusion coefficient D_{long} cannot be explained by the SD model and a comparison with the macroscopically measured interfacial viscosity by the ISR is still pending. One issue could also be that sufficient oil remains in the bilayer (as suggested by the dendritic shape of the domains) to lubricate the interleaflet flow [117].

The diffusive motion of the liquid condensed phases in the bilayer turns out to be strongly affected by non-uniform drift. Aggregates of fluorophore visible as white spots were tracked instead. The small size compared to the liquid condensed phase made them very diffusive and the large amount helped to reduce non-uniform drift more easily. The agreement of the slopes between the single-particle and two-particles tracking at long lag times confirms the de-drift and only the single particle MSD is further analyzed (see SI C.4). However, neither the long time nor the short time diffusive constants can be used to calculate interfacial viscosities with the SD model.

The measured short time diffusion coefficients for monolayer and bilayer are both larger than the maximum possible values predicted by the SD model as shown in Fig. 4.6B. One reason could be the presence of a compressible membrane as already indicated by the plateau in Fig. 4.5.

Possible sources of error are the not perfectly circular shape of the liquid condensed phases on the monolayer and an effective radius with the same area was used instead. Furthermore, monolayers have different viscosities one each side of the monolayer because the bulk phases are not identical.

Table 4.1: **Diffusion constants:** Temperature T, mean domain size α, and bulk viscosity η_b used in the SD model shown in Fig. 4.6B. Measured short-time (D_{short}) and long-time diffusion constants. $\eta_{s,SD\max}$ corresponds to the maximum of Eq. (4.1) at $D_{SD,\max}$.

		monolayer	bilayer
T	[°C]	25	39
α	[µm]	3.46	2.5
η_b	[mPa s]	1.5	0.67
D_{short}	[m^2 s^{-1}]	3.95×10^{-14}	4.5×10^{-13}
D_{long}	[m^2 s^{-1}]	1.13×10^{-12}	1.9×10^{-12}
$D_{SD,\max}$	[m^2 s^{-1}]	1.30×10^{-14}	2.13×10^{-14}
$\eta_{s,SD\max}$	[N s m^{-1}]	2.51×10^{-8}	1.61×10^{-8}

4.3 Conclusion

The phase separation of a lipid interface is used to mimic one aspect of crowding in interfaces. The phospholipid buffer–oil monolayer is prepared carefully to avoid pre-shear and overcome the identified problem in Chapter 3. The interface is compressed to relevant interfacial pressures, at temperatures above the melting temperature of the

LC phase, where no phase separation occurs and the interface remains fully fluid. The interface is cooled and then undergoes a *temperature induced phase separation* in contrast to the *pressure induced phase separation* discussed in the previous chapter. The area fraction of the solid-like liquid condensed phase (*i.e.* the extent of phase separation) is controlled by the temperature and the composition of the lipid monolayer. The phospholipid DOPC is added, which is incapable of forming the liquid condensed phase because of steric interactions originating from the unsaturated fatty acid tails. The norm of the complex interfacial shear viscosity is rescaled with a calculated medium viscosity of the liquid expanded phase. The resulting relative viscosity of the lipid monolayer follows an exponential dependence on area fraction of the liquid expanded phase. In contrast, a hard disk system, which is the two-dimensional analogue of a three dimensional suspension of hard spheres, is described by the Krieger-Dougherty model (Eq. (4.5)) and diverges with area fraction of the liquid condensed phase. This suggest that hydrodynamic interactions do not play a dominant role in these crowded states of the interface. One peculiarity of the liquid expanded phase is its finite compressibility. Interface compressibility could prevent the lubrication pressure between two approaching liquid condensed domains from diverging. Hence the interface remains fluidized. The presence of a phase coexistence enhances this effect because the lipid molecules can locally change the phase to accommodate for excess pressure. This raises the question regarding the mismatch in compressibility between the compressible interface and incompressible bulk phases. To resolve this issue, either complex circulations orthogonal to the interface has to occur or slip has to be present between the bulk and the lipid interface.

Preliminary tracking experiments to compare the fluidity in phospholipid monolayers with bilayers show diffusion coefficients larger than expected by the Saffman-Delbrück model (see Eq. (4.3) & Fig. 4.6). This model describes the lateral diffusive motion of a cylinder in an incompressible membrane with an interfacial viscosity which is surrounded by a bulk fluid. The results agree with the assumption of the interface being compressible which would lead to larger diffusion coefficients. Further investigation is necessary to find appropriate hydrodynamic models to verify weather the dominant mechanism is the finite compressibility of the interface or slip between interface and bulk phase. Yet as a conclusion we can state that a membrane which is able to phase separate will always retain some fluidity even in very crowded states.

4.4 Acknowledgments

The assistance of Maria Clara Novaes Silva for interfacial rheology measurements is greatly appreciated. Furthermore, Laura Stricker is thanked for image analysis (area fractions and tracking).

4.5 Materials and methods

Table 4.2: **Properties of the magnetic probes for the ISR:** l and m are the length and mass of the probe, respectively. k^{-1} is the instrument compliance and C_{I-F} the force constant described in Eq. (A.3). k and C_{I-F} result from the calibration. Individual fitting parameters for each experiment can be found in Table C.1.

	l [mm]	m [mg]	k [N m^{-1}]	C_{I-F} [N A^{-1}]
Needle	23.5	5.8	$(2.8 \pm 0.3) \times 10^{-5}$	$(4.4 \pm 0.2) \times 10^{-6}$
Microwire	11.7 ± 0.5	$(4.3 \pm 0.2) \times 10^{-3}$	$(2.1 \pm 0.6) \times 10^{-6}$	$(5.2 \pm 0.4) \times 10^{-8}$

4.5.1 Monolayer sample preparation

The Langmuir trough and barriers were thoroughly cleaned with detergent and repeatedly rinsed with technical grade propan-2-ol (IPA) and ethanol, and milli-Q water before the aqueous phase was added. A Wilhelmy plate (KSV NIMA) was flame treated and placed at the interface by a microbalance (KSV NIMA) together with the thermocouple provided by KSV. The glass channel of the ISR was rinsed with technical grade acetone, IPA, and water, plasma cleaned, and placed in the Langmuir trough. The cleanliness of the buffer–air interface was verified by a measurement of the surface tension of 71.9 mN m^{-1} at 25 °C and a maximum increase of surface pressure $\Delta\pi < 2\,\mathrm{mN\,m^{-1}}$ upon compression of the pristine interface was found to be acceptable. In a second step, the oil phase was added very gently and a second clean compression was performed to assess the quality of the buffer–oil interface.

After the ISR calibration and subsequent dropwise spreading of the lipid solution at the interface by a Hamilton syringe, the interface was heated to higher temperatures compared to the melting temperature of DPPC $T_{m,\mathrm{DPPC}} = 42\,°\mathrm{C}$, as shown in Fig. 4.1. The compression was then performed at this high temperature hence preventing a phase separation and avoiding pre-shear of the interface. After reaching the target surface pressure, the temperature of the interface was reduced at constant surface area, which lead to a *temperature induced phase separation* of the interface into liquid extended and liquid condensed phases. The rheology was then measured after equilibrating the interface at least for 15 min at appropriate temperatures. The resulting surface pressure was corrected by subtracting the effect of temperature on the interfacial tension of the clean interfaces.

4.5.2 Bilayer sample preparation

The LAMB setup developed by Beltramo et al. [4] was used to make free standing and planar bilayers. The setup uses a microfluidic bikewheel chip first introduced by [118] with the modification of an Elveflow MK3+ piezoelectric pressure control system [119].

The surface of the bikewheel chip was first made hydrophobic following the procedure of [4]. The chip was then cleaned by rinsing with IPA, ethanol, and milli-Q water and sonicated in milli-Q for 5 min. The lipid oil solution with composition of DOPC/DPPC = 2/3 in purified hexadecane was prepared according to [4] and sonicated for at least two hours before loading in the bikewheel chip. The chamber was filled with the buffer phase and the bilayer was formed at $T > T_{m,\mathrm{DPPC}}$. The bikewheel was then slowly cooled to initiate the phase separation.

4.5.3 Image analysis

Image processing

The area fraction ϕ is derived from the microscopy images as the ratio between the area of the solid-like DPPC domains (black regions) and the total area of the field of view. To this aim, the original gray-scale images are converted into black and white images by adopting the following procedure. Each stack of images is preprocessed by cropping, denoising (*i.e.* removal of dark and bright outliers) and background removal, where the background image is generated by blurring the original image by Gaussian filtering [120]. When required, we perform an additional contrast limited adaptive histogram equalization (CLAHE) [121]. The resulting preprocessed images are then binarized by thresholding. The image analysis is realized by means of an in-house code written in ImageJ macro language, based on the Fiji native plugins: 'Crop', 'Remove outliers', 'CLAHE', 'Threshold' as well as on the 'Pseudo flat field correction' plugin from the BioVoxxel toolbox [122]. The results are then visually inspected, to correct for misdetections. The total area covered by the DPPC domains is calculated by counting the black pixels. The geometric features of the DPPC domains, namely perimeter, circularity, aspect ratio, roundness and solidity, are extracted with the Extended Particle Analyzer plugin (BioVoxxel toolbox3).

Particle tracking

The tracking of the domains is performed by using the TrackMate plugin [123], with the CLIJ Voronoi Otsu particle detection algorithm [124] and the Linear Assignment Problem (LAP) tracker [125]. In order to remove the contribution of the homogeneous drift from the detected trajectories, we assume that their motion is given by the superposition of a diffusive and advective component, *i.e.* the drift. Hence, we write the time-dependent velocity of the i^{th} particle as $\boldsymbol{v}_i(t) = \boldsymbol{v}_{i,\text{diff}}(t) + \boldsymbol{v}_{i,\text{drift}}(t)$, where $\boldsymbol{v}_{i,\text{diff}}$ and $\boldsymbol{v}_{i,\text{drift}}$ represent the diffusive and the advective contributions, respectively. As the diffusive part of the motion is supposed to be random, the overall drift can be expressed as $\boldsymbol{v}_{\text{drift}} = \langle \boldsymbol{v}_i(t) \rangle$, where the brackets $\langle\rangle$ indicate the ensemble average over all particles. At each time t, the homogeneous drift-induced displacement can be expressed as $\boldsymbol{x}_{\text{drift}}(t) = \int_0^t \langle \boldsymbol{v}_i(t') \rangle dt'$. We then subtract $\boldsymbol{x}_{\text{drift}}$ from the detected displacement of each particle, before proceeding to further analysis of the trajectories. The instantaneous velocities of the particles are derived from their trajectories, with a time-discrete finite differences scheme, while the time integration is performed with the trapeze rule. We consider for the analysis only the smaller domains, namely the domains with an area A between $30\,\mu\text{m}^2$ and $40\,\mu\text{m}^2$. This choice is motivated by the necessity of using particles with similar areas and a high signal to noise ratio for the detected displacement. The selected domains satisfy such a requirement, as their minimum detected instantaneous displacement $|d\boldsymbol{x}_i|$ along their de-drifted trajectory satisfies the requirement $|d\boldsymbol{x}_i| > 1.2\sqrt{dA/\pi}$, where dA is the instantaneous variation of their area. The mean squared displacement (MSD) is calculated from the de-drifted trajectories, for different time intervals (lag times) τ, as $\langle \Delta x^2(\tau) \rangle = \langle |\boldsymbol{x}(t+\tau) - \boldsymbol{x}(t)|^2 \rangle$. The analysis is performed with an in-house Matlab code, based on the algorithms described in [126]. In addition to the MSD derived from single-particle tracking, we also perform a two-point microrheology analysis [127] and we derive the distinct mean square displacement (MSD$_D$) as $\langle \Delta x^2(\tau) \rangle_D = \frac{2R}{a} D_{rr}(R,t)$, where R represents the separation distance between two particles, $a = \sqrt{\langle A \rangle / \pi}$ the average size of the particles, and $D_{rr}(R,t) = \langle \Delta r_i(\tau) \Delta r_j(\tau) \rangle$ the correlation of the motion of two particles i, j along their line center, with $\Delta r_i = \Delta \boldsymbol{x}_i \cdot \boldsymbol{e}_{ij}$ the displacement of the i^{th} particle along the unit vector $\boldsymbol{e}_{ij}$ connecting the centers of particles i and j. Videos for monolayer tracking are acquired with 10 fps and for bilayers with 6 fps.

5 Conclusion and Outlook

A first important contribution of this thesis was presented in Chapter 2, and gave a definitive analysis of different macroscopic interfacial rheometers and defines clear operating windows. It gives an overview of the possible aspects which influence the accuracy of the obtained experimental data and derive operating windows where reliable data can be obtained. There are several aspects, some intrinsic and some device related, which render interfacial rheometry challenging. A first aspect which has been considered is the propagation of noise, which merits particular attention given that the torque or force response of the interface is weak. Calculating the noise propagation makes it possible to quantify the uncertainties $u_{|G_s^*|}$ and u_{δ_s} (Eqs. (2.22) & (2.23)) to define uncertainty bars on the measured data which will give a direct indication of the quality of each individual measurement. A complicating matter is that this noise propagation actually depends on the properties of the interface. In the present work we used a fatty alcohol as a challenging material to characterize. Interfaces comprised of other materials such as polymers, proteins or colloidal particles can be non-linear viscoelastic (e.g. visco-plastic, shear thinning). Substituting Eq. (2.19) & (2.20) with the appropriate constitutive equation allows the presented analysis to be used for other types of interfaces as long as there is no slip or artifacts such as fast dissolution of soluble surfactants present. Aspects such as the role of drift, instrument and fluid inertia, compliance and the role of subphase corrections all contribute to possible measurement errors. To summarize all these effects, Fig. 2.11 gives the operating windows for the different devices. Fig. 2.11 summarizes the excellent sensitivity of the ISR and the impressive dynamic measuring range of the DWR. The bi-cone does not appear to be suitable for investigating fatty alcohols but will be appropriate for interfaces with higher moduli and viscosities. The procedure outlined to measure the noise propagation can be used for those cases. An overview of all the different aspects discussed with the governing equations or relevant figures is given in Table 2.7, which should serve as a useful guide for interfacial rheometry practitioners.

Chapter 3 reported results on DPPC monolayers at fluid–fluid interfaces of pure water–air (W/A), buffer–air (B/A), pure water–oil (W/O), and buffer–oil (B/O). Because of the high melting temperature of the lipid tails ($T_{m,\mathrm{DPPC}} = 42\,^{\circ}\mathrm{C}$), the interfaces are annealed at $T > T_{m,\mathrm{DPPC}}$ in between spreading and compressing. This procedure leads to *thermally structured* interfaces as introduced by Hermans et al. [2], which enables us to reproduce the isotherms and initial conditions as we avoid the mechanical history. The DPPC interface phase separates into a liquid expanded (LE) and solid-like liquid condensed (LC) phase depending on temperature and interfacial pressure. The phase morphology of the liquid condensed phase at large interfacial pressures depends on a balance of attractive and repulsive forces between the lipid molecules. On the one hand, the repulsive forces can be reduced by changing the pure milli-Q subphase to an aqueous salt buffer because the ions screen the electric dipolar interactions. On the other hand, introducing oil as upper bulk phase allows the lipids to undergo van der Waals interactions with the oil molecules and swells the interface. This expected effect of the adjacent bulk phase on the interface is confirmed by three different measurements: compression isotherms, fluorescence microscopy, and interfacial shear rheology. Introducing the salt buffer as subphase for DPPC at liquid–air interfaces shows a more negative hysteresis in the compression-expansion isotherm, a less distinct dendritic shape instability of the LC phases and phases aggregate below percolation threshold, and the complex interfacial shear viscosity has a much lower norm with a small increase in the relative elastic contribution. All these effects are in favor of a more attractive system compared to DPPC at the pure milli-Q W/A interface. Replacing air with oil as upper phase has a significant consequence on the hydrophobic interactions. The interfacial pressure shows a much stronger increase during spreading of the same concentration of lipid molecules at the liquid–liquid interface. The compression-expansion hysteresis is very positive and very large for W/O and the interface becomes strongly viscoelastic with an order of magnitude increase of the complex interfacial shear viscosity. Introducing the salt buffer as subphase to the liquid–liquid system reduced the compression-expansion hysteresis dramatically which suggests a more subtle balance of attractive and repulsive interaction forces between the lipids. However, the effect on the complex interfacial shear viscosity is not significant. A comparison of the interfacial rheology and phase morphology at similar interfacial pressure and 25 °C is presented in Fig. 3.10 & 3.11. The effect of the hydrophobic chains by adding the oil phase have a stronger effect on the mechanical properties compared to the influence of the salt buffer on the hydrophilic head group.

Fig. 3.14 & 3.17 show that the elastic contributions to the complex interfacial shear viscosity of DPPC at W/A does not depend on interfacial pressure in a systematic way at temperatures of 25 °C and larger. The same holds for the B/O system for the entire temperature range. Fluorescence microscopy images reveal the presence of strongly and highly localized deformed LC phases when approaching high interfacial pressures, and shear banding or “slip lines” appear at elevated temperatures (see Fig. 3.16). Shear deformation is present during a compression in a conventional Langmuir trough because of the shape change of the interface during a compression. As a consequence of these localized events, the measured complex interfacial shear viscosity cannot be interpreted as a material function anymore. To overcome this problem, the interface has to be prepared in a way to limit pre-shear or delete shear history before measuring the rheological properties of the interface.

In Chapter 4, the phase separation of the lipid interface is used to mimic crowded interfaces. The phospholipid B/O monolayer is prepared carefully to avoid pre-shear and overcome the identified problem in Chapter 3. The interface is compressed to relevant interfacial pressures at temperatures larger than the melting temperature of the liquid condensed phase, where no phase separation occurs, and the interface remains fully fluid. The interface is then cooled and undergoes a *temperature induced phase separation* in contrast to the *pressure induced phase separation* discussed in the previous chapter. The area fraction of the solid-like liquid condensed phase (*i.e.* the extent of the phase separation) is controlled by temperature and the composition of the lipid monolayer. The phospholipid DOPC is added which is incapable of forming the liquid condensed phase because of steric interactions originating from the unsaturated fatty acid tails. The norm of the complex interfacial shear viscosity is rescaled with a calculated medium viscosity of the liquid expanded phase. The resulting relative viscosity of the lipid monolayer follows an exponential dependence on area fraction of the liquid condensed phase. In contrast, a hard disk system, which is the two-dimensional analogue of a three dimensional suspension of hard spheres, is described by the Krieger-Dougherty model (Eq. (4.5)) and diverges with area fraction of the liquid condensed phase. This demonstrates the absence of an important role of hydrodynamic interactions in these crowded states of the interface. One peculiarity of the liquid expanded phase is its finite compressibility. The presence of a compressibility could prevent the lubrication pressure between two approaching liquid condensed domains from diverging. Hence the interface is fluidized. The presence of a phase coexistence enhances this effect because the lipid molecules can locally change the phase to accommodate for excess pressure. This rises the question regarding the mismatch in compressibility between the compressible interface and incompressible bulk phases. To resolve this issue, either complex circulations orthogonal to the interface has to occur or slip has to be present between the bulk and the lipid interface.

Preliminary tracking experiments to compare the fluidity in phospholipid monolayers with bilayers show diffusion coefficients larger than expected by the Saffman-Delbrück model (see Eq. (4.3) & Fig. 4.6). This model describes the lateral diffusive motion of a cylinder in an incompressible membrane with an interfacial viscosity which is surrounded by a bulk fluid. The results agree with the assumption of the interface being compressible which would lead to larger diffusion coefficients. Further investigation is necessary to find appropriate hydrodynamic models to verify weather the dominant mechanism is the finite compressibility of the interface or slip between interface and bulk phase.

Bibliography

[1] D. Gallez and H. M. McConnell. "Coupling of Size and Shape Equilibration in Lipid Monolayer Domains". In: *The Journal of Physical Chemistry B* 104.7 (2000), pp. 1657–1662. DOI: `10.1021/jp993436d`.

[2] E. Hermans and J. Vermant. "Interfacial shear rheology of DPPC under physiologically relevant conditions". In: *Soft Matter* 10.1 (2014), pp. 175–186. DOI: `10.1039/c3sm52091a`.

[3] D. Marsh. "Lateral pressure in membranes". In: *Biochimica et Biophysica Acta - Reviews on Biomembranes* 1286.3 (1996), pp. 183–223. DOI: `10.1016/s0304-4157(96)00009-3`.

[4] P. J. Beltramo, R. V. Hooghten, and J. Vermant. "Millimeter-area, free standing, phospholipid bilayers". In: *Soft Matter* 12.19 (2016), pp. 4324–4331. DOI: `10.1039/c6sm00250a`.

[5] B. Alberts, A. Johnson, P. Walter, J. Lewis, and M. Raff. *Molecular Biology of the Cell.* 6th. W. W. Norton & Company, 2014. ISBN: 978-0-8153-4432-2.

[6] E. Gouaux and R. MacKinnon. "Principles of Selective Ion Transport in Channels and Pumps". In: *Science* 310.5753 (2005), pp. 1461–1465. DOI: `10.1126/science.1113666`.

[7] J. Loeb. "The Recent Development of Biology". In: *Science* 20.519 (1904), pp. 777–786. DOI: `10.1126/science.20.519.777`.

[8] U. Hintzenstern, W. Schwarz, M. Goerig, and H. Petermann. "Development of the "lipoid theory of narcosis" in German-speaking countries in the 19th century: from Bibra/Harless to Meyer/Overton". In: *International Congress Series* 1242 (2002), pp. 609–612. DOI: `10.1016/s0531-5131(02)00799-9`.

[9] H. Fricke. “THE ELECTRIC CAPACITY OF SUSPENSIONS WITH SPECIAL REFERENCE TO BLOOD”. In: *Journal of General Physiology* 9.2 (1925), pp. 137–152. DOI: `10.1085/jgp.9.2.137`.

[10] E. Gorter and F. Grendel. “ON BIMOLECULAR LAYERS OF LIPOIDS ON THE CHROMOCYTES OF THE BLOOD”. In: *Journal of Experimental Medicine* 41.4 (1925), pp. 439–443. DOI: `10.1084/jem.41.4.439`.

[11] F. S. Sjöstrand, E. Andersson-Cedergren, and M. M. Dewey. “The ultrastructure of the intercalated discs of frog, mouse and guinea pig cardiac muscle”. In: *Journal of Ultrastructure Research* 1.3 (1958), pp. 271–287. DOI: `10.1016/s0022-5320(58)80008-8`.

[12] J. D. Robertson. “THE OCCURRENCE OF A SUBUNIT PATTERN IN THE UNIT MEMBRANES OF CLUB ENDINGS IN MAUTHNER CELL SYNAPSES IN GOLDFISH BRAINS”. In: *Journal of Cell Biology* 19.1 (1963), pp. 201–221. DOI: `10.1083/jcb.19.1.201`.

[13] H. G. L. Coster and I. J. Kaplin. “The effect of pH on the OsO4-revealed structure of the plasma membrane of Chara corallina”. In: *Biochimica et Biophysica Acta (BBA) - Biomembranes* 330.2 (1973), pp. 141–146. DOI: `10.1016/0005-2736(73)90218-6`.

[14] E. Fahy, S. Subramaniam, R. C. Murphy, M. Nishijima, C. R. H. Raetz, T. Shimizu, F. Spener, G. van Meer, M. J. O. Wakelam, and E. A. Dennis. “Update of the LIPID MAPS comprehensive classification system for lipids”. In: *Journal of Lipid Research* 50 (2009), S9–S14. DOI: `10.1194/jlr.r800095-jlr200`.

[15] D. Marsh. *Handbook of Lipid Bilayers*. CRC Press, 2013. DOI: `10.1201/b11712`.

[16] J. Zimmerberg and M. M. Kozlov. “How proteins produce cellular membrane curvature”. In: *Nature Reviews Molecular Cell Biology* 7.1 (2005), pp. 9–19. DOI: `10.1038/nrm1784`.

[17] L. Meertens, X. Carnec, M. P. Lecoin, R. Ramdasi, F. Guivel-Benhassine, E. Lew, G. Lemke, O. Schwartz, and A. Amara. “The TIM and TAM Families of Phosphatidylserine Receptors Mediate Dengue Virus Entry”. In: *Cell Host & Microbe* 12.4 (2012), pp. 544–557. DOI: `10.1016/j.chom.2012.08.009`.

[18] G. van Meer, D. R. Voelker, and G. W. Feigenson. “Membrane lipids: where they are and how they behave”. In: *Nature Reviews Molecular Cell Biology* 9.2 (2008), pp. 112–124. DOI: `10.1038/nrm2330`.

[19] S. Wang, J. Gao, and Z. Wang. “Outer membrane vesicles for vaccination and targeted drug delivery”. In: *WIREs Nanomedicine and Nanobiotechnology* 11.2 (2018). DOI: `10.1002/wnan.1523`.

[20] S. Antimisiaris, S. Mourtas, and A. Marazioti. “Exosomes and Exosome-Inspired Vesicles for Targeted Drug Delivery”. In: *Pharmaceutics* 10.4 (2018), p. 218. DOI: `10.3390/pharmaceutics10040218`.

[21] A. Chonn, S. C. Semple, and P. R. Cullis. “Association of blood proteins with large unilamellar liposomes in vivo. Relation to circulation lifetimes.” In: *Journal of Biological Chemistry* 267.26 (1992), pp. 18759–18765. DOI: `10.1016/s0021-9258(19)37026-7`.

[22] B. Cˇeh, M. Winterhalter, P. M. Frederik, J. J. Vallner, and D. D. Lasic. “Stealth® liposomes: from theory to product”. In: *Advanced Drug Delivery Reviews* 24.2-3 (1997), pp. 165–177. DOI: `10.1016/s0169-409x(96)00456-5`.

[23] M. Bally, K. Bailey, K. Sugihara, D. Grieshaber, J. Vörös, and B. Städler. “Liposome and Lipid Bilayer Arrays Towards Biosensing Applications”. In: *Small* 6.22 (2010), pp. 2481–2497. DOI: `10.1002/smll.201000644`.

[24] C. Dagenais, A. Avdeef, O. Tsinman, A. Dudley, and R. Beliveau. “P-glycoprotein deficient mouse in situ blood–brain barrier permeability and its prediction using an in combo PAMPA model”. In: *European Journal of Pharmaceutical Sciences* 38.2 (2009), pp. 121–137. DOI: `10.1016/j.ejps.2009.06.009`.

[25] D. Boal. *Mechanics of the Cell.* Cambridge University Press, 2012. DOI: `10.1017/cbo9781139022217`.

[26] E. J. M. Helmreich. “Environmental influences on signal transduction through membranes: a retrospective mini-review”. In: *Biophysical Chemistry* 100.1-3 (2003), pp. 519–534. DOI: `10.1016/s0301-4622(02)00303-4`.

[27] S. J. Marrink, V. Corradi, P. C. T. Souza, H. I. Ingólfsson, D. P. Tieleman, and M. S. P. Sansom. “Computational Modeling of Realistic Cell Membranes”. In: *Chemical Reviews* 119.9 (2019), pp. 6184–6226. DOI: `10.1021/acs.chemrev.8b00460`.

[28] E. J. M. Helmreich. *The biochemistry of cell signalling.* Oxford University Press, USA, 2001. ISBN: 0-19-850820-4.

[29] A. D. Dupuy and D. M. Engelman. “Protein area occupancy at the center of the red blood cell membrane”. In: *Proceedings of the National Academy of Sciences of the United States of America* 105.8 (2008), pp. 2848–2852. DOI: `10.1073/pnas.0712379105`.

[30] M. Javanainen, H. Hammaren, L. Monticelli, J.-H. Jeon, M. S. Miettinen, H. Martinez-Seara, R. Metzler, and I. Vattulainen. “Anomalous and normal diffusion of proteins and lipids in crowded lipid membranes”. In: *Faraday Discussions* 161 (2012), pp. 397–417. DOI: `10.1039/c2fd20085f`.

[31] H. X. Zhou, G. Rivas, and A. P. Minton. “Macromolecular crowding and confinement: Biochemical, biophysical, and potential physiological consequences”. In: *Annual Review of Biophysics* 37 (2008), pp. 375–397. DOI: `10.1146/annurev.biophys.37.032807.125817`.

[32] W. Zhao, S. Prijic, B. C. Urban, M. J. Tisza, Y. Zuo, L. Li, Z. Tan, X. Chen, S. A. Mani, and J. T. Chang. “Candidate Antimetastasis Drugs Suppress the Metastatic Capacity of Breast Cancer Cells by Reducing Membrane Fluidity”. In: *Cancer Research* 76.7 (2016), pp. 2037–2049. DOI: `10.1158/0008-5472.can-15-1970`.

[33] M. Sok, M. Šentjurc, and M. Schara. “Membrane fluidity characteristics of human lung cancer”. In: *Cancer Letters* 139.2 (1999), pp. 215–220. DOI: `10.1016/s0304-3835(99)00044-0`.

[34] M. Sok, M. Šentjurc, M. Schara, J. Stare, and T. Rott. “Cell membrane fluidity and prognosis of lung cancer”. In: *The Annals of Thoracic Surgery* 73.5 (2002), pp. 1567–1571. DOI: `10.1016/s0003-4975(02)03458-6`.

[35] V. Adrien, G. Rayan, K. Astafyeva, I. Broutin, M. Picard, P. Fuchs, W. Urbach, and N. Taulier. “How to best estimate the viscosity of lipid bilayers”. In: *Biophysical Chemistry* 281.August 2021 (2022), p. 106732. DOI: `10.1016/j.bpc.2021.106732`.

[36] E. M. Furst and T. M. Squires. *Microrheology.* Oxford University Press, 2018. ISBN: 978-0-19-965520-5. DOI: `10.1093/oso/9780199655205.001.0001`.

[37] R. Dimova, C. Dietrich, A. Hadjiisky, K. Danov, and B. Pouligny. “Falling ball viscosimetry of giant vesicle membranes: Finite-size effects”. In: *European Physical Journal B* 12.4 (1999), pp. 589–598. DOI: `10.1007/s100510051042`.

[38] "Retraction for Harland et al., Phospholipid bilayers are viscoelastic". In: *Proceedings of the National Academy of Sciences of the United States of America* 108.35 (2011), pp. 14705–14705. DOI: `10.1073/pnas.1111381108`.

[39] A. Maestro, L. J. Bonales, H. Ritacco, T. M. Fischer, R. G. Rubio, and F. Ortega. "Surface rheology: Macro- and microrheology of poly(tert-butyl acrylate) monolayers". In: *Soft Matter* 7.17 (2011), pp. 7761–7771. DOI: `10.1039/c1sm05225j`.

[40] J. R. Samaniuk and J. Vermant. "Micro and macrorheology at fluid-fluid interfaces". In: *Soft Matter* 10.36 (2014), pp. 7023–7033. DOI: `10.1039/c4sm00646a`.

[41] T. T. Hormel, S. Q. Kurihara, M. K. Brennan, M. C. Wozniak, and R. Parthasarathy. "Measuring Lipid Membrane Viscosity Using Rotational and Translational Probe Diffusion". In: *Physical Review Letters* 112.18 (2014), p. 188101. DOI: `10.1103/physrevlett.112.188101`.

[42] P. Cicuta, S. L. Keller, and S. L. Veatch. "Diffusion of Liquid Domains in Lipid Bilayer Membranes". In: *Journal of Physical Chemistry B* 111.13 (2007), pp. 3328–3331. DOI: `10.1021/jp0702088`.

[43] J. R. Henriksen and J. H. Ipsen. "Measurement of membrane elasticity by micropipette aspiration". In: *European Physical Journal E* 14.2 (2004), pp. 149–167. DOI: `10.1140/epje/i2003-10146-y`.

[44] G. Espinosa, I. López-Montero, F. Monroya, and D. Langevin. "Shear rheology of lipid monolayers and insights on membrane fluidity". In: *Proceedings of the National Academy of Sciences of the United States of America* 108.15 (2011), pp. 6008–6013. DOI: `10.1073/pnas.1018572108`.

[45] S. Q. Choi, S. Steltenkamp, J. A. Zasadzinski, and T. M. Squires. "Active microrheology and simultaneous visualization of sheared phospholipid monolayers". In: *Nature Communications* 2.1 (2011), p. 312. DOI: `10.1038/ncomms1321`.

[46] L. M. C. Sagis. "Dynamic properties of interfaces in soft matter: Experiments and theory". In: *Reviews of Modern Physics* 83.4 (2011), pp. 1367–1403. DOI: `10.1103/RevModPhys.83.1367`.

[47] G. G. Fuller and J. Vermant. "Complex Fluid-Fluid Interfaces: Rheology and Structure". In: *Annual Review of Chemical and Biomolecular Engineering* 3.1 (2012), pp. 519–543. DOI: `10.1146/annurev-chembioeng-061010-114202`.

[48] R. V. Hooghten, V. E. Blair, A. Vananroye, A. B. Schofield, J. Vermant, and J. H. J. Thijssen. "Interfacial Rheology of Sterically Stabilized Colloids at Liquid Interfaces and Its Effect on the Stability of Pickering Emulsions". In: *Langmuir* 33.17 (2017), pp. 4107–4118. DOI: `10.1021/acs.langmuir.6b04365`.

[49] G. Dockx, S. Geisel, D. G. Moore, E. Koos, A. R. Studart, and J. Vermant. "Designer liquid-liquid interfaces made from transient double emulsions". In: *Nature Communications* 9.1 (2018), p. 4763. DOI: `10.1038/s41467-018-07272-0`.

[50] P. Bertsch, M. Diener, J. Adamcik, N. Scheuble, T. Geue, R. Mezzenga, and P. Fischer. "Adsorption and Interfacial Layer Structure of Unmodified Nanocrystalline Cellulose at Air/Water Interfaces". In: *Langmuir* 34.50 (2018), pp. 15195–15202. DOI: `10.1021/acs.langmuir.8b03056`.

[51] M. Felix, A. Romero, C. Carrera-Sanchez, and A. Guerrero. "Assessment of interfacial viscoelastic properties of Faba bean (Vicia faba) protein-adsorbed O/W layers as a function of pH". In: *Food Hydrocolloids* 90 (2019), pp. 353–359. DOI: `10.1016/j.foodhyd.2018.12.036`.

[52] E. Dickinson. "Adsorbed protein layers at fluid interfaces: Interactions, structure and surface rheology". In: *Colloids and Surfaces B: Biointerfaces* 15.2 (1999), pp. 161–176. DOI: `10.1016/S0927-7765(99)00042-9`.

[53] M. Bourrel and N. Passade-Boupat. "Crude Oil Surface Active Species: Consequences for Enhanced Oil Recovery and Emulsion Stability". In: *Energy Fuels* 32.3 (2018), pp. 2642–2652. DOI: `10.1021/acs.energyfuels.7b02811`.

[54] E. Hermans, M. Saad Bhamla, P. Kao, G. G. Fuller, and J. Vermant. "Lung surfactants and different contributions to thin film stability". In: *Soft Matter* 11.41 (2015), pp. 8048–8057. DOI: `10.1039/c5sm01603g`.

[55] A. K. Sachan and J. A. Zasadzinski. "Interfacial curvature effects on the monolayer morphology and dynamics of a clinical lung surfactant". In: *Proceedings of the National Academy of Sciences of the United States of America* 115.2 (2017), E134–E143. DOI: `10.1073/pnas.1715830115`.

[56] P. G. de Gennes. "Soft matter". In: *Reviews of Modern Physics* 64.3 (1992), pp. 645–648. DOI: `10.1103/RevModPhys.64.645`.

[57] G. T. Shahin. "The stress deformation interfacial rheometer". PhD thesis. University of Pennsylvania, 1986.

[58] S. Reynaert, C. F. Brooks, P. Moldenaers, J. Vermant, and G. G. Fuller. "Analysis of the magnetic rod interfacial stress rheometer". In: *Journal of Rheology* 52.1 (2008), pp. 261–285. DOI: `10.1122/1.2798238`.

[59] P. Erni, P. Fischer, E. J. Windhab, V. Kusnezov, H. Stettin, and J. Läuger. "Stress- and strain-controlled measurements of interfacial shear viscosity and viscoelasticity at liquid/liquid and gas/liquid interfaces". In: *Review of Scientific Instruments* 74.11 (2003), pp. 4916–4924. DOI: `10.1063/1.1614433`.

[60] S. Vandebril, A. Franck, G. G. Fuller, P. Moldenaers, and J. Vermant. "A double wall-ring geometry for interfacial shear rheometry". In: *Rheologica Acta* 49.2 (2010), pp. 131–144. DOI: `10.1007/s00397-009-0407-3`.

[61] K. Kim, S. Q. Choi, J. A. Zasadzinski, and T. M. Squires. "Interfacial microrheology of DPPC monolayers at the air–water interface". In: *Soft Matter* 7.17 (2011), pp. 7782–7789. DOI: `10.1039/c1sm05383c`.

[62] K. Kim, S. Q. Choi, Z. A. Zell, T. M. Squires, and J. A. Zasadzinski. "Effect of cholesterol nanodomains on monolayer morphology and dynamics". In: *Proceedings of the National Academy of Sciences* 110.33 (2013), E3054–E3060. DOI: `10.1073/pnas.1303304110`.

[63] I. Williams and T. M. Squires. "Evolution and mechanics of mixed phospholipid fibrinogen monolayers". In: *Journal of The Royal Society Interface* 15.141 (2018), p. 20170895. DOI: `10.1098/rsif.2017.0895`.

[64] A. K. Sachan, S. Q. Choi, K. H. Kim, Q. Tang, L. Hwang, K. Y. C. Lee, T. M. Squires, and J. A. Zasadzinski. "Interfacial rheology of coexisting solid and fluid monolayers". In: *Soft Matter* 13.7 (2017), pp. 1481–1492. DOI: `10.1039/c6sm02797k`.

[65] G. T. Gavranovic, R. E. Kurtz, K. Golemanov, A. Lange, and G. G. Fuller. "Interfacial rheology and structure of straight-chain and branched hexadecanol mixtures". In: *Industrial & Engineering Chemistry Research* 45.21 (2006), pp. 6880–6884. DOI: `10.1021/ie050965x`.

[66] E. Guzmán, J. Tajuelo, J. M. Pastor, M. Á. Rubio, F. Ortega, and R. G. Rubio. "Shear rheology of fluid interfaces: Closing the gap between macro- and micro-rheology". In: *Current Opinion in Colloid & Interface Science* 37 (2018), pp. 33–48. DOI: `10.1016/j.cocis.2018.05.004`.

[67] R. H. Ewoldt, M. T. Johnston, and L. M. Caretta. “Experimental Challenges of Shear Rheology: How to Avoid Bad Data”. In: *Complex Fluids in Biological Systems: Experiment, Theory, and Computation*. Ed. by S. E. Spagnolie. New York, NY: Springer New York, 2015, pp. 207–241. ISBN: 978-1-4939-2065-5. DOI: `10.1007/978-1-4939-2065-5_6`.

[68] J. Tajuelo, J. M. Pastor, and M. A. Rubio. “A magnetic rod interfacial shear rheometer driven by a mobile magnetic trap”. In: *Journal of Rheology* 60.6 (2016), pp. 1095–1113. DOI: `10.1122/1.4958668`.

[69] J. Tajuelo, M. A. Rubio, and J. M. Pastor. “Flow field based data processing for the oscillating conical bob interfacial shear rheometer”. In: *Journal of Rheology* 62.1 (2018), pp. 295–311. DOI: `10.1122/1.5012764`.

[70] N. Jaensson and J. Vermant. “Tensiometry and rheology of complex interfaces”. In: *Current Opinion in Colloid & Interface Science* 37 (2018), pp. 136–150. DOI: `10.1016/j.cocis.2018.09.005`.

[71] M. Pepicelli, T. Verwijlen, T. A. Tervoort, and J. Vermant. “Characterization and modelling of Langmuir interfaces with finite elasticity”. In: *Soft Matter* 13.35 (2017), pp. 5977–5990. DOI: `10.1039/c7sm01100h`.

[72] L. E. Scriven. “Dynamics of a fluid interface – Equation of motion for Newtonian surface fluids”. In: *Chemical Engineering Science* 12.2 (1960), pp. 98–108. DOI: `10.1016/0009-2509(60)87003-0`.

[73] S. Fitzgibbon, E. S. G. Shaqfeh, G. G. Fuller, and T. W. Walker. “Scaling analysis and mathematical theory of the interfacial stress rheometer”. In: *Journal of Rheology* 58.4 (2014), pp. 999–1038. DOI: `10.1122/1.4876955`.

[74] D. A. Edwards, H. Brenner, and D. T. Wasan. *Interfacial Rheology and Its Applications*. Butterworth-Heinemann series in chemical engineering. Butterworth-Heinemann, 1991, pp. 1–19. ISBN: 9780750691857. DOI: `10.1016/b978-0-7506-9185-7.50005-2`.

[75] J. Plateau. “ LIV. Experimental and theoretical researches into the figures of equilibrium of a liquid mass without weight .—Eighth series ”. In: *The London, Edinburgh, and Dublin Philosophical Magazine and Journal of Science* 38.257 (1869), pp. 445–455. DOI: `10.1080/14786446908640254`.

[76] C. Marangoni. “Ueber die Ausbreitung der Tropfen einer Flüssigkeit auf der Oberfläche einer anderen”. In: *Annalen der Physik* 219.7 (1871), pp. 337–354. DOI: `10.1002/andp.18712190702`.

[77] C. F. Brooks, G. G. Fuller, C. W. Frank, and C. R. Robertson. “An Interfacial Stress Rheometer To Study Rheological Transitions in Monolayers at the Air-Water Interface”. In: *Langmuir* 15.7 (1999), pp. 2450–2459. DOI: `10.1021/la980465r`.

[78] P. Gijsenbergh, M. Pepicelli, C. L. Wirth, J. Vermant, and R. Puers. “Langmuir monolayer characterization via polymer microtensiometers”. In: *Sensors and Actuators A: Physical* 229 (2015), pp. 110–117. DOI: `10.1016/j.sna.2015.03.041`.

[79] J. Tajuelo, J. M. Pastor, F. Martínez-Pedrero, M. Vázquez, F. Ortega, R. G. Rubio, and M. A. Rubio. “Magnetic microwire probes for the magnetic rod interfacial stress rheometer”. In: *Langmuir* 31.4 (2015), pp. 1410–1420. DOI: `10.1021/la5038316`.

[80] T. Verwijlen, P. Moldenaers, H. A. Stone, and J. Vermant. “Study of the Flow Field in the Magnetic Rod Interfacial Stress Rheometer”. In: *Langmuir* 27.15 (2011), pp. 9345–9358. DOI: `10.1021/la201109u`.

[81] J. Läuger, K. Wollny, and S. Huck. “Direct Strain Oscillation: A new oscillatory method enabling measurements at very small shear stresses and strains”. In: *Rheologica Acta* 41.4 (2002), pp. 356–361. DOI: `10.1007/s00397-002-0231-5`.

[82] O. H. Soo-Gun and J. C. Slattery. “Disk and biconical interfacial viscometers”. In: *Journal of Colloid and Interface Science* 67.3 (1978), pp. 516–525. DOI: `10.1016/0021-9797(78)90242-4`.

[83] H. H. Ku. “Notes on the use of propagation of error formulas”. In: *JOURNAL OF RESEARCH of the National Bureau of Standards - C. Engineering and Instrumentation* 70C.4 (1966). Ed. by N. B. of Standards, p. 263. DOI: `10.6028/jres.070c.025`.

[84] P. R. Bevington and D. K. Robinson. *Data reduction and error analysis for the physical sciences*. 3rd. Boston: McGraw-Hill, 2002. ISBN: 0-07-247227-8.

[85] P. K. Singh, J. M. Soulages, and R. H. Ewoldt. “On fitting data for parameter estimates: residual weighting and data representation”. In: *Rheologica Acta* 58.6 (2019), pp. 341–359. DOI: `10.1007/s00397-019-01135-1`.

[86] T. Verwijlen, P. Moldenaers, and J. Vermant. “A fixture for interfacial dilatational rheometry using a rotational rheometer”. In: *The European Physical Journal Special Topics* 222.1 (2013), pp. 83–97. DOI: `10.1140/epjst/e2013-01828-9`.

[87] M. T. Johnston and R. H. Ewoldt. “Precision rheometry: Surface tension effects on low-torque measurements in rotational rheometers”. In: *Journal of Rheology* 57.6 (2013), pp. 1515–1532. DOI: `10.1122/1.4819914`.

[88] J. A. Clements, R. F. Hustead, R. P. Johnson, and I. Gribetz. “Pulmonary surface tension and alveolar stability”. In: *Journal of Applied Physiology* 16.3 (1961), pp. 444–450. DOI: `10.1152/jappl.1961.16.3.444`.

[89] D. L. Leiske, S. R. Raju, H. A. Ketelson, T. J. Millar, and G. G. Fuller. “The interfacial viscoelastic properties and structures of human and animal Meibomian lipids”. In: *Experimental Eye Research* 90.5 (2010), pp. 598–604. DOI: `10.1016/j.exer.2010.02.004`.

[90] V. M. Kaganer, H. Möhwald, and P. Dutta. “Structure and phase transitions in Langmuir monolayers”. In: *Reviews of Modern Physics* 71.3 (1999), pp. 779–819. DOI: `10.1103/revmodphys.71.779`.

[91] S. W. Hui, D. F. Parsons, and M. Cowden. “Electron Diffraction of Wet Phospholipid Bilayers”. In: *Proceedings of the National Academy of Sciences of the United States of America* 71.12 (1974), pp. 5068–5072. DOI: `10.1073/pnas.71.12.5068`.

[92] C. A. Helm, H. Möhwald, K. Kjær, and J. Als-Nielsen. “Phospholipid Monolayer Density Distribution Perpendicular to the Water Surface. A Synchrotron X-Ray Reflectivity Study”. In: *Europhysics Letters (EPL)* 4.6 (1987), pp. 697–703. DOI: `10.1209/0295-5075/4/6/010`.

[93] V. T. Moy, D. J. Keller, and H. M. McConnell. “Molecular order in finite two-dimensional crystals of lipid at the air-water interface”. In: *The Journal of Physical Chemistry* 92.18 (1988), pp. 5233–5238. DOI: `10.1021/j100329a033`.

[94] H. E. Gaub, V. T. Moy, and H. M. McConnell. “Reversible formation of plastic two-dimensional lipid crystals”. In: *The Journal of Physical Chemistry* 90.8 (1986), pp. 1721–1725. DOI: `10.1021/j100399a051`.

[95] C. W. McConlogue and T. K. Vanderlick. “A Close Look at Domain Formation in DPPC Monolayers”. In: *Langmuir* 13.26 (1997), pp. 7158–7164. DOI: `10.1021/la970898e`.

[96] H. M. McConnell. “Structures and Transitions in Lipid Monolayers at the Air-Water Interface”. In: *Annual Review of Physical Chemistry* 42.1 (1991), pp. 171–195. DOI: `10.1146/annurev.pc.42.100191.001131`.

[97] H. M. McConnell and R. D. Koker. “Equilibrium Thermodynamics of Lipid Monolayer Domains”. In: *Langmuir* 12.20 (1996), pp. 4897–4904. DOI: `10.1021/la960411m`.

[98] J. M. Barakat and T. M. Squires. “Shape morphology of dipolar domains in planar and spherical monolayers”. In: *Journal of Chemical Physics* 152.23 (2020), p. 234701. DOI: `10.1063/5.0009667`.

[99] J. Ding, H. E. Warriner, and J. A. Zasadzinski. “Viscosity of Two-Dimensional Suspensions”. In: *Physical Review Letters* 88.16 (2002), p. 168102. DOI: `10.1103/physrevlett.88.168102`.

[100] A. Goebel and K. Lunkenheimer. “Interfacial Tension of the Water/n-Alkane Interface”. In: *Langmuir* 13.2 (1997), pp. 369–372. DOI: `10.1021/la960800g`.

[101] S. L. Duncan and R. G. Larson. “Comparing Experimental and Simulated Pressure-Area Isotherms for DPPC”. In: *Biophysical Journal* 94.8 (2008), pp. 2965–2986. DOI: `10.1529/biophysj.107.114215`.

[102] K. Danov, R. Aust, F. Durst, and U. Lange. “Influence of the Surface Viscosity on the Hydrodynamic Resistance and Surface Diffusivity of a Large Brownian Particle”. In: *Journal of Colloid and Interface Science* 175.1 (1995), pp. 36–45. DOI: `10.1006/jcis.1995.1426`.

[103] T. M. Fischer, P. Dhar, and P. Heinig. “The viscous drag of spheres and filaments moving in membranes or monolayers”. In: *Journal of Fluid Mechanics* 558 (2006), pp. 451–475. DOI: `10.1017/s002211200600022x`.

[104] P. G. Saffman and M. Delbrück. “Brownian motion in biological membranes.” In: *Proceedings of the National Academy of Sciences of the United States of America* 72.8 (1975), pp. 3111–3113. DOI: `10.1073/pnas.72.8.3111`.

[105] P. G. Saffman. “Brownian motion in thin sheets of viscous fluid”. In: *Journal of Fluid Mechanics* 73.4 (1976), pp. 593–602. DOI: `10.1017/s0022112076001511`.

[106] M. Javanainen, H. Martinez-Seara, R. Metzler, and I. Vattulainen. “Diffusion of Integral Membrane Proteins in Protein-Rich Membranes”. In: *The Journal of Physical Chemistry Letters* 8.17 (2017), pp. 4308–4313. DOI: `10.1021/acs.jpclett.7b01758`.

[107] M. Javanainen, O. H. S. Ollila, and H. Martinez-Seara. “Rotational Diffusion of Membrane Proteins in Crowded Membranes”. In: *The Journal of Physical Chemistry B* 124.15 (2020), pp. 2994–3001. DOI: `10.1021/acs.jpcb.0c00884`.

[108] S. Block. “Brownian Motion at Lipid Membranes: A Comparison of Hydrodynamic Models Describing and Experiments Quantifying Diffusion within Lipid Bilayers”. In: *Biomolecules* 8.2 (2018), p. 30. DOI: `10.3390/biom8020030`.

[109] H. A. Faizi, R. Dimova, and P. M. Vlahovska. “A vesicle microrheometer for high-throughput viscosity measurements of lipid and polymer membranes”. In: *Biophysical Journal* 121.6 (2022), pp. 910–918. DOI: `10.1016/j.bpj.2022.02.015`.

[110] D. Renggli, A. Alicke, R. H. Ewoldt, and J. Vermant. “Operating windows for oscillatory interfacial shear rheology”. In: *Journal of Rheology* 64.1 (2020), pp. 141–160. DOI: `10.1122/1.5130620`.

[111] R. A. Demel, W. S. M. G. van Kessel, R. F. A. Zwaal, B. Roelofsen, and L. L. M. van Deenen. “Relation between various phospholipase actions on human red cell membranes and the interfacial phospholipid pressure in monolayers”. In: *Biochimica et Biophysica Acta (BBA) - Biomembranes* 406.1 (1975), pp. 97–107. DOI: `10.1016/0005-2736(75)90045-0`.

[112] E. B. Watkins, C. E. Miller, W.-P. Liao, and T. L. Kuhl. “Equilibrium or Quenched: Fundamental Differences between Lipid Monolayers, Supported Bilayers, and Membranes”. In: *ACS Nano* 8.4 (2014), pp. 3181–3191. DOI: `10.1021/nn4052953`.

[113] J. F. Brady. “The Einstein viscosity correction in n dimensions”. In: *International Journal of Multiphase Flow* 10.1 (1983), pp. 113–114. DOI: `10.1016/0301-9322(83)90064-2`.

[114] M. Mooney. “The viscosity of a concentrated suspension of spherical particles”. In: *Journal of Colloid Science* 6.2 (1951), pp. 162–170. DOI: `10.1016/0095-8522(51)90036-0`.

[115] S. Reynaert, P. Moldenaers, and J. Vermant. “Interfacial rheology of stable and weakly aggregated two-dimensional suspensions”. In: *Physical Chemistry Chemical Physics* 9.48 (2007), p. 6463. DOI: `10.1039/b710825g`.

[116] J. Daillant, L. Bosio, and J. J. Benattar. “X-Ray Reflectivity Study of the Liquid-Expanded Liquid-Condensed Phase Transition”. In: *Europhysics Letters (EPL)* 12.8 (1990), pp. 715–720. DOI: `10.1209/0295-5075/12/8/008`.

[117] P. J. Beltramo, L. Scheidegger, and J. Vermant. “Toward Realistic Large-Area Cell Membrane Mimics: Excluding Oil, Controlling Composition, and Including Ion Channels”. In: *Langmuir* 34.20 (2018), pp. 5880–5888. DOI: `10.1021/acs.langmuir.8b00837`.

[118] L. G. C. Pereira, C. Johansson, H. W. Blanch, and C. J. Radke. “A bike-wheel microcell for measurement of thin-film forces”. In: *Colloids and Surfaces A: Physicochemical and Engineering Aspects* 186.1-2 (2001), pp. 103–111. DOI: `10.1016/s0927-7757(01)00488-5`.

[119] E. Chatzigiannakis and J. Vermant. “Breakup of Thin Liquid Films: From Stochastic to Deterministic”. In: *Physical Review Letters* 125.15 (2020), p. 158001. DOI: `10.1103/physrevlett.125.158001`.

[120] R. C. Gonzalez and R. E. Woods. *Digital Image Processing*. 4th. Pearson, 2017. ISBN: 978-0-13-335672-4.

[121] K. Zuiderveld. “Contrast limited adaptive histogram equalization”. In: *Graphics gems* (1994), pp. 474–485.

[122] J. Brocher. *biovoxxel/BioVoxxel-Toolbox: BioVoxxel Toolbox (v2.5.3)*. 2022. DOI: `10.5281/ZENODO.5986130`.

[123] D. Ershov, M.-S. Phan, J. W. Pylvänäinen, S. U. Rigaud, L. L. Blanc, A. Charles-Orszag, J. R. W. Conway, R. F. Laine, N. H. Roy, D. Bonazzi, G. Duménil, G. Jacquemet, and J.-Y. Tinevez. “Bringing TrackMate into the era of machine-learning and deep-learning”. In: *bioRχiv* (2021). DOI: `10.1101/2021.09.03.458852`.

[124] R. Haase, L. A. Royer, P. Steinbach, D. Schmidt, A. Dibrov, U. Schmidt, M. Weigert, N. Maghelli, P. Tomancak, F. Jug, and E. W. Myers. “CLIJ: GPU-accelerated image processing for everyone”. In: *Nature Methods* 17.1 (2020), pp. 5–6. DOI: `10.1038/s41592-019-0650-1`.

[125] K. Jaqaman, D. Loerke, M. Mettlen, H. Kuwata, S. Grinstein, S. L. Schmid, and G. Danuser. “Robust single-particle tracking in live-cell time-lapse sequences”. In: *Nature Methods* 5.8 (2008), pp. 695–702. DOI: `10.1038/nmeth.1237`.

[126] N. Tarantino, J.-Y. Tinevez, E. F. Crowell, B. Boisson, R. Henriques, M. Mhlanga, F. Agou, A. Israël, and E. Laplantine. “TNF and IL-1 exhibit distinct ubiquitin requirements for inducing NEMO–IKK supramolecular structures”. In: *Journal of Cell Biology* 204.2 (2014), pp. 231–245. DOI: `10.1083/jcb.201307172`.

[127] J. C. Crocker, M. T. Valentine, E. R. Weeks, T. Gisler, P. D. Kaplan, A. G. Yodh, and D. A. Weitz. “Two-Point Microrheology of Inhomogeneous Soft Materials”. In: *Physical Review Letters* 85.4 (2000), pp. 888–891. DOI: `10.1103/physrevlett.85.888`.

A Supplemental Information: Operating Windows

A.1 Subphase correction algorithm

In order to decouple the interfacial from the bulk flow contribution, the following algorithm is performed on the measured data.

An appropriate initial value for the complex Boussinesq number Bq^* is assumed which is used to calculate the flow field in the bulk and at the interface. From the flow field, the subphase and interfacial contributions to the complex amplitude ratio are calculated. The Boussinesq number is refined by comparing the calculated with the experimentally measured amplitude ratios. The algorithm is iterated until convergence of Bq^* is reached.

ISR

The iterative algorithm is published in [80] and sketched as

$$\left(\frac{F_0}{z_0}e^{-i\delta}\right)_{\text{calc}} = \underbrace{(i2l\omega\eta_b)Bq^*\left(-\frac{\partial g^*}{\partial p}\right)\Bigg|_{p=0,\theta=\pi/2}}_{\text{interfacial contribution}} + \underbrace{i2l\omega\eta_b\int_0^{\pi/2}\left(-\frac{\partial g^*}{\partial p}\right)\Bigg|_{p=0} d\theta}_{\text{bulk contribution}} + k - m\omega^2$$

$$Bq^*_{[n+1]} = \frac{\left(\frac{F_0}{z_0}e^{-i\delta}\right)_{\text{exp}}}{\left(\frac{F_0}{z_0}e^{-i\delta}\right)_{\text{calc}}}_{[n]} Bq^*_{[n]}$$

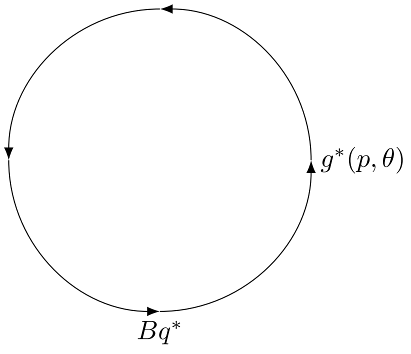

(A.1)

where the same coordinate system as in [80] is used ($p = \ln\lambda = \ln(R/r)$.

DWR

The iterative algorithm is published in [60] and sketched as

$$M_{\text{calc}} = \underbrace{2\pi\eta_s^* \left[\left(R_{\text{ring}}^{\text{inner}}\right)^3 \frac{\partial}{\partial r}\left(\frac{v_s^*}{r}\right)\bigg|_{r=R_{\text{ring}}^{\text{inner}}} - \left(R_{\text{ring}}^{\text{outer}}\right)^3 \frac{\partial}{\partial r}\left(\frac{v_s^*}{r}\right)\bigg|_{r=R_{\text{ring}}^{\text{outer}}} \right]}_{\text{interfacial contribution}}$$

$$- \underbrace{2\pi\eta_b \left[\int_{R_{\text{ring}}^{\text{inner}}}^{R_r} \frac{\partial v_b^*}{\partial p_1} r^2 dr + \int_{R_r}^{R_{\text{ring}}^{\text{outer}}} \frac{\partial v_b^*}{\partial p_2} r^2 dr \right]}_{\text{bulk contribution}}$$

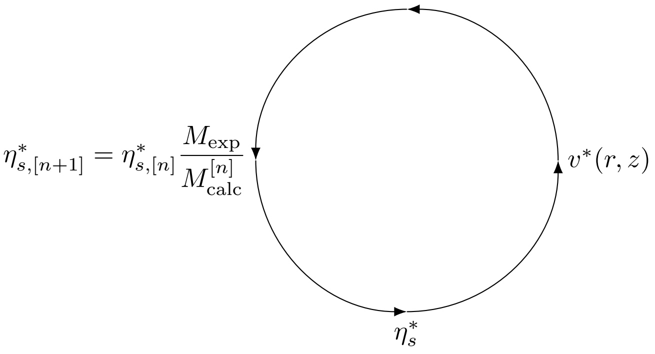
$\eta^*_{s,[n+1]} = \eta^*_{s,[n]} \dfrac{M_{\text{exp}}}{M^{[n]}_{\text{calc}}}$
$v^*(r,z)$
η_s^*

(A.2)

where R_r is the middle radius of the ring, v_s is the interfacial velocity, v_b is the bulk velocity and p_1 and p_2 are the directions perpendicular to the ring surface and pointing into the bulk phase.

A.2 ISR calibration example

In order to measure the instrument compliance k^{-1} and the constant E relating the force to displacement ratio in terms of ampere-per-pixel with newton-per-meter

$$E\left(\frac{F_0}{z_0}e^{-i\delta}\right)_{\mathrm{N/m}} = \left(\frac{F_0}{z_0}e^{-i\delta}\right)_{\mathrm{A/pixel}} \quad , \tag{A.3}$$

the ISR has to be calibrated.

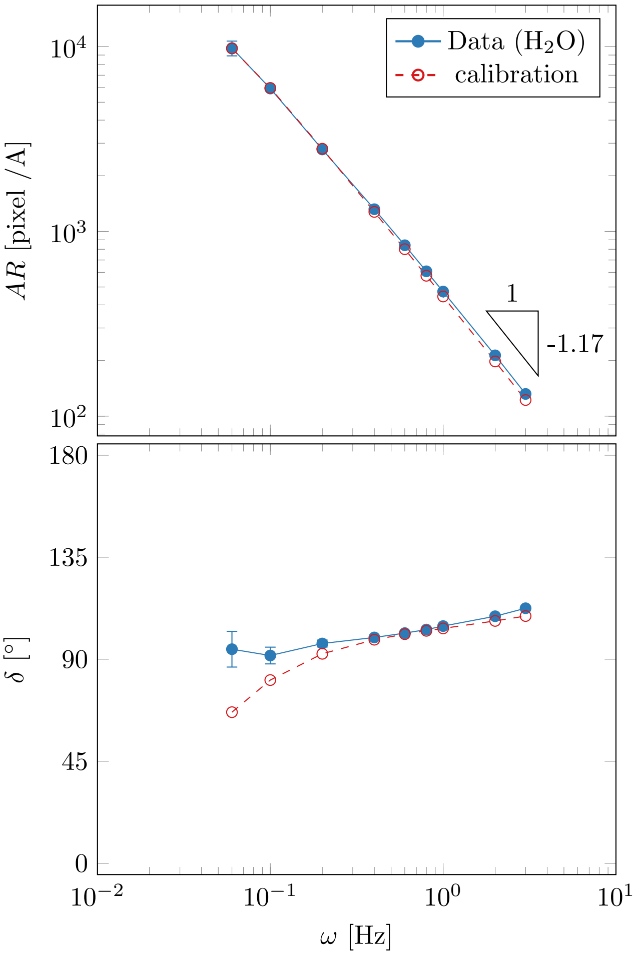

Figure A.1: **Calibration ISR:** Amplitude ratio and phase angle of the microwire measured on a clean water-air interface. The fit is shown as dashed line with open symbols. Error bars show the standard deviation of three measurements.

The magnetic probe is placed on a clean water-air interface and the resulting amplitude ratio AR in pixel-per-ampere and phase angle δ are plotted in Fig. S A.1. There are no clear inertia (slope -2) and compliance (slope 0) dominated regimes recognizable but an almost constant slope of −1.17.

Fig. S A.2 compares the different contributions to the *AR*. Because of the good alignment close to perfect Helmholtz configuration and the small mass of the microwire, the subphase drag is dominating compliance (open red symbols are bigger than open black symbols) and instrument inertia (closed blue symbols are bigger than closed black symbols) over the whole frequency range. This is the reason for the absence of a compliance and inertia dominated regime in Fig. S A.1.

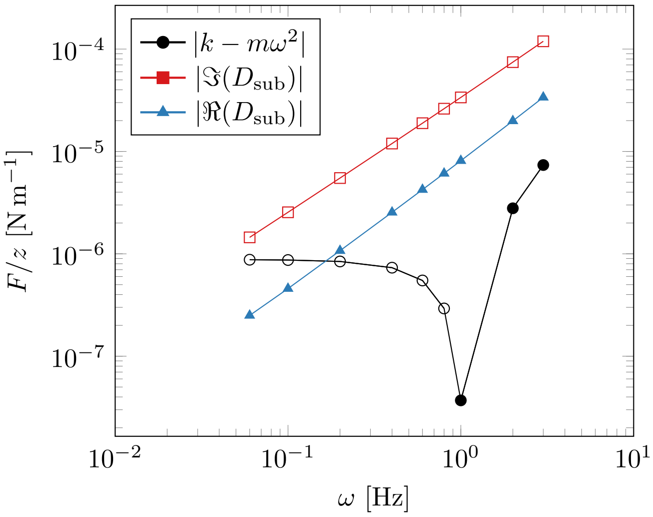

Figure A.2: **Calibration ISR:** The contributions to the amplitude ratio of the clean water-air interface: real and imaginary parts of the subphase drag, compliance and needle inertia. Open symbols denote positive sign before plotting the absolute values $|\ldots|$.

As a consequence, it is necessary to calculate the subphase drag and follow the calibration procedure proposed by Tajuelo et al. [79] instead of fitting a second order harmonic model as described by Brooks et al. [77]. The subphase correction is performed assuming that the complex Boussinesq number Bq^* is 0 for a clean water-air interface. With the resulting flow field in the bulk fluid, the bulk drag can be calculated and the remaining fitting parameters are the instrument compliance k^{-1} and the constant E.

The maximum residue

$$S(E,k) = \max \left| \frac{1}{E\left(\frac{F_0}{z_0}e^{-i\delta}\right)_{\mathrm{N/m}}} - \frac{1}{\left(\frac{F_0}{z_0}e^{-i\delta}\right)_{\mathrm{A/pixel}}} \right| , \tag{A.4}$$

where $\left(\frac{F_0}{z_0}e^{-i\delta}\right)_{\mathrm{N/m}} = \left(\frac{F_0}{z_0}e^{-i\delta}\right)_{\mathrm{calc}}$ of Eq. (A.1), is shown for a set of E and k in Fig. S A.3

where the minimum is marked with the red dot. The resulting fit is shown as open symbols in Fig. S A.1 and reproduces the behavior of the measured data.

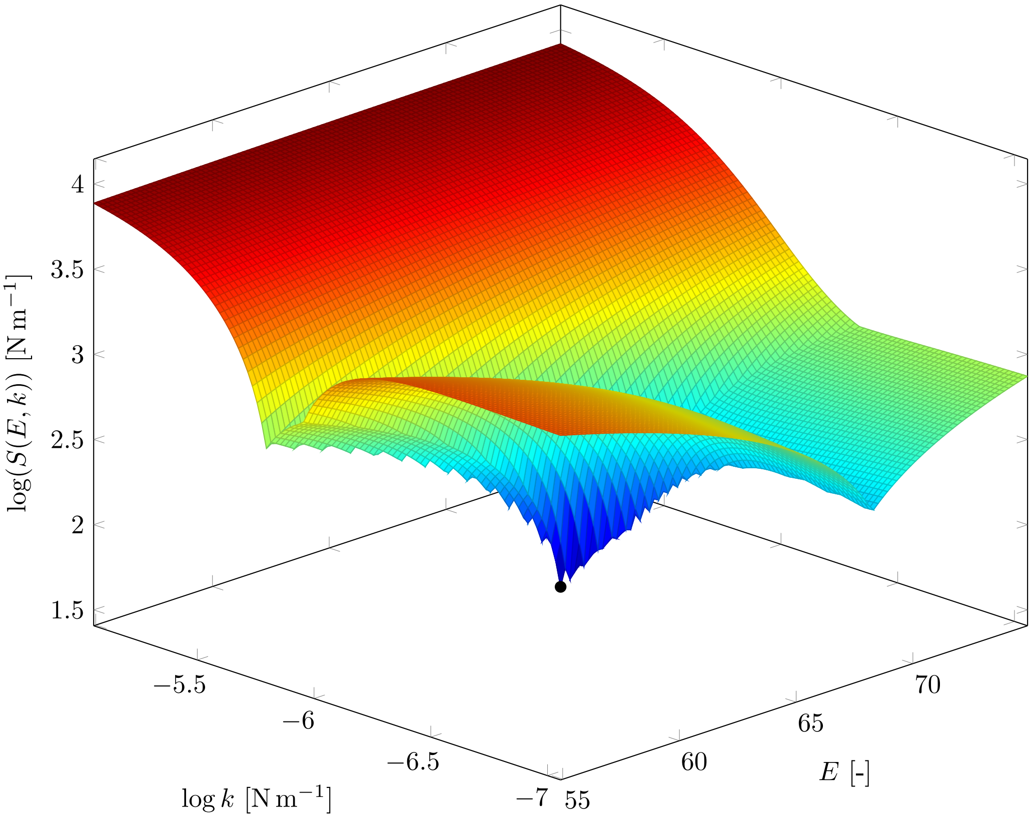

Figure A.3: **Calibration ISR:** Maximum residue S plotted as function of instrument compliance k^{-1} and constant E. The minimum is labeled with the black dot.

The force constant C_{I-F} relating the applied current I with the force F acting on the magnetic probe can be calculated from the constant E and meter-per-pixel ratio p as

$$C_{I-F} = \frac{p}{E} \quad . \tag{A.5}$$

Table A.1: **Calibration constants for the ISR probes:** k^{-1} is the instrument compliance, E transforms A/pixel to N/m and C_{I-F} is the force constant. k and E result from the calibration.

	k [N m^{-1}]	E [pA N^{-1}]^1	C_{I-F} [N A^{-1}]
Needle	2.9×10^{-5}	0.30	4.62×10^{-6}
Microwire	8.8×10^{-7}	64.91	2.16×10^{-8}

A.3 ISR bad data Fourier spectrum example

An example of a data set where the driving current amplitude is very small is shown in Fig. S A.4. The drift in $I(t)$ is clearly visible. Moreover, the position is completely drift dominated and the signal-to-noise ratio is around 1. The data in the frequency domain is fitted up to the vertical dashed line.

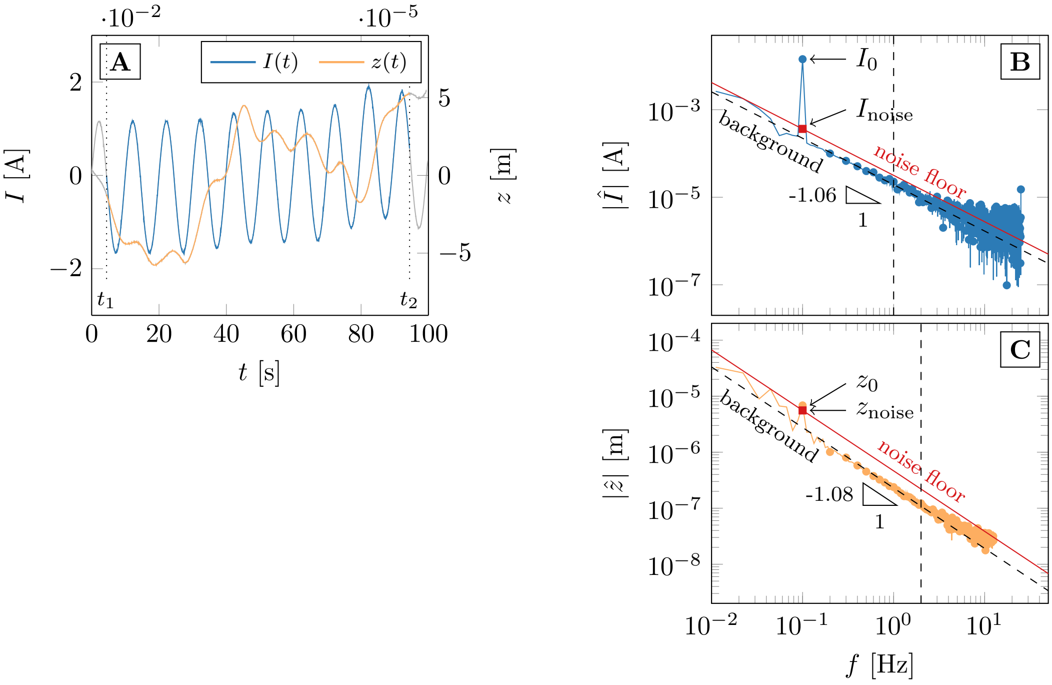

Figure A.4: **Drift dominated data set of an ISR experiment:** Primary observables **A:** Current $I(t)$ and displacement $z(t)$ in the time domain. **B:** Current signal in the frequency domain $|\hat{I}(f)|$ indicating I_0 and I_{noise}. **C:** Displacement signal in the frequency domain $|\hat{z}(f)|$ indicating z_0 and z_{noise}. Dots represent the integer harmonics of the fundamental.

A.4 Noise for DWR ring sizes and driving frequency

Fig. A.5 shows amplitude sweeps of clean water-air interfaces in order to compare the different ring sizes. Different minimal torque M_{min} and minimal displacement θ_{min} are defined for the different sizes of the ring whereas the 3d-printed ring behaves similar to the ring from TA with the same dimensions. In general, the closed loop stress controlled mode leads to slightly smaller limits compared to the strain controlled mode. There is no data shown for the open loop stress controlled mode since the drift in $\theta(t)$ is very big for clean water-air interfaces.

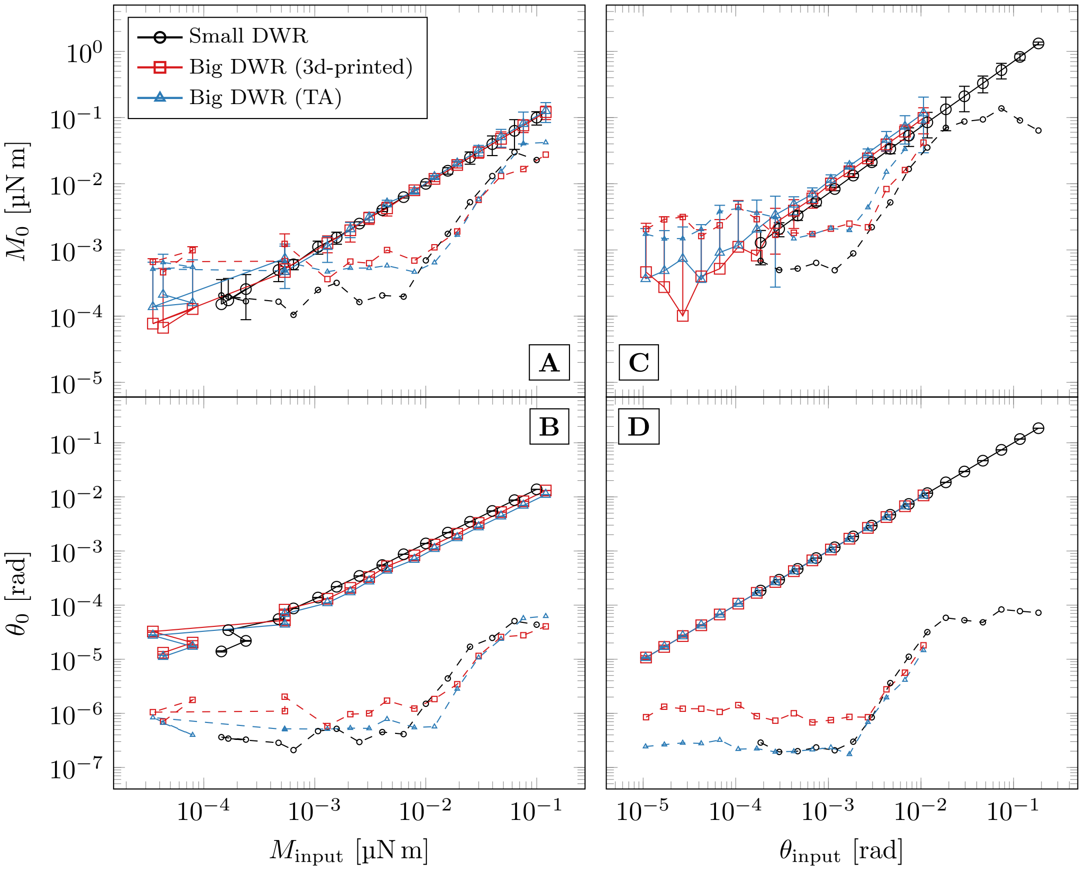

Figure A.5: **Noise of different DWR diameters:** Data measured at the clean water-air interface at $f = 0.1\,\mathrm{Hz}$. **A:** Torque amplitudes M_0 and **B:** displacement amplitudes θ_0 as a function of input torque for closed loop stress controlled experiments. **C:** Torque amplitudes M_0 and **D:** displacement amplitudes θ_0 as a function of input displacement for strain controlled experiments. Small symbols and error bars correspond to noise values.

The operating window is affected by the driving frequency as shown in Fig. S A.6. In the closed loop experiments, the maximum torque $M_{\max}$ is strongly decreased for smaller frequencies. As a consequence, it is not straightforward to use a measured noise limit at a single frequency for a frequency sweep. In the open loop case, the S/N ratio decreases for smaller frequencies but remains constant over the torque input range.

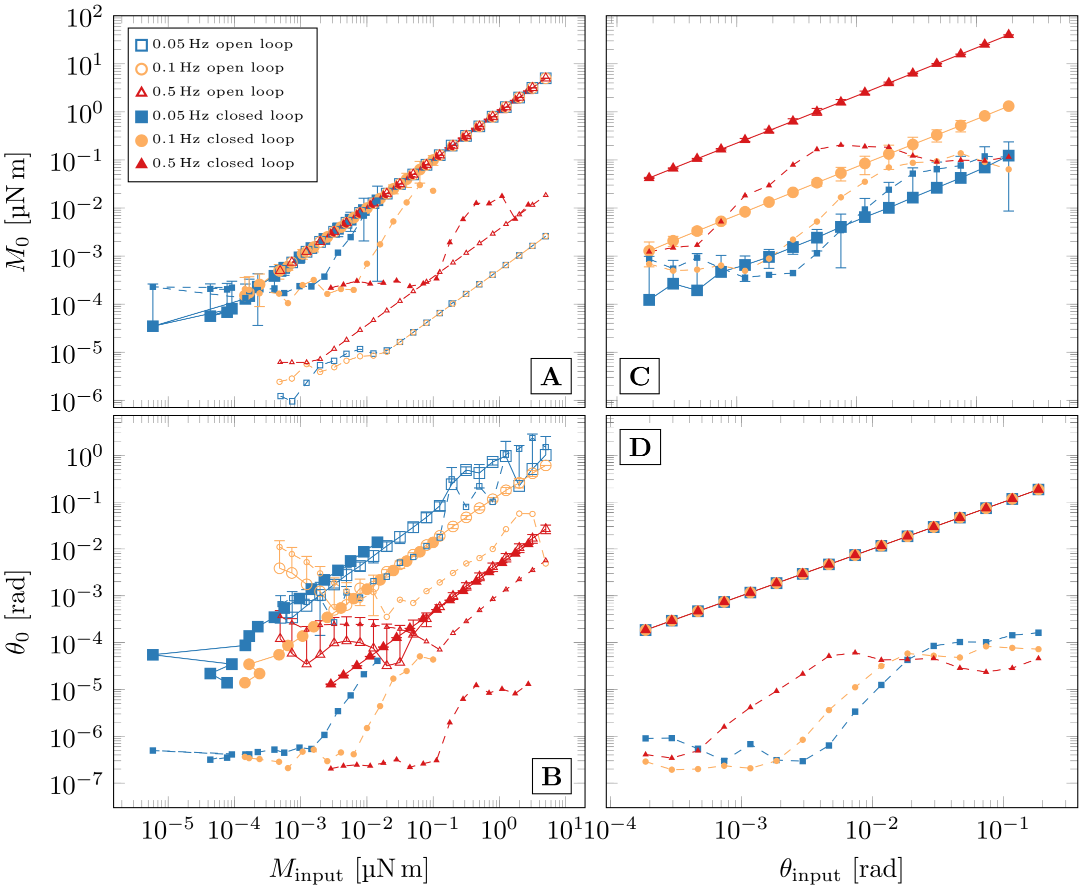

Figure A.6: **Effect of driving frequency on noise of the small DWR:** Data measured at the clean water-air interface. **A:** Torque amplitudes M_0 and **B:** displacement amplitudes θ_0 as a function of input torque for stress controlled experiments. **C:** Torque amplitudes M_0 and **D:** displacement amplitudes θ_0 as a function of input displacement for strain controlled experiments. Small symbols and error bars correspond to noise values. Open and closed symbols denote open and closed loop, respectively.

A.5 Bi-cone Fourier spectrum example and noise

Two typical data sets of the bi-cone (Anton Paar) measured with the strain and stress amplitude control mode are shown in Fig. S A.7 and S A.8. The software allowed to save only the last oscillation cycle of the time dependent primary variables (6 oscillation periods in total). The resulting amplitude and noise values are shown in Fig. S A.9.

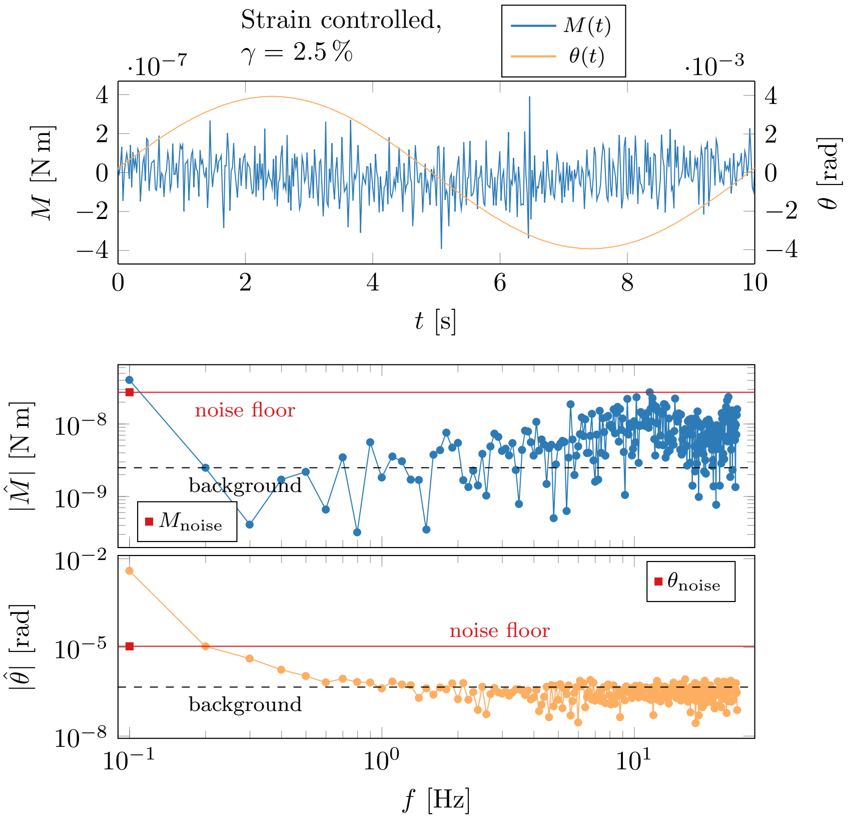

Figure A.7: **Strain amplitude controlled mode of the bi-cone (Anton Paar):** hexadecanol at $\pi = 45\,\mathrm{mN\,m^{-1}}$ and $f = 0.1\,\mathrm{Hz}$. *Top:* $M(t)$ and $\theta(t)$ *Middle:* Fourier transform of $M(t)$. *Bottom:* Fourier transform of $\theta(t)$. Only the last oscillation period is analyzed.

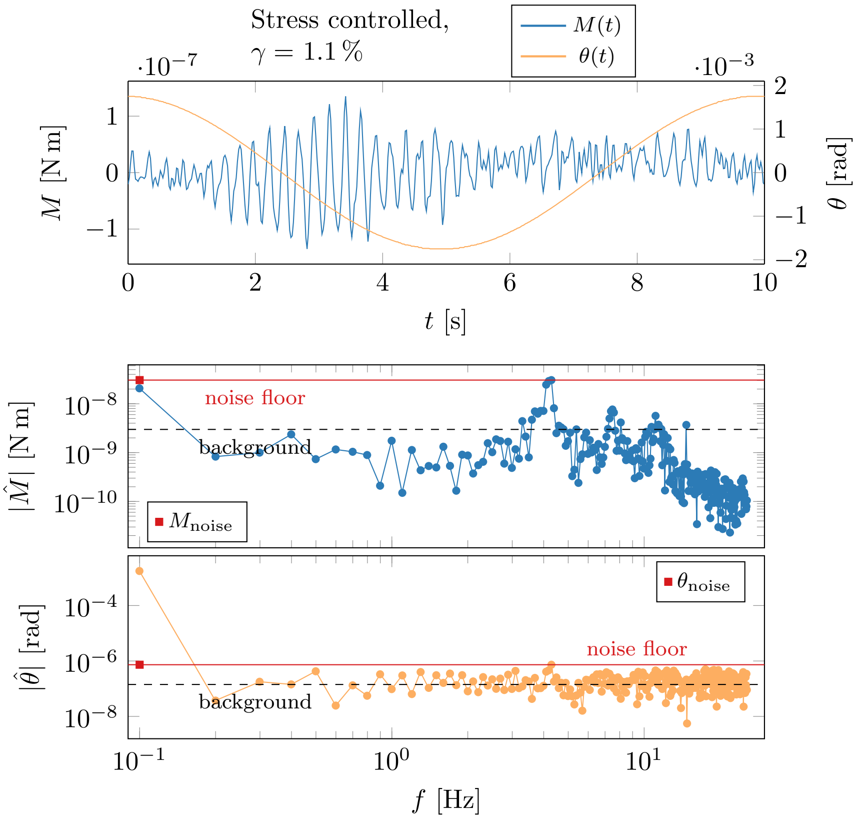

Figure A.8: **Stress amplitude controlled mode of the bi-cone (Anton Paar):** hexadecanol at $\pi = 45\,\mathrm{mN\,m^{-1}}$ and $f = 0.1\,\mathrm{Hz}$. *Top:* $M(t)$ and $\theta(t)$ *Middle:* Fourier transform of $M(t)$. *Bottom:* Fourier transform of $\theta(t)$. Only the last oscillation period is analyzed.

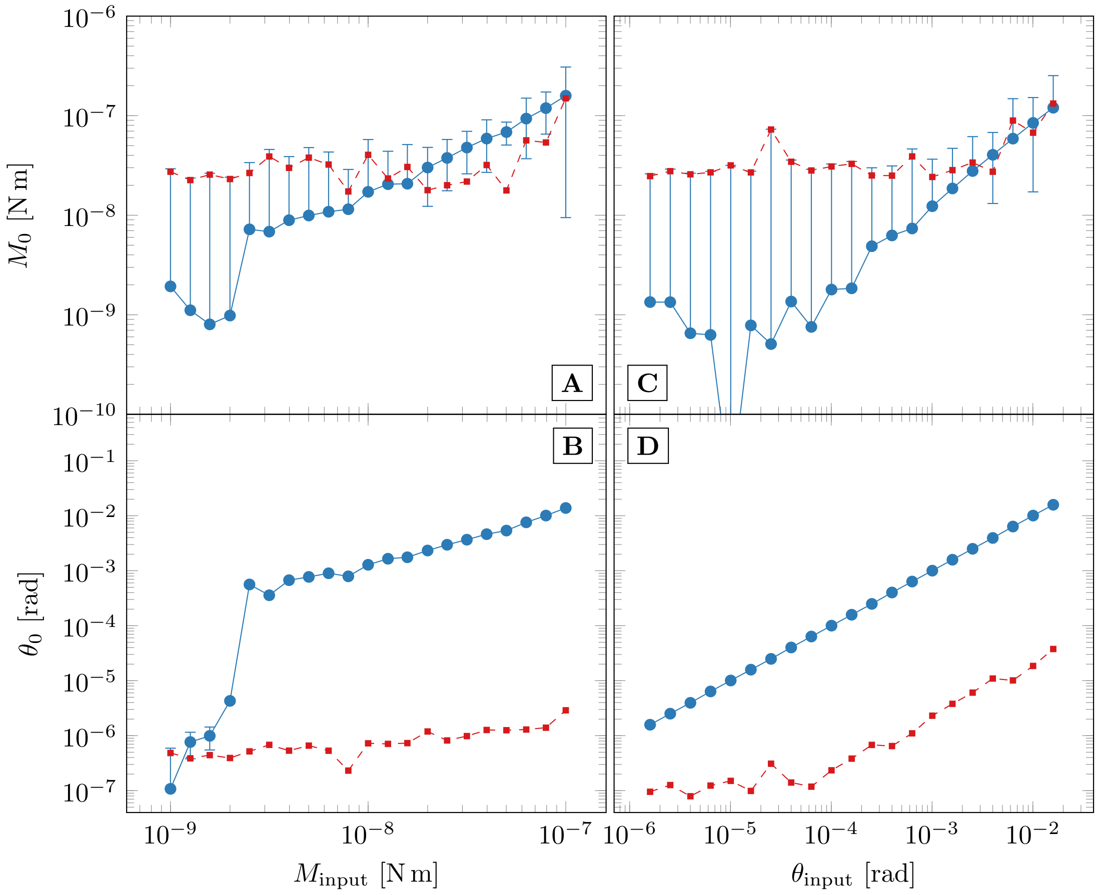

Figure A.9: **Amplitude and noise for the bi-cone (Anton Paar) in stress and strain controlled mode:** data for hexadecanol at the water-air interface at $\pi = 55\,\mathrm{mN\,m^{-1}}$ and $f = 0.1\,\mathrm{Hz}$. **A:** Torque amplitudes M_0 and **B:** displacement amplitudes θ_0 as a function of input torque for stress controlled experiments. **C:** Torque amplitudes M_0 and **D:** displacement amplitudes θ_0 as a function of input displacement for strain controlled experiments. Small red symbols and error bars correspond to noise values.

A.6 Conversion factors

ISR

The conversion from displacement z [m] to interfacial strain γ_s [-] depends on the channel radius R and the needle radius a

$$C_z = \frac{1}{R-a} \quad . \tag{A.6}$$

The conversion from current [A] to interfacial stress [Pa m] or [N m^{-1}] is dependent not only on the geometry but also on the magnetic properties of the needle. The applied current I leads to a gradient in the magnetic field B which again results in a force F acting on the magnetic probe. Since $F \propto \nabla B$ and $\nabla B \propto I$ also $F \propto I$ and the proportionality constant is contained in the constant E which results from the fit in the calibration process of the ISR. As a result, the stress constant can be written as

$$C_I = p\frac{1}{2LE} = \frac{C_{I-F}}{2L} \quad , \tag{A.7}$$

where p is the pixel-to-micro-meter ratio, L is the length of the magnetic probe and C_{I-F} is the force constant calculated from E.

DWR

The conversion from displacement θ [rad] to interfacial strain [-] is a geometric factor and depends on the inner ($R_{\text{inner ring}}$) and outer ($R_{\text{outer ring}}$) radii of the ring as well as the inner ($R_{\text{inner ring}}$) and outer ($R_{\text{inner cup}}$) radii of the cup

$$C_{\theta,\mathrm{DWR}} = \frac{1}{1-\frac{R^2_{\text{outer ring}}}{R^2_{\text{outer cup}}}} + \frac{1}{\frac{R^2_{\text{inner ring}}}{R^2_{\text{inner cup}}}-1} \quad . \tag{A.8}$$

The conversion from torque to interfacial stress [Pa m] is dependent on the the inner ($R_{\text{inner ring}}$) and outer ($R_{\text{outer ring}}$) radii of the ring

$$C_{M,\mathrm{DWR}} = \frac{1}{2\pi\left(R^2_{\text{inner ring}} + R^2_{\text{outer ring}}\right)} \quad . \tag{A.9}$$

Bi-cone

The conversion from displacement θ [rad] to interfacial strain [-] is a geometric factor and depends on the radius of the bi-cone R_b and cup R_c

$$C_{\theta,\text{bi-cone}} = \frac{R_c^2 + R_b^2}{R_c^2 - R_b^2} \quad . \tag{A.10}$$

The conversion from torque to interfacial stress [Pa m] is dependent on the radius of the bi-cone R_b

$$C_{M,\text{bi-cone}} = \frac{1}{2\pi R_b^2} \quad . \tag{A.11}$$

Table A.2: Numerical values of the conversion factors for the ISR, DWR and bi-cone.

	C_z [m^{-1}]	C_I [Pa m A^{-1}]	C_θ [rad^{-1}]	C_M [m^{-2}]
Microwire	167.15	1.39×10^{-6}		
Needle	172.41	9.84×10^{-5}		
Small ring			5.388	259.633
Big ring			9.393	64.948
bi-cone (TA)			6.201	118.575
bi-cone (Anton Paar)			6.280	137.152

A.7 Torque controlled frequency sweep

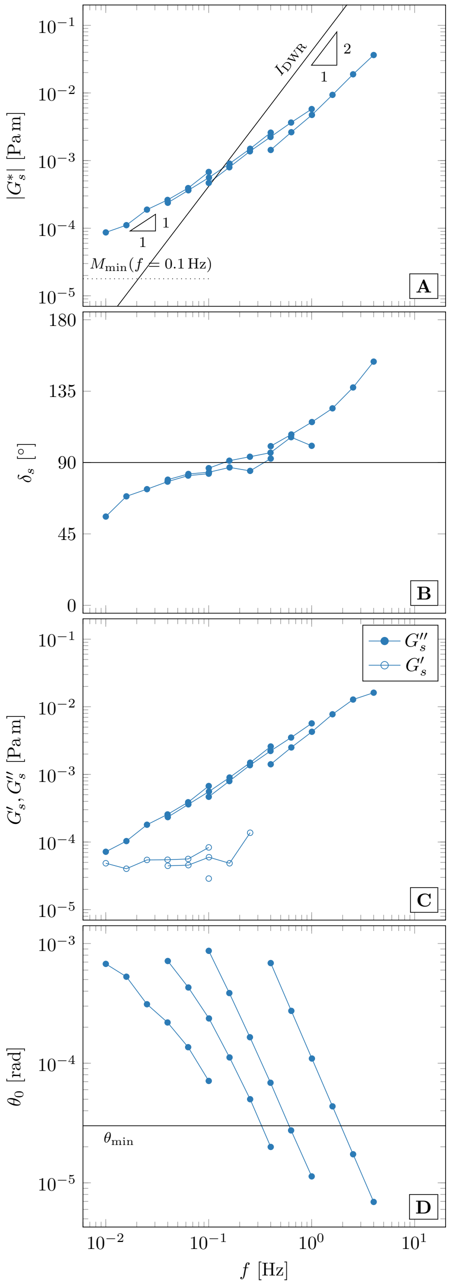

Figure A.10: **Repeat experiment of Fig 9 of the manuscript:** Open loop torque controlled frequency sweep of hexadecanol at $\pi = 25\,\text{mN}\,\text{m}^{-1}$ measured with the small DWR. **A:** norm and **B:** phase angle of the complex interfacial shear modulus. **C:** Elastic and viscous component of the complex interfacial shear modulus. **D:** Displacement amplitude. The torque amplitude was adjusted for the four data sets to ensure $\theta > \theta_{\text{min}}$.

A.8 DWR compliance

A small DWR (with modifications) was glued with epoxy to the bottom plate of the rheometer. After letting the epoxy cure for two days, a creep experiment with increasing stress was performed. The resulting creep and recoverable compliance as function of increasing stress are shown in Fig. S A.11. At low stress, the compliance varies because the measured displacements were very small ($< 10^{-6}$ rad). At $\tau_s > 0.1$ Pa m, there was a minute creep observed. Data points of these two regimes are neglected by the averaging. The resulting upper limit is found as apparent elastic modulus of 38 Pa m.

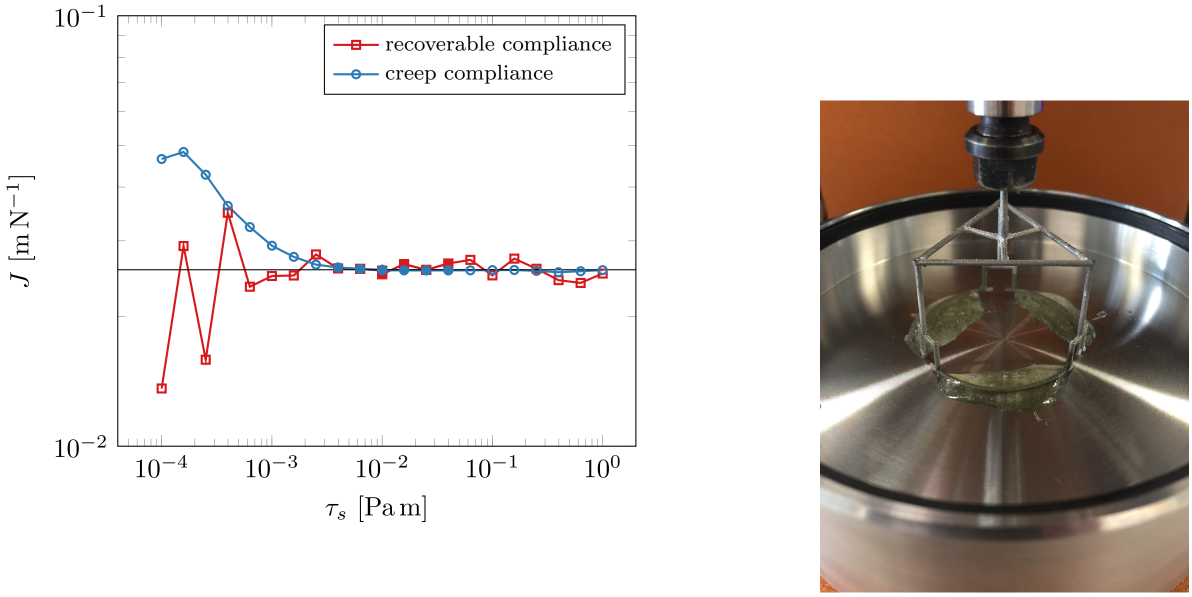

Figure A.11: **Compliance of small DWR**: The averaging is done over the filled blue symbols and represented by the black solid line. A picture of the glued ring is shown on the right hand side.

Should the epoxy not have been hard enough, the shown compliance would correspond to the compliance of the epoxy. In this very unlikely case, the compliance of the ring would even be smaller and the resulting limit would be shifted towards larger G_s^*.

A.9 Subphase correction

The norm and phase angles of the complex amplitude ratio are modulated as:

$$\text{Magnitude:} \qquad \left(\frac{F_0}{z_0}e^{i\delta}\right)_{\text{mod}} = \left(\frac{F_0}{z_0}\right)(1+\Delta)e^{i\delta_0} \tag{A.12a}$$

$$\text{Phase:} \qquad \left(\frac{F_0}{z_0}e^{i\delta}\right)_{\text{mod}} = \left(\frac{F_0}{z_0}\right)e^{i(\delta_0+\Delta)} \tag{A.12b}$$

The resulting uncertainties shown in Fig. S A.12 demonstrate that an error in magnitude will also affect the uncertainty in phase angle and vice versa. As a consequence, it is important to measure both the norm and phase angle with high accuracy. For $|Bq^*| < 1$ the propagation leads to very big uncertainties but the subphase correction is anyway not very accurate even at $\Delta = 0$ shown in Fig. 9 in the manuscript. At larger $|Bq^*|$, the propagated uncertainties are fairly small.

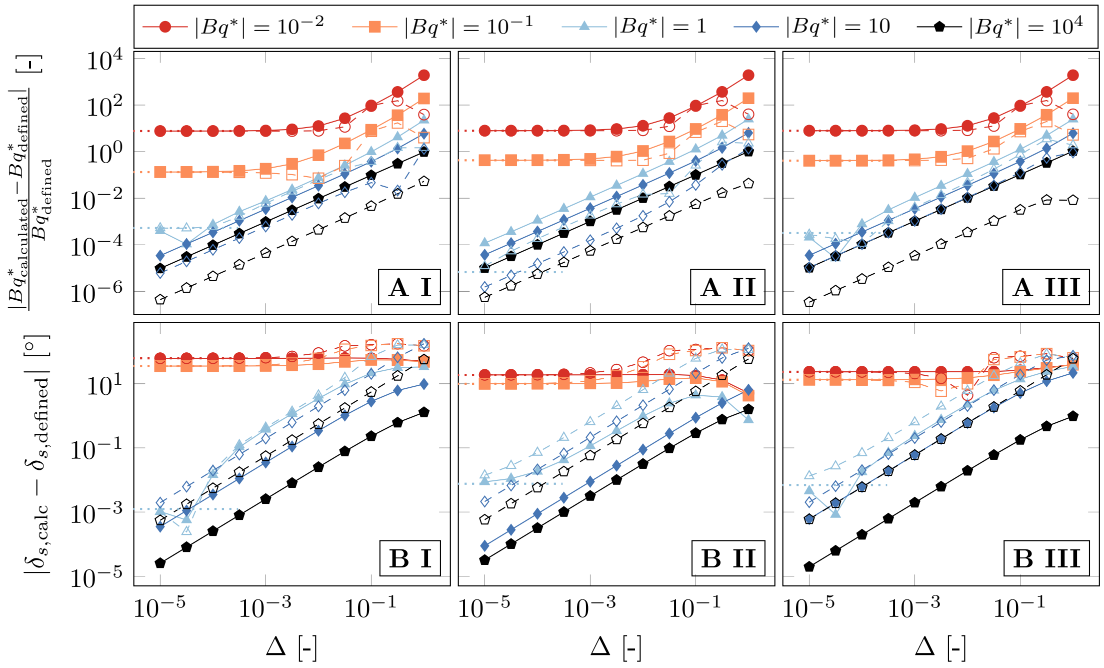

Figure A.12: **Error propagation for Bq^* in the subphase correction code**. The solid lines show modified magnitude of F/z, dashed lines show modified phase of F/z and the dotted lines show the value at $\Delta = 0$. **A:** Uncertainty of resulting $|Bq^*|$, **B:** Uncertainty of resulting δ_s at **I** $\delta_{\text{defined}} = 0°$, **II** $\delta_{\text{defined}} = 45°$ and **III** $\delta_{\text{defined}} = 90°$,

A.10 Probe positioning

Vertical positioning

The gap is varied during an open loop stress amplitude sweep of hexadecanol at $\pi = 25\,\mathrm{mN\,m^{-1}}$ at the water air interface with the small DWR. The resulting $|G_s^*|$ is shown in Fig. S A.13. Data is not corrected for bulk flow effects because $Bq \sim 1000$ and the effect of misplacement is not accounted for in the correction algorithm. Changes of the gap size between -200 to $+500\,\mathrm{\mu m}$ result in $|G_s^*|$ within 20 % of the zero position in the linear viscoelastic regime. By overestimating the interfacial strain if the interface is not perfectly horizontal results in a decrease in apparent $|G_s^*|$. This demonstrates that the pinning of the interface at the edges of the DWR works well.

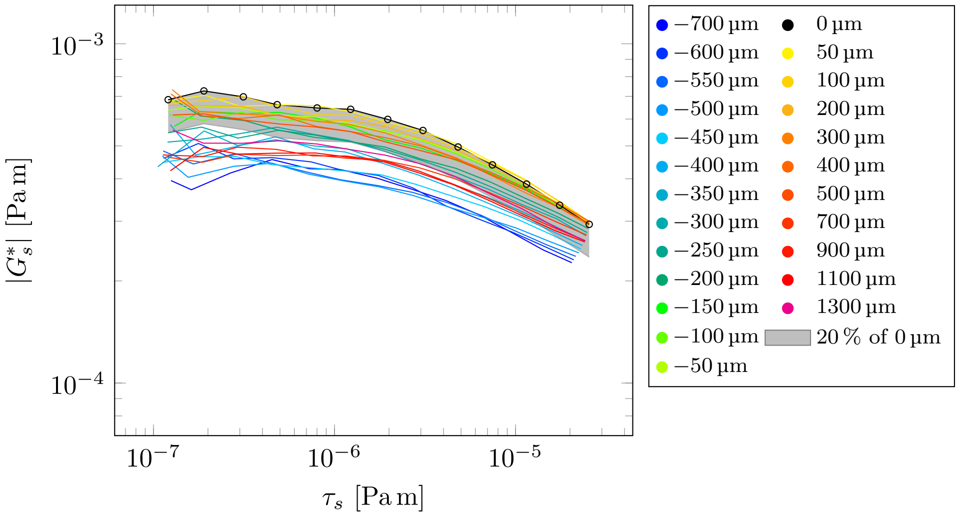

Figure A.13: **Vertical misplacement of the DWR:** The gap is varied as shown in the legend during open loop stress amplitude sweeps of hexadecanol at $\pi = 25\,\mathrm{mN\,m^{-1}}$ at the water-air interface with the small DWR at $f = 0.1\,\mathrm{Hz}$. Data is not corrected for bulk flow. The gray region shows 20 % of the zero position.

Contact angle

An amplitude ratio (AR) is calculated by defining a Boussinesq number and contact angle. The defined AR is used as input for a subphase correction assuming a contact angle of 90° and the resulting $Bq^*_{\text{calculated}}$ is compared with Bq^*_{defined} in Fig. S A.14. For weak interfaces, the uncertainty of Bq^* can reach up to 15 % while stronger interfaces are less affected (0.5 % at $Bq^* = 10^4$). At contact angles less than 90°, the needle is surrounded by more aqueous subphase and experiences a larger drag force. As a result, the analysis code is overestimating the interfacial rheological response. At the same time, the amount of moving fluid is underestimated hence the fluid inertia is underestimated and the resulting δ_s slightly too large.

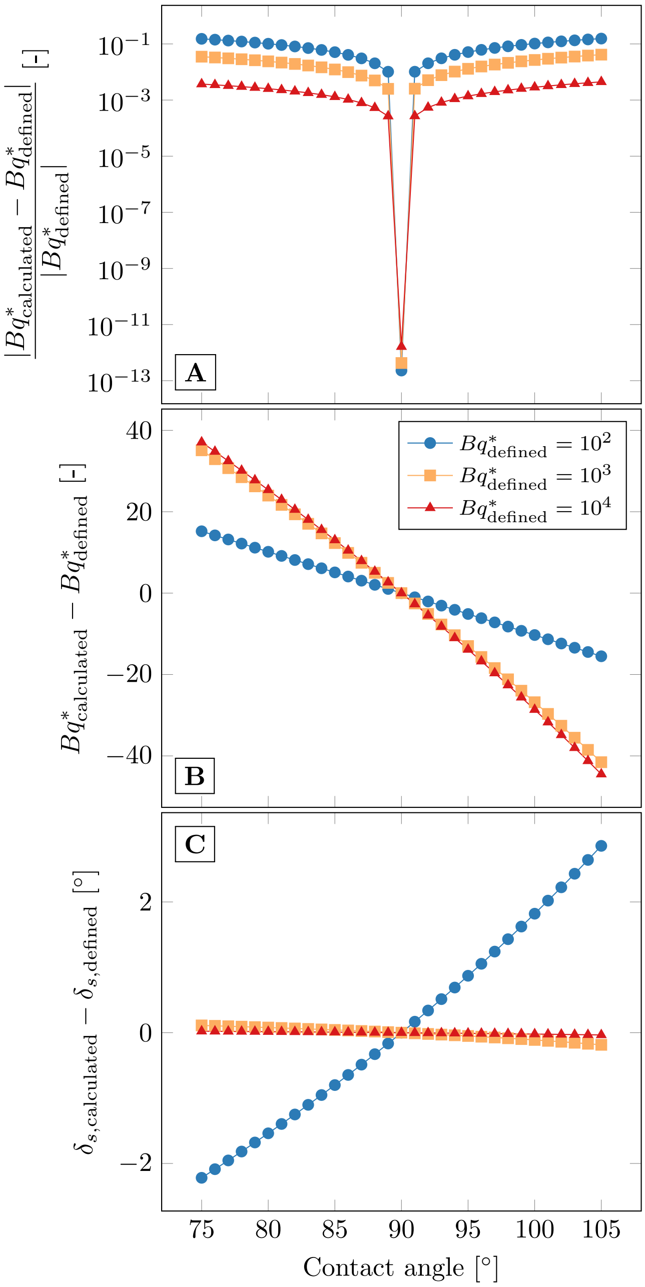

Figure A.14: **Effect of contact angle variations:** Calculated uncertainties of the subphase correction.

Horizontal positioning

The DWR cup is always positioned with a positioning tool to ensure that the center of the geometry is aligned with the rheometer shaft. Here, a linear stage from Thorlabs (Z825B) is used in order to purposely misplace the cup in a very controlled way, and lead it to be off-centered, i.e. moving the cup out of the optimal position parallel to the trough. The resulting apparent interfacial loss and storage moduli are shown in Fig. S A.15.

Displacements of the cup of up to 200 µm do not show a significant effect in the rheological data. Displacements in the range of 400–800 µm result in a slight increase in apparent elasticity. Due to the misplacement, the minimal distance between the ring and cup is reduced and capillarity effects of non-ideal wetting might become stronger. For displacements larger than 800 µm G'_s increases by many orders of magnitude most probably by the formation of a meniscus between the cup opening and the ring although no meniscus could have been observed by eye.

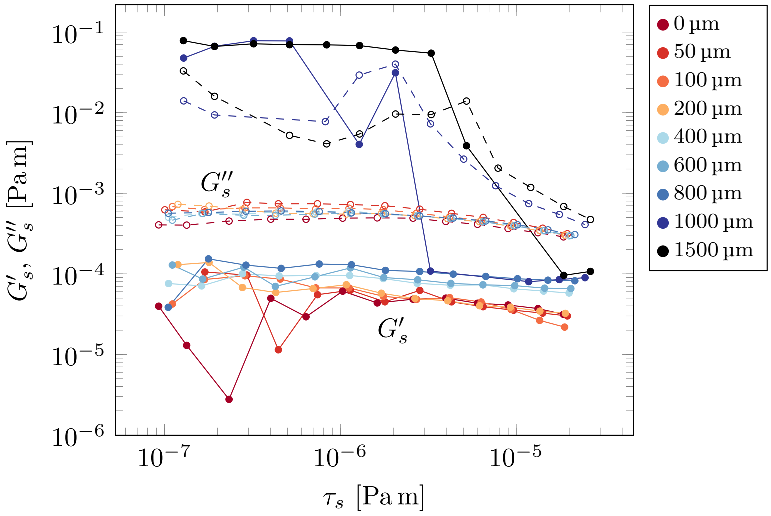

Figure A.15: **Horizontal misplacement of the DWR:** The small DWR cup is displaced away from the optimal position as shown in the legend during open loop stress amplitude sweeps of hexadecanol at $\pi = 25\,\mathrm{mN\,m^{-1}}$ at the water-air interface and $f = 0.1\,\mathrm{Hz}$. Data is not corrected for bulk flow. G'_s and G''_s are shown as solid lines with closed symbols and dashed lines with open symbols, respectively.

B Supplemental Information: DPPC Monolayers

B.1 Phase shift induced by inductance of magnetic coils

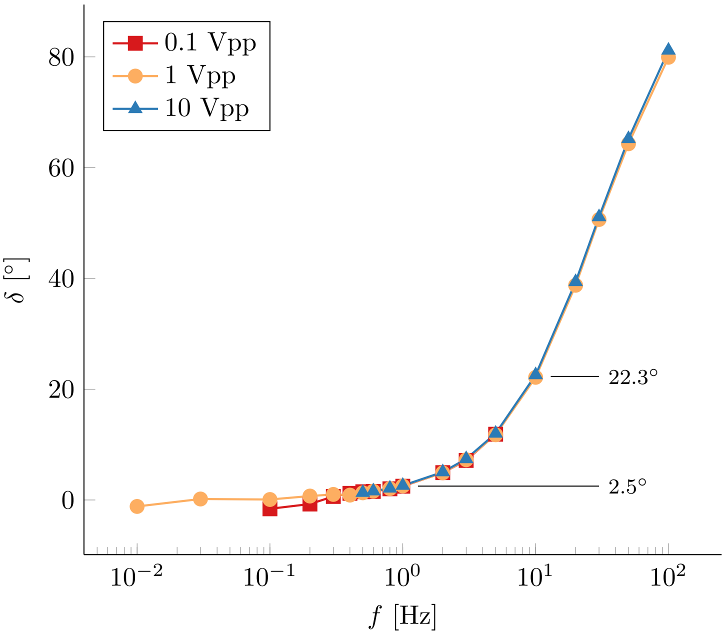

Figure B.1: **Inductance of the magnetic coils:** Phase shift δ of the current signal measured in parallel to the magnetic coils as a function of frequency f at three signal amplitudes.

The phase shift induced by measuring the voltage in parallel instead of in series with the magnetic coils to calculate the applied current is shown in Fig. B.1. The phase lag becomes significant at frequencies larger than 1 Hz and the effect on the applied frequency range for the ISR is weak, as shown in Fig. B.2.

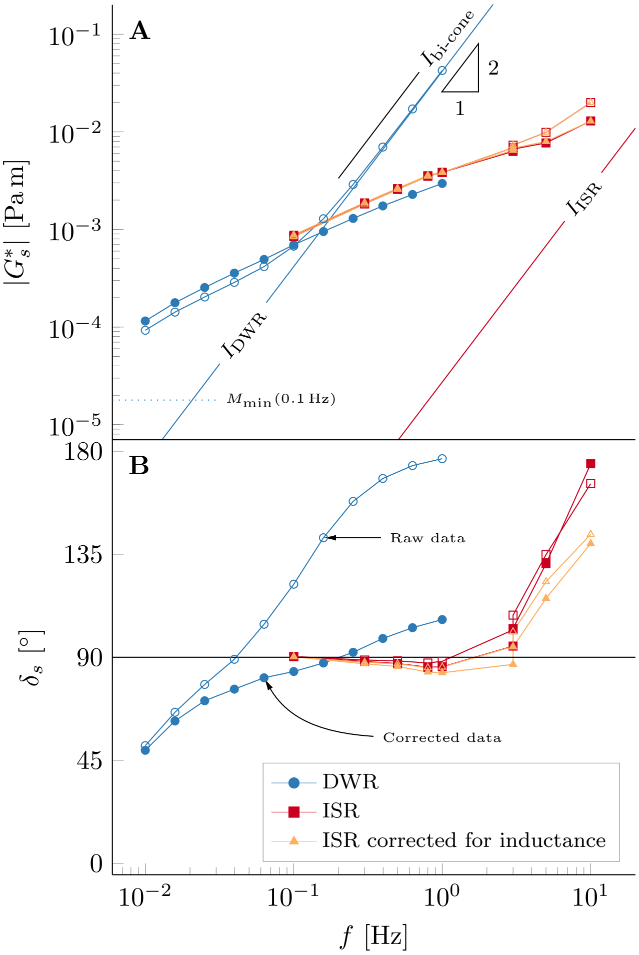

Figure B.2: **Effect of magnetic inductance in applied frequency range:** The ISR data in Fig. 2.8 is corrected for the shift measured in Fig B.1.

B.2 Brewster angle microscope of DPPC at water–air

Brewster angle microscopy images taken during the compression of DPPC spread at the water–air interface without any preceding temperature treatment are shown in Fig. B.3. The image at a mean molecular area of 98 Å^2/molecule shows areas with less structure than the liquid expanded phase. The liquid condensed phase appears first at 74 Å^2/molecule.

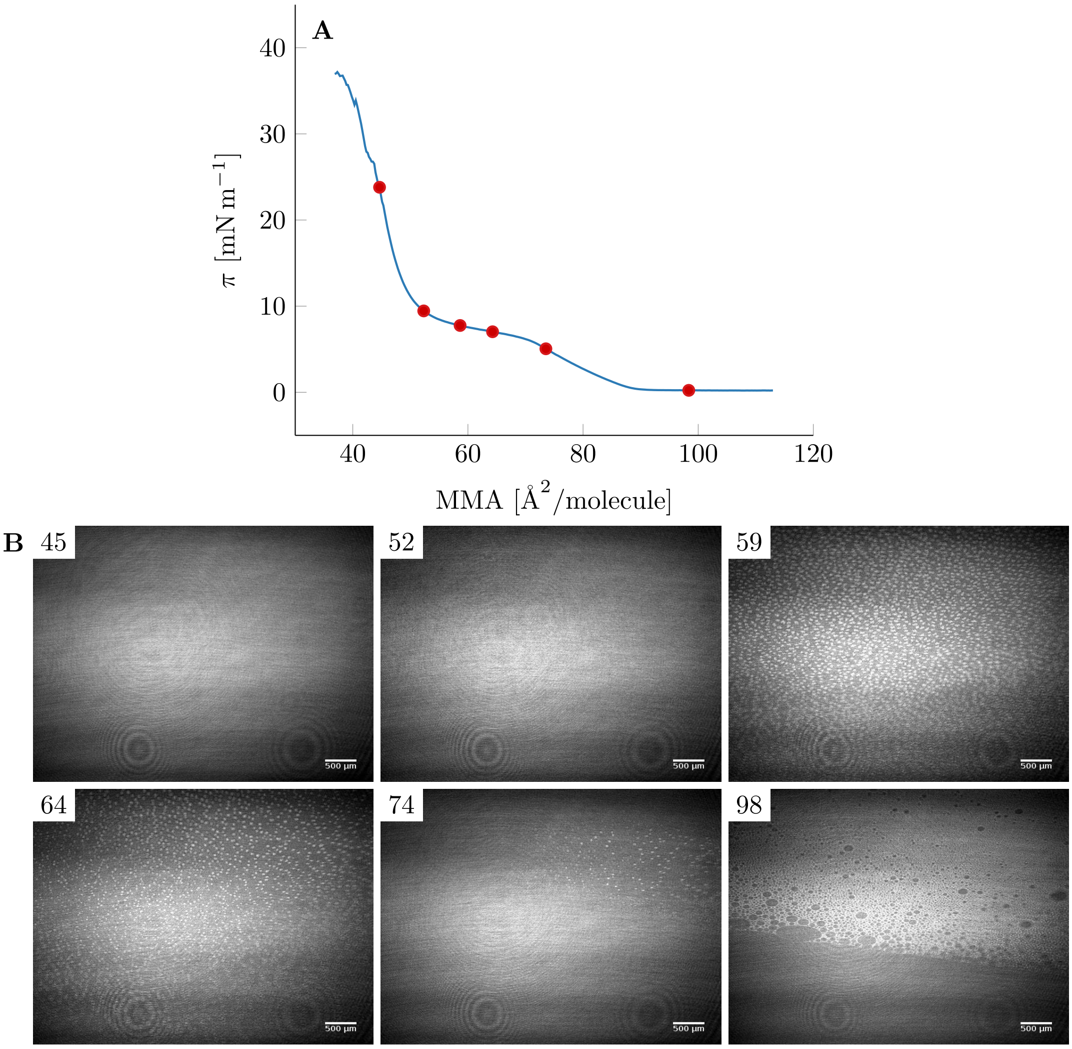

Figure B.3: **Brewster angle microscope: A)** Compression isotherm of DPPC at water–air and 25 °C without temperature treatment prior to compression. **B)** Brewster angle microscopy images corresponding to the filled circles in **(A)**. The MMA is indicated in upper left corner of each image in units of Å^2/molecule.

B.3 Second compression of DPPC at water–air

A second compression of DPPC at the water–air interface is shown in Fig. B.4A. A thermal annealing similar to the spreading procedure is performed in between the two compressions (Fig. B.4B). The annealing could not fully redisperse the DPPC molecules since the compression begins at a higher interfacial pressure compared to the first compression. Longer annealing processes would result in strong evaporation of the aqueous subphase.

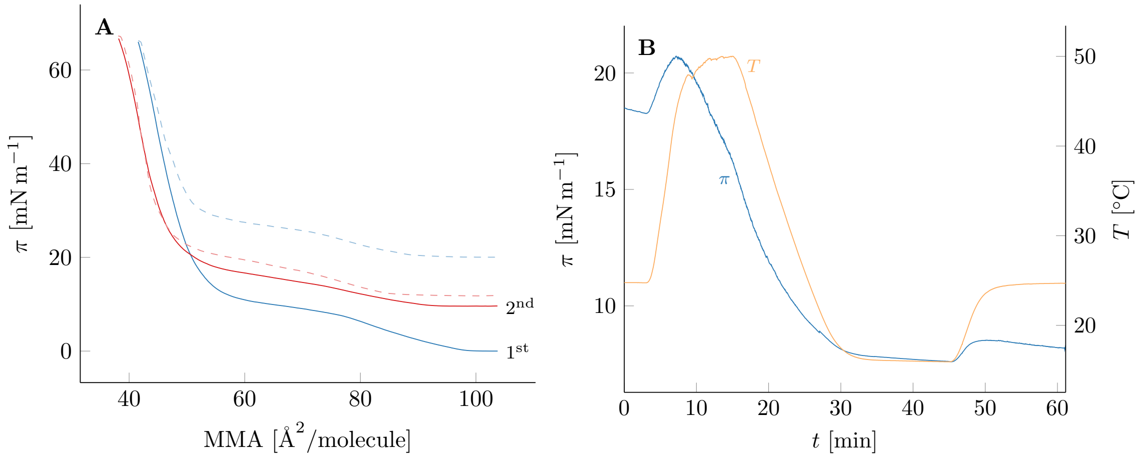

Figure B.4: **Second compression of DPPC at water–air: A)** Two consecutive compression isotherm of DPPC at water–air and 25 °C. Solid and dashed lines correspond to compression and expansion, respectively. **B)** Thermal annealing between the two compressions shown in **(A)**.

B.4 Second compression of DPPC at buffer–air

A second compression of DPPC at the buffer–air interface after the ISR experiment is shown in Fig. B.5. No thermal annealing procedure was performed in between the two compressions.

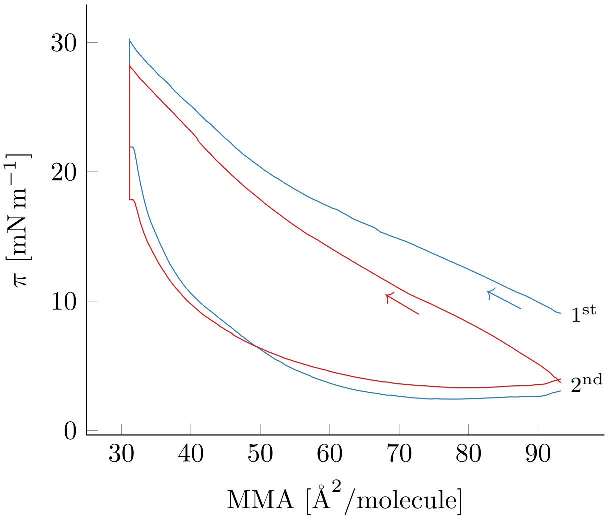

Figure B.5: **Second compression of DPPC at buffer–air:** Two consecutive compression isotherm of DPPC at buffer–air and 25 °C. The arrows indicate the compression. No thermal annealing has been performed between the two compressions.

B.5 Second compression of DPPC at water–oil

A second compression of DPPC at the water–oil interface is shown in Fig. B.6A. Even with very long annealing above the melting temperature of the LC phase (Fig. B.6B), the lipids could not be redispersed and the second compression follows the first expansion.

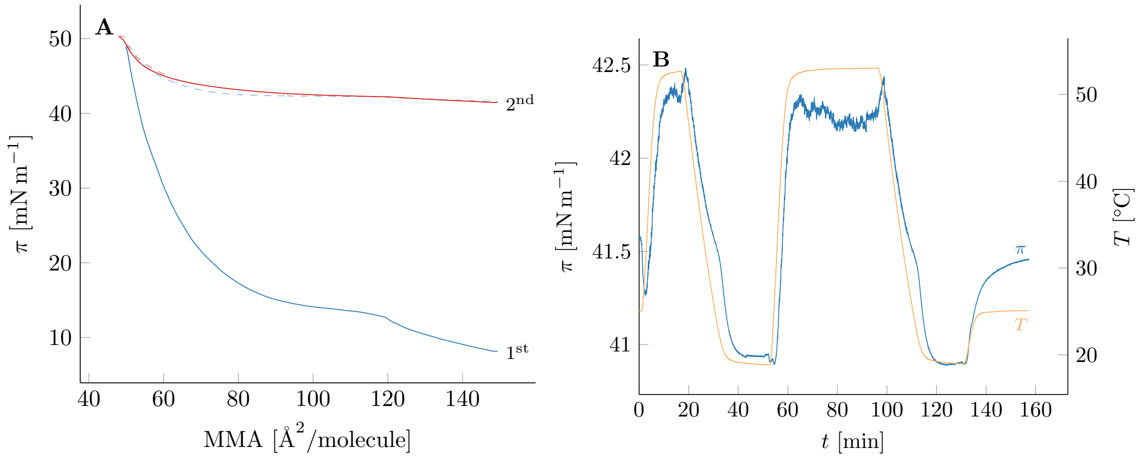

Figure B.6: **Second compression of DPPC at water–oil: A)** Two consecutive compression isotherm of DPPC at water–oi and 25 °C. Solid and dashed lines correspond to compression and expansion, respectively. **B)** Thermal annealing between the two compressions shown in **(A)**.

B.6 Compression without annealing

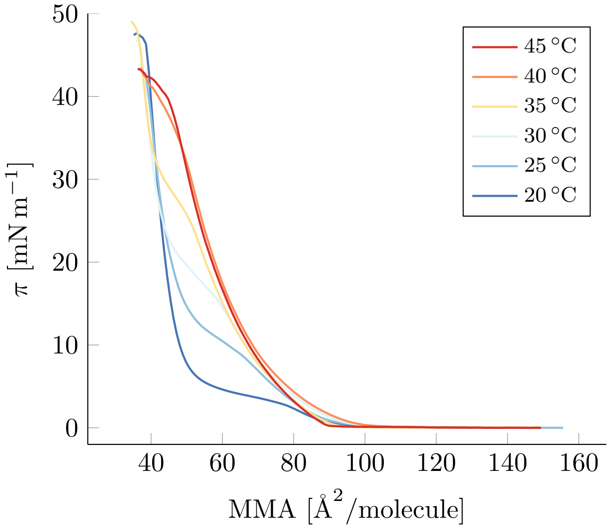

Figure B.7: **Compression without annealing:** Compression isotherms of DPPC at water–air without previous annealing.

C Supplemental Information: Crowded Interfaces

C.1 Magnetic probes

The properties of all magnetic probes used for the lipid monolayer measurements are listed in Table C.1.

Table C.1: **Properties of the individual magnetic probes for the ISR:** l, r and m are the length, radius and mass of the probe, respectively, R is the channel radius, and λ is the ratio of channel radius to probe radius. k^{-1} is the instrument compliance and C_{I-F} the force constant relating the input current with the resulting force acting on the interface. k and C_{I-F} result from the calibration.

Probe	Date	l [mm]	r [µm]	m [mg]	R [mm]	λ [-]	k $[\mathrm{N\,m^{-1}}]$	C_{I-F} $[\mathrm{N\,A^{-1}}]$
Needle	20210215	23.5	200	5.8	12	30	2.9×10^{-5}	4.2×10^{-6}
	20210217				12	30	6.1×10^{-6}	4.0×10^{-6}
	20210218				20	50	2.7×10^{-5}	4.2×10^{-6}
	20210219				12	30	2.7×10^{-5}	4.3×10^{-6}
	20210222				12	30	2.3×10^{-5}	4.1×10^{-6}
	20210224				12	30	2.9×10^{-5}	4.2×10^{-6}
Needle	20210311	23.5	200	5.8	20	50	3.2×10^{-5}	4.6×10^{-6}
	20210315				12	30	1.4×10^{-5}	4.9×10^{-6}
Needle	20210321	23.5	200	5.8	20	50	2.9×10^{-5}	4.8×10^{-6}
	20210322						3.3×10^{-5}	4.7×10^{-6}
	20210323						3.3×10^{-5}	4.3×10^{-6}
Needle	20210330	23.5	200	5.8	20	50	2.3×10^{-5}	4.3×10^{-6}
	20210420				20	50	3.2×10^{-5}	4.6×10^{-6}
	20210422				20	50	2.7×10^{-5}	4.5×10^{-6}
	20210428				20	50	2.9×10^{-5}	4.0×10^{-6}
	20210429				20	50	2.7×10^{-5}	4.6×10^{-6}
	20210504				20	50	2.9×10^{-5}	4.8×10^{-6}
	20210506				20	30	2.7×10^{-5}	4.6×10^{-6}
Needle	20210325	23.5	200	5.8	20	50	3.0×10^{-5}	5.0×10^{-6}
MW	20210326	23.9	17.5	8.7×10^{-3}	20	571	6.7×10^{-6}	1.0×10^{-7}
	20210327	5.5		2.0×10^{-3}	12	343	1.3×10^{-6}	1.5×10^{-8}
	20210328	5.5		2.0×10^{-3}	12	343	1.2×10^{-6}	1.7×10^{-8}
	20210329	5.5		2.0×10^{-3}	12	343	1.3×10^{-6}	1.6×10^{-8}
Needle	20210510	23.5	200	5.8	20	50	2.7×10^{-5}	4.3×10^{-6}
MW	20210519	12.2	17.5	4.5×10^{-3}	20	571	1.9×10^{-6}	4.9×10^{-8}
	20210520	12.2		4.5×10^{-3}	20	571	3.1×10^{-6}	5.1×10^{-8}
	20210526	11.3		4.1×10^{-3}	20	571	1.9×10^{-6}	5.5×10^{-8}
	20210531	11.3		4.1×10^{-3}	20	571	1.9×10^{-6}	5.5×10^{-8}
	20210601	11.3		4.2×10^{-3}	20	571	1.7×10^{-6}	4.9×10^{-8}
	20210603	11.3		4.2×10^{-3}	20	571	2.2×10^{-6}	4.3×10^{-8}

C.2 Stress amplitude sweeps as a function of resulting strain

The stress amplitude sweeps of DPPC at water–air, water–oil, and buffer–oil is shown as a function of resulting strain amplitude γ_s in Fig. C.1. The accepted range of $0.04\,\% < \gamma_s < 0.18\,\%$ for Fig. 4.3 is shown by the vertical lines.

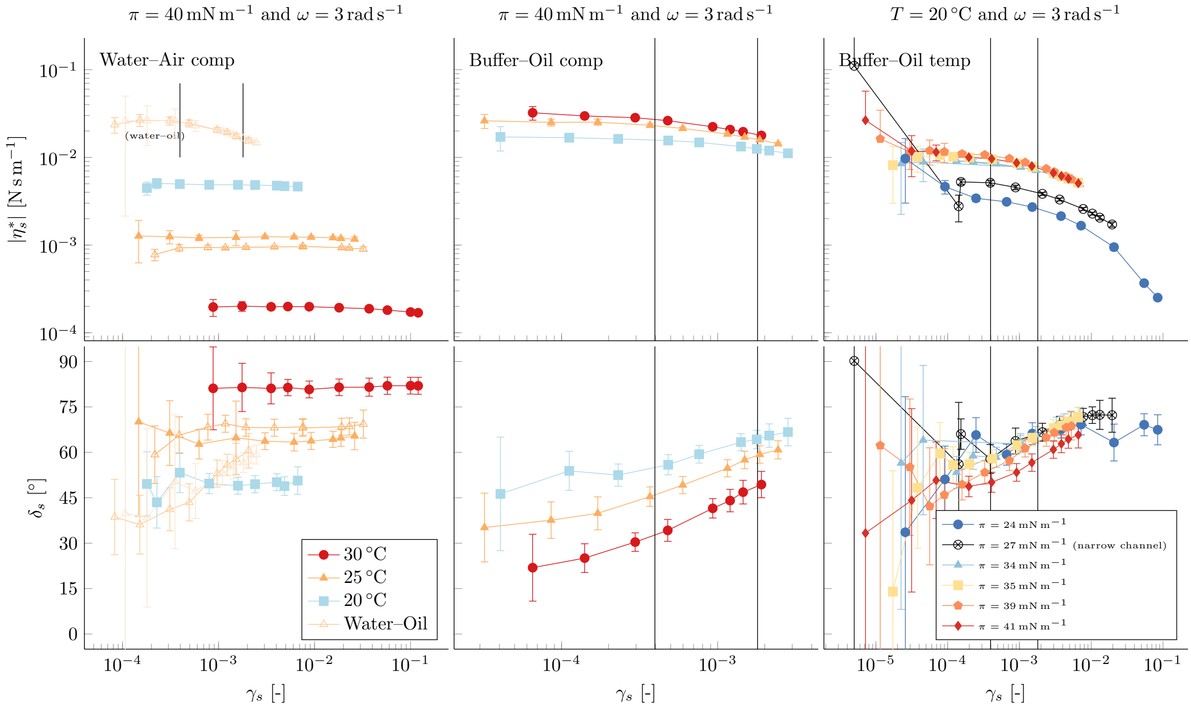

Figure C.1: **Stress amplitude sweep of DPPC monolayers:** complex interfacial shear modulus as a function of resulting strain amplitude γ_s.

C.3 Deformation of the liquid condensed phase

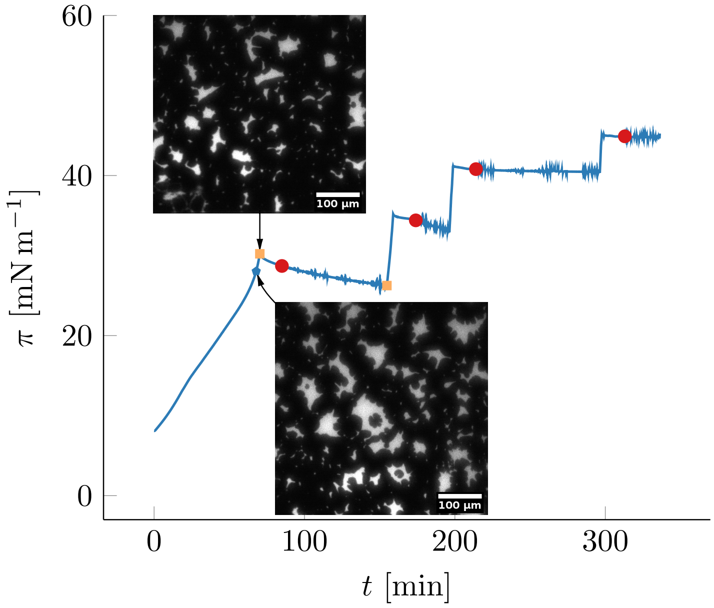

Figure C.2: **Step compression:** Interfacial stress π as a function of time t of pure DPPC at the buffer–oil interface during a step compression in a Langmuir trough. The fluorescent microscopy images are acquired at the times indicated by the arrows and the scale bar represents 100 µm. ISR experiments are conducted at the red points.

A step compression of pure DPPC at the buffer–oil interface is shown in Fig. C.2. The high melting point of DPPC ($T_{m,\mathrm{DPPC}} = 42\,^{\circ}\mathrm{C}$) requires the interface to undergo a thermal annealing at $T > T_{m,\mathrm{DPPC}}$ prior to isothermal compression as proposed by [2] to arrive at a *thermally structured* interface.

The phase separation is induced by an increase in surface pressure at constant temperature and the onset of deformation of these phases is identified by fluorescent microscopy and marked with a pentagon in the graph. The velocity of the barriers is set to zero at the orange square. The relaxation given by the two orange squares corresponds to the viscous contributions of the interfacial stresses and is equal to $4.0\,\mathrm{mN\,m^{-1}}$. The total interfacial extra stresses are expected to be even larger because the elastic contributions are not captured with this method. The applied interfacial stresses by the ISR (see Fig. 4.4A for the pure DPPC data) are an order of magnitude smaller than the extra stresses needed to deform the liquid condensed phases. Therefore, the liquid condensed phases are effectively solid like compared to the applied range of interfacial stresses during the ISR experiments.

C.4 Two-point tracking results

The particle tracking result considering LC domain radii of 3 µm to 3.5 µm for the lipid mixture of DPPC and DOPC with ratio 3/2 as monolayer at the buffer–oil interface is shown in Fig. C.3. The two-point mean squared displacement (MSD) contains much more noise than the single particle tracking. However, the slopes of the two curves are similar at large time.

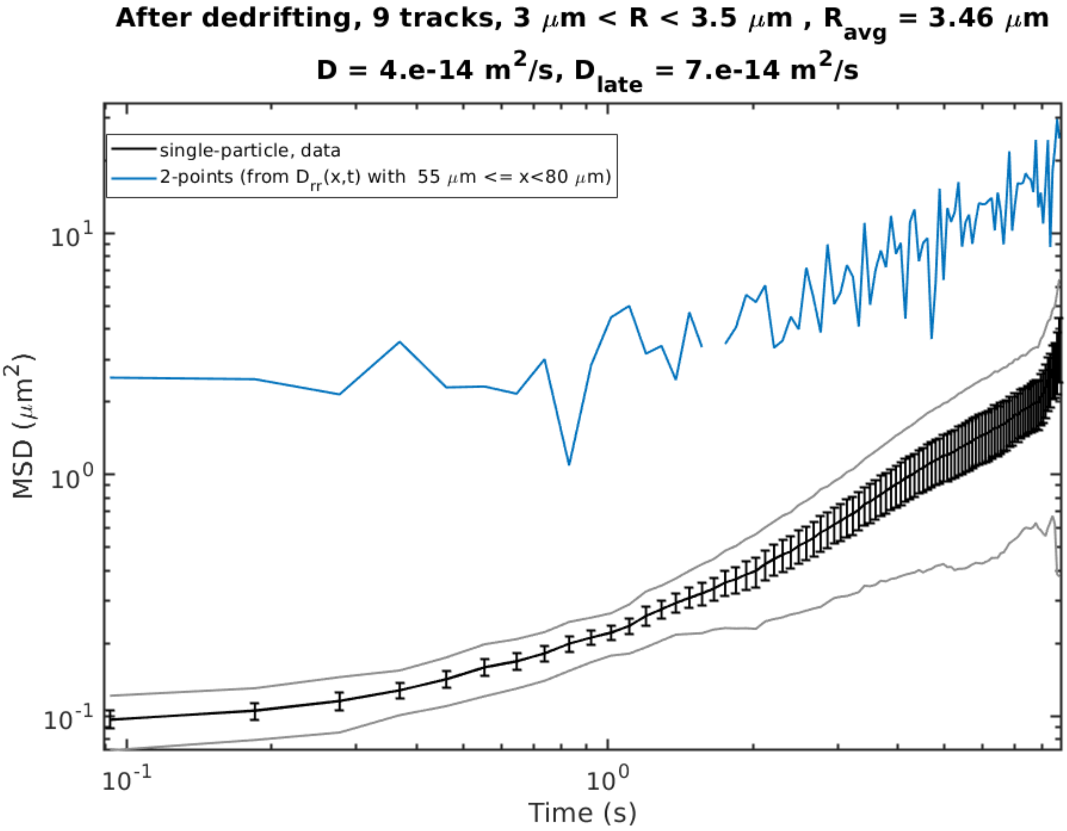

Figure C.3: **Particle tracking on monolayers:** DPPC/DOPC of 3/2 as a monolayer at the buffer–oil interface. Mean squared displacement (MSD) as a function of lag time. The fitted D corresponds to the short-time diffusion coefficient of the single-particle data. Data is de-drifted.

The particle tracking result considering fluorophore aggregates with radius of 5 µm for the lipid mixture of DPPC and DOPC with ratio 3/2 as bilayers is shown in Fig. C.4. The two-point mean squared displacement (MSD) contains much more noise than the single particle tracking.

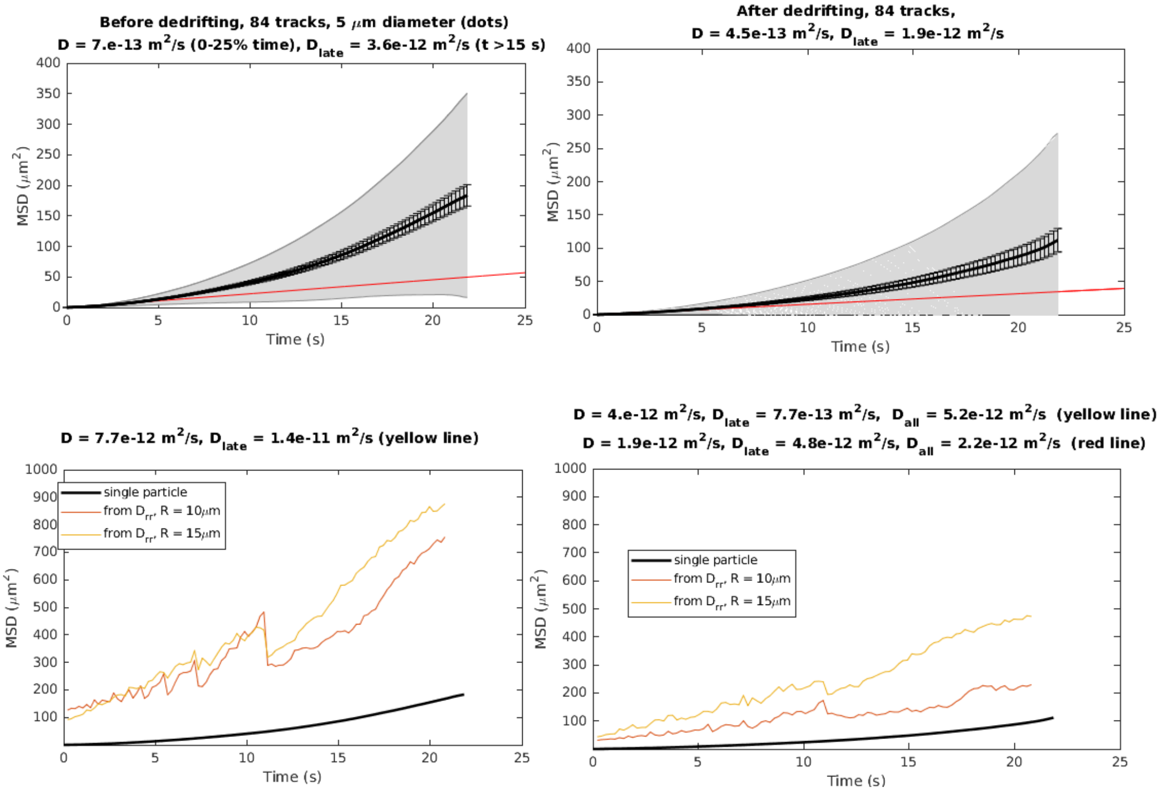

Figure C.4: **Particle tracking on bilayers:** DPPC/DOPC of 3/2 as a bilayers. Mean squared displacement (MSD) as a function of lag time. The fitted D corresponds to the short-time diffusion coefficient of the single-particle data. The fit is shown by the red line. *Left:* Raw data. *Right:* Data is de-drifted.

D Scientific Achievements

D.1 Publications in peer-reviewed scientific journals

(1) D. Renggli, A. Alicke, R. H. Ewoldt, and J. Vermant. “Operating windows for oscillatory interfacial shear rheology”, *Journal of Rheology* **64**, 141 (2020); doi: 10.1122/1.5130620

(2) Kilian Dietrich, Giovanni Volpe, Muhammad Nasruddin Sulaiman, Damian Renggli, Ivo Buttinoni, and Lucio Isa. “Active Atoms and Interstitials in Two-Dimensional Colloidal Crystals”, *Phys. Rev. Lett.* **120**, 268004 (2018); doi: 10.1103/PhysRevLett.120.268004

(3) Madhura Marathe, Damian Renggli, Mehmet Sanlialp, Maksim O. Karabasov, Vladimir V. Shvartsman, Doru C. Lupascu, Anna Grünebohm, and Claude Ederer. “Electrocaloric effect in $BaTiO_3$ at all three ferroelectric transitions: Anisotropy and inverse caloric effects”, *Phys. Rev. B* **96**, 014102 (2017); doi: 10.1103/PhysRevB.96.014102

(4) Kilian Dietrich*, Damian Renggli*, Michele Zanini, Giovanni Volpe, Ivo Buttinoni and Lucio Isa. “Two-dimensional nature of the active Brownian motion of catalytic microswimmers at solid and liquid interfaces”, *New Journal of Physics* **19**, 065008 (2017); doi: 10.1088/1367-2630/aa7126

* Equal contribution.

Submitted articles

(1) Alesya Mikhailovskaya, Emmanouil Chatzigiannakis, Damian Renggli, Jan Vermant, Cécile Monteux. “From individual liquid films to macroscopic foam dynamics: a

comparison between polymers and a non-ionic surfactant", *Langmuir*, Manuscript ID: la-2022-009007 (2022)

(2) Y. Tein, B. Thompson, C. Majkrzak, B. Maranville, D. Renggli, J. Vermant, N. Wagner. "Instrument for measurement of interfacial structure-property relationships with decoupled interfacial shear and dilatational flow: *Quadrotrough*", *Review of Scientific Instruments*, Publication ID: 934538 (2022)

In preparation

(1) Damian Renggli, Maria Clara Novaes Silva, Laura Stricker, and Jan Vermant. "Phospholipid membranes are crowded, yet fluid."

(2) Damian Renggli and Jan Vermant. "Interfacial rheology of phospholipid monolayer and their shape morphology".

(3) Damian Renggli, "Interfacial rheometry : from lipid monolayers towards bilayers", Ph.D Thesis.

Unpublished work

(1) Damian Renggli, "Active Janus Particles Propelled by Hydrogen Peroxide Decomposition", MSc Thesis, 2016.

(2) Damian Renggli, "Photocatalytic Characterization of Multicomponent Aerogels", BSc Thesis, 2013.

D.2 Contributions to conferences

Oral presentations

- AERC (Annual European Rheology Conference), "Interfacial rheology of crowded phospholipid monolayers shows a fluid behaviour", D. Renggli and J. Vermant; Sevillia ES, April 2022
- ACS (the American Chemical Society spring meeting), "Crowded phospholipid monolayers are fluid as measured by interfacial rheology", D. Renggli and J. Vermant; San Diego CA, March 2022

- AIChE (annual meeting of the American Institute of Chemical Engineers), “Interfacial rheology of phospholipid monolayers”, D. Renggli and J. Vermant; Boston MA, Nov. 2021
- SSD (28th edition of the Swiss Soft Day), “Interfacial rheology of phospholipid monolayers”, D. Renggli and J. Vermant; Lausanne CH, Oct. 2021
- SOR (annual meeting of the Society of Rheology), “Interfacial rheology of phospholipid monolayers”, D. Renggli and J. Vermant; Bangor ME (online), Oct. 2021
- AERC (Annual European Rheology Conference), “Interfacial rheology of phospholipid monolayers”, D. Renggli and J. Vermant; online, April 2021
- ICR (Internatial Congress on Rheology), “Interfacial rheology of phospholipid monolayers”, D. Renggli and J. Vermant; online, Dec. 2021
- SOR (annual meeting of the Society of Rheology), “Operating windows for interfacial rheometry”, D. Renggli, A. Alicke, R. H. Ewoldt, and J. Vermant; Raleigh NC, Oct. 2019
- International Soft Matter Conference, “Operating windows for interfacial rheometry”, D. Renggli, R. H. Ewoldt, and J. Vermant; Edinburgh GB-SCT, June 2019
- AERC (Annual European Rheology Conference), “Operating windows for interfacial rheometry”, D. Renggli, R. H. Ewoldt, and J. Vermant; Portoroz Sl, April 2019

Poster

- MaP Graduate Symposium (Competence Center for Materials and Processes), “Operating windows for Interfacial Rheometry”, D. Renggli, A. Alicke, R. H. Ewoldt, and J. Vermant; online, June 2021

D.3 General contributions to science

SOFT MATTER : WHERE CHEMISTRY, PHYSICS AND BIOLOGY MEET ENGINEERING (2016). Grant approved by the Swiss University Conference to fund four graduate meetings organized in the series of the *Swiss Soft Days*: 2017 at EPFL, 2018 at ETH, 2019 at Nestlé Research, and 2021 online with invited speakers from Europe, US, and industry.

E Curriculum Vitae

Omitted in the electronic version.

F List of Symbols

The list is organized as follows:

- Table F.1: Abbreviations
- Table F.2: Mathematical symbols and operators
- Table F.3: Non-dimensional groups
- Table F.4: Rheological properties
- Table F.5: Primary observables and constants

Table F.1: **Abbreviations**

Symbol	Description
B/A	buffer–air interface
B/O	buffer–oil interface
CHOL	cholesterol
dft	discrete Fourier transform
DOPC	1,2-dioleoyl-*sn*-glycero-3-phosphocholine
DOPE-Rhod	head labeled DOPC with Rhod fluorophore
DPPC	1,2-dipalmitoyl-*sn*-glycero-3-phosphocholine
DPPE-Rhod	head labeled DPPC with Rhod fluorophore
DWR	double wall ring
ER	endoplasmatic reticulum
FITC	fluorescein isothiocyanate
FRAP	fluorescence recovery after photobleach
GSER	generalized Stokes-Einstein relation
GUV	giant unilamellar vesicles
IPA	propan-2-ol
ISR	interfacial needle shear rheometer
KD	Krieger-Dougherty
LAMBs	large area model biomembranes
LC	liquid condensed phase
LE	liquid expanded phase
milli-Q	ultra pure water
MW	microwire
N	needle
NBD	7-nitro-2-1,3-benzoxadiazol-4-yl fluorescent dye
NBD-PPC	tail labeled DPPC with NBD fluorophore
PC	phosphocholine head group
PE	phosphatidyl ethanolamine head group
PL	phospholipid
POM	polyoxymethylene
Rhod	Lissamine rhodamine B sulfonyl fluorescent dye
SD	Saffman-Delbrück
S/N	signal-to-noise ratio
TEM	transmission electron microscopy
TRITC	tetramethylrhodamine isothiocyanate
W/A	water–air interface
W/O	water–oil interface

Table F.2: **Mathematical symbols and operators**

Symbol	Description
$\frac{D}{Dt}$	surface material derivative
∇	gradient operator
$\boldsymbol{\nabla}_s$	surface gradient operator
$\boldsymbol{I}_s$	surface unit tensor
$\boldsymbol{n}$	unit vector normal to the surface
$\lvert \ldots \rvert$	norm of a complex number
$\lvert\lvert \ldots \rvert\rvert$	jump terms
$\Re$	real part
$\Im$	imaginary part
i	imaginary number
$\hat{f}(\omega)$	Fourier transform of $f(t)$
$\lvert\hat{f}(\omega)\rvert$	magnitude of the single sided spectrum of $\hat{f}(\omega)$

Table F.3: **Non-dimensional groups**

Symbol	Description	Unit
Bd	Bond number	[-]
Bq	Boussinesq number	[-]
Bq^*	complex Boussinesq number	[-]
Re	Reynolds number	[-]
Re_s	interfacial Reynolds number	[-]
A_s	area between probe and bulk phase	[m^2]
a	macroscopic characteristic length scale $\frac{A_s}{P_s}$	[m]
L_s, L_b	lengths over which V decays	[m]
l	characteristic length scale	[m]
l_ω	Stokes boundary layer length scale	[m]
l_ω^s	interfacial characteristic length scale	[m]
P_s	perimeter between probe and interface	[m]
V	velocity	[m s^{-1}]

Table F.4: **Rheological properties**

Symbol	Description	Unit
b_T, b_R	translational and rotational mobility	$[\mathrm{m(Ns)^{-1}}]$, $[\mathrm{(Nms)^{-1}}]$
δ_s	phase angle of G_s^*	[°]
$\boldsymbol{D}_s$	interfacial rate-of-deformation tensor	$[\mathrm{s^{-1}}]$
D_T, D_R	translational and rotational diffusion coefficient	$[\mathrm{m^2\,s^{-1}}]$
D_{short}, D_{long}	short and long time diffusion coefficient	same as D
$D_{SD,\mathrm{max}}$	maximum D_T of the SD model	same as D_T
η, η_b, η_{bulk}	bulk shear viscosity	[Pa s]
η_r	ratio of total to medium shear viscosity	[-]
$\eta_{SD,\mathrm{max}}$	interfacial viscosity corresponding to $D_{SD,\mathrm{max}}$	as η_s
η_s	interfacial shear viscosity	$[\mathrm{N\,m^{-1}\,s}]$ or [Pa m s]
η_s^*	complex interfacial shear viscosity	as η_s
η_s'	dynamic interfacial shear viscosity	as η_s
η_s''	out-of-phase interfacial shear viscosity	as η_s
$\lvert\eta_s^*\rvert$	magnitude or norm of η_s^*	as η_s
$\eta_{s,\mathrm{LE\text{-}DPPC}}$	η_s of the LE phase of DPPC	as η_s
$\eta_{s,M}$	calculated medium η_s of the LE phase	as η_s
$[\eta_s]'$	intrinsic shear viscosity	[-]
ϕ	area fraction of the LC phase	[-]
Γ	surface excess concentration	$[\mathrm{mol\,m^{-2}}]$
γ_s	interfacial strain	[-]
G_s^*	complex interfacial shear modulus	[Pa m] or $[\mathrm{N\,m^{-1}}]$
G_s'	interfacial elastic shear modulus	as G_s^*
G_s''	interfacial viscous shear modulus	as G_s^*
$\lvert G_s^*\rvert$	magnitude or norm of G_s^*	same as G_s^*
κ_s	interfacial dilatational viscosity	$[\mathrm{N\,m^{-1}\,s}]$ or [Pa m s]
ν	kinematic viscosity	$[\mathrm{m^2\,s^{-1}}]$
π	surface and interfacial pressure	$[\mathrm{N\,m^{-1}}]$
ρ_s	interfacial density	$[\mathrm{kg\,m^{-2}}]$
$\langle r^2\rangle$	mean squared displacement	$[\mathrm{m^2}]$
$\boldsymbol{\sigma}$	bulk stress tensor	[Pa]
$\boldsymbol{\sigma}_s$	interfacial stress tensor	[Pa m] or $[\mathrm{N\,m^{-1}}]$
σ	surface and interfacial tension	$[\mathrm{N\,m^{-1}}]$
$\sigma(\Gamma)$	σ of the laden interface	$[\mathrm{N\,m^{-1}}]$
σ_{clean}	σ of the clean interface	$[\mathrm{N\,m^{-1}}]$
$\boldsymbol{\tau}$	interfacial extra stress tensor	same as $\boldsymbol{\sigma}_s$
τ_s	interfacial stress	same as $\boldsymbol{\tau}$
$\langle\theta^2\rangle$	mean squared rotation	$[\mathrm{rad^2}]$
T	(absolute) temperature	[K] or [°C]
$\boldsymbol{v}_s$	interfacial velocity	$[\mathrm{m\,s^{-1}}]$
χ_{DOPC}	weight fraction of DOPC in the lipid mixture	[-]

Table F.5: **Primary observables and constants**

Symbol	Description	Unit
α	particle radius	[m]
C_{I-F}	force constant translating current to force	[N A^{-1}]
$C_{\Box}$	geometrical factors relating $\Box$ with τ_s or γ_s	depends on $\Box$
δ_I	current phase shift of $I(t)$	[rad]
δ_M	torque phase shift of $z(t)$	[rad]
δ_θ	angular displacement phase shift of $\theta(t)$	[rad]
δ_z	displacement phase shift of $z(t)$	[rad]
d	dynamic range	[-]
$\phi_{\max}$	maximum packing of hard disks in 2 dimensions	0.906
$F_{\text{Drag, bulk}}$	drag force on the probe from the bulk subphase	[N]
$F_{\text{Drag, interface}}$	drag force on the probe from the interface	[N]
f	driving frequency	[Hz]
f_{noise}	noise of the variable $f(t)$	as $f(t)$
g	gravitational force of the Earth per unit mass	$9.81\,\text{m}\,\text{s}^{-1}$
$I(t)$	time dependent current	[A]
I_0	current amplitude of $I(t)$	[A]
I_g, I_{instr}	geometry and instrument inertia	[kg m^2]
k^{-1}	instrument compliance	[m N^{-1}]
k_B	Boltzmann's constant	$1.38 \times 10^{-23}\,\text{J}\,\text{K}^{-1}$
λ	ratio of channel to probe radius	[-]
l	length of the probe	[m]
$M(t)$	time dependent torque	[N m]
M_0	torque amplitude	[N m]
MMA	mean molecular area	[Å^2/molecule]
m	mass of the probe	[kg]
ω	characteristic and driving frequency	[rad s^{-1}]
ρ_{needle}, ρ_{bulk}	density of the needle and bulk	[kg/m^3]
R	resistance of a coil	[Ω]
$R^{\text{outer, inner}}_{\text{cup, ring}}$	radius of the cup and the ring	[m]
r	radius of the probe	[m]
$\theta(t)$	time dependent angular displacement	[rad]
θ_0	angular displacement amplitude	[rad]
T_m	melting temperature	[°C]
$T_{m,\text{DOPC}}$	melting temperature of the LC phase of DOPC	$-17\,^\circ\text{C}$
$T_{m,\text{DPPC}}$	melting temperature of the LC phase of DPPC	$42\,^\circ\text{C}$
t	time	[s]
t_1, t_2	borders of the time window	[s]
$u_{\Box}$	uncertainty of the quantity $\Box$	as $\Box$
V_1, V_2	voltage signals of coil 1 and 2	[V]
V_{input}	input voltage of the function generator	[V$_{\text{pp}}$]
$z(t)$	time dependent displacement	[m]
z_0	displacement amplitude of $z(t)$	[m]

G List of Tables

1.1 **Lipid terminology:** Abbreviations for the chemical compounds presented in the presented work. 6

2.1 **Properties of the magnetic probes for the ISR:** l, r and m are the length, radius and mass of the probe, respectively and λ is the ratio of channel radius to probe radius. k^{-1} is the instrument compliance and C_{I-F} the force constant described in Eq. (A.3). k and C_{I-F} result from the calibration. 23

2.2 **Properties of the rings for the DWR:** $R_{\circ}^{\square}$ denotes the outer and inner ($\square$) radius of the cup and the ring ($\circ$). I_g is the geometry inertia and the instrument inertia is $I_{\text{instr}} = 20.93\,\text{mg}\,\text{m}^2$. 24

2.3 **Properties of the bi-cone geometries:** R_{cup} and R_{ring} are the radii of the cup and the ring, respectively, h is the penetration depth, β is the cone angle and I_g is the geometry inertia. Instrument inertia of the MCR 302 is $I_{\text{instr}} = 92.04\,\text{mg}\,\text{m}^2$. 26

2.4 **Primary measurable variables Limits:** Minimum and maximum for S/N ≥ 5 according to the Fourier analysis for the ISR and DWR. No limits could be found for the bi-cone which agree with S/N ≥ 5. Superscript * denotes values for large η_s. 32

2.5 **Dynamic ranges Eq.** (2.31) **of ISR and DWR:** The ISR is an open loop stress controlled instrument. Only the open loop mode with the DWR is truly stress controlled. No operating window could be defined for both bi-cones. 42

2.6 **Characteristic length scale a:** and resulting $|\eta_s^*|$ for $|Bq^*| = 1$ and $\eta_{\text{bulk}} = 1\,\text{mPa}\,\text{s}$ imposing a lower limitation. 43

2.7 Overview of contributing effects. 51

4.1 **Diffusion constants:** Temperature T, mean domain size α, and bulk viscosity η_b used in the SD model shown in Fig. 4.6B. Measured short-time (D_{short}) and long-time diffusion constants. $\eta_{s,SD\text{max}}$ corresponds to the maximum of Eq. (4.1) at $D_{SD,\text{max}}$. 103

4.2 **Properties of the magnetic probes for the ISR:** l and m are the length and mass of the probe, respectively. k^{-1} is the instrument compliance and C_{I-F} the force constant described in Eq. (A.3). k and C_{I-F} result from the calibration. Individual fitting parameters for each experiment can be found in Table C.1. 105

A.1 **Calibration constants for the ISR probes:** k^{-1} is the instrument compliance, E transforms A/pixel to N/m and C_{I-F} is the force constant. k and E result from the calibration. 131

A.2 Numerical values of the conversion factors for the ISR, DWR and bi-cone. 139

C.1 **Properties of the individual magnetic probes for the ISR:** l, r and m are the length, radius and mass of the probe, respectively, R is the channel radius, and λ is the ratio of channel radius to probe radius. k^{-1} is the instrument compliance and C_{I-F} the force constant relating the input current with the resulting force acting on the interface. k and C_{I-F} result from the calibration. 156

F.1 **Abbreviations** 168

F.2 **Mathematical symbols and operators** 169

F.3 **Non-dimensional groups** 169

F.4 **Rheological properties** 170

F.5 **Primary observables and constants** 171

H List of Figures

1.1 **An artist's interpretation of a cell membrane:** Proteins and other molecules are embedded in the phospholipid bilayer. Reproduced from Version 8.25 of the textbook *Anatomy and Physiology*, OpenStax, published April 25, 2013 (`https://openstax.org/books/anatomy-and-physiology/pages/3-1-the-cell-membrane`). 1

1.2 **Proof of the bilayer structure:** Transmission electron micrographs of **(A)** a synaptic complex and microdensiometer (reproduced from Robertson [12]) and **(B)** a single plasma membrane at pH 7 with the numerically averaged absorbance profile **(C)** (reproduced from Coster et al. [13]). . . 2

1.3 **Chemical structures of membrane phospholipids:** Variations in the phosphoglycerides are shown in the hydrophilic head groups phosphatidylserine (PS), -ethanolamine (PE), -choline (PC), -inositole (PI), and the hydrophobic tail. Image adapted from Wikipedia (`https://commons.wikimedia.org/w/index.php?curid=63827468`, 2022). 4

1.4 **Lipid synthesis and steady-state composition of cell membranes:** The lipid composition is shown as percentage of the total phospholipid (PL) as molar ratio of cholesterol (in mammals, blue) and ergosterol (in yeast, light blue). The site of synthesis is shown for major phospholipids (blue) and lipids that are involved in signaling (red). Abbreviations are explained in Table 1.1 and the given reference. *R* are remaining lipids. Image reproduced from Meer et al. [18]. 5

1.5 **Model of the plasma membrane in full complexity:** A large variety of embedded proteins, actin, cytoskeleton, ions, and solutes are shown. Image reproduced from Marrink et al. [27]. 7

1.6 **Effect on membrane fluidity on cancer metastasis:** Four independent datasets showing the percentage of human breast cancer patients free of distant metastasis over time. ABCA1 is a membrane cassette transport protein which serves as a cholesterol efflux channel and therefore reduces the membrane fluidity. Image reproduced from Zhao et al. [32]. 8

2.1 **Commonly used interfacial rheometry setups: A)** ISR with inset showing magnetic needle and glass channel (reprinted with permission from [80] © 2011 American Chemical Society), **B)** DWR and **C)** bicone. **D)** Modification of small DWR and cup (reproduced from [2] with permission from The Royal Society of Chemistry). 20

2.2 **Representative data set of an ISR experiment:** Primary observables **A)** Current $I(t)$ and displacement $z(t)$ in the time domain. **B)** Current signal in the frequency domain $|\hat{I}(f)|$ indicating I_0 and I_{noise}. **C)** Displacement signal in the frequency domain $|\hat{z}(f)|$ indicating z_0 and z_{noise}. Dots represent integer harmonics of the fundamental. 27

2.3 **Current and displacement signal amplitudes and the respective noise for the ISR:** data for hexadecanol at different surface pressure at the water-air interface measured with the ISR at $f = 0.1\,\text{Hz}$ as a function of input voltage of the function generator (V peak-to-peak). **A)** Current signal amplitude I_0 and noise I_{noise}. **B)** Position signal amplitude z_0 and noise z_{noise}. Big symbols and solid lines are signals, small symbols and dashed lines are noise while open and closed symbols denote the magnification of the objective (4× and 10×, respectively). The magnetic probe MW (microwire) and N (needle) is specified in the legend. 29

2.4 **Torque, strain and noise for the DWR (small diameter ring in conjunction with a Langmuir trough) and bi-cone: A)** Torque M_0 and **B)** displacement θ_0 signal amplitudes as a function of input torque for stress controlled experiments. *Closed loop* uses a feedback loop to avoid drift in $\theta(t)$. **C)** M_0 and **D)** θ_0 as a function of displacement for strain controlled experiments. Noise is shown as small symbols with dashed lines as well as error bars. Large symbols and solid lines are signal amplitudes. Min and max lines correspond to S/N = 5. Hexadecanol at different surface pressures at the water-air interface measured at $f = 0.1\,\text{Hz}$. . . . 30

2.5 **Uncertainties of $|G_s^*|$ and δ_s measured with the ISR:** Data from Fig. 2.3 and corrected for bulk flow effects. **A)** $|G_s^*|$ and δ_s measured with the microwire. **B)** $|G_s^*|$ and δ_s measured with the needle, for different surface pressures and corresponding uncertainties calculated by Eq. (2.22) & (2.23). Open and closed symbols correspond to different magnifications of the objective (4× and 10×, respectively). 33

2.6 **Operating window for the ISR:** $|G_s^*|$ as function of interfacial stress amplitude **(A)** and interfacial strain amplitude **(B)**. Limits are defined in Table 2.4. The overlayed experimental data shows hexadecanol at the water-air interface measured at $f = 0.1\,\mathrm{Hz}$ at different surface pressures indicated by small numbers. Error bars on the data are the calculated S/N ratios and symbols are filled for S/N $\geq$ 10. Lines for $|Bq^*| = 10$ for the microwire (MW) and needle (N) are drawn to guide the eye and the direction of increasing $|Bq^*|$ is indicated by arrows. Examples of maximal and minimal measurable $|G_s^*|$ are indicated for the needle as $|G_{s,\max}^*|$ and $|G_{s,\min}^*|$. 35

2.7 **Operating windows for the DWR (small diameter ring in conjunction with a Langmuir trough):** $|G_s^*|$ as function of **(A)** interfacial stress amplitude and **(B)** interfacial strain amplitude. The overlayed experimental data shows hexadecanol at the water-air interface measured at $f = 0.1\,\mathrm{Hz}$ and $\pi = 25\,\mathrm{mN\,m^{-1}}$ and are linked to the operation mode by the color code. Error bars denote S/N ratios of $|G_s^*|$ and filled symbols show S/N $\geq$ 10. Lines showing $|Bq^*| = 10$ are drawn for the DWR and bi-cone to guide the eye and the direction of increasing $|Bq^*|$ is indicated by the arrow. The magnitude of the contribution of the instrument and geometry inertia is indicated with the dashed line. 37

2.8 **Effects of Instrument inertia:** Frequency sweeps of hexadecanol at $\pi = 25\,\mathrm{mN\,m^{-1}}$ measured by the small diameter DWR in conjunction with a Langmuir trough (blue circles) and ISR (red squares). **A)** $|G_s^*|$ and **B)** δ_s. Open symbols are raw data and closed symbols are inertia and subphase flow corrected data. The solid lines $I_\square$ correspond to Eq. (2.28) for the ISR, small DWR and bi-cone. 39

2.9 **Uncertainty of subphase correction:** Error of the magnitude $|Bq^*|$ (**A**) and phase angle δ_s (**B**) for defined Bq^*. Filled and empty symbols correspond to the non-linear and linear subphase correction of the ISR. Parameters of the microwire are used. 45

2.10 **Contact line variations leading to an apparent surface elasticity:** Data of a clean water-air interface measured with the small DWR in conjunction with a Langmuir trough and closed-loop stress controlled mode at $f = 0.1\,\mathrm{Hz}$. **A)** Norm and **B)** phase angle of complex interfacial modulus G_s^*. The operating window is shown in green and $|Bq^*| = 100$ is indicated to guide the eye. The pictures are taken at different times during an oscillation. 48

2.11 **Operating windows for ISR and the small diameter DWR:** as function of **(A)** interfacial stress and **(B)** interfacial strain. The overlaid experimental data show the response of hexadecanol at the water-air interface at different surface pressure and $f = 0.1\,\mathrm{Hz}$. The small diameter ring is used in conjunction with a Langmuir trough. 50

2.12 **Compression isotherm of hexadecanol:** Surface pressure π as function of mean molecular area MMA at $T = 23\,^{\circ}\mathrm{C}$. 52

2.13 **Comparing operation modes of the DWR:** hexadecanol at $\pi = 25\,\mathrm{mN\,m^{-1}}$ and $0.1\,\mathrm{Hz}$ measured with the small diameter ring in conjunction with a Langmuir trough. *Top:* $M(t)$ and $\theta(t)$ *Middle:* Fourier transform of $M(t)$. *Bottom:* Fourier transform of $\theta(t)$. Dots indicate integer harmonics of the signal. 53

2.14 **Operating windows for the small and big DWR** as function of input interfacial stress amplitude τ_s and input interfacial strain amplitude γ_s. Limits determined for a clean water-air interface and at a driving frequency $f = 0.1\,\mathrm{Hz}$. The small diameter ring is used in conjunction with a Langmuir trough. $|Bq^*| = 10$ is indicated to guide the eye. 54

3.1 **Structural formulas of phospholipids:** *(a)* DPPC, *(b)* DOPC, *(c)* NBD-PPC (tail labeled DPPC), *(d)* DPPE-Rhod (head labeled DPPC), and *(e)* DOPE-Rhod (head labeled DOPC). 59

3.2 **Fluo-ISR:** A custom built device combines a Langmuir trough with a polyurethane coating indicated by the green color, interfacial needle shear rheometer, and upright epi-illumination fluorescence microscope. The detailed view in **(A)** is shown enlarged in **(B)**. 61

3.3 **Protocol for obtaining a thermally structured interface:** Interfacial pressure π and temperature T as a function of time t for DPPC at **(A)** water–air and **(B)** buffer–oil. The spreading of DPPC is marked with a red asterisk and the interface is annealed at $T > T_{m,\mathrm{DPPC}}$ for at least 10 min. The shown examples prepare for compressions at 25 °C. 63

3.4 **DPPC at W/A and 25 °C: A)** Interfacial pressure (π) as a function of mean molecular area (MMA) with solid and dashed lines as compression and expansion, respectively. **B)** Compression of the same color as a function of time (t). Fluorescent images with the tail labeled NBD-PPC (**C** & **D**) at the position marked by the triangles in **(A)**, and head labeled DPPE-Rhod (**D** & **E**). The numbers denote the interfacial pressures in $\mathrm{mN\,m^{-1}}$. Solid dots in **(A)** & **(B)** mark the locations of ISR experiments. 65

3.5 **DPPC at B/A and 25 °C: A)** Interfacial pressure (π) as a function of mean molecular area (MMA) with solid and dashed lines as compression and expansion, respectively. **B)** Compression of the same color as a function of time (t). Fluorescent images with the head labeled DPPE-Rhod (**C**, **D** & **E**) at the position marked by the triangles in **(A)**. The numbers denote the interfacial pressures in $\mathrm{mN\,m^{-1}}$. Solid dots in **(A)** & **(B)** mark the locations of ISR experiments. 67

3.6 **DPPC at W/O and 25 °C: A)** Interfacial pressure (π) as a function of mean molecular area (MMA) with solid and dashed lines as compression and expansion, respectively. **B)** Compression of the same color as a function of time (t). Fluorescent images with the head labeled DOPC-Rhod (**C** & **D**) at the position marked by the triangles in **(A)**. The numbers denote the interfacial pressures in $\mathrm{mN\,m^{-1}}$. **E)** Image taken after a second annealing at fully open barrier position. Solid dots in **(A)** & **(B)** mark the locations of ISR experiments. 69

3.7 **DPPC at B/O and 25 °C: A)** Interfacial pressure (π) as a function of mean molecular area (MMA) with solid and dashed lines as compression and expansion, respectively. **B)** Compression of the same color as a function of time (t). Fluorescent images with the head labeled DOPC-Rhod (**C**, **D**, **E**, and **F**) at the position marked by the triangles in **(A)**. The numbers denote the interfacial pressures in $\mathrm{mN\,m^{-1}}$. Solid dots in **(A)** & **(B)** mark the locations of ISR experiments. 71

3.8 **Compression rate variation: A)** Compression isotherms of DPPC at B/O interface and 25 °C with different compression rates on the same interface. Solid and dashed lines represent compression and expansion, respectively. The annotation labels the first compression. **B)** enlarged version of **(A)** with the first compression shown as dashed line and the filled circles mark the first observation of LC phases. **C)** Fluorescence microscopy images at $\pi = 28\,\mathrm{mN\,m^{-1}}$ where the compression speed is given in each frame in $\mathrm{mm\,min^{-1}}$. The interface was annealed ($T > 42\,°\mathrm{C}$ for at least 10 min) in between each compression. 73

3.9 **Compression isotherms at 25 °C:** A representative example of each DPPC system showing interfacial pressure (π) as a function of mean molecular area (MMA). 74

3.10 **Frequency sweep of DPPC monolayers at 25 °C:** Complex interfacial shear viscosity η_s^* as a function of frequency f in the linear viscoelastic regime. Data shown in two representations *top:* as norm and phase angle ($|\eta_s^*|$, δ_s) and *bottom:* as viscous and elastic contributions (η_s', η_s'') to η_s^*. The numbers show the interfacial pressure in $\mathrm{mN\,m^{-1}}$ of each measurement. Empty symbols show repetitions of the same test. 75

3.11 **Fluorescent images of DPPC: (A)** W/A with NBD-PPC (& E with DPPE-Rhod), **(B)** B/A with DPPE-Rhod, **(C)** W/O with DOPE-Rhod, **(D)** B/O with DOPE-Rhod. Images taken at 25 °C and compressed to a surface pressure of $20\,\mathrm{mN\,m^{-1}}$. 77

3.12 **Stress amplitude sweep of DPPC monolayers:** Complex interfacial shear viscosity η_s^* as a function of interfacial stress τ_s. Data shown in two representations *top:* as norm and phase angle ($|\eta_s^*|$, δ_s) and *bottom:* as viscous and elastic contributions (η_s', η_s'') to η_s^* at 25 °C and 40 mN m^{-1} apart for the B/A interface, which was measured at 20 mN m^{-1}. All measurements were conducted at $\omega = 3\,\mathrm{rad\,s^{-1}}$. 78

3.13 **Temperature dependence on compression isotherms:** DPPC at **(A)** W/A and **(B)** B/O at different temperatures. The filled symbols identify the ISR experiments shown in Fig. 3.14 and 3.17. 79

3.14 **Interfacial rheology of DPPC at W/A:** Norm and phase angle of the complex interfacial shear viscosity as a function of frequency. Empty symbols are repetitions with different stress amplitudes, dashed lines are test after an amplitude sweep. The numbers denote the interfacial pressure in mN m^{-1}. 80

3.15 **Temperature effect on phase morphology at W/A:** DPPC at **(A)** 15 °C, **(B)** 20 °C, **(C)** 25 °C, and **(D)** 30 °C. All images were captured at $\pi = 20\,\mathrm{mN\,m^{-1}}$ and all samples used the tail labeled NBD-PPC lipid. . . 82

3.16 **Shear banding:** DPPC at W/A at **(A)** 25 °C and **(B)** 30 °C towards the end of the compression at 30 mN m^{-1}. 83

3.17 **Interfacial rheology of DPPC at B/O:** Norm and phase angle of the complex interfacial shear viscosity as a function of frequency. Empty symbols are repetitions with different stress amplitudes, dashed lines are test after an amplitude sweep. The numbers denote the interfacial pressure in mN m^{-1}. 83

3.18 **Temperature effect on phase morphology at B/O:** DPPC at **(A)** 20 °C, **(B)** 25 °C, **(C)** and **(D)** 30 °C. All images were captured at $\pi =$ 20 mN m^{-1} apart from **(D)** at 30 mN m^{-1} and all samples used the head labeled DOPE-Rhod lipid. 84

4.1 **Temperature induced phase separation:** Interfacial pressure π and temperature T as a function of time t. The procedure is composed of spreading, heating, compression, and stepwise cooling and measuring of the interfacial rheology. A pure DPPC monolayer at the buffer–oil interface is shown in this example. The microscopy images are taken at the times indicated by the filled circles and the scale bar corresponds to 100 µm. . 92

4.2 **Interfacial rheology of DPPC undergoing temperature induced phase separation:** Norm of the complex interfacial shear viscosity and phase angle. **(A)** Stress amplitude sweeps and **(B)** frequency sweep of DPPC at buffer–oil. 93

4.3 **Comparison between sample preparations:** Norm of the complex interfacial shear viscosity η_s^*, phase angle δ_s, and area fraction of the liquid condensed phase ϕ as a function of **(A)** surface pressure, **(B)** inverse temperature. *comp:* interfacial pressure and *temp* temperature induced phase separation, respectively. 95

4.4 **Rheology of mixed lipid monolayers:** viscous (η_s', closed symbols) and elastic (η_s'', open symbols) contribution to the complex interfacial shear viscosity of lipid mixtures at the buffer–oil interface as function of (**A**) interfacial stress amplitude τ_s at 20 °C and $3\,\mathrm{rad\,s^{-1}}$, and (**B**) frequency at small strains ($\gamma_s < 2\,\%$) and 25 °C. All samples were measured at $\pi = 40\,\mathrm{mN\,m^{-1}}$ apart from the largest DOPC concentration at $\pi = 45\,\mathrm{mN\,m^{-1}}$. The weight fraction of DOPC is indicated by χ_{DOPC}. **C**) Fluorescence microscopy images correspond to the data in B with χ_{DOPC} indicated in each upper left corner. The scale bar represents 100 µm and all samples contained 0.5 mol % of DOPE-Rhod. 96

4.5 **Crowding of the lipid monolayers:** norm of the complex interfacial shear viscosity η_s^* of DPPC-DOPC mixtures at the buffer–oil interface, rescaled by a calculated medium viscosity $\eta_{s,M}$, as a function of area fraction of the liquid condensed phase ϕ. The weight fraction of DOPC is indicated by χ_{DOPC}. All data is at $\pi = 40\,\text{mN}\,\text{m}^{-1}$ apart from the largest DOPC concentration at $\pi = 45\,\text{mN}\,\text{m}^{-1}$. The solid and dashed lines represent a Krieger-Dougherty equation with intrinsic viscosities $[\eta_s]' = 2$ (hard disks) and $[\eta_s]' = 5$, respectively. Both use $\phi_{\text{max}} = 0.906$ for maximum packing of disks in two dimensions. 99

4.6 **Comparison to lipid bilayers: (A)** Mean squared displacement $\langle r^2 \rangle$ as a function of lag time t showing the translational diffusive motion of LC domains in monolayers **(C)** and bilayers **(D)**. The dashed line shows the fit and the inset is the same data with axes in linear scale. **(B)** predictions of the Saffman-Delbrück model Eq. (4.3) for the two systems. Horizontal lines show the measured diffusion coefficients. 102

A.1 **Calibration ISR:** Amplitude ratio and phase angle of the microwire measured on a clean water-air interface. The fit is shown as dashed line with open symbols. Error bars show the standard deviation of three measurements. 129

A.2 **Calibration ISR:** The contributions to the amplitude ratio of the clean water-air interface: real and imaginary parts of the subphase drag, compliance and needle inertia. Open symbols denote positive sign before plotting the absolute values $|\dots|$. 130

A.3 **Calibration ISR:** Maximum residue S plotted as function of instrument compliance k^{-1} and constant E. The minimum is labeled with the black dot. 131

A.4 **Drift dominated data set of an ISR experiment:** Primary observables **A:** Current $I(t)$ and displacement $z(t)$ in the time domain. **B:** Current signal in the frequency domain $|\hat{I}(f)|$ indicating I_0 and I_{noise}. **C:** Displacement signal in the frequency domain $|\hat{z}(f)|$ indicating z_0 and z_{noise}. Dots represent the integer harmonics of the fundamental. 132

A.5 **Noise of different DWR diameters:** Data measured at the clean water-air interface at $f = 0.1\,\mathrm{Hz}$. **A:** Torque amplitudes M_0 and **B:** displacement amplitudes θ_0 as a function of input torque for closed loop stress controlled experiments. **C:** Torque amplitudes M_0 and **D:** displacement amplitudes θ_0 as a function of input displacement for strain controlled experiments. Small symbols and error bars correspond to noise values. 133

A.6 **Effect of driving frequency on noise of the small DWR:** Data measured at the clean water-air interface. **A:** Torque amplitudes M_0 and **B:** displacement amplitudes θ_0 as a function of input torque for stress controlled experiments. **C:** Torque amplitudes M_0 and **D:** displacement amplitudes θ_0 as a function of input displacement for strain controlled experiments. Small symbols and error bars correspond to noise values. Open and closed symbols denote open and closed loop, respectively. . . 134

A.7 **Strain amplitude controlled mode of the bi-cone (Anton Paar):** hexadecanol at $\pi = 45\,\mathrm{mN\,m^{-1}}$ and $f = 0.1\,\mathrm{Hz}$. *Top:* $M(t)$ and $\theta(t)$ *Middle:* Fourier transform of $M(t)$. *Bottom:* Fourier transform of $\theta(t)$. Only the last oscillation period is analyzed. 135

A.8 **Stress amplitude controlled mode of the bi-cone (Anton Paar):** hexadecanol at $\pi = 45\,\mathrm{mN\,m^{-1}}$ and $f = 0.1\,\mathrm{Hz}$. *Top:* $M(t)$ and $\theta(t)$ *Middle:* Fourier transform of $M(t)$. *Bottom:* Fourier transform of $\theta(t)$. Only the last oscillation period is analyzed. 136

A.9 **Amplitude and noise for the bi-cone (Anton Paar) in stress and strain controlled mode:** data for hexadecanol at the water-air interface at $\pi = 55\,\mathrm{mN\,m^{-1}}$ and $f = 0.1\,\mathrm{Hz}$. **A:** Torque amplitudes M_0 and **B:** displacement amplitudes θ_0 as a function of input torque for stress controlled experiments. **C:** Torque amplitudes M_0 and **D:** displacement amplitudes θ_0 as a function of input displacement for strain controlled experiments. Small red symbols and error bars correspond to noise values. 137

A.10 **Repeat experiment of Fig 9 of the manuscript:** Open loop torque controlled frequency sweep of hexadecanol at $\pi = 25\,\mathrm{mN\,m^{-1}}$ measured with the small DWR. **A:** norm and **B:** phase angle of the complex interfacial shear modulus. **C:** Elastic and viscous component of the complex interfacial shear modulus. **D:** Displacement amplitude. The torque amplitude was adjusted for the four data sets to ensure $\theta > \theta_{\mathrm{min}}$. 140

A.11 **Compliance of small DWR**: The averaging is done over the filled blue symbols and represented by the black solid line. A picture of the glued ring is shown on the right hand side. 141

A.12 **Error propagation for Bq^* in the subphase correction code**. The solid lines show modified magnitude of F/z, dashed lines show modified phase of F/z and the dotted lines show the value at $\Delta = 0$. **A:** Uncertainty of resulting $|Bq^*|$, **B:** Uncertainty of resulting δ_s at **I** $\delta_{\mathrm{defined}} = 0°$, **II** $\delta_{\mathrm{defined}} = 45°$ and **III** $\delta_{\mathrm{defined}} = 90°$, ... 142

A.13 **Vertical misplacement of the DWR:** The gap is varied as shown in the legend during open loop stress amplitude sweeps of hexadecanol at $\pi = 25\,\mathrm{mN\,m^{-1}}$ at the water-air interface with the small DWR at $f = 0.1\,\mathrm{Hz}$. Data is not corrected for bulk flow. The gray region shows 20 % of the zero position. 143

A.14 **Effect of contact angle variations:** Calculated uncertainties of the subphase correction. 144

A.15 **Horizontal misplacement of the DWR:** The small DWR cup is displaced away from the optimal position as shown in the legend during open loop stress amplitude sweeps of hexadecanol at $\pi = 25\,\mathrm{mN\,m^{-1}}$ at the water-air interface and $f = 0.1\,\mathrm{Hz}$. Data is not corrected for bulk flow. G_s' and G_s'' are shown as solid lines with closed symbols and dashed lines with open symbols, respectively. 145

B.1 **Inductance of the magnetic coils:** Phase shift δ of the current signal measured in parallel to the magnetic coils as a function of frequency f at three signal amplitudes. 147

B.2 **Effect of magnetic inductance in applied frequency range:** The ISR data in Fig. 2.8 is corrected for the shift measured in Fig B.1. 148

B.3 **Brewster angle microscope: A)** Compression isotherm of DPPC at water–air and 25 °C without temperature treatment prior to compression. **B)** Brewster angle microscopy images corresponding to the filled circles in **(A)**. The MMA is indicated in upper left corner of each image in units of Å^2/molecule. 149

B.4 **Second compression of DPPC at water–air: A)** Two consecutive compression isotherm of DPPC at water–air and 25 °C. Solid and dashed lines correspond to compression and expansion, respectively. **B)** Thermal annealing between the two compressions shown in **(A)**. 150

B.5 **Second compression of DPPC at buffer–air:** Two consecutive compression isotherm of DPPC at buffer–air and 25 °C. The arrows indicate the compression. No thermal annealing has been performed between the two compressions. 151

B.6 **Second compression of DPPC at water–oil: A)** Two consecutive compression isotherm of DPPC at water–oi and 25 °C. Solid and dashed lines correspond to compression and expansion, respectively. **B)** Thermal annealing between the two compressions shown in **(A)**. 152

B.7 **Compression without annealing:** Compression isotherms of DPPC at water–air without previous annealing. 153

C.1 **Stress amplitude sweep of DPPC monolayers:** complex interfacial shear modulus as a function of resulting strain amplitude γ_s. 157

C.2 **Step compression:** Interfacial stress π as a function of time t of pure DPPC at the buffer–oil interface during a step compression in a Langmuir trough. The fluorescent microscopy images are acquired at the times indicated by the arrows and the scale bar represents 100 µm. ISR experiments are conducted at the red points. 158

C.3 **Particle tracking on monolayers:** DPPC/DOPC of 3/2 as a monolayer at the buffer–oil interface. Mean squared displacement (MSD) as a function of lag time. The fitted D corresponds to the short-time diffusion coefficient of the single-particle data. Data is de-drifted. 159

C.4 **Particle tracking on bilayers:** DPPC/DOPC of 3/2 as a bilayers. Mean squared displacement (MSD) as a function of lag time. The fitted D corresponds to the short-time diffusion coefficient of the single-particle data. The fit is shown by the red line. *Left:* Raw data. *Right:* Data is de-drifted. 160